White-Noise Studies in the Fly Lamina

Andrew Charles James

THE AUSTRALIAN
LIBRARY
NATIONAL UNIVERSITY

A thesis submitted for the degree of Doctor of Philosophy of the

Australian National University

Canberra, July 1990

Declaration

The electrophysiological recordings used in this thesis were made with the technical assistance of Dr Daniel Osorio, as described in section 2.5. All other aspects of the thesis are entirely my own work.

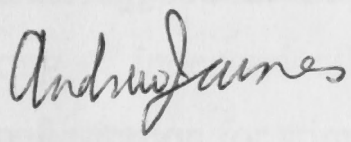

Andrew James

Acknowledgments

I would like to thank Daniel Osorio for his pleasant and effective collaboration; I thank MV Srinivasan for his careful reading of the manuscript, and I thank Adrian Horridge for inviting me to come to Canberra, and for making everything possible in the vision group.

Lastly, I thank the many members of the ANU community who provided suggestions, conversations and diversions throughout the project.

Abstract

Intracellular recordings were made from the photoreceptors and large monopolar cells of the fly visual system. Two species of fly were used, *Eristalis tenax* and *Calliphora vicina*.

Binary white-noise stimuli were presented at a frame-rate of $500\,Hz$, at two mean levels of illumination. Two spatial configurations were used: a 15×15 array of independently modulating square checks, and a dual channel spot-annulus configuration for stimulation of receptive field centre and surround.

Kernel estimation is formulated in terms of linear regression, and the least-squares estimates of the kernels are obtained by correcting the cross-correlation estimates by an iterative procedure.

Linear spatiotemporal kernels are derived from the checkerboard stimulus, characterising in detail the dynamic image processing operations taking place in the initial stages of the visual system. The on-axis LMC kernel is biphasic, producing temporal high-pass filtering. The LMC kernel is not space-time separable. Spatial antagonism is weaker than antagonism in time, and is more variable between cells, involving a broadening in space of the later, antagonistic phase of the kernel, and in some cases the presence of laterally extending antagonistic regions at shorter latency.

The strength of antagonism as a function of spatial location is examined by means of simulated step-responses. In general, this indicates the presence of two antagonistic regions, arranged horizontally or diagonally relative to the receptive field centre.

Simulation of electrical circuits modelling the flow of current in the receptor-lamina array indicates that when the capacitance of elements is taken into account both the lateral antagonism and the temporal high-pass filtering can be explained in terms of the fluctuation of extracellular potential within lamina cartridges.

For the spot-annulus experiments, kernels are estimated to second degree in centre and surround and to third degree in centre alone. Nonlinear components contribute

around 5% of signal power in the receptor responses and around 20% in the LMC responses. For the LMCs, linear and cubic kernels exhibit comparable time-courses, while the equivalent parts of the quadratic kernels have shorter latencies. The LMC quadratic kernel appears to have two components, which vary in relative amplitude.

A number of structural models are considered. Tests indicate that none of the kernel sets can be fitted by a single cascade of linear, static nonlinear and linear mappings. A compact notation for representing polynomial time-invariant operators is devised, allowing fluent expression and manipulation of models in terms of networks of operators. Models are fitted decomposing the LMC response into a transduction step, represented by the receptor response, and transmission steps. Stimulation in the surround appears to have two effects: optical cross-talk to the central receptors, and a component transmitted from the surrounding receptors with some additional delay.

Analysis of the statistical properties of signal and noise in the response indicates that the LMC signal is generally skewed towards positive values, and that noise in the LMC is not additive, having less power when the signal has positive value.

The relationship between quadratic nonlinearities and light adaptation of the linear dynamics is examined.

The results are summarised in terms of the empirical findings, the implications for underlying mechanisms and the function of the system, and some comments are made on the system identification techniques used.

Contents

Chapter 1

Introduction

1.1 The study of insect visual systems

The first question that one might ask is why study the visual systems of insects at all. For me the answer follows three steps of logic. Firstly, nervous systems are fascinating systems to study, being the domain where intelligence seems most clearly to meet the physical world. They are also systems of exceptional complexity, seemingly including more levels of organisation than any other considered by science, and inherently involving topics of great current interest such as nonlinear dynamics, complexity theory, and, from the point of view of technological application, the processing of information by parallel architectures.

Given this complexity, empirical research into neurobiological systems faces great methodological difficulties; there are immense numbers of active elements, of tiny size. Multiple unit recordings and optical techniques are appearing, but most physiological work still proceeds with the recording of a single unit's activity. With this paucity of output data it is desirable to maximise the complexity and control with which stimulation may be applied, and the study of visual systems achieves this. Visual systems take a very high-dimensional input; the fluctuation of radiant energy over space and time. With computer graphics technology, finely controlled presentation of complex stimuli is possible. The amount of information that can be extracted from the system is thus potentially greater than in the study of a system accepting a simpler input.

Finally, the use of insects for study has a number of advantages. The systems are simpler than vertebrates, both in the number of anatomical elements and in the range of

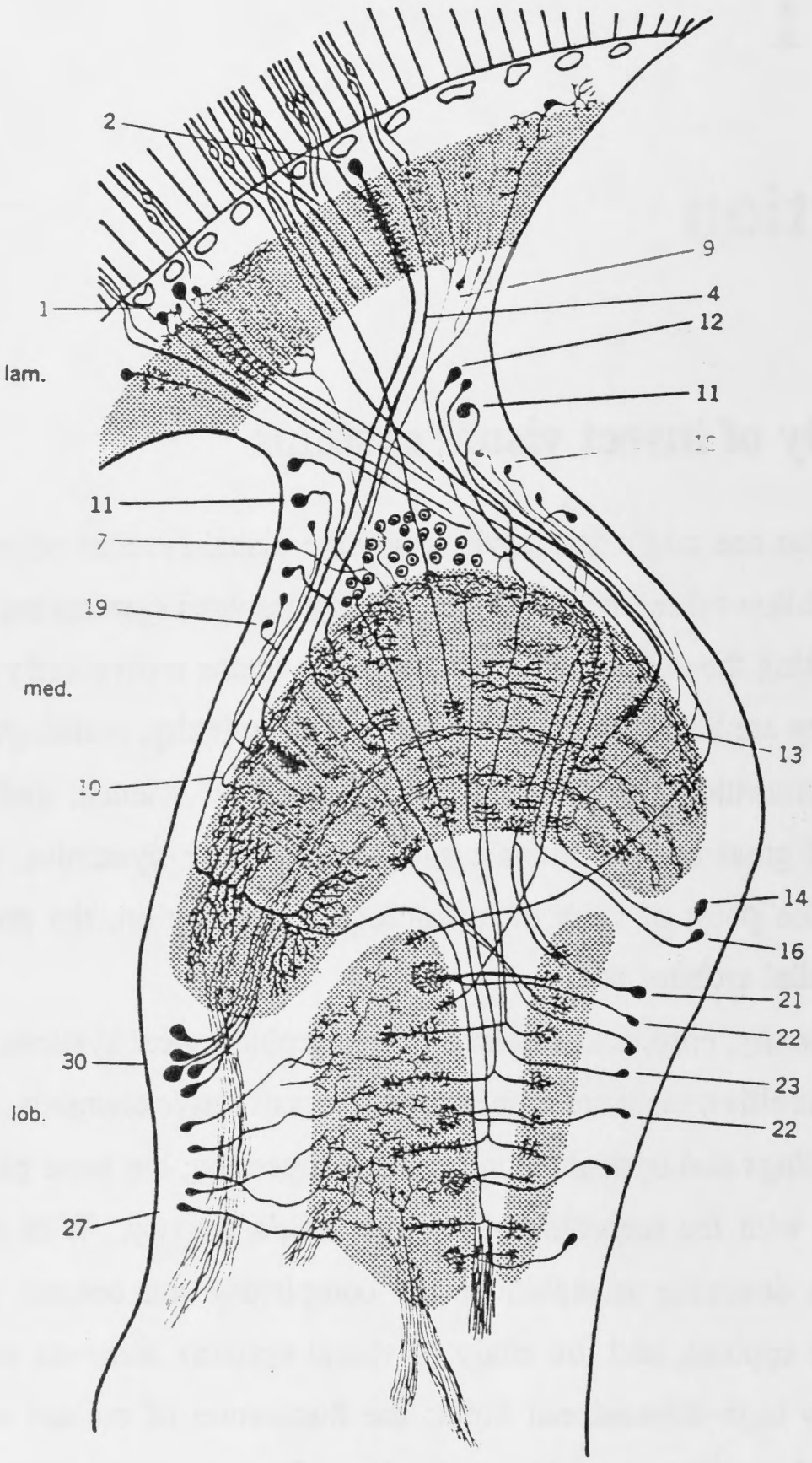

Figure 1: The optic lobe of the fly *Calliphora*. The three optic ganglia indicated are the *lamina*, the *medulla* and the *lobula*. A large monopolar cell (LMC) is labelled number 2. Reproduced from Bullock and Horridge (1965), adapted from Cajal and Sánchez (1915).

behaviours produced. They also have much greater regularity, with identical topologies of neurons found across individuals of a species, as well as within the individual, where certain groups of neurons are repeated identically across arrays. Conversely, the diversity of the insect world gives extensive scope for comparative studies. The use of insects in experimentation also reduces the impact of many complications, both technical and philosophical.

The experimental methodology used in this study is that of system identification. The essence of this approach is the representation of system behaviour in terms of mathematical mappings from system inputs to system outputs, where inputs and outputs are considered as quantities varying dynamically with time.

Vision may be studied at a range of levels. In the initial stages of the system it can be treated as a biophysical transduction process, while the overall faculty in higher animals clearly involves all aspects of intelligence, including the role of knowledge in perception and the direction of attention of the observer. This thesis deals with early visual processing, by the photoreceptors and the first-order interneurons in visual systems, where it is assumed that quantitative models treating the systems as mappings between input and output are still valid.

The thesis thus seeks to develop quantitative descriptions of the behaviour of these classes of neurons in response to visual stimulation, which will allow interpretation in terms of the underlying mechanisms, and in terms of the function of this subsystem within the overall visual system of the fly.

1.2 Anatomy of the fly visual system

The data for this study are drawn from two species of fly, both belonging to the order Diptera: the drone fly *Eristalis tenax*, a honeybee mimic which can be captured on flowering bushes during the Summer months in Canberra, and the blowfly *Calliphora vicina*, raised in captivity for year-round study.

The relevant anatomical features of these visual systems will now be described, following mainly the reviews of Shaw (1981, 1984), Laughlin (1981a) and Hardie (1985). A number of published diagrams are reproduced for the reader's convenience.

The compound eye of the fly is covered by a cornea consisting of an array of facets, around five thousand per eye in *Calliphora* (Hardie 1985), giving a field of view

Fig. 2. The precision 'wiring' pattern of the photoreceptors on to the first synaptic region in a cyclorrhaphid fly like *Musca*, used to increase light-capture efficiency. The receptors in every ommatidium are ordered in the particular trapezoidal pattern of Fig. 1*c*. Shown at the left, six ommatidia (three shown in detail) lying in exactly this same trapezoidal formation, send one axon each into a particular synaptic column or cartridge. Note that the parent cells participating in this projection, R1–R6, occupy the same position in the ommatidia that their ommatidium holds in the larger pattern; this ensures that only the six receptors with identical lines of sight combine information at each single cartridge. To achieve the proper convergence on each column, the axons from a *single* ommatidium must diverge and interweave amongst their neighbours, as shown for the ommatidium at the right. Because a simple positive lens like that of the fly facet rotates the image through 180° on to the rhabdomeres, the required divergence geometry is into a trapezoidal arrange of cartridges that is 180° rotated from the pattern of rhabdomeres. This is achieved by a 180° twist imparted during morphogenesis on the axon bundles, as shown. R7–R8 grow directly through the lamina without making synapses. The outline of a cartridge with its two large monopolar cells L1 and L2 is shown at the bottom; for detailed structure, see Fig. 3.

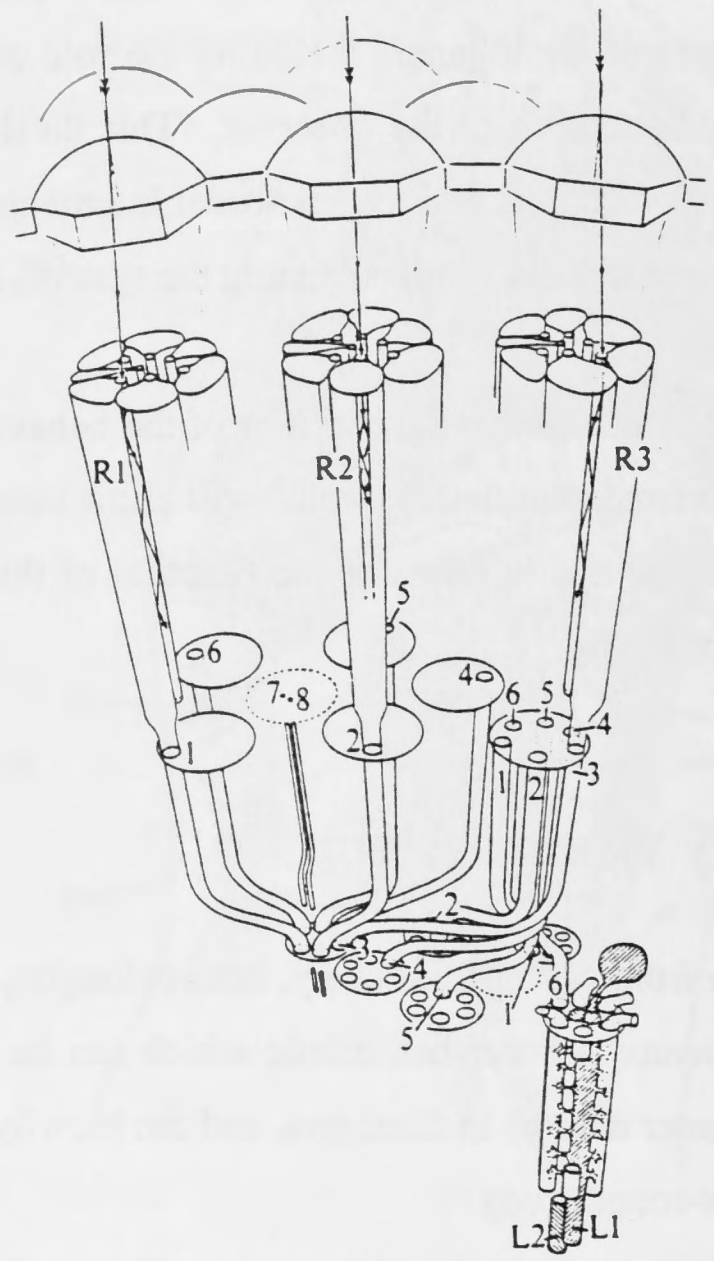

Figure 2: Arrangement of receptors within the retina and their projection to the lamina. Reproduced from Shaw (1981).

covering all the surrounding sphere of space except for a small blind spot directly behind the animal.

Behind each facet of the cornea lies a group of eight photoreceptors, forming an *ommatidium* (little eye). With certain variations between regions, the structure of the ommatidium is repeated across the eye. The two subsequent neuropiles, termed the *lamina* and the *medulla*, also consist of well-defined arrays of units in one-to-one correspondence with the ommatidia of the retina. The optic lobe of the fly *Calliphora* is illustrated in figure 1.

1.2.1 Retina and retina-lamina projection

Figure 2 illustrates the arrangement of receptors within the retina and their projection to the lamina. Behind the optical apparatus the eight photoreceptors are oriented perpendicular to the cornea. Light is absorbed in an optical waveguide structure termed the *rhabdomere* formed by around 10^4 *microvilli* projecting along the side of each receptor towards the centre of the ommatidium.

In most insect orders the microvilli of the eight receptors are stacked together to form one waveguide, the *fused rhabdom*, whereas here the receptors maintain separate waveguides, and hence have differing fields of view. The receptors denoted R1 to R6 extend down the full length of the ommatidium. Five of them lie on the vertices of a hexagon, with the receptor denoted R3 lying eccentrically. At the centre of this hexagon is another waveguide, the distal part consisting of the rhabdomere of R7, and the proximal part being the rhabdomere of R8.

Forming the proximal boundary of the retina is the *basement membrane*, a complex structure of cellular and extracellular components, with oval fenestrations through which the receptor axons pass to the lamina. The axons of R1–6 form large terminals, ending in the lamina, while the slender axons of R7 and R8 pass through the lamina without making synaptic contacts to end in the medulla. An exception occurs in the medio-dorsal region of the males of some species, where R7 terminates like R1–6. Recordings from receptor cells in this study are all made within the lamina, and are assumed to be from the larger terminals rather than from the axons of R7–8.

The divergence of field of view of the receptors within an ommatidium closely corresponds to the divergence of optical axes of neighbouring facets due to the curvature of the eye. The axons of receptors sharing the same field of view are

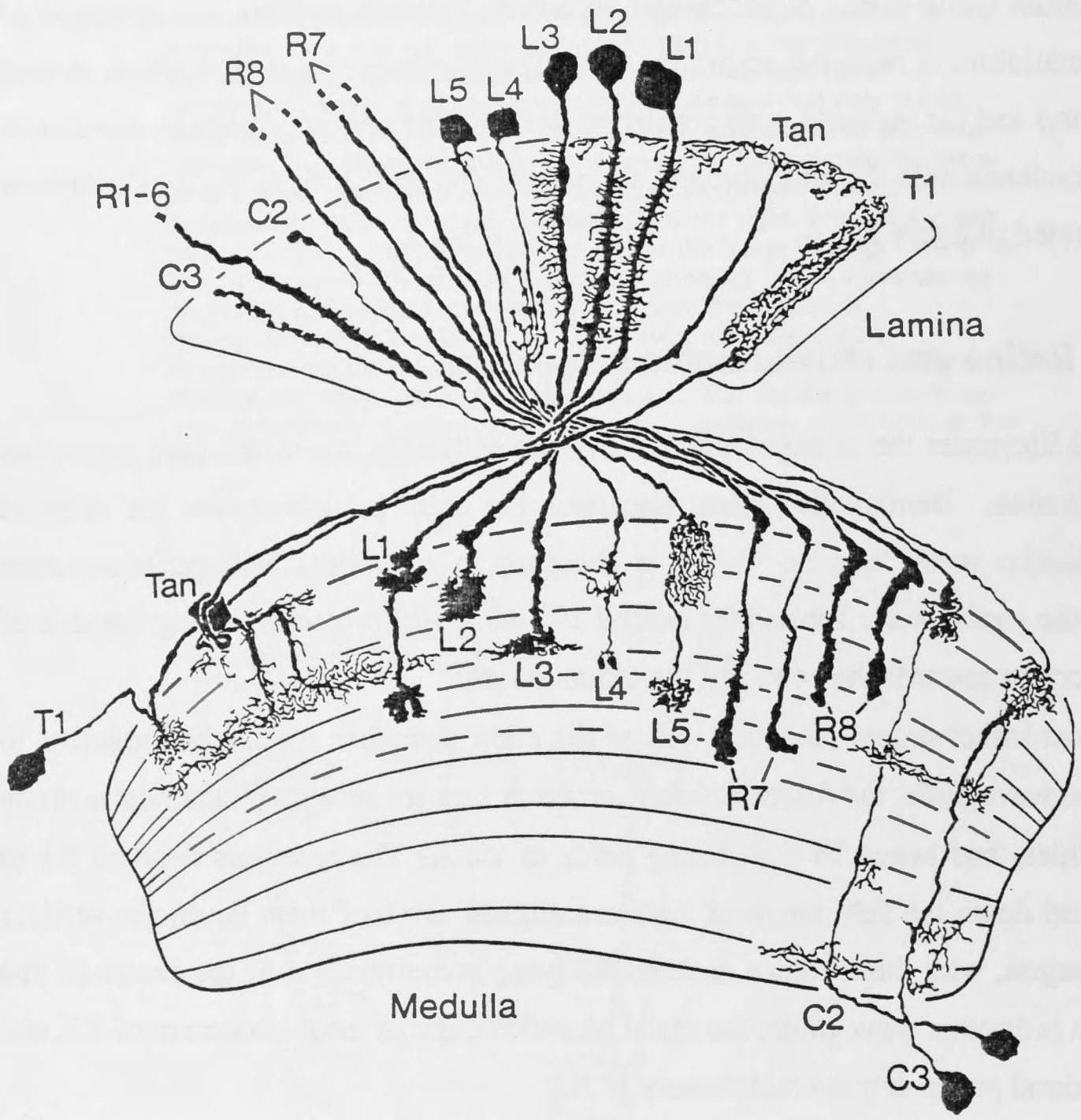

Fig. 4. The neuronal types of the *Drosophila* lamina, based originally upon a Golgi study by Fischbach (1983). Most of the cells are immediately recognizable from the descriptions of similar neurons by Strausfeld (1976), from calyptrate flies like *Musca*. Differences occur in the branching of L4 (see Fig. 5), in the more uniform distribution of L3's neurites, and in the radically different medulla arborization of C3, but most of the neurons are remarkably similar to those of *Musca*, given the difference in size and the rather large phylogenetic distance. Two subtypes of axon terminals of photoreceptors R7 and R8 are now recognized, but amacrine neurons, known to exist from Hauser-Holschuh (1975), fail to impregnate. Only one type of tangential cell is known (see text). Figure courtesy Dr. K. F. Fischbach, from Fischbach and Dittrich (in preparation)

Figure 3: The neurons of the *Drosophila* lamina, and their connections within the medulla. Reproduced from Shaw (1989). Figure by Dr K. F. Fischbach.

collected by the lamina cartridge axial with that field of view, as shown in figure 2. This neural superposition allows the signal gathered by six facets to be pooled while not diminishing the spatial resolution of the system (Kirschfeld 1967, Braitenberg 1967).

1.2.2 The fly lamina

The first optic ganglion, the lamina, consists of a retinotopic array of units termed *cartridges*. The cartridges are clearly delineated, being embedded in a matrix of glial cells. Fifteen classes of neurons are recognised in the lamina (Shaw 1984). The morphology of the neuron classes and their connections to the medulla are illustrated in figure 3. Figure 4 illustrates the arrangement of the neurons within each cartridge in diagrammatic form, while figure 5 provides a more anatomical representation.

Axons of the receptors R1–6 from the appropriate ommatidia enter the cartridge and fatten to form a ring of terminals running the length of the cartridge. The axons of R7 an R8 pass through the lamina slightly removed from the other neurons.

Each cartridge contains five monopolar cells, L1 to L5, with soma in the distal part of the lamina, and sending axons to the medulla. L1 and L2 are termed *large monopolar cells* (LMCs), each collecting synaptic input from all six receptor terminals along the length of the cartridge. L3 is similar but smaller, collecting receptor input in the distal part of the cartridge. The lamina cell recordings in this study are assumed to come from these cell classes, by comparison with known electrophysiological properties. L1 and L2 are primarily distinguished by their termination in different levels of the medulla. L4 and L5 are third order cells, of smaller size.

The other cell class receiving input directly from receptors is a class intrinsic to the lamina, the *amacrines*. These are relatively irregular, aperiodic neurons, each sending what are termed α-processes into several different cartridges. It seems that different amacrine cells may have processes present in a given cartridge, but there is always exactly one amacrine process running along each receptor terminal.

For each cartridge there is a basket cell, T1, which sends a process, termed a β-process, along each receptor terminal, dual to the amacrine α-process. An axon connects to a narrow arborisation in the medulla. It has been suggested that the T1 cell receives input from the receptors (Strausfeld and Nässel 1981), whereas Shaw (1984) suggests that it receives input only from the amacrine processes and L2. Although the

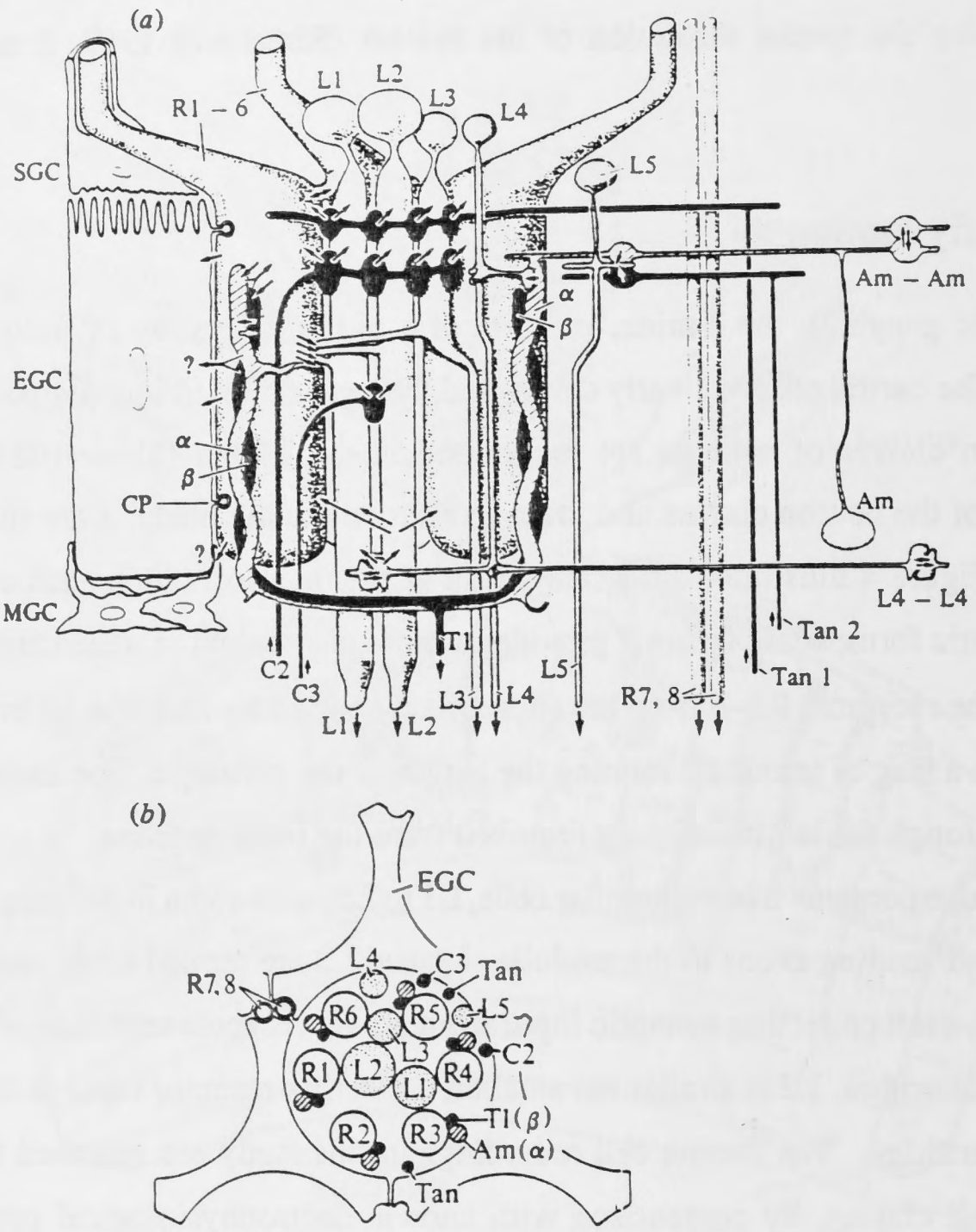

Fig. 3. (*a*) Diagram of the neuronal types and their synaptic interconnections, in a single optic cartridge in the lamina synaptic nucleus of the fly's eye, based on Table 1. Direct sensory input to each cartridge (downwards arrows) comes solely from the six photoreceptors with short axons, R1–R6, one each from a different ommatidium (see Fig. 2), and three of which are illustrated. R1–R6 form numerous small tetrad (1 → 4) synapses at their points of contact with the grouped lateral spines of the second-order monopolar cells L1–L3 (which form the main lamina output), plus an α-amacrine process. In addition to an internal loop within the lamina from L2 back to R1–R6 and L1, four other *efferent feedback pathways* from the medulla reach back into each cartridge, three of which involve receptor terminals and/or L1–L3: C2, C3 (narrow field) and Tan 1, Tan 2 (wide field). Two *laterial interaction pathways* across

Figure 4: Arrangement of neurons and their synaptic interconnections within a lamina cartridge. Reproduced from Shaw (1981).

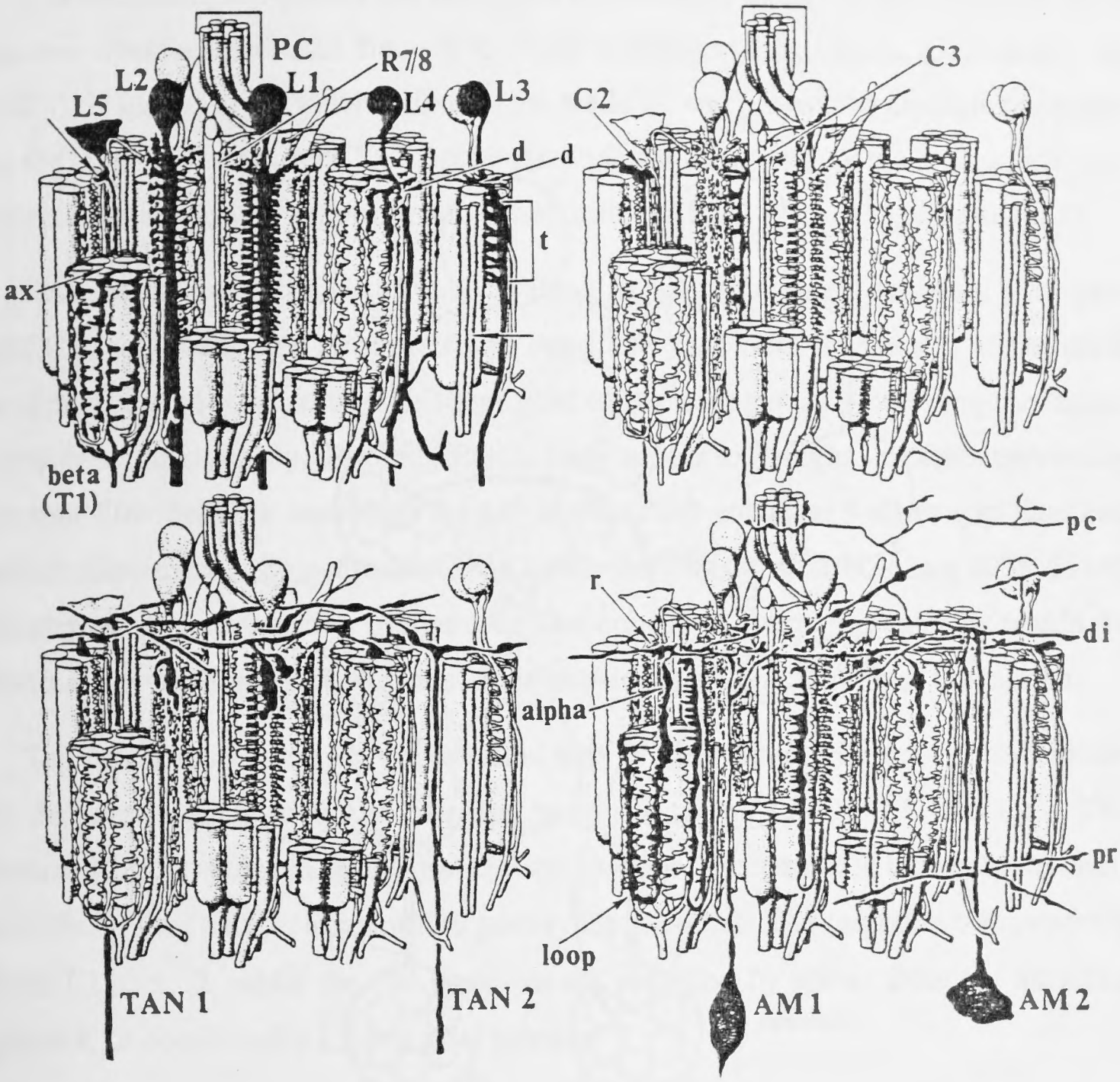

Fig. 37. Neuronal element in the lamina of *Musca domestica*, shown against a background of ten "dissected" optic cartridges. *L1*, *L2*, and *L3* are the three monopolar cells which derive input from a set of six receptor endings. *T1* (beta) is the basket of dendrites of a fourth direct centripetal relay to the medulla. *C2* and *C3* are narrow-field centrifugal endings associated with *L1–L3* and receptors, and *L1/L2*, respectively. Two forms of tangential centrifugals are shown, lower left. The two species of amacrine cells are shown lower right. *Am 2* has special relationships with bundles of receptor axons above the level of their decussation to optic cartridges. *Am 1* is characterized by looped processes that give rise to alpha fibres and by tangential processes that give rise to rosette *(r)* and blebbed specializations. *ax*, pairs of axial fibres of L1 and L2; *pc*, pseudocartridge (bundles of R-axons before their decussation) *d*, dendrites of L3 and L4 in the outer one-third ofthe lamina; *t*, level of triad dendritic configurations between receptors and *L1*, *L2*, and *L3* monopolars. (Adapted from STRAUSFELD, 1971)

Figure 5: Arrangement of neurons within the lamina cartridge of *Musca domestica*. Reproduced from Strausfeld and Nässel (1981).

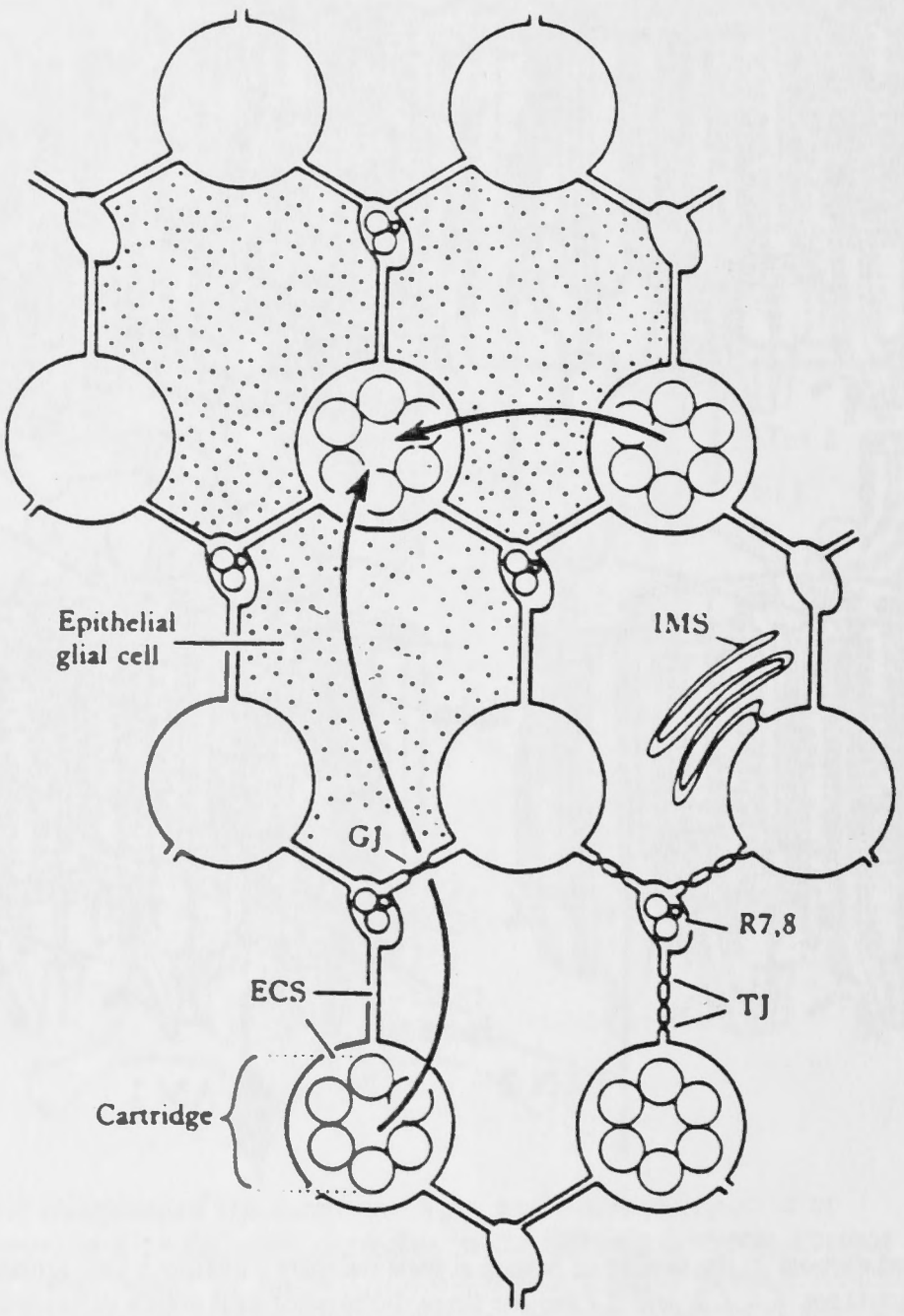

Fig. 8. Idealized scheme of the lamina, after Boschek (1971), illustrating how each cartridge is surrounded and isolated by three epithelial glial cells (EGCs, stippled). The only access routes from one cartridge to the next therefore run along the extracellular clefts leading to and from R7/8, at which site three different EGCs meet. Tight junctions (TJ) along these clefts therefore cut off extracellular access from one cartridge to the next. Photocurrents can be detected travelling laterally between cartridges, and must presumably pass transcellularly through the EGCs (arrows), using the gap junctions known to connect them. The geometry of cartridge packing suggests that currents should spread more readily in the horizontal than the vertical dimension, and this is observed. IMS, an extensive internal membrane system, invaginating from the EGC's surface membrane.

Figure 6: The isolation of lamina cartridges by epithelial glial cells (EGCs), and the routes for current flow across the lamina array. Reproduced from Shaw (1984).

cell body lies near the medulla, along with the cell bodies of two efferent classes, this cell is not considered to be an efferent.

The remaining cell classes are thought to be efferents. Cells C2 and C3 project from narrow arborisations in the medulla to single cartridges in the lamina. Conversely, the cell TAN1/2 has broad arborisations in the medulla, and projects to multiple cartridges in the lamina. The efferent TAN3 projects along the distal edge of the lamina, and may release the transmitter seratonin non-synaptically (Nässel *et al* 1983, Nässel 1988).

Each lamina cartridge is surrounded along its length by three *epithelial glial cells* (EGCs), while *satellite glial cells* and *marginal glial cells* are present at the distal and proximal ends respectively. These glial cells create a matrix, isolating the lamina cartridges anatomically. Between EGCs there appear to be tight junctions preventing current flow between cartridges by any extracellular route, as well as gap junctions which allow current flow intracellularly across the glial cell matrix (Shaw 1975, 1984), illustrated in idealised form in figure 6. This control of lateral current flow within the lamina may be of great importance in the physiological functioning of the lamina.

The predominant synapse present, and that of most direct relevance to this thesis, is the transmission from the receptor terminals to the LMCs, L1 and L2. This transmission is achieved by around 200 synapses per receptor cell, the synapses being tetradic, having a linear array of four post-synaptic spines. The central two spines come from L1 and L2, while the end positions are occupied by spines from the amacrine process, or occasionally L3 or a glial process.

The next most prominent synapses in the lamina are dyadic synapses from the amacrine and T1 processes to the epithelial glial cells (Shaw 1984). By multiplying the number and size of the synapse classes found within the lamina, Shaw assigns an anatomical rating for the EGC inputs equal to 25% of the receptor output rating. Although these synapses have not been proven to be effective, this strong presence gives further suggestion that the EGCs play an active role in the physiology of the lamina; there are no apparent synaptic output from the EGCs, but the input may serve to control the conductivity of the EGC membrane, thus affecting current flow within the lamina.

Two other common synapse types are feedbacks onto the receptor terminals, from amacrine or amacrine and T1 processes, and from the monopolar L2.

1.3 Physiology of receptors and large monopolar cells

The principal characteristics of the physiological behaviour of the neuron classes under investigation will be briefly reviewed; further aspects will be introduced where appropriate in the following chapters.

The receptors of insect eyes undergo a graded depolarisation in response to light, in contrast with the hyperpolarisation of vertebrate photoreceptors. The absorption of photons by rhodopsin embedded in the membranes of receptor microvilli initiates a chain of biochemical reactions culminating in an increase in receptor membrane sodium conductance (review, Fein and Payne 1989).

Recent work by Weckström *et al* (in press) estimates the dark adapted resting potential for receptors in *Calliphora* to be -60 mV, with the reversal potential for the light response being -6 mV. This gives a total dynamic range of around 56 mV, which is denoted as V_{max} for the system.

At very low light levels the voltage response is a sequence of discrete bumps, established to be due to the absorption of single photons (Scholes 1964; Lillywhite 1977). As the background light intensity increases, these bumps fuse to give a graded depolarisation, which increases to an asymptote of around 50% V_{max} in full daylight.

The receptor responds to incremental flashes of light with a depolarisation that is monophasic at low levels of background illumination. As the background level of illumination is raised the dynamics of receptor response become faster, and the contrast gain increases (French 1979, Howard *et al* 1984). The response also becomes more biphasic, with the DC gain approaching zero at high light levels, attributed to the activation of voltage or calcium dependent potassium conductances (Howard *et al* 1987).

Transmission from receptor to LMC is characterised by four features: inversion of the signal, amplification, high-pass temporal filtering, and lateral inhibition.

Inversion of the signal now appears to be due to the activation of chloride conductances (Zettler and Straka 1987, Hardie 1989) in response to the transmitter histamine (Hardie 1987). In darkness, the LMC membrane is not highly polarised, with estimated values varying from +20 mV (Zettler and Järvilehto 1971) to $-15\,mV$ (Laughlin and Hardie 1978). Stimulation by light leads to transient hyperpolarisations, up to 30 mV in amplitude. At higher light levels the resting potential appears to be unchanged, and the cell responds with graded hyperpolarisations and depolarisations

to increments and decrements of light respectively.

The amplification between receptor and LMC is by a factor of around six, due to the high sensitivity of the transmitter release mechanism (Laughlin *et al* 1987). The large number of synaptic contacts ensures that the amount of synaptic noise is low in spite of the high gain of transmission (Laughlin 1984).

High-pass filtering attenuates low frequencies and removes the sustained response of the receptors, leaving a signal which can be amplified without saturating the response range of the LMC (Laughlin and Hardie 1978). The mechanisms underlying this filtering include presynaptic inhibition (Laughlin and Osorio 1989) and will be discussed further in chapter 3.

The presence of lateral inhibition has been inferred from step-response data (Zettler and Järvilehto 1972, Laughlin 1974), and from the modulation transfer functions derived from responses to drifting sinusoids (Dubs 1982).

1.4 Systems and models

The term *system* will be used in the sense of any orderly, interconnected arrangement of components, and will generally be used to refer to the actual system under study: the functioning network of neurons comprising the retina and lamina of the fly. In contrast the term *model* will refer to any conceptual structure meant to be in analogy with the actual system. Ideally the model is related to the system as a homomorphic image, a conceptual structure having parts which represent parts of the system, with the behaviour of the model reflecting some of the observed behaviour of the system.

The models in this thesis will be mathematical, having not only well-defined mathematical structure, but also numerical estimates of parameters, allowing quantitative comparison between model and observation.

Models will be classified into three categories, dependent on the level at which the model attempts to describe the system. At an intermediate level, an *empirical model* is purely descriptive, seeking to give a homomorphic image of some system observables. White-noise analysis is archetypal of this form of modelling, seeking a mathematical mapping which predicts some observable termed system output as a function of other observables termed system input, while making a minimum of assumptions about the system's mechanisms or purpose.

At a lower level, a *mechanistic model* proposes physical structures and processes which produce the system's behaviour. In visual neurophysiology this includes physical processes such as the absorption of photons, cascades of biochemical reactions, electrochemical current flow within and between cells, and synaptic transmission by release and binding of chemical transmitters. This is the most traditional form of mathematical modelling, the physical assumptions generally leading to sets of differential or difference equations involving parameters which are then estimated to give model behaviour in accordance with observation.

This level of modelling will be developed in two areas. Firstly, to produce a description of current flow in the fly lamina array. This will give a quantitative model based on a concept which has existed for some time, that the mechanisms of antagonism in the fly lamina involve the extracellular potential within lamina cartridges (Laughlin 1974, Shaw 1975). Secondly, models of nonlinear mechanisms likely to exist in the system will be considered, and the kernel components predicted by the models are compared with the observed kernels.

At a higher level, *functional models* attempt to explain the behaviour of the system in terms of the system's function within the organism. The regularity and detailed anatomical characterisation of the insect retina-lamina system make it an ideal system for the study of early visual processing. Transmission from receptors to LMCs can be viewed as a dynamic image processing operation, which can be evaluated using the criteria of information theory (review, Laughlin 1989a).

The development of any quantitative analysis of image processing performance requires a formalisation of what the goal of the system is to be. Parameters will be involved, concerning the statistics of visual scenes expected, the properties of the sensory transduction processes and the levels of noise introduced in the system. Given a mathematical formalisation, optimisation techniques can predict what would be the optimal image transformation, and comparison can be made with the observed behaviour. Such models can provide insight into the behaviour of a system, although in some cases different formalisations can appear consistent with observation, and it can be a long inferential step to identify the purpose of a system in neurophysiology.

Some discussion of the results from this perspective will be presented in the conclusion, but quantitative development of functional models will not be presented in this thesis.

In short, the three levels of modelling defined describe *what* is happening in a system, *how* the behaviour is produced and *why* the system is so constituted. The categorisation applies only at a given level of organisation; where the system is conceived as existing in a heirarchy, being composed of component subsystems and forming a part of a supersystem, the mechanism of one level may be seen as the function of the lower level.

Note that the terminology defined here is different from terminology sometimes used in white-noise literature, where *functional* systems identification is used to denote empirical description of system behaviour, differing from the meaning both in normal English and in biology, where purpose is clearly implied.

The term *structural* modelling will also be used, meaning the fitting of a model containing substructure, such as the so-called sandwich model, but without necessarily proposing the underlying physical mechanisms.

1.5 The white-noise technique in visual science

The white-noise technique is a method of systems identification based on a proposal of the mathematician Norbert Wiener that a suitable test input for nonlinear systems would be a broad-band stochastic process, termed a white-noise. From the resulting output a model for the system could be constructed involving linear and higher degree operators relating input and output by combination of the input with kernels in multiple integrals, related to the series of functionals, or functions of a function, studied by Frechet (1910) and Volterra (1958).

Since the original proposal, elaborated in Wiener's book of 1958, many theoretical and technical developments have been made in the technique and related techniques, and a range of applications have been made, many of them in visual sciences. The technique is in many ways ideally suited to visual science, where the system input is the visual stimulus for a preparation and the system output is the recorded response of a neuron. Quantitative models can be constructed describing the mapping from stimulus to response, involving linear and nonlinear components, as are clearly present in many pathways in the visual system. The stimulus consists of modulation of intensity about a mean level, which mimics the fluctuation of intensity which photoreceptors experience as an animal passes its eyes over a natural scene. The test input is of

high entropy, eliciting a large amount of information about the system in a limited amount of recording time. The technique is also readily extendible to multiple channel stimuli; a number of spatial regions can be simultaneously stimulated, or a general spatiotemporal stimulus can be applied, involving intensity fluctuating in time and across the two-dimensional field of view of the visual system.

Early applications in visual science include a study of the human pupillary reflex (Stark 1969), the analysis of receptive field responses in the catfish retina (Marmarelis and Naka 1972, 1973a,b,c), and a study of the fly visual system (Marmarelis and McCann 1973). The technique has now had considerable use in visual science. Useful reviews include Sakuranaga *et al* (1986) and Sakai *et al* (1988), and use of the technique in the study of physiological systems has been described in a book (Marmarelis and Marmarelis 1978). Two other books have been written discussing theoretical aspects of kernel models at great length (Schetzen 1980, Rugh 1981).

White-noise analysis was used at an early date in the study of the fly visual system, as mentioned above, and also subsequently (McCann 1974, McCann *et al* 1977), but not apparently for the study of the LMCs of the lamina. White-noise has also been used as a stimulus for visual cells in the fly, but without the calculation of nonlinear kernels (French and Järvilehto 1978).

The characterisation of visual system response to stimulation varying in space as well as time has developed more slowly, due to the technical difficulty of delivering the complex stimulus, and the size of the subsequent data analysis operations. One approach is to consider a stimulus varying in one space dimension only, presenting a row of bars which are independently modulated. This technique has been used to study catfish retinal neurons (Powers and Arnett 1981), and has been used with great effect to study directional selectivity in cortical units, where the bars are rotated to the preferred orientation and the test stimuli are then applied (*eg* Emerson *et al* 1987).

Spatiotemporal analysis on the full two-dimensional space domain has been developed a number of times. Implementations have been reported by Sutter (1975), Yasui *et al* (1979), Hida and Naka (1982), Mizuno *et al* (1985) and Citron *et al* (1988). These reports aim primarily at demonstrating the viability of the technique rather than producing new scientific results. It has been concluded that "progress in this challenging area has been painfully slow" (Sakai *et al* 1988), and it is clear that spatiotemporal system identification has not in the past fulfilled its potential in visual

science.

Chapter 2

The White-Noise Technique

2.1 Operator models of system behaviour

This study seeks to derive explicit, quantitative mathematical representations of the image processing operations occurring in the initial stages of the visual system of the fly.

Time-varying quantities such as the visual stimulus, membrane conductances, intracellular voltages and rates of transmitter release are modelled by functions on the domain of time. In the general case of visual input the stimulus is modelled as a function on a spatiotemporal domain, representing the two dimensional field of view and the passing of time. Relationships between these time-varying quantities are modelled by *operators*, that is mappings from an input function space to an output function space. The overall system, in which many time-varying quantities are interacting, then leads to a model comprising an *operator network* with function spaces as the nodes and operators mapping between them.

2.1.1 Basic notation and definitions concerning operators

The operators which will initially be considered will represent the mapping from a visual stimulus to the voltage response of a neuron. For the following formulation of the operator representation, the input and output functions will be denoted $s(t)$ and $r(t)$ respectively, suggesting stimulus and response. In general however these may stand for any quantities considered as the input and output of a system.

The function spaces are treated as linear spaces, with the operations of addition and

scalar multiplication being defined pointwise. That is, functions can be added and multiplied by a scalar in the following way:

$$(r_1 + r_2)(t) = r_1(t) + r_2(t)$$
$$(\alpha r)(t) = \alpha(r(t))$$

A relationship between two quantities is modelled by an operator between the function spaces representing the quantities. For example, if a response represented by the function $r(t)$ is considered to be dependent on a stimulus represented by $s(t)$, an operator F may be hypothesised, with:

$$r = Fs$$

For brevity of notation parentheses will generally not be placed around the input function symbol. The application of the operator to the input function is denoted by simple juxtaposition, with operator application being given a higher precedence than function evaluation, thus the response at time t is written as:

$$r(t) = Fs(t)$$

Such a model can be represented graphically by a mapping diagram:

$$s \xrightarrow{F} r$$

Throughout this thesis systems will be represented by mapping diagrams such as this. This follows the mathematical convention whereby functions are placed at the nodes of the network, with operators represented by the edges. In engineering and most systems identification literature the dual notation is preferred, drawing flowcharts with the operators in boxes at the nodes of a network, with signals represented by edges.

The mathematical convention is used here for two reasons. Firstly, in most cases the symbols for operators will be derived systematically from their input and output functions. The operators thus need not be explicitly represented, producing less cluttered diagrams. The second reason is more philosophical: in engineering the communications device is the more concrete entity, with the signals appearing more ephemeral. In science it is generally the reverse, with the signals being the primary data while the operators represent hypothetical models inferred from the signals.

The operator may in general be nonlinear; it is linear when the following hold

$$F(s_1 + s_2) = Fs_1 + Fs_2$$
$$F(\alpha s) = \alpha(Fs)$$

for a scalar multiplier α. This property is also called *superposition*, whereby the responses to separate input components superimpose.

The set of possible operators between two given function spaces also forms a linear space with the operations of addition and scalar multiplication being induced by the corresponding operations on the outputs:

$$(F_1 + F_2)s = F_1 s + F_2 s$$
$$(\alpha F)s = \alpha(Fs)$$

Thus if the relationship of response to stimulus is modelled as a sum of n components, the operator model is written as a sum of n component operators: $F = F_1 + \cdots + F_n$.

The composition of two operators is also used, representing a cascade in which the output of one system is the input to a second. This will be written by juxtaposition, so that

$$GFs = G(F(s))$$

corresponding to the mapping diagram:

$$s \xrightarrow{F} X \xrightarrow{G} r$$

where X represents the intermediate signal and r the final output. Note in particular that juxtaposition represents the composition of operators and not the pointwise product of operators, which is not required in this thesis.

In white-noise analysis the inner product of two operators is also defined, as will be discussed below.

System identification involves selecting appropriate spaces to represent input and output, obtaining sample runs of observed input-output data, selecting a subset of the possible operators between these spaces by making certain assumptions, and then estimating parameters to choose which element of the model subset provides the best agreement with the observed input-output behavior. *Active* systems identification allows the experimenter to choose the particular instance of stimulus, which may be optimised to provide the most efficient estimation.

In any real study assumptions must be made to reduce the the class of representations considered. For the phenomenological type of representation sought here these assumptions are of a very general kind; the success of the identification performed is measured by the extent to which relevant system properties are captured. This contrasts with the other principle method of system modelling, whereby some underlying physical processes are assumed, generally leading to the solution of a set of differential equations, whose parameters are estimated to provide the best fit with observed data. When such specific physical assumptions are made it is possible for the model to be fundamentally wrong. The kernel operator models used here are more empirical, seeking only to describe the observed behaviour; interpretation in terms of mechanism can then follow, on the basis of the fitted kernels.

2.1.2 Polynomial time-invariant operators

The class of model operators used in this study can be termed polynomial time-invariant operators.

The first assumption for these operators is that of time-invariance, that is, the same input applied at different times produces the same output, correspondingly shifted in time. Defining the forward time-shift operator T^u as

$$T^u s(t) = s(t+u)$$

time-invariance means that if an operator maps $s \mapsto r$ then it also maps $T^u s \mapsto T^u r$, for any shift T^u. In other words the operator commutes with any time-shift T^u.

For such an operator it is only necessary to know the output at time zero for any input; the output at time t is then given by

$$Fs(t) = T^t Fs(0) = FT^t s(0)$$

which is the output at time zero for the input $T^t s$.

A time-invariant operator can thus be represented by a *functional*, a mapping from the input function to a single number, the output at time zero. The mathematics of time-invariant operators derives largely from the properties of functionals, and the term functional is often used in place of time-invariant operator, as in the so-called Wiener G-functionals. However we will generally consider the models as operators. This emphasises that the output is itself a function of time, which may form the

input to a further system. The composition of two time-invariant operators is another time-invariant operator, whereas functionals do not compose.

The operators will be assumed to be *causal*, so that $Fs(t)$ only depends on $s(t_1)$ for times $t_1 < t$. For explicit numerical representation of the operator, processing time and storage limitations mean that only a finite memory can be considered, hence the model gives $Fs(t)$ as a function of s on the interval $[t-m, t]$, for some memory length m. Inspection of the resulting model operator generally indicates if sufficient memory length has been considered. Even if insufficient memory length is used the white-noise technique still gives useful results, describing the short-term dependence of response on stimulus.

Polynomial time-invariant operators result from the 'conceptual tensor product' of two elementary mathematical concepts: the *polynomial* and the *linear time-invariant system*. The close correspondence whereby polynomial time-invariant operators can be viewed as a generalisation of polynomial functions to account for temporal dynamics will be seen repeatedly throughout this work.

A linear time-invariant system gives an output which is the convolution of the input with the system's impulse response:

$$Fs(t) = \int_0^m k(t_1)s(t-t_1)\,dt_1$$

The impulse response k is also called the *kernel* of the system. The integral is taken over the range of latencies t_1 up to the memory length of the operator, m.

Adopting for a moment the representation of a time-invariant operator by a functional, the response at time zero, $r(0)$, is a function of the past input, which may be denoted by $p(t_1)$:

$$p(t_1) = s(-t_1), 0 \leq t_1 \leq m$$

The response of a linear system at time zero is a linear functional of this past input:

$$r(t) = \int_0^m k(t_1)p(t_1)\,dt_1$$

The kernel k lies in the *dual space* of the space of past inputs, and the combination of kernel and input is a *dual pairing* operation. The kernel can be thought of as a sensitivity function, giving the sensitivity of the output to input strength over a given domain of latencies.

A quadratic operator can be formed by taking a bilinear functional of the past input:

$$\int_0^m \int_0^m k_2(t_1, t_2)p(t_1)p(t_2)\, dt_1\, dt_2$$

The second degree kernel k_2 gives the sensitivity to the product of input strengths at latencies t_1 and t_2.

In like manner, the general degree n operator involves an n-linear functional of the input past:

$$\int_0^m \cdots \int_0^m k_n(t_1, \ldots, t_n)p(t_1) \cdots p(t_n)\, dt_1 \cdots dt_n$$

These monomial functionals can be added to form polynomial functionals, and an infinite series of monomials can be considered, analogous to the Taylor series. This form of functional was introduced by Volterra around the turn of the century. He thought of the input function as a line, so that the functional was termed a "function of a line" (*eg* Volterra 1959) . The convergence properties of the power series were established by Frechet (1910).The kernels of such a representation are termed the *Volterra kernels*, and the power series is termed a *Volterra series*.

Now consider the system output over time t. Replacing $p(t_1)$ by $s(t-t_1)$ the Volterra series for an operator F has the form:

$$Fs(t) = \sum_{n=0}^{\infty} \int_0^m \cdots \int_0^m k_n(t_1, \ldots, t_n)s(t - t_1) \cdots s(t - t_n)\, dt_1 \cdots dt_n$$

The zero degree term is a constant giving the output offset for zero input. The linear term is a convolution, as previously stated:

$$F_1 s(t) = \int_0^m k_1(t_1)s(t - t_1)\, dt_1$$

This can be compactly written using a symbol for convolution, usually the asterisk:

$$F_1 s = k_1 * s$$

The monomial term of degree n is given by:

$$F_n s(t) = \int_0^m \cdots \int_0^m k_n(t_1, \ldots, t_n)s(t - t_1) \cdots s(t - t_n)\, dt_1 \cdots dt_n$$

Surprisingly, despite decades of writing lengthy expressions such as this, no compact notation appears to have come into use. A number of notations were invented and tried during this thesis work. The following notation I have found to be useful in promoting fluency in dealing with polynomial time-invariant operators.

The monomial expression above is a convolution over an n-dimensional domain, except that the result is only evaluated at the diagonal points $t_1 = \ldots = t_n = t$, giving a function of a single time variable. The operation is in a sense something between a full convolution, which gives a result defined on R^n, and a dual pairing, which gives a scalar valued result.

This 'diagonal of the convolution' operation will be represented as follows. Let g be an element from a space of functions on R^n. The kernel k_n enclosed in square brackets will denote the operator $[k_n]$ which maps the function g to a function of time $[k_n]g$ such that:

$$\begin{aligned}[k_n]g(t) &= (k_n * g)(t, t \ldots, t) \\ &= \int_0^m \ldots \int_0^m k_n(t_1, \ldots, t_n) g(t - t_1, \ldots, t - t_n)\, dt_1 \ldots dt_n\end{aligned}$$

It is appropriate that the notation is not symmetric with respect to k_n and g, as in general they belong to spaces dual to each other. For example, in the case of ideal white-noise the input involves generalised functions while the kernel lies in the dual space, comprising a class of infinitely differentiable functions.

In the case of polynomial time-invariant operators the function g is an n-fold tensor product of input functions. In general the inputs may be distinct functions of time $s_1, \ldots, s_n$. The tensor product of two functions produces a function on the Cartesian product of their domains. The n-fold tensor product of input functions produces a function of n time variables such that:

$$s_1 \otimes \ldots \otimes s_n(t_1, \ldots, t_n) = s_1(t_1) s_2(t_2) \ldots s_n(t_n)$$

When n copies of the same input function are involved, we will abbreviate the expression by defining the *tensor power* to degree n as the tensor product of a function with itself n times:

$$s^{n\otimes} = s \otimes s \otimes \ldots \otimes s \ \ (n \text{ times})$$

The Volterra series can now be written succinctly as:

$$Fs = \sum_{n=0}^{\infty} [k_n] s^{n\otimes}$$

showing clearly the relationship with the Taylor series:

$$f(x) = \sum_{n=0}^{\infty} a_n x^n$$

As a further abbreviation, the operator $[k_n]$ will be given an additional capability. When the argument is a single function of time it is implicitly raised to the correct tensor power, thus $[k_n]s$ and $[k_n]s^{n\otimes}$ are equivalent. The square brackets thus associate a kernel k_n with the corresponding *kernel-operator* $[k_n]$, which maps an input to an output function. The square brackets are reminiscent of the box in which a kernel might appear in a flowchart.

The Volterra series for an operator F now has the rather minimalist form:

$$F = \sum_{n=0}^{\infty} [k_n]$$

2.1.3 Symmetric and upper-triangular canonical forms

Two kernels will implement the same operator if their difference is a skew-symmetric function in its arguments. Illustrating with the quadratic case, if g is a skew-symmetric function of two variables, that is,

$$g(t_1, t_2) = -g(t_2, t_1)$$

then the resulting quadratic form in the input function s,

$$\int_0^m \int_0^m g(t_1, t_2) s(t - t_1) s(t - t_2)\, dt_1\, dt_2$$

is zero, for any input s. For any kernel k, k alone and the kernel $k + g$ produce identically-valued quadratic forms.

The set of all possible kernels is thus partitioned into equivalence classes, with all the kernels of a given class implementing the same operator.

It is convenient to choose a canonical form for the kernel, that is, a unique element from each equivalence class. Two canonical forms will be used here. The *symmetric* form, where $k_2(t_1, t_2) = k_2(t_2, t_1)$ is used for plotting. The *upper-triangular* form, where $k_2(t_1, t_2) = 0$ unless $t_1 \leq t_2$, is the one estimated, as it has full degrees of freedom over the upper-triangular elements. The symmetric kernel can be obtained from any other form by *symmetrisation*. To symmetrise, the following assignment is made:

$$k_2(t_1, t_2) := \frac{k_2(t_1, t_2) + k_2(t_2, t_1)}{2}$$

For the set of degree n kernels, symmetry is correspondingly taken over the $n!$ permutations of the arguments $t_1, \ldots, t_n$, and the upper-triangular kernel is non-zero only for $t_1 \leq t_2 \leq \ldots \leq t_n$.

2.1.4 Intensity and contrast kernels

A Taylor series is expanded about a certain point. Writing $x = x_0 + \Delta x$ the series becomes:

$$y = \sum_{n=0}^{\infty} a_n \Delta x^n$$

where the coefficients a_n are dependent on x_0. Similarly the Volterra series is expanded about some constant level of stimulation. This accords well with the fact that natural visual stimulation will generally involve relatively small fluctuations of intensity about some mean level dependent on the ambient illumination of the scene. If the visual stimulus, measured in some units of physical light intensity, is written as $I(t) = I_0 + \Delta I(t)$, then the Volterra series has the form

$$r = \sum_{n=0}^{\infty} [K_n] \Delta I^{n\otimes}$$

where, for this section, capital K will denote the *intensity kernels* of the system.

At any set level of illumination it is more convenient to measure fluctuations relative to the mean intensity, defining the term *contrast*:

$$s(t) = \Delta I(t)/I_0$$

Although contrast is a dimensionless quantity, it may for clarity be denoted by the unit C.

Contrast will be the usual measure of visual stimulus strength in this thesis, giving the Volterra series in terms of *contrast kernels*, k_n:

$$r = \sum_{n=0}^{\infty} [k_n] s^{n\otimes}$$

In discussing adaptation in chapter 4 it will be convenient to switch between contrast and intensity kernels. The relationship between the two kernel types can be seen by equating the degree-n terms of the series, to give:

$$K_n = k_n / I_0^n$$

The neurons being studied here all give a graded response to light, hence response will be measured in millivolts, mV. Time will generally be measured in milliseconds, ms. The units of the contrast kernel k_n are then $mV/(C\ ms)^n$. For the linear monomial $r = [k_1]s$, the kernel can be thought of roughly as the response over time in millivolts to a stimulus consisting of a flash of unit contrast and duration one millisecond.

The variation in the kernels as the mean intensity varies represents the adaptation of the system to varying illumination. The size of the contrast kernels changes by a few times over the total operating range of the visual system, increasing with light adaptation, while the intensity kernels decrease in size by orders of magnitude. This study considers two levels of intensity, and comparison of the kernels will show the changes in contrast gain, in temporal dynamics and in nonlinearities of the systems.

2.1.5 The discrete-time case

The data used in this study give a discrete-time representation of stimulus and response, with both being specified at intervals of $\Delta t = 2\,ms$. The stimulus comes from a raster-scanned CRT with a frame rate of 500 Hz, while the response is sampled in synchrony, but $1\,ms$ after the raster scanned the centre of the screen.

This introduces two additional coordinate systems for time, together called *discrete-time*. In the discrete-time context the symbol t denotes an integer giving the number of time units passed. The stimulus is represented by a sequence of values, with $s(t)$ denoting the stimulus value at the continuous-time $t\Delta t\,ms$. For the response and all kernels discrete-time t corresponds to continuous-time $t\Delta t + 1\,ms$, due to the $1\,ms$ delay between the stimulus presentation and the sampling of the response.

These three coordinate systems are necessarily kept distinct throughout the data processing, however all graphical and numerical results are presented in terms of continuous-time in milliseconds. In algebraic expressions the coordinate system can be inferred from the context. Note that discrete-time indices are placed in parentheses rather than attached as subscripts, since subscripts are required for other denotations.

The assumptions of time-invariance, causality and finite memory now imply that the response $r(t)$ is a function of preceding stimulus values. We define a memory length of m to mean dependence on the m values $s(t - t_1)$ for $t_1 = 0 \ldots m - 1$.

This function may be approximated by a power series in these m input variables. This is now genuinely a Taylor series in m variables, however we will refer to it as a discrete-time Volterra series, regarding it as an approximation to the continuous time Volterra series.

The series has the same representation in compact notation, where the convolutions

are now discrete-time convolutions:

$$[k_n]s^{n\otimes}(t) \;=\; \sum_{t_1=0}^{m-1} \ldots \sum_{t_n=0}^{m-1} k_n(t_1,\ldots,t_n)\, s(t-t_1)\ldots s(t-t_n)$$

This gives the kernels in terms of unit time steps. The kernel values can be divided by Δt^n to be in terms of physical time, with units $mv/(C\,ms)^n$.

The symmetric and upper-triangular canonical forms are defined as before. The kernel k_n with memory length m has m^n elements, but with redundancy the number of effective degrees of freedom is equal to the number of non-zero elements of the upper-triangular matrix. These are the elements with $t_1 \le t_2 \le \ldots \le t_n$. Each of these corresponds to an unordered selection with possible repeats of n indices from the m possible index values, and is thus given by the combination:

$$\left(\begin{array}{c} m+n-1 \\ n \end{array} \right)$$

We will see shortly that for the binary stimulus used in this study the number of degrees of freedom of the degree n kernel is equal to the number of kernel points with all indices different, and hence is the smaller number:

$$\left(\begin{array}{c} m \\ n \end{array} \right)$$

In this study, two spatial patterns of stimulation were used, illustrated in figure 7: a checkerboard pattern of squares, and a spot-annulus stimulus. The appropriate extensions of the basic one-input system are now described.

2.1.6 The linear spatiotemporal model

The general visual stimulus may be given as a function defined on a space-time domain, specifying the contrast at each time step and each location within the receptive field.

The general linear time-invariant transformation from this input to an output on time is then

$$r(t) = \int_{\mathcal{D}_y} \int_{\mathcal{D}_x} \int_0^m k_1(x,y,t_1)\, s(x,y,t-t_1)\, dt_1\, dx\, dy$$

where k_1 is the spatiotemporal linear kernel, integration is done over the spatial domain $\mathcal{D}_x \times \mathcal{D}_y$, and convolution is done over time.

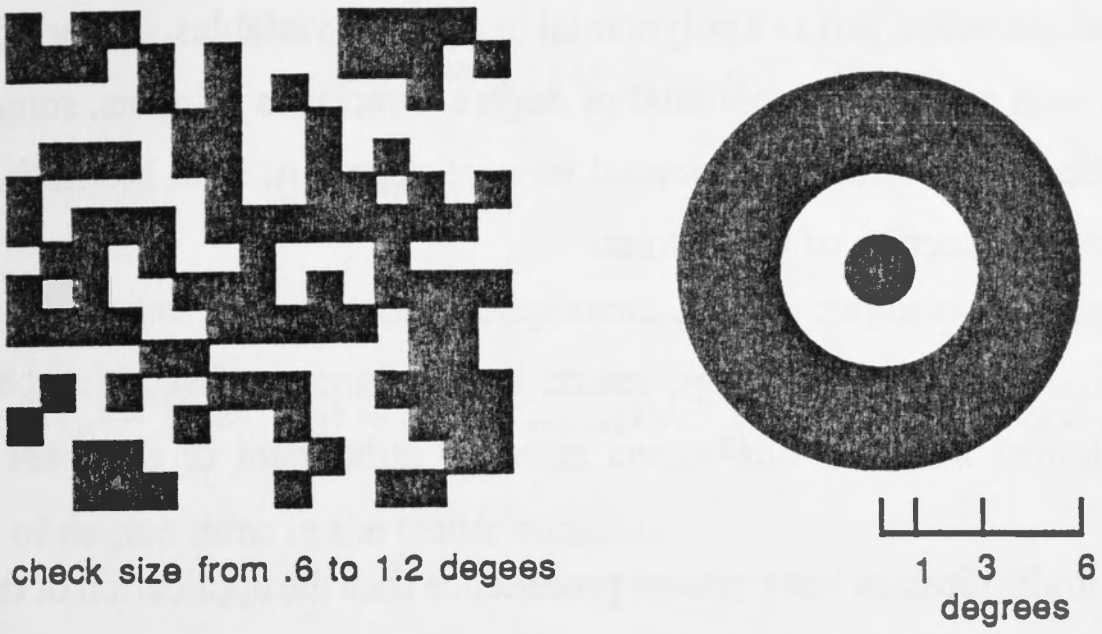

Figure 7: The spatial stimulus patterns. **Left**, checkerboard, producing general spatiotemporal stimulus. **Right**, spot–annulus, stimulating centre and surround independently.

The spatiotemporal stimulus used in this study was a checkerboard of fifteen by fifteen spatial regions, each of which could be independently controlled in contrast on each frame, at the rate of 500 frames per second. The stimulus is thus discretised in space and time, and can be written as $s(x, y, t)$, with $x, y = 0, \ldots, 14$ numbering the checks.

The discrete system representation is:

$$r(t) = \sum_{y=0}^{14} \sum_{x=0}^{14} \sum_{t_1=0}^{m-1} k_1(x, y, t_1)\, s(x, y, t - t_1)$$

The non-zero size of the checks means that the discrete kernel value $k_1(x, y, t_1)$ is not a sample of the continuous kernel at a point, but is the *integral* of the continuous kernel over the check indexed by (x, y). Allowance is made for this when parametric surfaces are fitted to the spatiotemporal kernels in chapter 3. Since the phosphor of the stimulating screen decays rapidly, the continuous kernel is estimated in time essentially at discrete time-points.

2.1.7 Centre-surround stimulation

A system receiving multiple inputs $s_1, \ldots, s_n$ and giving one output can be modelled by a multiple-input operator, $r = F(s_1, \ldots, s_n)$. A polynomial time-invariant operator can contain mixed terms, just as a polynomial in multiple variables, $f(x, y)$, can contain mixed terms such as axy. A monomial of degree n receives n inputs, some of which may be identical. The general monomial term of degree n, with kernel k_n, involves the tensor product function of the n inputs

$$[k_n]s_1 \otimes \ldots \otimes s_n(t) = \int_0^m \cdots \int_0^m k(t_1, \ldots, t_n)s_1(t - t_1) \cdots s_n(t - t_n)\, dt_1 \cdots dt_n$$

where tensor multiplication has a greater precedence than the application of the operator $[k_n]$, and evaluation at time t is done last of all. The discrete-time case involves the corresponding summations.

Kernels of degree higher than one were partially calculated for the checkerboard stimulus, but this was not pursued due to the large amount of processing required, and the unwieldy nature of the resulting kernels; the second order spatiotemporal kernel is a function of 6 variables, and even on a small sized domain contains more points than the original data record.

Instead, nonlinear effects were studied by defining two subregions of the receptive field, a spot on centre of diameter two degrees, and an concentric annulus extending from three to six degrees radius.

This stimulus was intended to elucidate nonlinear transmission of stimulation on axis, and the effect of lateral inhibition by stimulation in the surround.

The stimulus may then be represented by two functions of time, describing contrast on centre and contrast on the surround, labeled respectively $A(t)$ and $B(t)$.

The polynomial operator representation was fitted to second degree in centre and surround, and third degree in the centre stimulus. The two-input representation is a straightforward generalisation of the single-input case. A relatively convenient notation is obtained by using superscripts on the kernels to represent the input signals, with the number of inputs indicating the degree of the kernel. Superscripts on the kernels are thus paired with input symbols A and B, suggesting the dual-pairing

involved in combining kernel and stimulus. The representation is then written:

$$\begin{aligned} r &= F(A,B) \\ &= k_0 + [k^A]A + [k^B]B \\ &\quad + [k^{AA}]A^{2\otimes} + [k^{AB}]A \otimes B + [k^{BB}]B^{2\otimes} \\ &\quad + [k^{AAA}]A^{3\otimes} \end{aligned}$$

The response consists of a constant component, linear components caused by centre and surround, self-quadratic components caused by centre and surround, a cross-term describing response to interaction between centre and surround stimulation and a component of degree three in the centre stimulus.

2.2 White-noise stimulation

Norbert Wiener suggested that a suitable test stimulus for the identification of nonlinear systems would be a stochastic process termed a *white-noise* (Wiener 1958). Ideal white-noise is a generalised stochastic process, equal to the derivative of a Brownian motion stochastic process. Differentiation in this context is as defined for generalised functions, in the same way that the Dirac delta function is the derivative of the unit step function. Ideal white-noise would be a stochastic process having a flat power spectrum over all frequencies. In practice a stochastic input is used having a power spectrum approximately flat over the bandwidth of the system under study.

The strength of the white-noise is measured by the power spectral density over this flat portion of the spectrum, usually denoted P.

Continuation of the stimulus power to frequencies beyond the bandwidth of the system will increase the total power of the stimulus, equal to the area under the power spectral density curve, while providing no additional power in the response.

For discrete-time systems the corresponding stimulus may be defined more simply: a discrete-time white-noise stimulus $s(t)$ is just a sequence of independent random variables, indexed by t. Various distributions for the random variables may be chosen. For a visual stimulus measured in terms of contrast, the strength of the stimulus is given by the variance of the variables, σ_s^2, in units C^2; in terms of physical time this becomes $P = \sigma_s^2 \Delta t$ in units C^2/KHz.

Two properties of white-noise stochastic processes are relevant to their use in white-noise analysis. Firstly, they are *stationary* stochastic processes, meaning that the distribution of the time-shifted process $T^u s$ is the same as the distribution of s. This implies in particular that a time-invariant operator having the process as input will have an output with the same distribution at each time t.

Second, they have the property of *ergodicity* which ensures, by means of the ergodic theorems, that the time-average of the output of any time-invariant operator having the process as input will converge to the ensemble average, as the duration of averaging increases. Denoting time-averaging by an overline and the ensemble average by the *expected value* operator, E, this means

$$\overline{Fs} \rightarrow E[Fs(t)]$$

as the length of the time-average tends to infinity. There are two ergodic theorems, one establishing convergence in mean-square, the other establishing convergence with probability one.

2.2.1 The inner-product of two operators

The specification of a probability distribution on the space of inputs induces an inner-product operation on the space of time-invariant operators taking this input, given by the ensemble cross-correlation of the outputs of two operators. That is, for time-invariant operators F, G the inner-product is defined as:

$$(F, G) = E[Fs(t).Gs(t)]$$

Stationarity of the input process ensures that this is independent of t.

Two operators are *orthogonal* relative to this input distribution if their outputs are uncorrelated.

The inner-product also defines the *norm* of an operator, a measure of its magnitude, given by the root mean square (RMS) output:

$$\|F\| = \sqrt{E[Fs(t)^2]}$$

The corresponding *metric* is also defined, giving the distance between two operators as the RMS value of the difference of their outputs.

This defines a measure of the *error of approximation* of one operator by another, as the distance between them in the inner-product space. By the principle of ergodicity, time-averages produce estimates of the above quantities which converge to the ensemble averages as the run length increases. The time-averaged RMS error between fitted and observed responses is the measure of goodness of fit of the operator representation to the recorded behaviour of the system, and the parameter estimation is done to minimise this RMS error.

2.3 Orthogonalisation of the Volterra series

In practice, only a low degree polynomial operator can be fitted to the data, due to the combinatorial explosion in the number of kernel elements. Using the RMS error as the criterion of fit, estimates may be obtained for the kernels.

The monomials in the Volterra series are not orthogonal relative to the white-noise input. Even if infinite run length is assumed, so that the time-averages are equal to ensemble averages, the kernels estimated will depend on the point at which the series is truncated.

It is more convenient to consider a series which has been orthogonalised relative to the input process, so that the truncation at any degree yields the least-squares fit polynomial operator of that degree.

2.3.1 Hermite polynomials

The concept of orthogonalisation can be illustrated by considering the simpler case of the approximation of a function of one variable:

$$y = f(x)$$

This may represent a static system, which takes a single input value and produces a single output value.

The Taylor series can be described as the best form of approximation at a point, since the truncation at degree n gives an error of order Δx^{n+1} for small deviations Δx.

If the input values x were to be random variables, drawn from a known distribution, an approximation $p(x)$ may be sought from a model-subspace of functions which

provides the least RMS error in output, that is, minimising the distance between function and approximation relative to this input distribution:

$$\|f - p\| = \sqrt{E[(f(x) - p(x))^2]}$$

This distance is minimised when the residual $f - p$ is orthogonal to all elements in the model-subspace.

It is then convenient to consider a series representation in terms of orthogonal polynomials

$$f(x) = \sum_{n=0}^{\infty} a_n p_n(x)$$

where the polynomial p_n is of degree n, and is orthogonal to all lower degree polynomials with respect to the given input distribution. This ensures that the truncation at any degree n will give the least RMS approximation of that degree, as the residual

$$\sum_{k=n+1}^{\infty} a_k p_k(x)$$

is orthogonal to all degree n polynomials. The coefficient of degree n is equal to:

$$a_n = \frac{E[f(x)p_n(x)]}{E[p_n(x)^2]}$$

The orthogonal polynomials can be produced by applying the Gram-Schmidt orthogonalisation procedure to the sequence of power functions $1, x, x^2, \ldots$ When the input has a standard normal distribution the result is the *Hermite polynomials*.

2.3.2 The Wiener G-functionals

Wiener described the corresponding orthogonalisation of the continuous-time Volterra series, relative to an ideal Gaussian white-noise input of a given power spectral density P (Wiener 1958). The result is a series of polynomials now called the Wiener G-functionals:

$$Fs = \sum_{n=0}^{\infty} G_n(h_n, s)$$

Each term $G_n(h_n, s)$ is itself a polynomial operator of degree n in the input. This may be written as a polynomial

$$G_n(h_n, s) = \sum_{p=0}^{n} [h_{np}]s$$

where the kernel h_{np} is the degree p kernel in the degree n G-functional. The orthogonalisation imposes constraints on the kernels within this polynomial, so that

the kernels h_{np} are all determined by the kernel of the leading term, h_{nn}, which is simply written h_n, and appears as a parameter in the G-functional.

These functionals are found in Wiener (1958), and have been quoted many times since. Assuming the symmetric form for the kernels, to degree three the Wiener functionals are:

$$
\begin{aligned}
G_0(h_0, s)(t) &= h_0 \\
G_1(h_1, s)(t) &= [h_1]s(t) \\
G_2(h_2, s)(t) &= [h_2]s(t) - P\int_0^m h_2(v, v)\, dv \\
G_3(h_3, s)(t) &= [h_3]s(t) - 3P\int_0^m h_3(v, v, t_1)s(t - t_1)\, dv\, dt_1
\end{aligned}
$$

Note that the degree n functional contains only terms of degree with the same parity as n. The functional G_2 has the constant term $h_{20} = -P\int h_2(v, v)\, dv$ to be orthogonal to all zero degree operators, and the functional G_3 has a linear term with kernel $h_{31}(t_1) = -3P\int h_3(v, v, t_1)\, dv$ to be orthogonal to all linear operators.

2.3.3 Binary white-noise

In this study, a binary distribution of stimulus values was used. With each time step $\Delta t = 2\ ms$ each stimulus region was set to a high value or a low value with equal probability. The low value had intensity close to zero, hence the stimulus values in terms of contrast were ± 1, and the variance of the stimulus was $\sigma_s^2 = 1$, giving a power spectral density $P = \sigma_s^2 \Delta t = 2$ in units C^2/KHz.

Choosing a binary input provided the maximum stimulus variance, given a limited dynamic range of intensity available on a CRT screen. It also allowed many of the operations in the data analysis to be performed by logical operations, since multiplication of the values $+1, -1$ is isomorphic to addition modulo 2.

The orthogonalisation of the discrete-time Volterra series for this input will now be calculated.

We first consider the expected value of a product of binary variates drawn from a stimulus sequence:

$$E[s(t_1)s(t_2)\ldots s(t_n)]$$

If the indices $t_1, \ldots, t_n$ can be formed into equal pairs in *any* way, the product will be

constant and equal to one. Otherwise the product will be another binary variate, with expected value zero. In particular the expected value is zero if n is odd.

Contrast this with the expected value of a product of Gaussian variates with unit variance. In the Gaussian case this is equal to the *number* of ways that the variates can be put into equal pairs, which may be greater than one. For example the expected value of an even power is:

$$E[s^{2k}] = \frac{(2k)!}{k!2^k}$$

For the binary white-noise input the orthogonal polynomial series may be written in terms of polynomials $B_n(h_n, s)$, corresponding to the Wiener G- functionals for the Gaussian case:

$$r = \sum_{n=0}^{\infty} B_n(h_n, s)$$

These B-polynomials could be found by considering the general degree n polynomial

$$B_n(h_n, s) = \sum_{p=0}^{n} [h_{np}]s$$

and calculating the constraints necessary to make it orthogonal to all lower degree operators.

Instead, the correct orthogonalisation can be derived for terms of all degrees by a more general argument. We start by inspecting the leading term of the degree n polynomial B_n:

$$[h_n]s(t) = \sum_{t_1=0}^{m-1} \cdots \sum_{t_n=0}^{m-1} h_n(t_1, \ldots, t_n)s(t - t_1) \ldots s(t_n)$$

The m^n terms of this sum fall into two classes, those that have all the indices $t_1, \ldots, t_n$ distinct, and those that have at least one pair equal.

The terms with all indices distinct are orthogonal to all lower degree operators, as there will be no way of pairing the factors in the product

$$s(t - t_1) \ldots s(t - t_n)$$

with the factors in any product of less than degree n.

For a term with a repeated index, the two identical factors cancel to give a value of one, and the term is thus equivalent to an operator of lower degree than n.

The orthogonalisation required is then clear, lower degree operators equivalent to the terms of the second class must be subtracted from the above sum. This will

produce a polynomial operator equivalent, for binary white-noise inputs, to the sum of the terms in the first class, and hence orthogonal to any operator of degree less than n.

The orthogonal polynomial operators up to degree three can now be derived using this principle. For generality, consider a binary white-noise input taking on the two values $\pm\sigma_s$.

The constant and linear terms need no modification, as they are already orthogonal.

In the second degree monomial

$$[h_2]s(t) = \sum_{t_1,t_2=0}^{m-1} h_2(t_1,t_2)s(t-t_1)s(t-t_2)$$

the terms with $t_1 \neq t_2$ are orthogonal to lower degree operators. Any term with $t_1 = t_2$ is equal to the constant value $\sigma_s^2 h(t_1,t_1)$ for this input, and so this equivalent constant operator must be subtracted. The orthogonalised second order polynomial is thus:

$$[h_2]s + h_{20}$$

where the constant is:

$$h_{20} = -\sigma_s^2 \sum_{v=0}^{m-1} h_2(v,v)$$

For the third degree monomial

$$\sum_{t_1,t_2,t_3=0}^{m-1} h_3(t_1,t_2,t_3)s(t-t_1)s(t-t_2)s(t-t_3)$$

any term with at least two indices equal is equivalent to a linear operator for the binary white-noise input. The sum of these terms is:

$$\sigma_s^2 \sum_{u=0}^{m-1} \left(\sum_{v=0}^{m-1} (h_3(t_1,v,v) + h_3(v,t_1,v) + h_3(v,v,t_1)) - 2h_3(t_1,t_1,t_1) \right) s(t-t_1)$$

Note that the triple-diagonal term $h_3(t_1,t_1,t_1)$ is counted three times in the inner sum, whereas it should only appear once. This is corrected by the subtraction of $2h_3(t_1,t_1,t_1)$.

The linear term in the third degree orthogonal polynomial operator is thus $[h_{3\,1}]s$, where the kernel is:

$$h_{3\,1}(t_1) = -\sigma_s^2 \sum_{v=0}^{m-1} (h_3(t_1,v,v) + h_3(v,t_1,v) + h_3(v,v,t_1)) + 2\sigma_s^2 h_3(t_1,t_1,t_1)$$

If the kernel h_3 is in symmetric form, this can be simplified to:

$$h_{3\,1}(t_1) = -3\sigma_s^2 \sum_{v=0}^{m-1} h_3(t_1,v,v) + 2\sigma_s^2 h_3(t_1,t_1,t_1)$$

The correction for the triple-diagonal term is the only way in which the orthogonalisation differs from the Gaussian case, and the difference is due to the difference in the expected value of the power $s(t)^4$, which has a factor of three in the Gaussian case, and not in the binary case.

This correction is in practice small, and becomes smaller as the time-discretisation becomes finer; the correction involves the single value on the diagonal, which will be dominated by the sum over non-diagonal elements. It will be ignored during calculation of the Wiener form for a sandwich system in chapter 4, as the Gaussian case gives a particularly simple result. The correction in the case of some sample runs is illustrated in figure 8.

Summarising the results above, the orthogonalisation for a binary white-noise input is precisely to subtract from each monomial any terms with at least one repeated index. This means that the predicted output for the test input is independent of all kernel values with at least one repeated index, hence these kernel values cannot be estimated.

These values will however be required to predict the output to inputs which do not consist only of the values $\pm\sigma_s$. In this study estimates are made of the missing diagonal elements by cubic interpolation from the four nearest neighbours in a line perpendicular to the diagonal.

The usage of interpolation to estimate diagonal points of the kernel is unfortunate in that it would be better to directly estimate the values, however it is entirely acceptable theoretically. This contrasts with a previous paper (Marmarelis and McCann 1977), which points out that the Lee-Schetzen cross-correlation technique for kernel estimation will produce estimates of the diagonal points equal to zero; a second degree kernel is then plotted with a spurious line of zeros along the diagonal. The point is rather that with binary white-noise, the diagonal points do not receive estimates of zero, but are left undefined. When the orthogonalisation for binary white-noise is applied, we note that the fitted response is independent of the diagonal points, hence the experiment contains no direct information from which to estimate them. The diagonal points are free variables and can be set to anything. To specify them additional assumptions are required, and assuming some form of smoothness of the kernel justifies interpolation procedures.

2.3.4 Input-output cross-correlations

An important property of the orthogonalised series

$$r = \sum_{n=0}^{\infty} B_n(h_n, s)$$

concerns the input-output cross-correlation of degree n in the input:

$$E[r(t)s(t-t_1)\dots s(t-t_n)]$$

By the stationarity of the input process and the time-invariance of the operator, this is a function of $t_1, \dots, t_n$ and is independent of t.

Consider a given set of indices $t_1, \dots, t_n$ which are distinct. Then the elementary operator having output

$$s(t-t_1)\dots s(t-t_n)$$

is a monomial operator of degree n. Hence it is orthogonal to all terms $B_k(h_k, s)$ for $k > n$. As the indices are all distinct, r' is also orthogonal to all operators of degree less than n. This leaves only the leading term of B_n:

$$[h_n]s(t) = \sum_{v_1,\dots,v_n=0}^{m-1} h_n(v_1, \dots, v_n)s(t-v_1)\dots s(t-v_n)$$

The inner-product of the elementary operator with the terms of this sum yields

$$\sigma_s^{2n} h_n(t_1, \dots, t_n)$$

when the indices $v_1, \dots, v_n$ can be paired with equal indices $t_1, \dots, t_n$, otherwise zero. This pairing happens $n!$ times. Assuming the kernel is in symmetric form, the cross-correlation is thus

$$E[r(t)s(t-t_1)\dots s(t-t_n)] = n!\sigma_s^{2n} h(t_1, \dots, t_n)$$

when the indices $t_1, \dots, t_n$ are distinct.

This expression forms the basis of the Lee-Schetzen technique for kernel estimation (Lee and Schetzen 1965). The time-average cross-correlation is used as an estimate of the ensemble average, and the symmetric kernel of degree n is then estimated as

$$h_n(t_1, \dots, t_n) = \frac{1}{n!\sigma_s^{2n}} \overline{r(t)s(t-t_1)\dots s(t-t_n)}$$

with the time-average taken over index i. By the ergodicity of the input process this will converge to the real value as the run-length increases.

2.3.5 Relationship between the Volterra and Wiener kernels

To compare the Volterra and Wiener series we rewrite the Wiener series in the following way. Note that the even degree polynomials only contain terms of even degree, and similarly for the odd degrees. The first few terms are:

$$\begin{aligned} r = {} & [h_0] \\ & + [h_1] \\ & + [h_{20}] \quad + [h_2] \\ & + [h_{31}] \quad + [h_3] \\ & + \ldots \end{aligned}$$

The Volterra series will be produced by collecting terms of like degree. The Volterra kernel of degree p thus contain components from all Wiener polynomials of degree p and higher of the same parity:

$$k_p = \sum_{n=p,p+2,\ldots}^{\infty} h_{np}$$

If the series is zero beyond a certain point then the last two nonzero Volterra kernels are equal to the corresponding Wiener kernels. For example, if the system is assumed to have no components of degree greater than three, the Volterra and Wiener kernels of degree two and three are equal. The linear terms can be equated to give:

$$k_1 = h_1 + h_{31}$$

Using the results from the orthogonalisation gives:

$$k_1(t_1) = h_1(t_1) - 3\sigma_s^2 \sum_{v=0}^{m-1} h_3(t_1, v, v) + 2\sigma_s^2 h_3(t_1, t_1, t_1)$$

The difference between k_1 and h_1 thus increases in proportion to the input power σ_s^2 and the size of the third degree kernel. These components are illustrated in figure 8. In this study kernels are calculated to degree three, however some experiments appear to have power beyond this.

The Volterra series provides the appropriate representation of a system for inputs of very low contrast, close to some constant input I_0, while the Wiener series gives the least squares approximation to a system over a distribution of inputs having a given mean power.

The Volterra kernels can be useful as they can often be derived as exact mathematical expressions from an analytical model of the system. They also combine in a simple

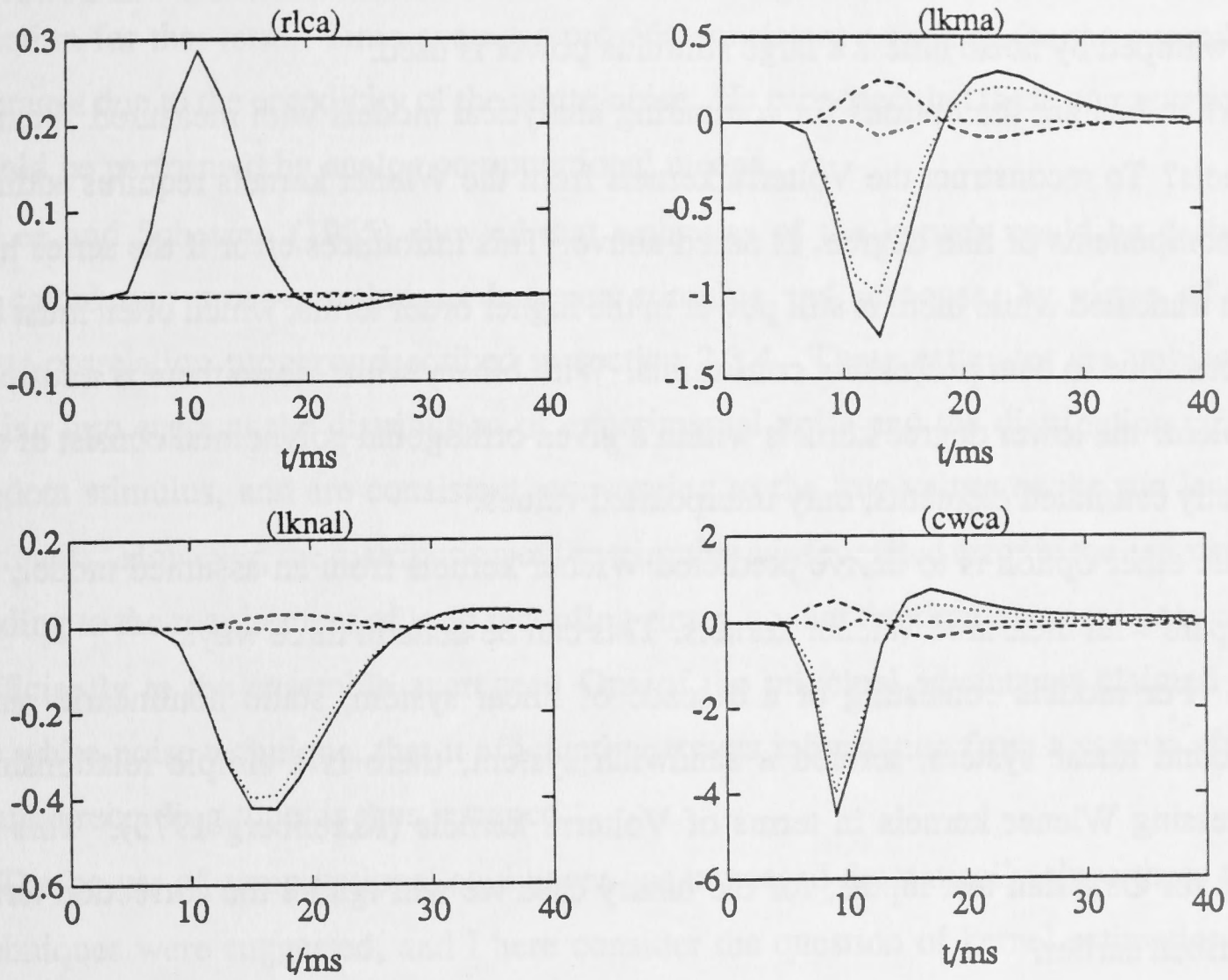

Figure 8: Examples of linear kernels from the Wiener series. **Solid lines**, the linear Wiener kernels h_1. **Dashed lines**, the linear kernel of the third degree orthogonal polynomial, $h_{3\,1}$. **Dotted lines**, an approximation to the Volterra kernel, $k_1 = h_1 + h_{3\,1}$. **Dot-dash**, the extra term in $h_{3\,1}$ when binary white-noise is used relative to Gaussian white-noise (see text). The four examples illustrated are from: an *Eristalis* receptor, an *Eristalis* LMC at high mean intensity, an *Eristalis* at low mean intensity and a *Calliphora* LMC. Run identifiers are indicated in parentheses. Note that the linear term $h_{3\,1}$ is significant for the LMCs, but has a similar profile to the kernel h_1 and hence causes only a change of amplitude rather than a change of shape of the kernel.

way when systems are cascaded. Manipulations are similar to manipulations required when dealing with power series functions of a single variable.

The Wiener kernels however are the ones which can realistically be estimated experimentally. Direct measurement of the Volterra kernels requires study of the system with vanishingly small test inputs. For example, the linear Volterra kernel is equal to the impulse response of the system per unit stimulus energy, in the limit as the test flash tends to zero strength. Estimates of the nonlinear kernels will however be swamped by noise unless a large stimulus power is used.

What then are the options for comparing analytical models with measured Wiener kernels? To reconstruct the Volterra kernels from the Wiener kernels requires adding the components of like degree, as noted above. This introduces error if the series has been truncated while there is still power in the higher order terms, which often must be the case due to data processing constraints. With binary white-noise there is a further problem: the lower degree kernels within a given orthogonal polynomial consist of no directly estimated elements, only interpolated values.

The other option is to derive predicted Wiener kernels from an assumed model, to compare with measured Wiener kernels. This can be done in three ways:

1. For models consisting of a cascade of linear system, static nonlinearity and a second linear system, termed a sandwich system, there is a simple relationship expressing Wiener kernels in terms of Volterra kernels (Korenberg 1973). This is exact for Gaussian test inputs; for the binary case we will ignore the correction term described earlier.

2. Exact expressions for the Wiener kernels could be obtained from the cross-correlation property described in 2.3.4. This involves the calculation of expected values, which may be intractable.

3. A simulation may be done, running a white-noise experiment on the model system, and comparing the resulting kernels with the experimental kernels.

2.4 Kernel estimation by linear regression

Wiener's original proposal (Wiener 1958) for the estimation of the kernels was to write each kernel h_n as a series in terms of n-fold tensor products of Legendre polynomials. Each term would again define a system orthogonal to all other terms, relative to the white-noise input. This gives a Fourier series for the entire system, and the coefficient for a particular term is equal to the expected product of the overall system and the basis function for that term. Time averages provide consistent estimates for the ensemble averages due to the ergodicity of the white-noise. He proposed that these computations would be performed by analog computational means.

Lee and Schetzen (1965) showed that estimates of the kernels could be derived by calculating cross-correlations between stimulus and response, by virtue of the cross-correlation property described in section 2.3.4. These estimates are unbiased, taking into account the distribution of experimental noise and the distribution of the random stimulus, and are consistent, converging to the true values as the run length increases. However, the distribution of the stimulus causes added error in the estimates, leading to the requirement of long recording-times, so that the time-averages converge sufficiently to the ensemble averages. One of the principal advantages claimed for the white-noise technique, that it efficiently extracts information from a system given limited recording time, is thus lessened.

The power of computational equipment has increased dramatically since these two techniques were suggested, and I here consider the question of kernel estimation *ab initio* as a problem in linear regression.

We note first that the polynomial representation, although having terms of increasing degree in the stimulus, is linear in each of the kernels. This stems from the principle that an n-linear function on a vector space can be represented by a linear function on the n-fold tensor product space. Thus kernel estimation, even for a nonlinear model, is a linear estimation problem.

Linear regression is most elegantly expressed in terms of a matrix formulation. If a column vector $\underline{r}$ of n response data points is modeled as being a linear combination of p regression vectors $\underline{x}_1, \ldots, \underline{x}_p$ with regression coefficients $\beta_1, \ldots, \beta_p$, plus an error vector $\underline{\epsilon}$, the model can be written:

$$\underline{r} = X\underline{\beta} + \underline{\epsilon}$$

The $n \times p$ matrix X is the *design matrix*, having as columns the regression vectors, representing the independent variables. The vector $\underline{\beta}$ is the *parameter vector*, containing the regression coefficients.

The estimate $\underline{b}$ of $\underline{\beta}$ which minimises the residual sum of squares $D = \|\underline{\epsilon}\|^2$ occurs when the residual vector $\underline{\epsilon}$ is orthogonal to all columns of X, so that $X'\underline{\epsilon} = 0$, where X' denotes the transpose of X. This leads to the *normal equation*:

$$X'\underline{r} = X'X\underline{b}$$

The matrix $X'X$ is termed the *normal matrix*. If it is invertible the equation has the unique solution $\underline{b}^*$ given by:

$$\underline{b}^* = (X'X)^{-1}X'\underline{r}$$

2.4.1 The design matrices of polynomial operator models

For the systems identification application, $\underline{r}$ is the vector containing the response signal, of length n_t. We now derive the design matrices for the Wiener series polynomial model, given a binary white-noise stimulus, assuming a stimulus normalised to have unit variance, $\sigma_s^2 = 1$.

The polynomial operator model to degree 1 is:

$$Fs(t) = h_0 + \sum_{t_1=0}^{m-1} h_1(t_1)s(t - t_1)$$

The parameters are thus h_0 and $h_1(t_1) \ : \ t_1 = 0 \ldots m-1$. The design matrix consists of two blocks, $X = [X_0 X_1]$. The zero degree block X_0 is just a column of ones. The first degree block X_1 has columns given by,

$$[s(t - t_1) \ : \ t = 1 \ldots n_t]$$

for t_1 ranging over latencies $0 \ldots m-1$. The block X_1 thus has a Tœplitz structure, having constant values down each diagonal.

For a degree 2 model, the following quadratic term is added:

$$F_2 s(t) = \sum_{0 \le t_1 < t_2 \le m-1} h_2(t_1, t_2)s(t - t_1)s(t - t_2)$$

The sum is taken over $t_1 < t_2$, which assumes the upper-triangular canonical form for the kernel, to avoid redundant parameterisation. The diagonal terms, $t_1 = t_2$ are

removed by the orthogonalisation procedure. This adds the parameters $h_2(t_1, t_2)$: $0 \leq t_1 < t_2 \leq m-1$ to the model. The design matrix is augmented by the block X_2, having columns,

$$[s(t-t_1)s(t-t_2) \ : \ t = 1 \ldots n_t]$$

for the range of t_1, t_2 given above.

The third degree term is be similarly added, with indices taking on the values $0 \leq t_1 < t_2 < t_3 \leq m-1$. Terms are also added for the second stimulus channel B in the two channel spot-annulus stimulation experiment. For this model linear kernel estimates were calculated for 248 latencies, corresponding to a memory length of 500 ms, and the nonlinear kernels were calculated for 23 latencies, up to memory length 50 ms. This gave the total number of parameters $n_p = 3303$. The repeat-length of the white-noise stimulus was $n_t = 32768$, lasting 65 seconds.

For the spatiotemporal model, describing stimulation with the 15×15 checkerboard indexed by spatial coordinates (x, y), the model linear response is:

$$F_1 s(t) = \sum_{t_1=0}^{m-1} \sum_{x,y=0}^{14} h_1(x, y, t_1) s(x, y, t - t_1)$$

The design matrix can be written as m blocks, each block having 225 columns corresponding to the 225 spatial locations. The m blocks will be the same except for differing vertical shifts corresponding to the range of latencies. Kernels were calculated for 23 latency values, up to 50 ms, giving a total number of parameters $n_p = 5175$, with stimulus repeat-length $n_t = 32768$, as above.

2.4.2 Relation to the Lee-Schetzen method

As the stimulus is discrete-time white-noise, that is, a sequence of independent, zero-mean random variables, the columns of the design matrix will be approximately orthogonal. This is true even for the higher degree columns, involving pointwise products of stimulus vectors. The normal matrix $X'X$ is thus close to a multiple of the identity matrix I of size n_p. For the case of binary white-noise of unit variance, the diagonal elements will be exactly equal to the repeat-length n_t, while the off-diagonal elements have mean zero and standard deviation $\sqrt{n_t}$.

Using the approximation $X'X \approx n_t I$, the inverse can be approximated as $(X'X)^{-1} \approx 1/n_t \, I$. The parameter estimate then becomes:

$$\underline{b} = 1/n_t \, X' \underline{r}$$

These estimates are in fact the cross-correlations between stimulus and response. Symmetrisation of the degree n kernel involves division by $n!$, thus giving identity with the Lee-Schetzen estimate derived in section 2.3.4. These estimates are treated in this thesis as initial estimates, which must be corrected by multiplication by the inverse of the matrix $A = 1/n_t\, X'X$ to obtain the true least-squares estimates.

2.4.3 An efficient technique for solution of the normal equations

For designs involving a small number of parameters the matrix $A = 1/n_t\, X'X$ can be calculated and inverted. This was done in this study for designs involving up to around 500 parameters. For larger designs this is not practical, due not only to the difficulty of inverting the matrix, but more due to the large size of the inverse once obtained. For example, the spatiotemporal design used in this thesis has a kernel with dimension $n_p = 5175$. Using single precision and storing only the upper triangular part this would require 51 megabytes of storage.

The correction can be made relatively easily by taking advantage of two properties of the matrix A: it is close to an identity matrix, and it has symmetries due to the Tœplitz nature of the design matrix.

The first property suggests attempting to expand the inverse in a Taylor series about the identity matrix. The matrix can be written as $A = (I + E)$, where I is the n_p dimensional identity and E is capital epsilon, a matrix of small elements. The Taylor series for A^{-1} would then be:

$$(I + E)^{-1} = I - E + E^2 - E^3 + \cdots$$

This series will converge if the eigenvalues of E all have modulus less than one. The Lee-Schetzen estimate can be regarded as having zero-order correction, and can be written as b_0. The parameters corrected to order k are then:

$$\underline{b}_k = \underline{b}_0 - E\underline{b}_0 + E^2\underline{b}_0 - \cdots E^k\underline{b}_0$$

Note that the term $E^i\underline{b}_0$ is much more easily evaluated by doing the multiplications starting from the right hand side! Furthermore, roundoff error can be reduced by factoring the expression as:

$$\underline{b}_k = \underline{b}_0 - E(\underline{b}_0 - E(\underline{b}_0 - \cdots - E\underline{b}_0))$$

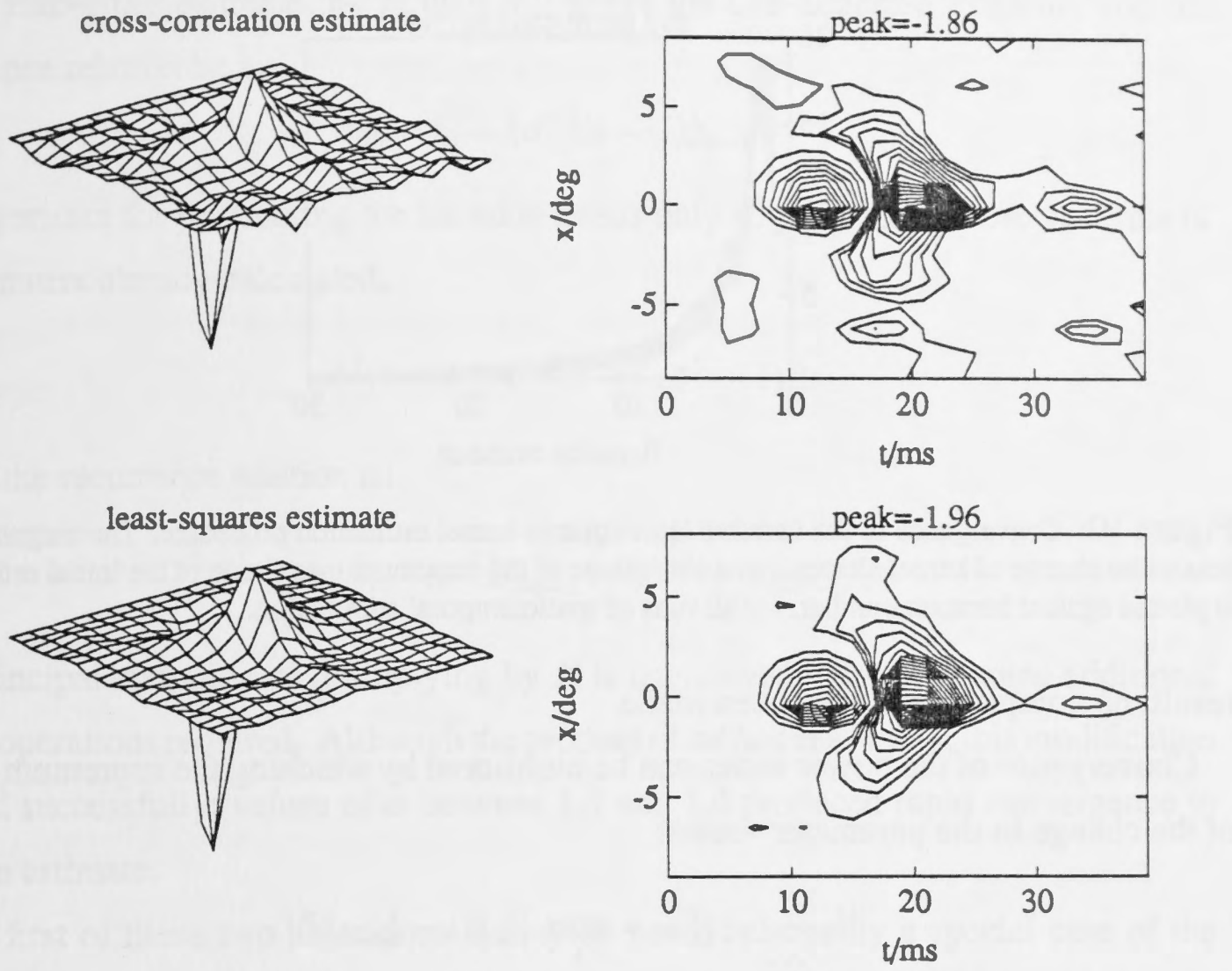

Figure 9: The effect of kernel estimate correction. The data is from an *Eristalis* LMC, stimulated with spatiotemporal white-noise. The kernel is the horizontal marginal kernel, obtained by integrating the spatiotemporal kernel over the y dimension, described fully in the following chapter. **Upper**, the cross-correlation estimate. **Lower**, the corrected least-squares estimates. Left and right plot the same data, in perspective and as contours. Contour step size for negative range is 10% of peak value as indicated, and for positive range is 2% of peak value; the zero contour is omitted.

This suggests the recurrence relation

$$\underline{b}_k = \underline{b}_0 - E\underline{b}_{k-1}$$

for which a program can be easily written. The second property of A is used to reduce storage requirements. The matrix $E = A - I$ is symmetric, and also has a structure which could be called block-Tœplitz. Only the top row of m blocks of size 225×225 need be stored; these blocks are repeated down the upper diagonals of the matrix, and are repeated transposed down the lower diagonals. Each iteration of the above recurrence requires 4 seconds on an Apollo DN10000 computer, thus correction to a high order can be done in reasonable time.

The value of this technique can be gauged from the results of the correction illustrated in figure 9. The least-squares kernel clearly is less contaminated by noise, and in contrast with most data-smoothing operations, the smoother data is the correct

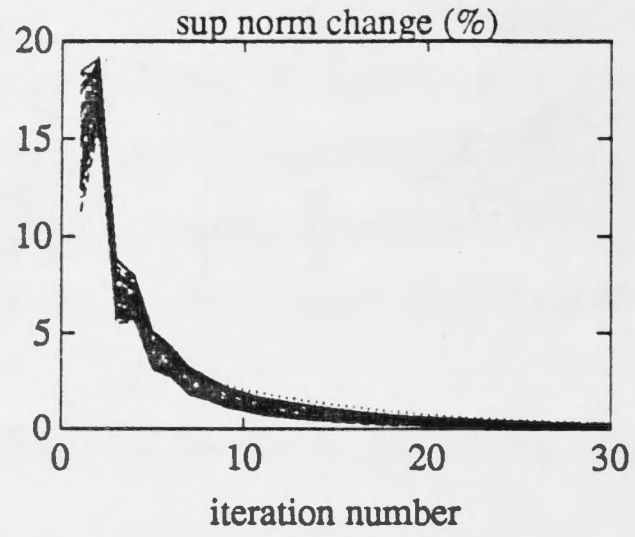

Figure 10: Convergence of the iterative least-squares kernel estimation procedure. The magnitude of maximum change of kernel element, as a percentage of the maximum magnitude of the initial estimates, is plotted against iteration number, for all runs of spatiotemporal stimulation.

result; no compromises have been made.

Convergence of the power series can be monitored by watching the supremum norm of the change in the parameter vector:

$$\|\underline{b}_k - \underline{b}_{k-1}\|_\infty = \max_i |\underline{b}_k(i) - \underline{b}_{k-1}(i)|$$

Expressed as a percentage of the maximum absolute value of the initial parameter vector, $\|\underline{b}_0\|_\infty$, figure 10 shows the convergence with iteration for this data set. Typically the maximum change was up to 18% of the peak value, and drops below 1% only after around 12 iterations.

The equivalent operation was performed for the spot-annulus design, involving $n_p = 3303$ parameters for kernels up to cubic degree. Initially the results did not look correct, and increasing the number of iterations revealed that the series was diverging, implying that for this design the matrix E had at least one eigenvalue greater than one.

It seemed possible that the series might converge when expanded about some other point, however the point must be chosen such that its inverse is of simple form. The simplest point to try is αI, for some scalar α. We then express A as:

$$\begin{aligned} A &= \alpha I + (A - \alpha I) \\ &= \alpha \left(I + (\alpha^{-1} A - I) \right) \end{aligned}$$

The inverse has the power series

$$A^{-1} = \alpha^{-1} \left(I - (\alpha^{-1} A - I) + (\alpha^{-1} A - I)^2 - \cdots \right)$$

which will converge if $(\alpha^{-1} A - I)$ has eigenvalues of modulus less than one.

The zero-order estimate, $\underline{b}_0$, is then α^{-1} times the Lee-Schetzen estimate, and the recurrence relation is:

$$\underline{b}_k = \underline{b}_0 - (\alpha^{-1}A - I)\underline{b}_{k-1}$$

The algorithm for performing the iteration needs only slight modification. In terms of the E matrix already calculated,

$$\alpha^{-1}A - I = \alpha^{-1}E + (\alpha^{-1} - 1)I$$

and so the recurrence relation is:

$$\underline{b}_k = \underline{b}_0 - \alpha^{-1}E\underline{b}_{k-1} - (\alpha^{-1} - 1)\underline{b}_{k-1}$$

The principal operation of multiplying by E is unchanged, with only some additional vector operations required. Although the product of *ad hoc* reasoning, this modification worked successfully; values of α between 1.1 and 1.4 produced rapid convergence to a stable estimate.

The first of these two algorithms it may be noted is actually a special case of the *Jacobi iteration* algorithm, or *method of simultaneous displacements*. Jacobi iteration can be given a matrix formulation as follows: it solves an equation of the form $Ab = b_0$ by writing the matrix A as the sum of its diagonal part and its non-diagonal part, hence

$$Ab = (A_d + A_n)b = b_0$$

where A_d is zero off the leading diagonal, and A_n is zero on the leading diagonal. The equation can be rearranged as:

$$b = A_d^{-1}(b_0 - A_n b)$$

This defines a recurrence relation for which the required solution b is the fixed point, if convergence occurs. In the binary white-noise application the leading diagonal of A consists of unit elements, hence this is precisely the recurrence relation used above, although the derivation in terms of the Taylor series for A^{-1} is unusual. The modified algorithm, expanding about αI seems to be a genuine extension of the Jacobi method.

The size of this calculation is of interest, both in terms of operations performed and storage required. For a general linear model with n_t observations and n_p parameters the calculation of the normal matrix $X'X$ is the largest step, requiring around $n_p^2 n_t/2$ operations, and producing $n_p^2/2$ elements for the upper-triangular region of the normal

matrix. Utilising the symmetries in the design due to the correlation nature of the model reduces both these figures; for the spatiotemporal design here the reduction is by a factor of 23. This calculation is performed once, since the same stimulus signal is used in each experiment. Note that it is not necessary to store the entire design matrix X, both because of Tœplitz symmetries present and, when the stimulus is produced by a deterministic algorithm, parts of the stimulus can be regenerated when required.

To calculate the inverse of the normal matrix would require around $2/3n_p^3$ operations, and would produce severe storage problems for large designs. Solution of the normal equations separately for each experiment is thus necessary. Most algorithms are asymptotically of the order of n_p^3 operations. By contrast the iterative method requires n_p^2 operations for each of less than 20 iterations, and almost no further storage. This is a considerable saving when $n_p = 5175$.

The value of obtaining least-squares estimates for the kernels has been pointed out by other researchers, and two algorithms have been suggested, the *orthogonal algorithm* (Korenberg *et al* 1988a) and the *fast orthogonal algorithm* (Korenberg 1988). I find that both algorithms are clarified by formulation in matrix terms. The first involves Gram-Schmidt orthogonalisation of the columns of the design matrix X. This essentially factors it as $X = WU$, where W is $n_t \times n_p$ with orthogonal columns, and U is upper-triangular with unit values on the diagonal. The normal equations then become:

$$U'W'WU\underline{b} = U'W'\underline{r}$$

The algorithm calculates W, U, the diagonal matrix $W'W$ and $W'\underline{r}$, and then solves the equation

$$U\underline{b} = (W'W)^{-1}W'\underline{r}$$

for the kernel estimates $\underline{b}$.

The fast orthogonal algorithm recognises that W need not be explicitly calculated, and calculates only $U, W'W$ and $W'r$, taking advantage of the symmetries of the design to avoid redundant calculations. The algorithm is equivalent to a Cholesky decomposition of the normal matrix, writing it as $X'X = R'R$ where R is upper-triangular (Dongarra *et al* 1979). Korenberg *et al* (1988b) report use of the algorithm for system identification of the response of the cockroach femoral tactile spine, estimating $n_p = 351$ kernel elements from $n_t = 15,000$ data points. The algorithm still has an asymptotic order of n_p^3, and requires storage of the $n_p^2/2$ elements of

the upper triangular matrix U. It has the advantage that it will produce an answer without requiring convergence of an iterative procedure, however when applicable the recurrence algorithm used in this thesis is more efficient, both in terms of storage and computation, allowing much larger designs to be used.

The use of precise least-squares estimates produces better kernel estimates from white-noise stimulation, however the orthogonal design techniques described below achieve the same effect, while not requiring any extra computation beyond the cross-correlation, thus rendering these algorithms redundant in the context of active systems identification. A more important application in the future may be in the identification of systems where the stimulus is not precisely controlled by the experimenter. If the stimulus must be sampled along with the response, and does not have orthogonal or even approximately orthogonal properties, then the regression approach described here still allows a nonlinear kernel model to be fitted. This vastly increases the range of application of nonlinear system identification, to what might be termed *passive nonlinear system identification.*

2.4.4 Statistical properties of kernel estimates

The above techniques assume a model of the form

$$\underline{r} = X\underline{\beta} + \underline{\epsilon}$$

giving the response $\underline{r}$ as a design matrix X times a parameter vector $\underline{\beta}$ plus a residual $\underline{\epsilon}$. The algorithms produce the least-squares estimate $\underline{b}^* = (X'X)^{-1}X'\underline{r}$ of the parameters, minimising the residual sum of squares $\|\epsilon\|^2$. Further statements can be made concerning the statistical properties of the estimates, if assumptions are made about the distribution of the residuals.

If the residual $\underline{\epsilon}$ is a zero-mean random process, then $\underline{b}^*$ is an unbiassed estimate of $\underline{\beta}$:

$$E[\underline{b}^*] = \underline{\beta}$$

In contrast, the cross-correlation estimate $\underline{b}_{\text{corr}} = 1/n_t\, X'\underline{r}$ is biassed:

$$E[\underline{b}_{\text{corr}}] = X'X\underline{\beta}$$

Over the distribution of all stimulus realisations $\underline{b}_{\text{corr}}$ is unbiassed, since $E[1/n_t\, X'X] = I$. But since the realisation of the stimulus is known, there is a known bias which should be removed.

If the residual consists of independent identically distributed Gaussian variates, then $\underline{b}^*$ is also the maximum likelihood estimate of the parameter $\underline{\beta}$. The maximum likelihood estimate of the variance of the residuals σ_ϵ^2 is given by s_ϵ^2, with:

$$s_\epsilon^2 = \|\underline{\epsilon}\|^2/(n_t - n_p)$$

The variance of the estimate $\underline{b}^*$ is:

$$V[\underline{b}^*] = \sigma_\epsilon^2(X'X)^{-1}$$

Of course we have sought to avoid evaluating $(X'X)^{-1}$, however we can give an approximation of its expected value over the distribution of white-noise stimuli. Using the previous notation, $X'X = n_t(I + E)$, the variance is:

$$V[\underline{b}^*] = \sigma_\epsilon^2/n_t\ (I - E + E^2 - \cdots)$$

Consider then the expected value of this, remembering that $E[\ ]$ is the expected value operator, while E is capital epsilon, a matrix. The diagonal elements of E are exactly zero. Each off-diagonal element is the mean of a binary white-noise signal, and thus has expected value zero and variance $1/n_t$. Furthermore these elements are independent, apart from the symmetry $E_{ij} = E_{ji}$. For the first degree term we have $E[E] = 0$. For the term E^2, the off-diagonal elements are sums of products of independent zero-mean variates, hence have zero mean. The diagonal elements are sums of squares of $n_p - 1$ variates of variance $1/n_t$, and thus have mean $(n_p - 1)/n_t$. Hence $E[E^2] = (n_p - 1)/n_t\, I$, and the variance of $\underline{b}^*$ can be approximated by:

$$V[\underline{b}^*] \approx \sigma_\epsilon^2(1 + n_p/n_t)$$

This is estimated using the estimate s_ϵ^2 of σ_ϵ^2.

2.4.5 Orthogonal design techniques

It should be mentioned that least-squares estimates can be obtained, while avoiding any need to deal with large matrices, by utilising the principle of orthogonal design, selecting the stimulus so that the columns of the design matrix are precisely orthogonal. White-noise analysis can be described as an approximately orthogonal design, or a design which is orthogonal in the mean, over the distribution of white-noise stimulus realisations. Precisely orthogonal designs involve deterministic stimuli,

which nevertheless contain sufficient complexity to reveal system properties up to some degree of nonlinearity. Several such techniques have been developed; I mention the following two examples.

A technique has been developed by Dr Erich Sutter, at the Smith-Kettlewell Institute in San Francisco, using a stimulus called an m-sequence, produced by a simple recurrence relation. Interestingly, such sequences were considered as generators of pseudo-random white-noise at an earlier time, but were rejected due to certain higher order correlation properties. Sutter has turned these properties to advantage (Sutter 1987).

For an m-sequence $[s(t) : t = 1 \ldots n_t]$ the shifted versions $[s(t - t_1) : t = 1 \ldots n_t]$ for each latency t_1 are precisely orthogonal to each other. Further, the set of stimulus signals at all possible time-shifts is closed under pointwise multiplication, so that each higher degree regression vector is equal to the stimulus s shifted by some other delay. A choice of m-sequence can be made so that the shifts corresponding to the regression vectors at the required degrees and memory lengths are all distinct. Due to the precise orthogonality the cross-correlation estimates are the exact least-squares estimates, and from the multiplication property the required regression coefficients of all degrees are present in the first order cross-correlation. A modified Walsh transform is used to calculate this cross-correlation efficiently.

Another deterministic technique producing an orthogonal design is the sum-of-sinusoids technique of Victor, Shapley and Knight (1977, Victor and Knight 1979, Victor and Shapley 1980). This uses a stimulus composed of the sum of (typically) eight sinusoids, all harmonics of some much lower base frequency. A nonlinear system gives response components at the original frequencies and frequencies equal to the various sums and differences of the original frequencies. By fitting the gains and phases of these components, points of the *frequency kernels* of the system are estimated. From Fourier theory it is well-known that the harmonic components are all orthogonal, hence the estimation problem has orthogonal design, and is computationally very efficient.

I have implemented this technique to estimate first and second order frequency kernels for a locust photoreceptor responding to a point source, but it is not clear how to extend the technique to produce a general spatiotemporal stimulus.

2.5 Preparation and recording techniques

The first two years of this PhD course were spent in developing skills in the techniques of intracellular recording and computer controlled stimulus generation and data acquisition. Large amounts of data were collected from the photoreceptors and LMCs of *Locusta migratoria* and the fly *Eristalis tenax*, using flash and sinusoidal stimuli generated by light emitting diodes.

The development of the white-noise system was a large task, involving the development and maintenance of the hardware, software and concepts for the generation of high frame-rate spatiotemporal stimulation, synchronised data acquisition and subsequent data analysis. The maintenance of a high standard of elecrophysiological recording is itself a full-time task, which seems better to perform every day for a period rather than occasionally. The project was thus expanded into a collaboration, with a very useful division of labour. Dr Daniel Osorio prepared the insects and obtained most of the impalements of the cells; I then ran the experiments and handled the data processing. For complex computer-based experimentation to be attempted I would suggest that a division of labour of this kind is the most efficient way to proceed, although in insect electrophysiology the lone experimenter seems at present still to be the norm.

Two species of fly were used, *Eristalis tenax*, caught from the wild during the summer months, and *Calliphora vicina*, from a culture maintained in the Research School of Biological Sciences, but frequently replenished from the wild. The data in this thesis was obtained from female flies at 2–7 days post-eclosion. The insect was mounted on wax, and a hole 4–7 facets wide was made in the cornea. Micropipette electrodes were made from borosilicate glass stock (Hilgenberg), of external diameter 1 mm, internal diameter 0.5 mm. They were pulled on a Brown-Flaming P77 micropipette puller. Micropipettes were filled with a 3M potassium acetate electrolyte, and had resistances of 150–200 $M\Omega$.

The electrode was advanced into the left eye, until a cell was penetrated. Recordings could be routinely made from photoreceptors in the retina and from large monopolar cells in the lamina, identified by a hyperpolarising response to light. In all recordings used, cells were held with stability for over an hour and often much longer. All cells had a field of view approximately equatorial and 5–20° from midline.

Once a stable recording was obtained, I carried out the remainder of the experiment as follows. A mirror was positioned so that the stimulating oscilloscope filled

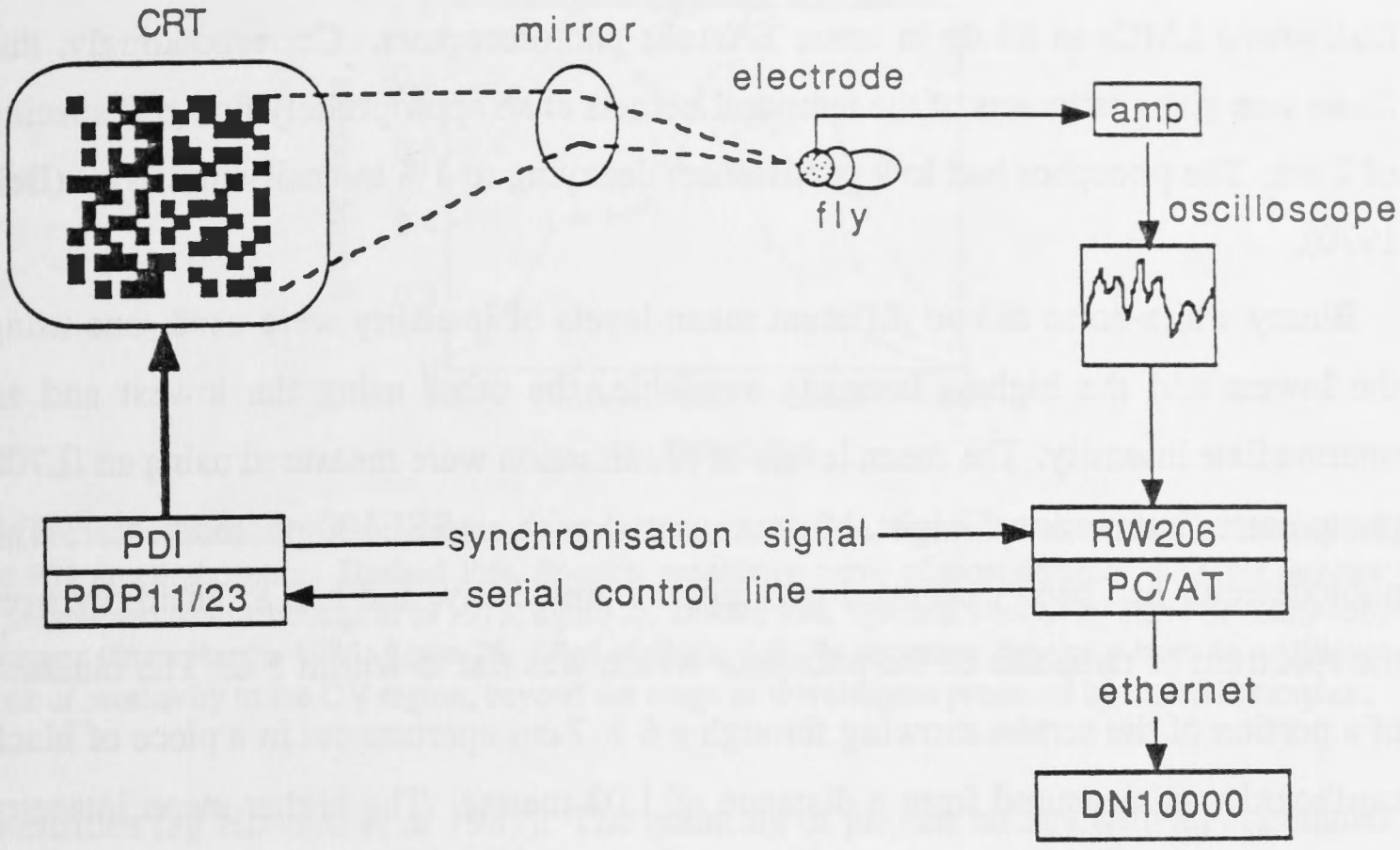

Figure 11: Schematic representation of the data-flow in the experimental setup. On the left an autonomous subsystem generates the visual stimulus, on the right the intracellular response is amplified, digitised and processed.

the field of view of the cell. The display on the oscilloscope was rotated until it appeared in upright orientation, as observed looking into the mirror in line with the fly. Various impulse responses were recorded, and then a sequence of runs of white-noise experimentation were made. The number of white-noise runs obtained from a cell varied from 1 to 16. In all, 148 useful runs were recorded, from a total of 28 lamina cells and 9 photoreceptors.

The temperature was measured at the start of each recording session, and varied between 22 and 25° C.

2.5.1 Stimulus generation and response digitisation

Figure 11 represents schematically the equipment for stimulation and response recording. The stimuli were produced on a Joyce oscilloscope, model DM2, with a green phosphor, denoted P31. Although specifications indicate a maximum frame rate of 200 Hz for this monitor, it was found that the rate could be increased to 500 Hz, with a consequent reduction in the number of lines displayed to 70. Inspection of power spectra indicates that this covers well the bandwidth of the systems under study; the

rolloff in power spectral density of response at 250 Hz ranges from 12 db in some *Calliphora* LMCs to 24 db in some *Eristalis* photoreceptors. Correspondingly, this frame rate gives estimates of the temporal kernels at an appropriately fine grid spacing of 2 ms. The phosphor had low persistence, decaying to 1% intensity in 250 μs (Bell 1970).

Binary white-noise at two different mean levels of intensity were used, one using the lowest and the highest intensity available, the other using the lowest and an intermediate intensity. The mean levels of illumination were measured using an IL700 photometer (International Light, Massachusetts) with an SEE100 photodetector. The photodetector had been calibrated two months previously, and had a sensitivity over the spectrum of radiation of the phosphor which was flat to within 5%. The radiance of a portion of the screen showing through a $6 \times 7\,cm$ aperture cut in a piece of black cardboard was measured from a distance of 1.02 metres. The higher mean intensity was measured in this way as $(1.2 \pm .2) \times 10^{-4}\,W\,cm^{-2}\,sr^{-1}$. The relationship between the higher and the lower mean intensities was determined with the detector placed against the screen. The lower mean intensity was less by a factor of 190, that is, 2.28 log units.

These figures are to be taken as the official calibration of the stimulus intensity. Some other quantities will be estimated, as useful measures of intensity. As these require information from a variety of diverse sources, they are given only as rough estimates, not as calibrations.

The spectral composition curve for the P31 phosphor can be taken from Bell (1970). Using this the intensity of illumination in terms of photons can be estimated as $3 \times 10^{14}\,ph\,s^{-1}\,cm^{-2}\,sr^{-1}$.

The spectral composition of the radiation in terms of photons is proportional to the power density multiplied by the wavelength. This is plotted, renormalised, in figure 12, along with estimated relative photon sensitivities for the two fly species.

Dual pairing between spectral photon composition and spectral photon sensitivity curves gives estimates of the spectral efficiency of this phosphor relative to the same number of photons delivered at the most effective wavelength, λ_{max}, for the two cases, and hence the equivalent intensity in $ph\,s^{-1}\,cm^{-2}\,sr^{-1}$ at λ_{max} for the two flies.

A useful measure of intensity is the number of absorbed photons per receptor per second, assuming linear extrapolation from the photon capture rate at very low

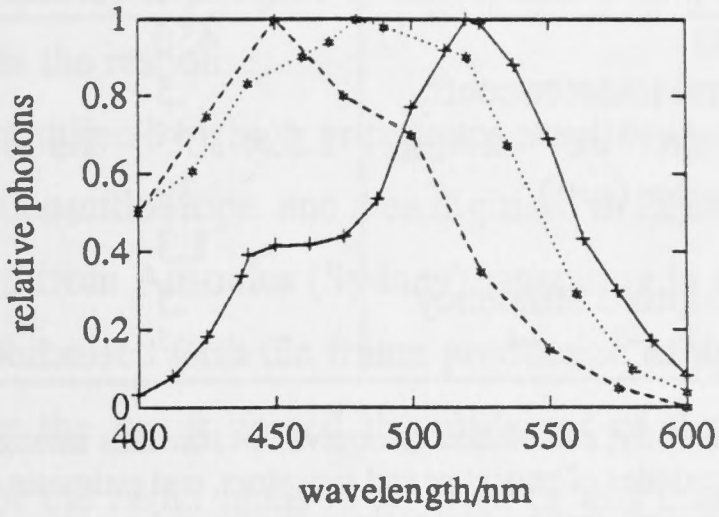

Figure 12: Spectral photon transfer characteristics. **Solid line,** relative photon emission density for the P31 green phosphor. **Dashed line,** Spectral sensitivity curve of most common *Eristalis* receptor type (adapted from Horridge *et al* 1975, figure 2). **Dotted line,** Spectral sensitivity curve of *Calliphora* receptor (from Hardie 1985, figure 23, filled circles). *NB* Fly receptors generally have an additional peak of sensitivity in the UV region, beyond the range of wavelengths produced by the P31 phosphor.

intensities (*eg* Howard *et al* 1987). The counting of photon bumps with an attenuated stimulus was not done, however some estimate of the rate of arrival of photons per receptor can be made using the following information, as in Dubs *et al* (1981). The facet diameter in the frontal region of *Calliphora* is estimated as 39 μm (Hardie 1985). The same estimate is used for *Eristalis*. Values of the half-width of the spatial sensitivity are obtained from the spatiotemporal white-noise experiments. Assuming a Gaussian spatial sensitivity, the effective angle of acceptance is $2\pi\Delta\rho^2/(8\ln 2)$. For photons incident on the receptor the quantum capture efficiency is taken as 0.5, (Dubs *et al* 1981).

Table 1 gives results for these calculations. In short, the higher mean intensity is indicated as around $I_0 = 10^6\ ph\ s^{-1}\ rec^{-1}$ for the two species of fly, and the lower mean intensity is 2.3 log units less. The estimated intensity in $W\ cm^{-2}\ sr^{-1}$ is however the preferred calibration.

Two different spatial arrangements of stimulus were used, illustrated in figure 7. The first was a general spatiotemporal stimulus, a 15×15 array of checks, with width varying from 0.6 to 1.2 degrees, as seen from the eye. The second assumed a concentric organisation of receptive field, and consisted of a spot of diameter 2 degrees, which was placed on the cells most sensitive area, and a surrounding annulus extending from a radius of 3 degrees to a radius of 6 degrees.

These patterns were generated by the prototype of a frame buffer called the *Psychophysics Display Interface* designed and built by Dr Paul Mackerras of the

	Eristalis	*Calliphora*
$\lambda_{\max}$ (nm)	450	495
P31 spectral transfer coeff.	.5	.73
equiv. $ph\,cm^{-2}\,sr^{-1}$ at $\lambda_{\max}$	1.5×10^{14}	2.3×10^{14}
facet diameter (μm)	39	39
$\Delta\rho^{\circ}$	1.3	1.4
quantum capture efficiency	.5	.5
absorbed $ph\,s^{-1}\,rec^{-1}$	7×10^{5}	1×10^{6}

Table 1: For the two species of fly, calculation of equivalent stimulus intensities at peak wavelength accounting for spectral characteristics of phosphor and receptors, and estimates of the photon absorption rates, accounting for facet diameters, receptor acceptance angles and quantum capture efficiency.

Australian National University, operating in a PDP11/23 computer. The spatial patterns were stored in an 8 bit per pixel video memory, while the intensity displayed in each region could be set by reloading a Z-lookup table on each frame.

To supply the high rate of random numbers required for the spatiotemporal stimulus the following scheme was devised. A vector of 16384 pseudorandom intensities was stored in the computer's memory. On each frame a single random address was generated. The 225 intensities required for the next frame were then loaded from memory, starting at that address, into the Z- lookup table. The stimulus value at each time and place is thus

$$s(x, y, t) = I(a(t) + x + 15y)$$

where I is the vector of random intensities; $a(t)$ is the address produced at time t; and x, y are spatial coordinates, ranging from $0 \ldots 14$.

The random numbers were produced by a simple recurrence relationship,

$$x' = 12869x + 6925 \pmod{32768}$$

and then scaled to give binary intensities or addresses. The scheme for combining intensities and addresses provides an additional randomisation. Note that since regression is used in the estimation of the kernels, the 'quality' of randomness is not crucial. Any part of the stimulus signal was readily recreated whenever required during data analysis.

The stimulus had a period of 32768 frames, and was repeated 8.03 times, giving a total run length of 8 minutes 46 seconds. Repeating the stimulus allowed averaging, reducing the response variance by a factor of eight before the more arduous cross-correlation calculations began. It also allowed a distinction to be made between

the noise in the system and any higher order nonlinearities, which would produce a periodic component in the response.

Responses were amplified by a high impedance amplifier built in RSBS by Dr. Gert Stange and a Textronix oscilloscope, and then digitised to 12 bit precision by an RW206 data acquisition board from Ausonics (Sydney), operating in a PC/AT computer. The digitisation was synchronised with the frame production of the stimulus. The sample was taken $1\,ms$ after the raster passed the midpoint of the stimulus pattern. The non-zero scan time of the raster leads to an error of less than $0.2\,ms$ in estimates of delays between stimulus and response.

No analogue filtering was used before digitisation, in order to avoid any phase distortion. This will produce estimates of the kernels which are unbiassed at the latencies sampled. Some additional variance is introduced in the digitised responses, as noise at frequencies above 250 *Hz* is aliased to lower frequencies. However analysis of the errors of kernel estimates indicated below 1% relative RMS error, due to the long recording times. It was thus judged more important to avoid any consistent *bias* in the estimates than to further reduce the variance. As mentioned above, there is little signal power above 250 *Hz*.

2.5.2 Data analysis

Response data was transferred to UNIX workstations for data analysis, initially a SUN 3/60C, later an Apollo DN10000. Baseline drift in responses was removed by digital filtering. An alternative technique is the fitting of low degree polynomials to the data (Marmarelis and Marmarelis 1978). This data sometimes contains large jumps or oscillations in baseline, while otherwise appearing to contain a good signal, as judged by comparing segments of the eight repeats. Polynomial fitting thus would have to be piecewise. This procedure seemed too *ad hoc*, and the more systematic technique of filtering was used, to eliminate low-frequency noise. The signal will be distorted at low frequencies, however this is of little interest as kernels were mainly considered only to a memory length of $50\,ms$.

Initially, filtering was performed by subtracting a symmetric 1001 point running average from the response, corresponding to a frequency transfer of $1 - \sin(2\pi\nu)/2\pi\nu$. This introduces no phase distortion, and above 20 *Hz* causes less than 1% distortion in amplitude. This process was later replaced by a recursive digital filter equivalent to

a fifth order Butterworth high-pass filter with a cut-off frequency of .5 Hz. The data was filtered forwards and then backwards in time, to result in zero phase distortion (Little and Shure 1988).

Filtered responses were averaged over the eight repeats, decomposing the response into average and deviation components:

$$\text{filtered} = \text{averaged} + \text{deviance}$$

Crosscorrelation using the averaged response produced the Lee-Schetzen kernel estimates, and the previously described recursive algorithms corrected these estimates to give least-squares kernel estimates. Model responses were then calculated from these kernels.

Data 'quality control' was monitored by a number of indices, and by a summary plot for each run, such as that shown in figure 13. This shows the fluctuation in baseline voltage and RMS response throughout the run, the eight response repeats superimposed for a short segment of the stimulus period, fitted and residual responses for a short segment of the run, and estimated power spectra of response components. Note in this case the large fluctuations in baseline voltage in what otherwise appears to be good quality data, necessitating the use of filtering to remove the baseline fluctuations.

After the initial calculations of kernels and model responses, subsequent manipulation and plotting of results was done using the Matlab interactive package from The Mathworks, Massachusetts. Power spectra of signals were calculated using segmentation with 50% overlap and a Welch window, as described in Press *et al* (1988, p441). Nonlinear parametric models were fitted using the Marquardt-Levenberg algorithm (Press *et al* 1988, p542) or the Nelder-Meade algorithm (Press *et al* 1988, p305).

A note on the format of plots may be of use. Data is plotted without smoothing and with only trapezoidal interpolation, unless indicated. Data on a two dimensional domain is generally plotted with perspective and contour plots side by side. For the contour plots, the extreme, or 'peak', value is indicated and the contour step size is set at a given percentage of this peak value. In some cases the step size for the positive range is set at a different percentage, to illustrate a region of the function with smaller values.

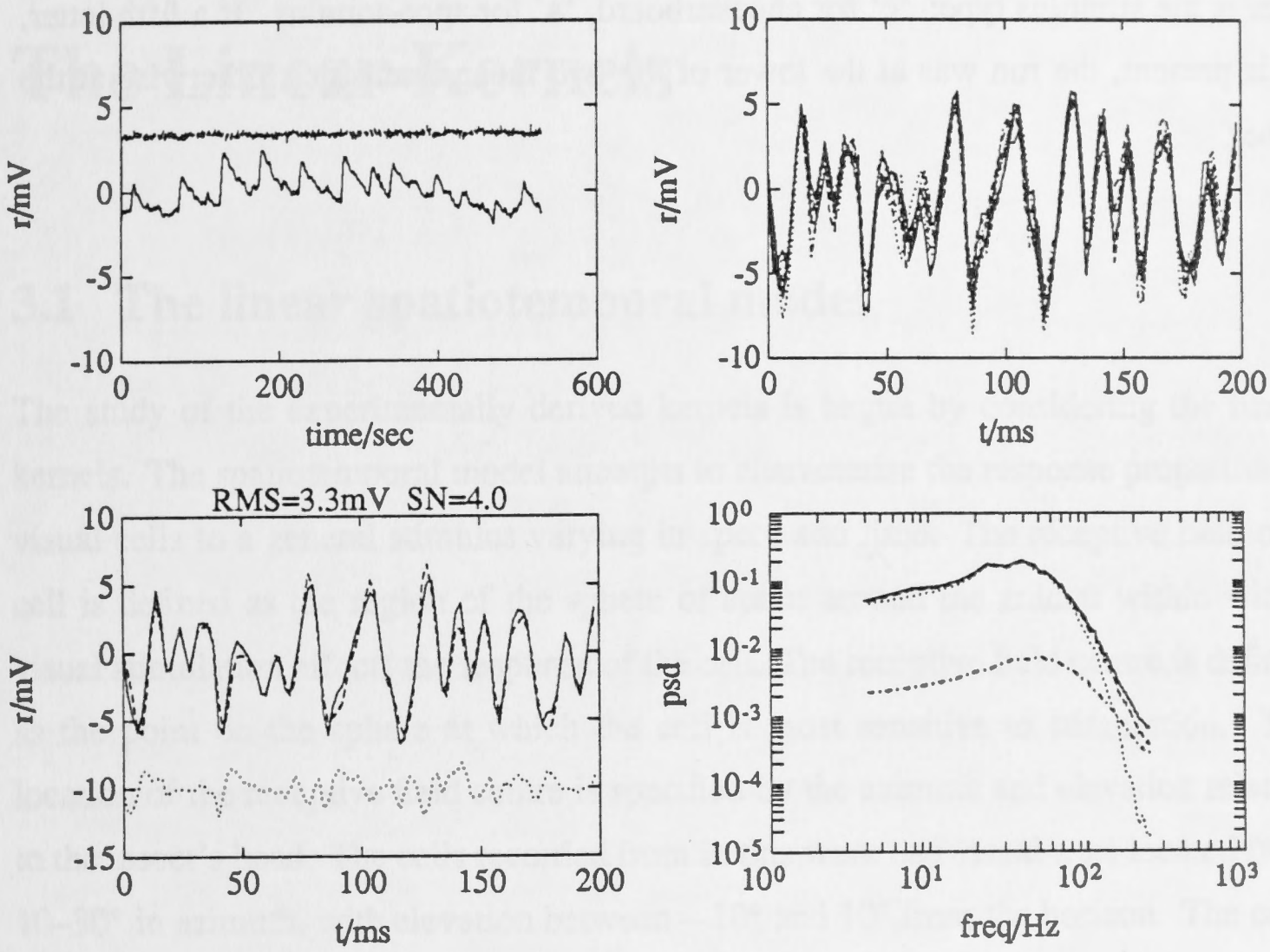

Figure 13: Summary plot indicating experimental run quality. The run is from an *Eristalis* LMC (lkkc), in response to the checkerboard stimulus. **Upper left**, for the entire run-length: fluctuation in the baseline voltage (solid line), and in the RMS response (dashed line). **Upper right**, for a 200 ms segment of the stimulus period, the eight response repeats are shown superimposed. **Lower left**, for a 200 ms segment of the stimulus period, the averaged response (solid line) and linear model response (dashed line) are shown, and the residual, offset by 5 mV (dotted line). The RMS averaged response and averaged-to-deviance RMS ratio, representing signal-to-noise (sn), are as indicated. **Lower right**, estimated power spectral densities, in mV^2/Hz: filtered response (solid line), averaged response (dashed line), linear model response (dotted line), and deviance (dot-dash).

2.5.3 Labelling of experimental runs

Plots will be labelled where appropriate with an identifier in parentheses indicating the experimental run, to allow detailed comparison between results. The run identifiers can be interpreted as follows. The first letter indicates the cell-type: 'r' for *Eristalis* receptor, 'l' for *Eristalis* LMC, 'c' for *Calliphora* LMC. The second letter indexes the cells recorded from. The third letter indexes the runs made from that cell. The fourth letter is the stimulus type: 'c' for checkerboard, 'a' for spot-annulus. If a fifth letter, 'l', is present, the run was at the lower of the two mean intensities, otherwise at the higher.

Chapter 3

The Linear Kernels

3.1 The linear spatiotemporal model

The study of the experimentally derived kernels is begun by considering the linear kernels. The spatiotemporal model attempts to characterise the response properties of visual cells to a general stimulus varying in space and time. The receptive field of a cell is defined as the region of the sphere of space around the animal within which visual stimulation affects the response of the cell. The receptive field centre is defined as the point on the sphere at which the cell is most sensitive to stimulation. The location of the receptive field centre is specified by the azimuth and elevation relative to the insect's head. The cells recorded from in this work had visual axes located from 10–30° in azimuth, with elevation between $-10°$ and 10° from the horizon. The cells studied had narrow receptive fields, and the largest stimulus region considered had diameter 15°. Coordinates within the receptive field are thus approximately equivalent to rectangular coordinates, which will be specified as (x, y) coordinates in degrees relative to the receptive field centre. The visual image viewed by the cell is represented as a function $s(x, y, t)$ giving the contrast at time t at the spatial location (x, y) within the receptive field of the cell.

The linear spatiotemporal model of a visual cell's response properties combines the stimulus with a kernel h_1 by integration over space and convolution over time:

$$F_1 s(t) = \int_{\mathcal{D}_y} \int_{\mathcal{D}_x} \int_0^m h_1(x, y, t_1)\, s(x, y, t - t_1)\, dt_1\, dx\, dy$$

The spatial coordinates (x, y) vary over a spatial domain $\mathcal{D}_x \times \mathcal{D}_y$, and the latency t_1 extends to memory length m.

The model contains information corresponding to the more traditional impulse responses and receptive field profiles, while giving a more comprehensive characterisation of properties.

From the checkerboard stimulus a model is derived on discrete time and space. The receptive field is covered by a 15 × 15 array of checks of size $\Delta x \times \Delta y$, which are indexed by integers x, y running from 0 to 14. The check size used varied from .6° to 1.2°. Each check fluctuates in contrast with an inter-frame interval of $\Delta t = 2\ ms$. The kernel was estimated up to a memory of 50 ms, at latencies from 3 to 25 frames. The discrete spatiotemporal model is thus:

$$F_1 s(t) = \sum_{x=0}^{14} \sum_{y=0}^{14} \sum_{t_1=3}^{25} h_1(x, y, t_1) s(x, y, t - t_1)$$

Estimates of kernels on continuous space-time are obtained by dividing the discrete space-time kernels by $\Delta x \Delta y \Delta t$. Allowance can also be made for the spatially extended nature of the checks, to be described below.

3.1.1 Kernel sections and marginal kernels

The full spatiotemporal kernel is difficult to portray in its entirety, being a function defined on a three dimensional domain. To examine aspects of the system properties in detail, kernels of two principal kinds can be derived on lower dimensional domains: kernel sections and marginal kernels.

A kernel section is extracted by taking fixed values in one or more dimensions and considering the kernel as a function on the remaining dimensions. For example, taking each spatial point (x, y) separately the kernel can be plotted as an array of temporal kernels each corresponding to the response component due to a single check. This gives the temporal dynamics of response at 225 receptive field positions, extracted in parallel, which saves recording time and avoids experimental bias due to drift in the amplitude of system response. Figure 14 shows these kernels for the 8 × 8 central locations for an *Eristalis* LMC.

These temporal kernels can be compared with impulse response data, although it must be remembered that they are extracted from Wiener kernels, which provide the best linear fit to the response properties, and hence are influenced by the nonlinearity of the system. The units of the kernel, are millivolts per contrast-millisecond-degree-squared, $mV/(C\ ms\ deg^2)$. As a rule of thumb each temporal kernel can be thought

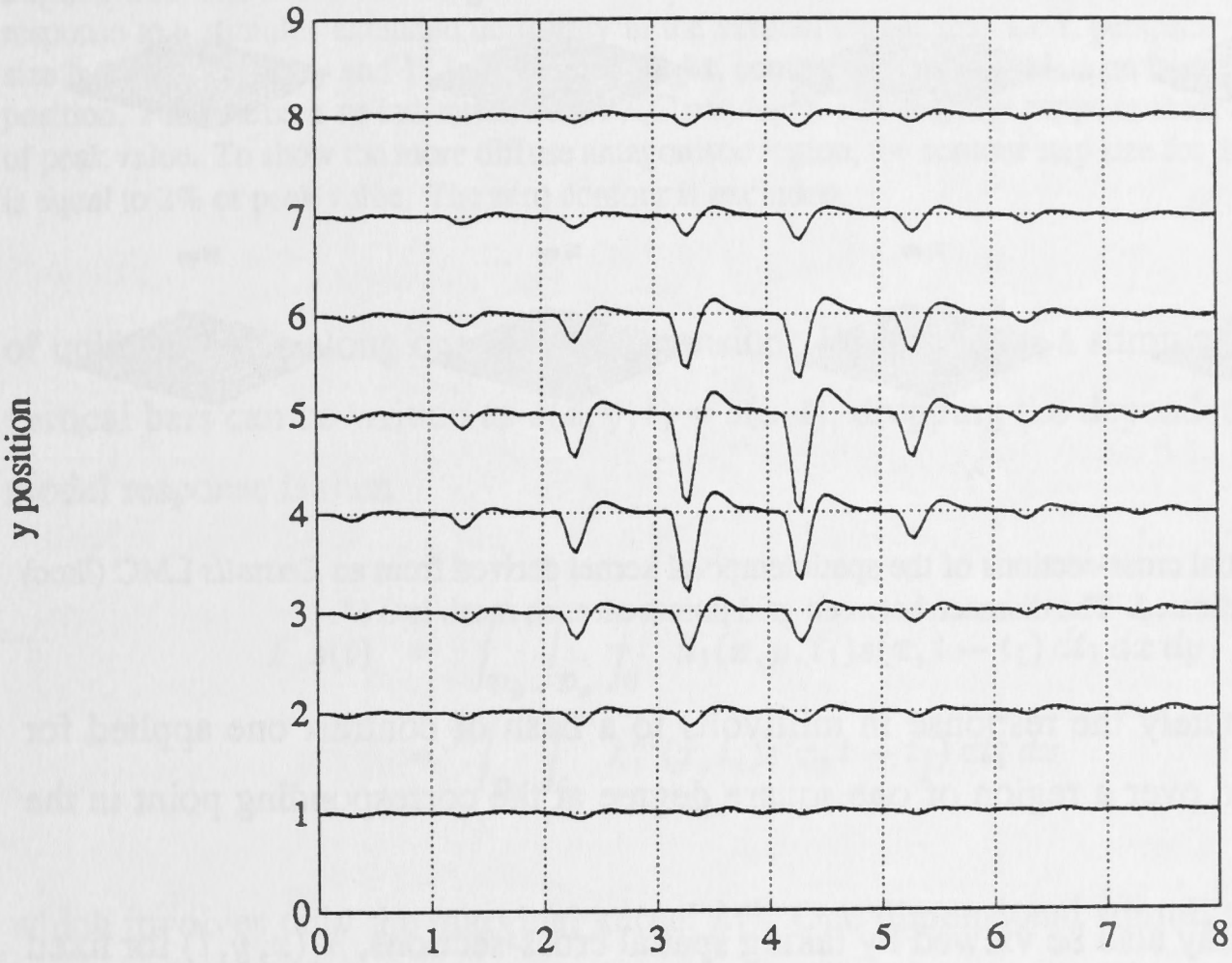

Figure 14: A linear spatiotemporal kernel derived from an *Eristalis* LMC (lkoc) plotted as an array of temporal kernels corresponding to the central 8 by 8 checks of the stimulus array. The check size is 0.6°. At each spatial location the kernel $h_1(x, y, t)$ is plotted for latencies t from 0 to 40 ms.

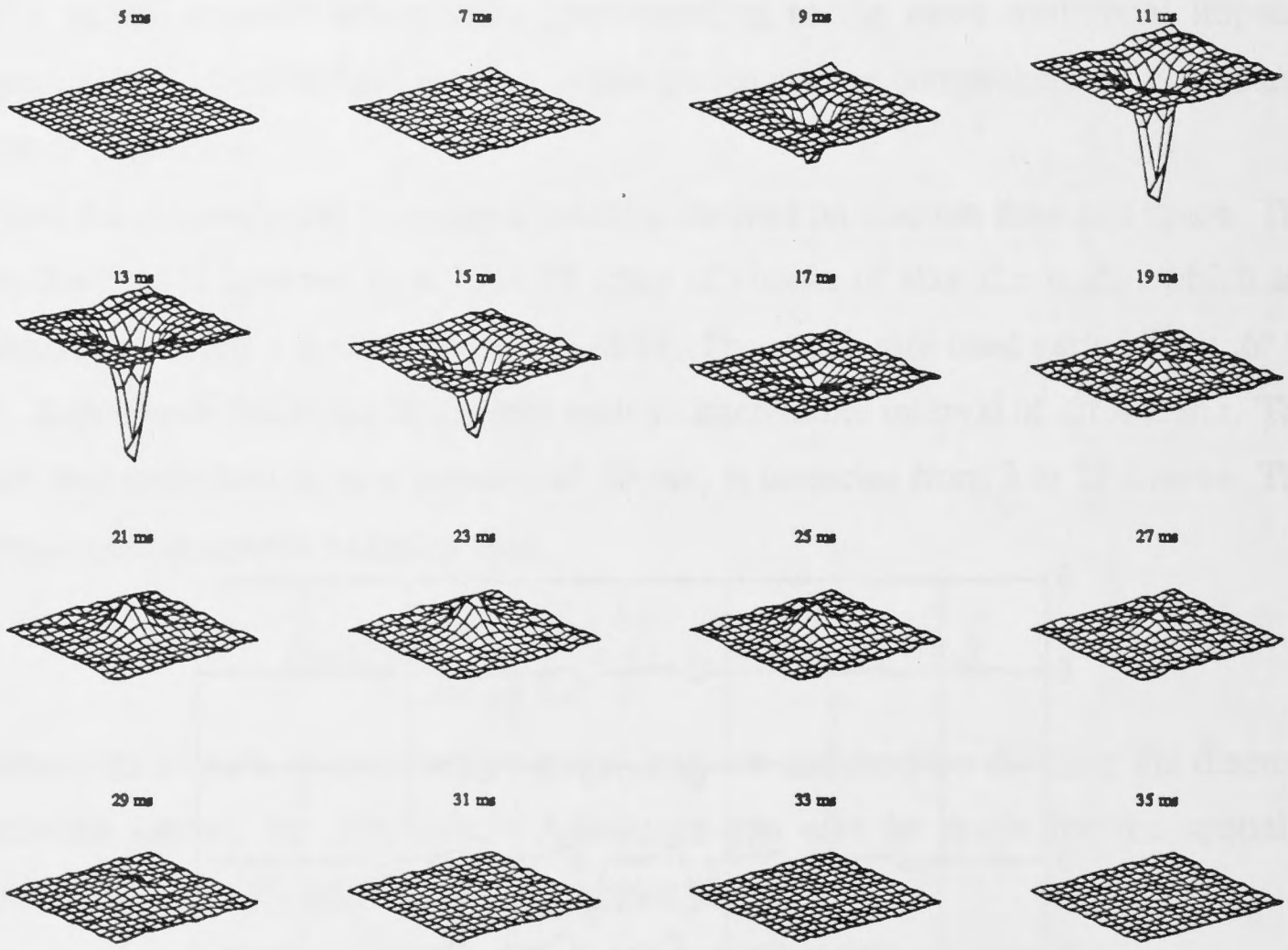

Figure 15: Spatial cross-sections of the spatiotemporal kernel derived from an *Eristalis* LMC (lkoc) at the latencies indicated. The distance between grid points on each mesh is 0.6°.

of as approximately the response in millivolts to a flash of contrast one applied for one millisecond over a region of one square degree at the corresponding point in the receptive field.

The kernel may also be viewed by taking spatial cross-sections, $h_1(x, y, t)$ for fixed values of latency t. This represents the spatial sensitivity of the system at each successive latency. It is plotted in this way in figure 15.

We will also define *marginal kernels* by analogy with the concept of marginal distribution in probability. The horizontal marginal kernel is the function of x and t obtained by integrating h_1 along the vertical dimension of its domain.

$$h_1^{xt}(x, t) = \int_{\mathcal{D}_y} h_1(x, y, t)\, dy$$

When rigour is desired the kernel can be distinguished by the superscripts xt, otherwise context will be used, so that $h_1(x, t)$ is assumed to denote the horizontal marginal kernel. The vertical marginal kernel is similarly defined. Marginal kernels are important as they are sufficient to give the predicted response to a stimulus which is

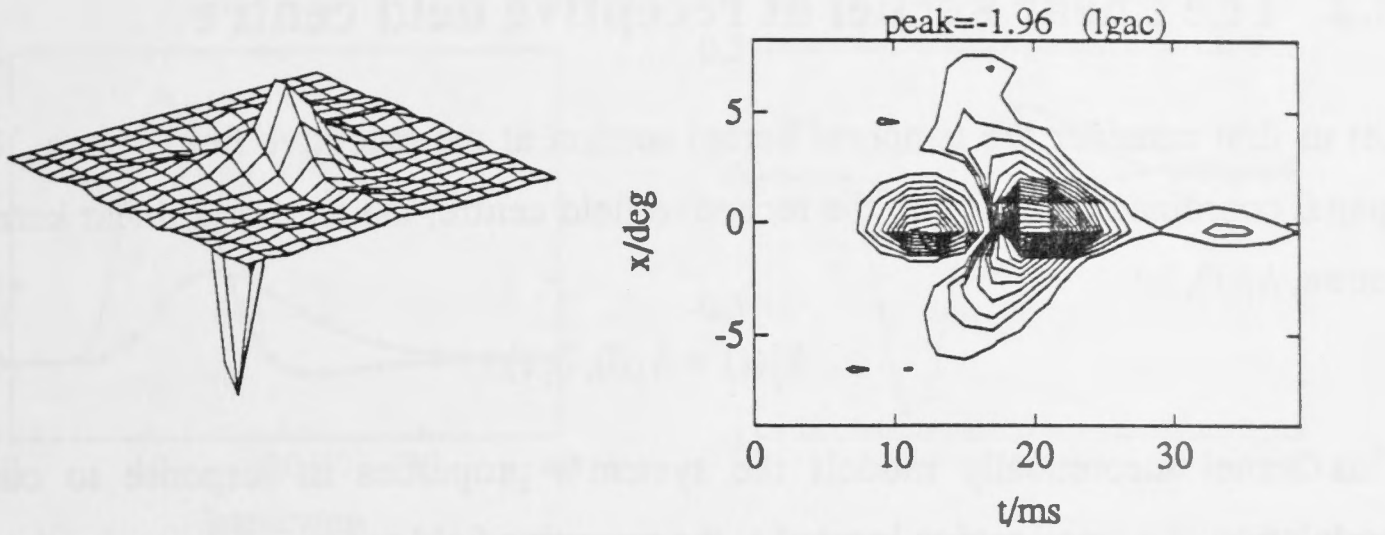

Figure 16: The horizontal marginal kernel h_1^{xt} from an *Eristalis* LMC (lgac). The kernel models the response to a stimulus extended uniformly in the vertical dimension. **Left,** perspective plot, grid step size is $2\,ms$ for latency and $1°$ for location. **Right,** contour plot of same data on latency and horizontal position. Peak value is as indicated, in $mV/(C\,ms\,deg^2)$. For negative range contour step size is 10% of peak value. To show the more diffuse antagonistic region, the contour step size for the positive range is equal to 2% of peak value. The zero contour is excluded.

of uniform value along one spatial dimension. For example, a stimulus consisting of vertical bars can be written as $s(x, y, t) = s(x, t)$, dropping the dependence on y. The model response is then

$$\begin{aligned} F_1 s(t) &= \int_{\mathcal{D}_y} \int_{\mathcal{D}_x} \int_0^m h_1(x, y, t_1) s(x, t - t_1)\, dt_1\, dx\, dy \\ &= \int_{\mathcal{D}_x} \int_0^m h_1^{xt}(x, t_1) s(x, t - t_1)\, dt_1\, dx \end{aligned}$$

which involves only the marginal kernel h_1^{xt}. One dimensional stimuli are commonly used in experimentation, as well as being the form of image seen when an extended edge passes through the receptive field of a cell.

Figure 16 shows the horizontal marginal kernel from an *Eristalis* LMC, both in perspective and contour plots. These plots give a clear view of the linear transfer properties of the system on the space-time domain. The kernel has two regions, the primary region, of larger amplitude, which generates a response of opposite sign to the contrast of a visual stimulus, and an antagonistic region, generating a response opposing the primary response. Together the components achieves high-pass filtering in time and space.

We will now examine some aspects of the linear kernels in detail, by consideration of these lower-dimensional derived kernels.

3.2 The linear kernel at receptive field centre

Let us first consider the temporal kernel section at the receptive field centre. Using spatial coordinates relative to the receptive field centre, the temporal linear kernel on centre, $h_1^c(t)$, is:

$$h_1^c(t) = h_1(0, 0, t)$$

This kernel theoretically models the system's properties in response to contrast modulation of a small region located at the receptive field centre. If the region has area A, small relative to the extent of the receptive field, the model response is the simple linear time-invariant operator:

$$Fs(t) = A \int_0^m h_1^c(t_1) s(t - t_1)\, dt_1$$

This kernel is estimated by taking the temporal kernel corresponding to the most effective check in the checkerboard stimulus, and scaling the amplitude to allow for the spatial extent of the check, according to a procedure to be described below.

The linear kernel derived from the centre-stimulation in the spot-annulus experiment also provides a measure of response properties to on-axis stimulation. The spot had diameter 2°, greater than the size of the checks. The kernel was divided by a coefficient estimating the spatial effectiveness of the spot relative to stimulation precisely on centre. This gives units of $mV/(C\, ms\, deg^2)$, corresponding to the spatiotemporal kernel. Nevertheless the waveform is slightly different due to the greater area stimulated; the kernels derived from the spot stimulus will be plotted with dashed lines in this section.

3.2.1 Qualitative features of the kernels

Figure 17 shows typical kernels derived from a receptor and an LMC of the fly *Eristalis*, at the two levels of illumination used in the study. Kernel estimates are obtained at $2\, ms$ steps in latency, corresponding to the frame rate of stimulation. The estimated kernel values are fitted by a smooth function described below.

The receptor kernel is primarily positive, indicating a depolarisation in response to light increment, attributed to an increase in membrane sodium conductance. At the higher level of illumination the response is faster, and is slightly biphasic.

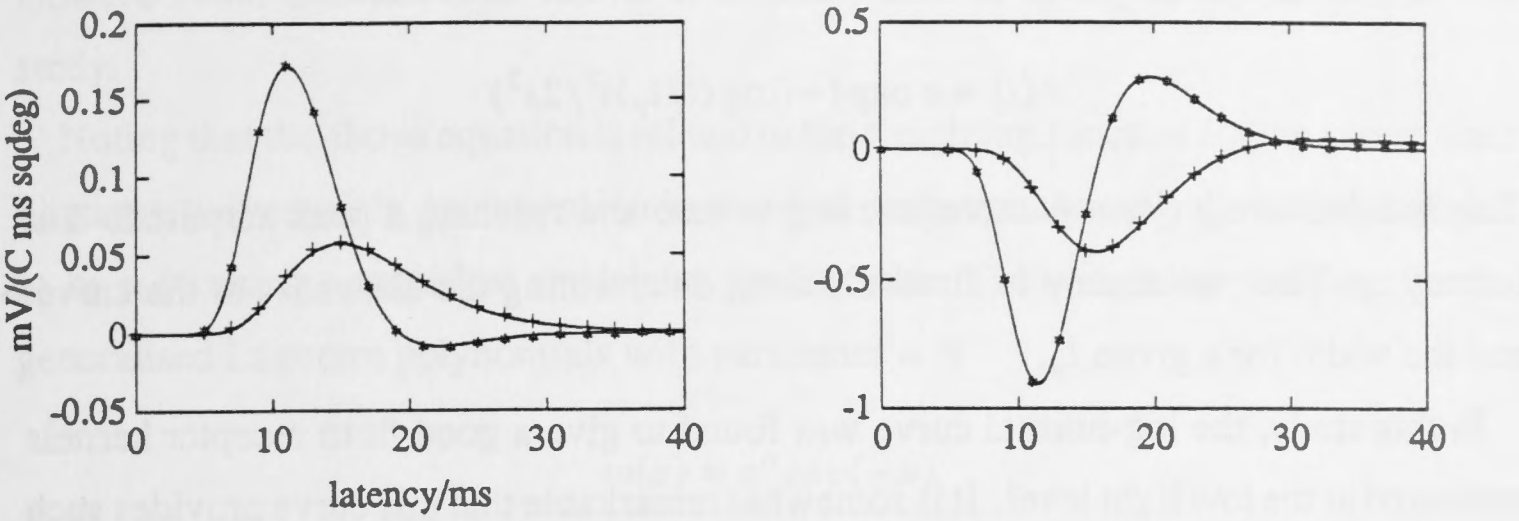

Figure 17: Temporal linear kernels for on-axis stimulation $h_1^c(t)$, derived from *Eristalis*. **Left**, from a photoreceptor (rlac,rlbcl). **Right**, from a large monopolar cell (lkcc,lkpcl). **Asterisks**, higher mean intensity. **Plus signs**, lower mean intensity, 2.3 log units less. **Solid lines**, parametric fits, see text.

Comparison of the receptor and LMC kernels illustrates three of the principal characteristics of transmission at the first synapse of the fly visual system: the signal is inverted, it is amplified, and it is high-pass filtered.

The amplification is frequency dependent, with higher frequencies being amplified at the expense of low frequencies, so that the resulting signal does not saturate the LMC response range. This high-pass filtering is reflected in the biphasic waveform of the LMC kernel, with the initial primary component being followed by an antagonistic phase.

Comparison of kernels from the two light levels used indicates considerable light adaptation of the linear kernel. The gain of the receptor in terms of stimulus contrast has increased, and the response has quickened. Transmission from receptor to LMC seems to be without additional increase in gain, but with a sharpening of the antagonistic component of the kernel.

3.2.2 Parametric fits to the kernels

A parametric curve giving good approximation to the kernels was sought for the following reasons: to summarise the data, to allow numerical comparison between kernels, to allow the estimation of parameters such as time-to-peak and to give a parametric form for use in simulations.

Payne and Howard (1981) found that the log-normal curve provided a good fit to monophasic receptor impulse response data. This is a curve with the same shape as the probability density function of a log-normal variate, that is, a variate whose logarithm

is normally distributed. The form is

$$h(t) = a \exp\left(-(\log(t/t_p))^2/2s^2\right)$$

This is a positively skewed curve, starting at zero and reaching a peak amplitude a at latency t_p. The parameter s is dimensionless, determining the skewness of the curve, and the width for a given t_p.

In this study, the log-normal curve was found to give a good fit to receptor kernels measured at the low light level. It is somewhat remarkable that this curve provides such a good fit as the number of parameters is the minimum one could expect; providing scaling on the ordinate and abscissa, and the relative width on the abscissa.

For biphasic kernels, particularly the LMC kernels, the monophasic log-normal curve will clearly not fit. The family of curves can be generalised by adding another term of identical form but opposite polarity to fit the second phase of response. Indexing the two components by 1 and 2, this double log-normal curve has the form:

$$h(t) = a_1 \exp\left(-(\log(t/t_{p1}))^2/2s_1^2\right) + a_2 \exp\left(-(\log(t/t_{p2}))^2/2s_2^2\right)$$

This was found to provide a good fit to all the biphasic kernels, up to a latency of 50 ms. This curve was fitted to temporal kernels using the Marquardt-Levenberg algorithm (Press *et al* 1988). The curve is deemed to fit when the deviance is small and when the residuals have no apparent pattern over time, appearing to have a stationary white-noise distribution. The relative error of fit was measured by the estimated standard deviation, expressed as a percentage of the maximum data magnitude. The curve was fitted to the 109 kernels in the study, with a mean relative error of around 1%.

Several other families of curves were also considered. One of the most obvious families to try has the form:

$$h(t) = K(t/\tau)^{n-1} \exp\left(-t/\tau\right)$$

This is the form of the overall kernel for a cascade of n linear first order systems with equal time constants, τ. It was used by Fuortes and Hodgkin (1964) to fit impulse responses from the photoreceptors of *Limulus*. It has previously been found that this model does not give convincing fits to insect receptor responses, having too symmetric a form and requiring large and variable estimates of the number of stages n (Payne and

Howard 1981; Howard *et al* 1984). It similarly fails to fit any of the kernels in this study.

Noting that the above equation is related to the weighting function for the generalised Laguerre polynomials, an expansion in terms of these orthogonal polynomials seemed to be a promising empirical model for the kernels. The weighting function for the generalised Laguerre polynomials with parameter α is

$$w(x) = x^{\alpha} exp(-x)$$

and the polynomial of degree n is denoted by $L_n^{(\alpha)}(x)$ (Abramowitz and Stegun 1984). This means that the functions

$$w(x)^{1/2} L_n^{(\alpha)}(x)$$

are orthogonal with respect to Lebesgue measure on the real line.

The function $w(x)^{1/2}$ can be equated with the Fuortes-Hodgkin model by setting

$$\begin{aligned} \alpha/2 &= n-1 \\ x/2 &= t/\tau \end{aligned}$$

with appropriate amplitude K.

In this way a kernel having the form of the Fuortes-Hodgkin model will be fitted exactly by the zero-order term of the series, while higher order terms will allow a wide class of kernels to be fitted. The approach is also reminiscent of Wiener's original proposal, which was to represent kernels as Laguerre series, corresponding to $\alpha = 0$ in the generalised Laguerre case.

The model was fitted allowing the time constant τ and the exponent α to vary, as well as the first four coefficients of the series. Surprisingly, even with six parameters, the model did not provide as close a fit as the double log-normal family, and was abandoned.

3.2.3 The population of kernels

Quantitatively, there is considerable data available on the dynamics of insect photoreceptor responses, particularly at lower light levels (Howard *et al* 1984; French 1979, 1980a; Kuster and French 1985). There is less quantitative data concerning the dynamics of LMC response. Statistics from 109 runs on 32 cells are presented here,

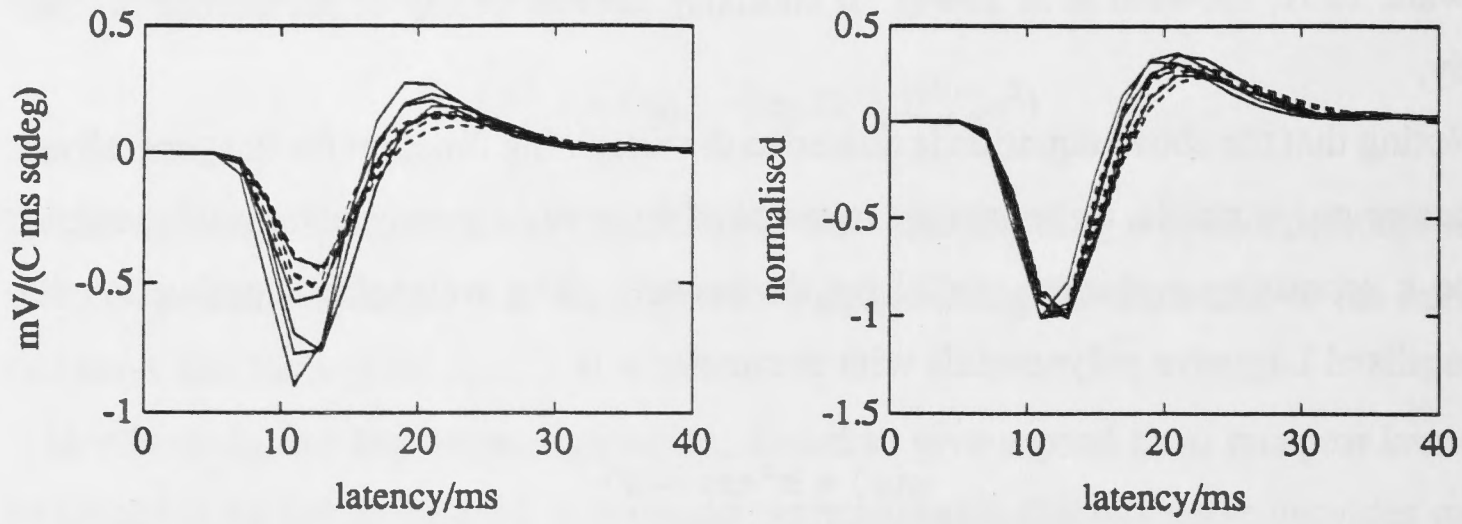

Figure 18: The 16 temporal linear kernels for on-axis stimulation derived from an *Eristalis* LMC (lk), with trapezoidal interpolation. **Left**, actual size, in units $mV/(C\,ms\,deg^2)$. **Right**, normalised in amplitude. **Solid line**, from checkerboard stimulus. **Dashed line**, from spot stimulus.

derived from the photoreceptors and LMCs of *Eristalis*, and the LMCs of *Calliphora*, at two mean intensities of illumination.

Although corrected for differing spatial properties of the stimulus, there was further variation in the amplitude of response. The repeatability of the kernel measurement is illustrated in figure 18, showing the 16 kernels derived from one cell, in both actual and normalised plots. The kernels from the spot and the checkerboard stimuli are distinguished by line-type.

The entire database of on-axis linear kernels is shown in figure 19, normalised in amplitude. Kernels for the three cell types are shown, at the two levels of mean intensity. Kernels from checkerboard and from spot stimulation are distinguished by line type.

From the double log-normal fit to each kernel the following quantities are extracted: the extreme value, termed the *peak value*, the *peak-time*, being the latency at which the peak value is achieved, and the *half-width*, the width of the curve at half of the peak value. Population statistics of these parameters are given in table 2. Peak values are highly variable, while the timing of kernels shows less variance, with standard deviations around 10% of means. For *Eristalis* the LMC kernel reaches a peak around $1\,ms$ after the receptor. The *Calliphora* LMC has a peak-time similar to the *Eristalis*, but a shorter half-width, reflecting the higher bandwidth of the *Calliphora* system. Adaptation of the system to the lower level of mean illumination increases both peak-time and half-width by around $5\,ms$ for *Eristalis*, and by around $2\,ms$ for *Calliphora*.

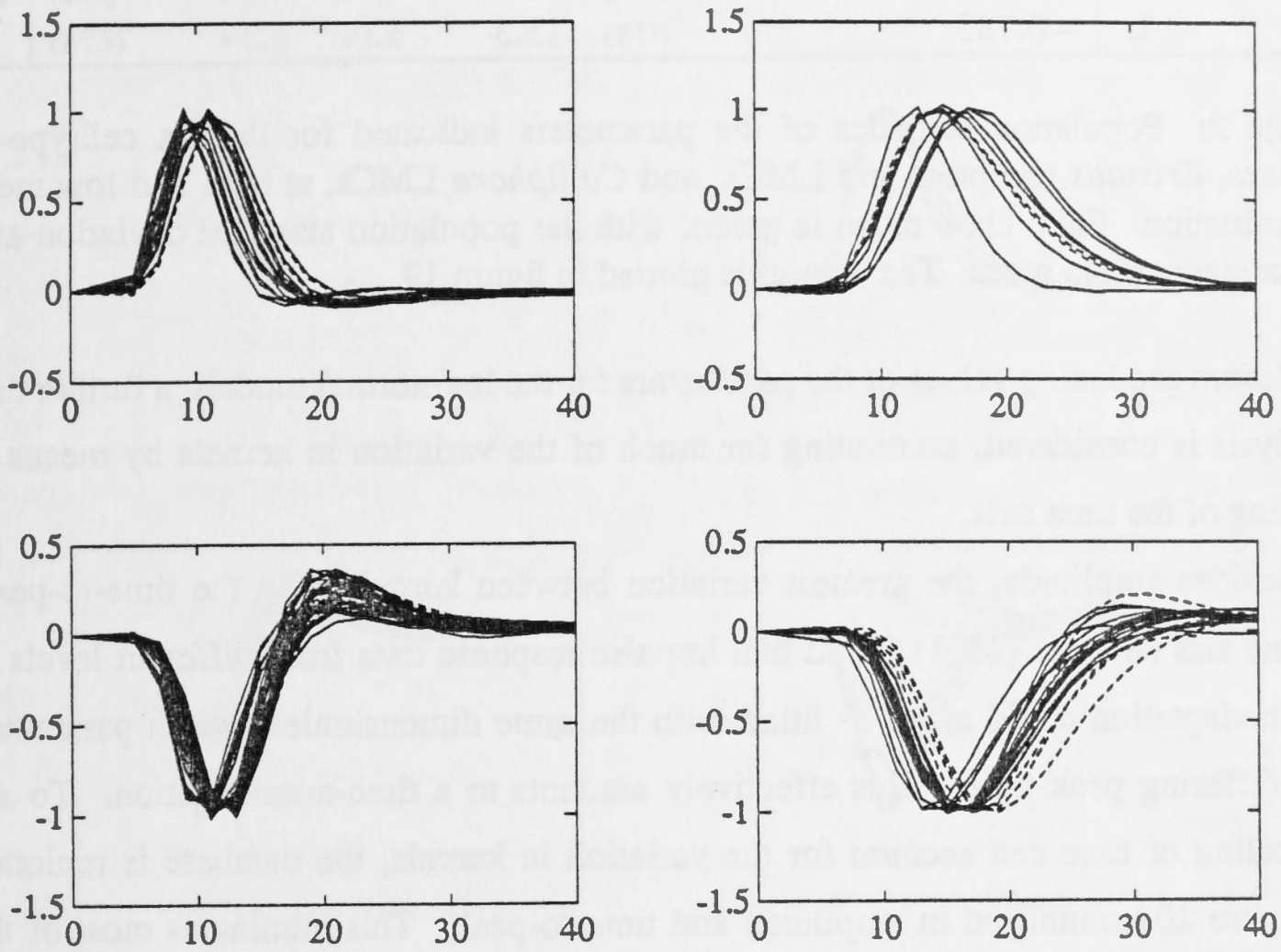

Figure 19: The database of linear kernels for on-axis stimulation, normalised in amplitude. **Upper**, *Eristalis* receptors. **Middle**, *Eristalis* LMCs. **Lower**, *Calliphora* LMCs. **Left**, high mean intensity. **Right**, low mean intensity. **Solid line**, from checkerboard stimulation. **Dashed line**, from stimulation with 2° spot.

celltype	I_0	peak value, $mV/(C\,ms\,deg^2)$		peak-time, ms		half-width, ms		n
E recep	H	0.215	(79%)	10.2	(8.6%)	5.87	(11%)	19
	L	0.0513	(58%)	15.1	(11%)	10.5	(15%)	8
E LMC	H	−0.769	(67%)	11.6	(6.1%)	5.6	(8.2%)	39
	L	−0.246	(64%)	16.1	(8.3%)	9.75	(11%)	18
C LMC	H	−1.63	(83%)	11.2	(13%)	4.86	(14%)	17
	L	−0.783	(75%)	13.3	(6.1%)	6.34	(4.7%)	8

Table 2: Population statistics of the parameters indicated for the six celltype–I_0 classes, *Eristalis* receptors and LMCs, and *Calliphora* LMCs, at high and low mean illumination. Each class mean is given, with the population standard deviation as a percentage of the mean. The dataset is plotted in figure 19.

Before producing values of the parameters for the log-normal models, a further data analysis is considered, accounting for much of the variation in kernels by means of scaling of the time axis.

Besides amplitude, the greatest variation between kernels is in the time-to-peak. Payne and Howard (1981) found that impulse response data from different levels of light adaptation could often be fitted with the same dimensionless width parameter, but differing peak-time. This effectively amounts to a time-normalisation. To see if scaling of time can account for the variation in kernels, the database is replotted in figure 20 normalised in amplitude and time-to-peak. This eliminates most of the variation for the *Eristalis* receptors and the *Calliphora* LMCs, while the *Eristalis* LMCs still show varying strengths of temporal antagonism.

For the double log-normal model, the amplitude parameters a_1, a_2 can be divided by the peak value to give relative amplitudes $\hat{a}_1, \hat{a}_2$. The time parameters t_{p1}, t_{p2} are similarly divided by the peak-time to give relative time parameters $\hat{t}_{p1}, \hat{t}_{p2}$. Population statistics of the resulting parameters, and the dimensionless width parameters s_1, s_2 are given in table 3. For *Eristalis* receptors at the low intensity the single log-normal curve is fitted.

The resulting statistics, along with those of peak value and peak-times of table 2 provide idealised kernels for use in subsequent simulations.

3.3 Spatial properties of the kernels

The shape of the kernels on two dimensional space will be considered in two aspects. Firstly, the spatial sensitivity of the primary, negative part of the kernel. Second,

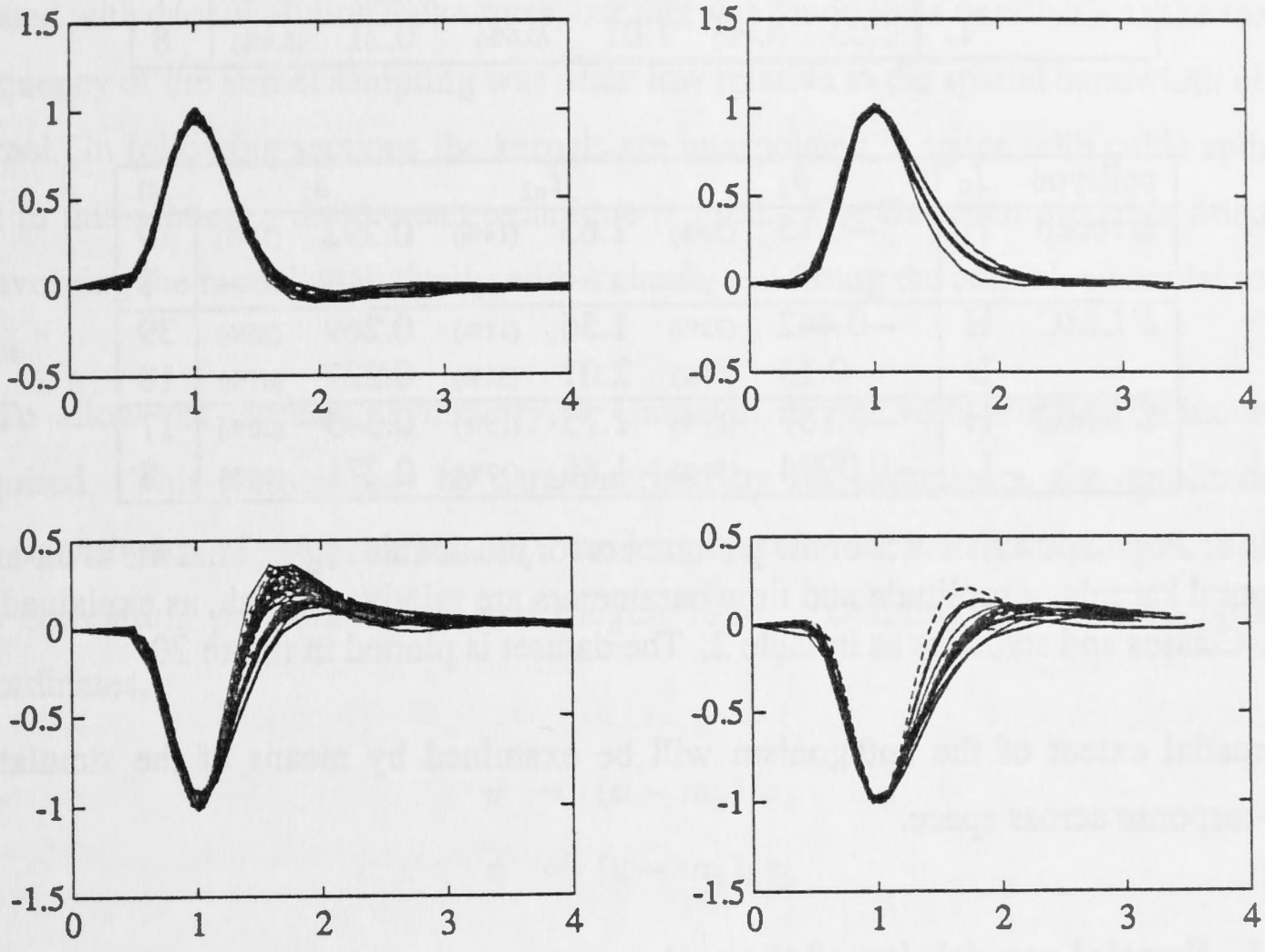

Figure 20: The database of linear kernels for on-axis stimulation, normalised in amplitude and normalised in time to give unit time-to-peak. **Upper**, *Eristalis* receptors. **Middle**, *Eristalis* LMCs. **Lower**, *Calliphora* LMCs. **Left**, high mean intensity. **Right**, low mean intensity. **Solid line**, from checkerboard stimulation. **Dashed line**, from stimulation with 2° spot.

celltype	I_0	$\hat{a}_1$		$\hat{t}_{p1}$		s_1		n
E recep	H	1.05	(5.1%)	1.01	(0.87%)	0.262	(4.7%)	19
	L	1	—	1	—	0.29	(8.1%)	8
E LMC	H	1.17	(20%)	1.03	(3.6%)	0.236	(6.9%)	39
	L	1.02	(2.9%)	1	(1.2%)	0.263	(6.6%)	18
C LMC	H	1.06	(5.5%)	1.01	(0.45%)	0.197	(9.4%)	17
	L	1.03	(4.4%)	1.01	(0.6%)	0.21	(8.8%)	8

celltype	I_0	$\hat{a}_2$		$\hat{t}_{p2}$		s_2		n
E recep	H	−0.15	(39%)	1.63	(14%)	0.292	(31%)	19
	L	—	—	—	—	—	—	8
E LMC	H	−0.442	(73%)	1.56	(11%)	0.269	(26%)	39
	L	−0.13	(64%)	2.01	(32%)	0.227	(67%)	18
C LMC	H	−0.167	(27%)	1.75	(13%)	0.345	(20%)	17
	L	−0.0994	(50%)	1.86	(17%)	0.271	(28%)	8

Table 3: Population statistics of the parameters for the double log-normal fits to on-axis temporal kernels. Amplitude and time parameters are relative to peak, as explained in text. Classes and statistics as in table 2. The dataset is plotted in figure 20.

the spatial extent of the antagonism will be examined by means of the simulated step-response across space.

3.3.1 Spatial sensitivity of the primary response

The spatial sensitivity of the primary response process can be seen by considering the spatial cross-section of a kernel at the peak-time. This surface was fitted with a two-dimensional Gaussian bell. The Gaussian shape is intended to provide a parametric fit to the spatial sensitivity over the central region of large amplitude, to give estimates of half-widths and ellipticity. Spatial sensitivity surfaces often departed from Gaussian shape away from the receptive field centre, the receptor kernels having additional sensitivity, while the LMC kernels sometimes show lateral antagonism. Nevertheless the central region of large amplitude has far greater leverage in the least-squares fitting procedure, and the fit essentially models the primary response alone.

If the stimulus used in these experiments had consisted of a spatial array of point sources, then the derived spatial sensitivity values would correctly estimate the spatial sensitivity of the cell at the corresponding points. As it is, the finite size of the checks means that what is estimated is actually the integral of the spatial sensitivity over the area of each check. The resulting array of spatial sensitivity values is thus

spatially smoothed relative to the true sensitivity, giving an impression of lessened spatial acuity.

This smoothing is precisely equal to convolution of the true function with a function constant over one check centred at the origin and zero elsewhere. The array may be treated with deconvolution techniques, but this was found to be unreliable as the spatial frequency of the kernel sampling was often low relative to the spatial bandwidth of the kernel. In following sections the kernels are interpolated in space with cubic splines, but in this section a more exact technique is used. The Gaussian model is fitted by convolving the model analytically with a check, and fitting the convolved model to the data.

To allow for circular asymmetry, a Gaussian model with elliptical contours is required. This surface may be paramaterised by six parameters, the amplitude a, the coordinates of the peak m_x, m_y, the length scales in two dimensions s_x, s_y and the correlation ρ (Abramowitz and Stegun 1984). Defining standardised position coordinates,

$$\begin{aligned} u &= (x - m_x)/s_x \\ v &= (y - m_y)/s_y \end{aligned}$$

the surface has the form:

$$h(x,y) = a \exp\left(-1/2 \frac{u^2 - 2\rho uv + v^2}{1-\rho^2}\right)$$

The convolution of this with a check does not have a readily apparent analytic form. However, assuming ρ to be close to zero, a power series in this parameter can be used.

Let $H(x,y)$ denote the following integral of the kernel:

$$H(x,y) = \int_{-\infty}^{y}\int_{-\infty}^{x} h(x_1,y_1)\,dx_1\,dy_1$$

After some substitution of variables, the following expression can be derived from an expression given in Abramowitz and Stegun (1984)

$$H(x,y) = a\,(2\pi s_x s_y \sqrt{1-\rho^2}) \sum_{i=0}^{\infty} P^{(i)}(u)P^{(i)}(v)\rho^i/i!$$

where $P^{(i)}$ is the ith derivative of the standard normal distribution function and u, v are the standardised coordinates previously defined.

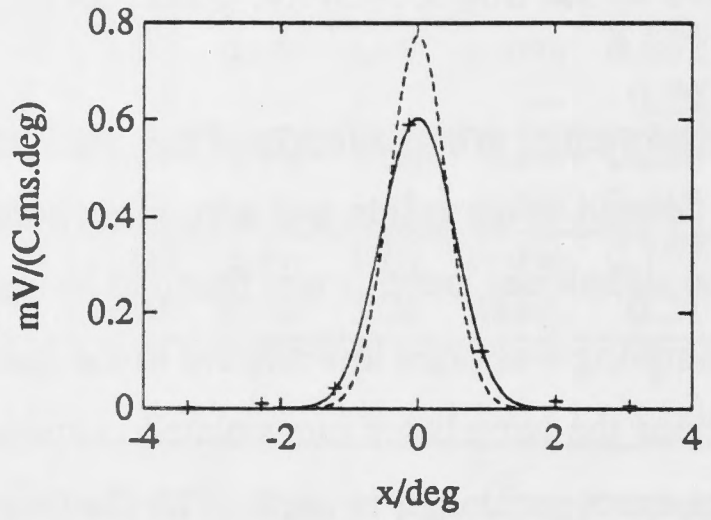

Figure 21: Illustration of the Gaussian fit to spatial sensitivity, allowing for check size. A one dimensional kernel is considered, the cross-section through the horizontal marginal kernel $h_1(x,t)$ of an *Eristalis* receptor (rqac) at the peak-latency. **Plus signs**, the estimated kernel values. **Solid line**, least-squares fit of a Gaussian convolved with the profile of a check. **Dashed line**, the underlying Gaussian curve, which is inferred to be the actual kernel profile. The figure shows an extreme case, where a cell with a narrow receptive field was stimulated with a coarse checkerboard, $\Delta x = 1.2°$. Assuming an underlying Gaussian sensitivity profile, the parameters can still be inferred by using this technique.

Using the discrete spatial coordinate system in which the check is of unit size the convolution of the Gaussian model with the stimulus check at the point (x, y) is given by:

$$H(x+1/2, y+1/2) - H(x+1/2, y-1/2) - H(x-1/2, y+1/2) + H(x-1/2, y-1/2)$$

This convolved model is fitted to the array of data points using the Marquardt-Levenberg algorithm, including terms of the above series up to the third power of ρ, giving the least-squares estimates of the parameters of the assumed Gaussian model for the underlying spatial sensitivity. Figure 21 illustrates the concept for a one dimensional case. The continuous-space coordinate system is then defined for the experiment by shifting the origin to the receptive field centre (m_x, m_y) and scaling by Δx to give degrees.

For the Gaussian model the contour of half-maximum sensitivity is an ellipse. The principal axes of this ellipse are calculated, giving the half-width along the major axis, $\Delta\rho_1$, along the minor axis, $\Delta\rho_2$. As an index of ellipticity, the percentage by which $\Delta\rho_1$ exceeds $\Delta\rho_2$ is calculated, and termed the excess.

This model is fitted to the spatial cross sections of all kernels at the peak-time. Table 4 gives the relevant estimated parameters. The estimates of half-width must be taken as upper bounds, as instability of the preparation causing shifting of the receptive field will lead to broadening of apparent spatial sensitivity. For the cells included in

celltype	I_0	$\Delta\rho_1^\circ$		$\Delta\rho_2^\circ$		%excess		n
E recep	H	1.42	(14%)	1.16	(18%)	23.1	(58%)	9
	L	1.48	(1.6%)	1.28	(0.13%)	15.3	(11%)	2
E LMC	H	1.81	(14%)	1.46	(18%)	25.1	(44%)	29
	L	1.84	(12%)	1.49	(14%)	24.2	(42%)	15
C LMC	H	1.61	(14%)	1.23	(9.1%)	31	(35%)	8
	L	1.62	(0.026%)	1.32	(1.1%)	22.3	(6.3%)	2

Table 4: Spatial parameters of Gaussian fit to central lobe of spatial sensitivity at peak-latency. The values given are means and population standard deviations as percentages of the means. $\Delta\rho_1$ is the length of the major axis of the elliptical contour at 50% sensitivity. $\Delta\rho_2$ is length of the minor axis. The %excess is $(\Delta\rho_1 - \Delta\rho_2)/\Delta\rho_2 * 100$, which I find gives a more intuitive measure of lengthening than the ellipticity coefficient used in the geometry of conic sections.

these statistics good stability could be inferred by comparison of the response signals over the eight repetitions of the stimulus. The values of half-width for receptors are slightly less than estimates given by Hardie (1985) of $\Delta\rho$ = 1.5°–3°, with the lower figure applying to receptors in the frontal region of the eye.

The mean values of the excess of major axis over minor axis length suggest departure from circular symmetry. To see if the orientation of ellipticity is consistent, the dataset of 50% ellipses and major axes are plotted in figure 22, indicating a tendency towards elongation in a direction inclined slightly clockwise from the vertical.

3.3.2 Spatial properties of lateral antagonism

The antagonistic part of the linear kernels is largest on-axis, forming the second, positive phase of the on-axis kernel. In the surrounding regions of the receptive field the antagonism is smaller, and is not consistently seen in kernel cross-sections. The distribution of antagonism on the two dimensional spatial domain is seen most clearly by considering the simulated step-response of the system.

From the linear spatiotemporal kernel $h_1(x, y, t)$ the response to a step in intensity, of unit contrast, over a 1° square check with centre at position (x, y) is predicted by the cumulative integral over time of the kernel:

$$r(x, y, t) = \int_0^t h_1(x, y, t)\, dt$$

This will be called the simulated step-response over space. At locations where the kernel is biphasic, the simulated step-response rises to a peak and then declines towards a plateau value. These two values provide convenient measures of response amplitude as a function of spatial location.

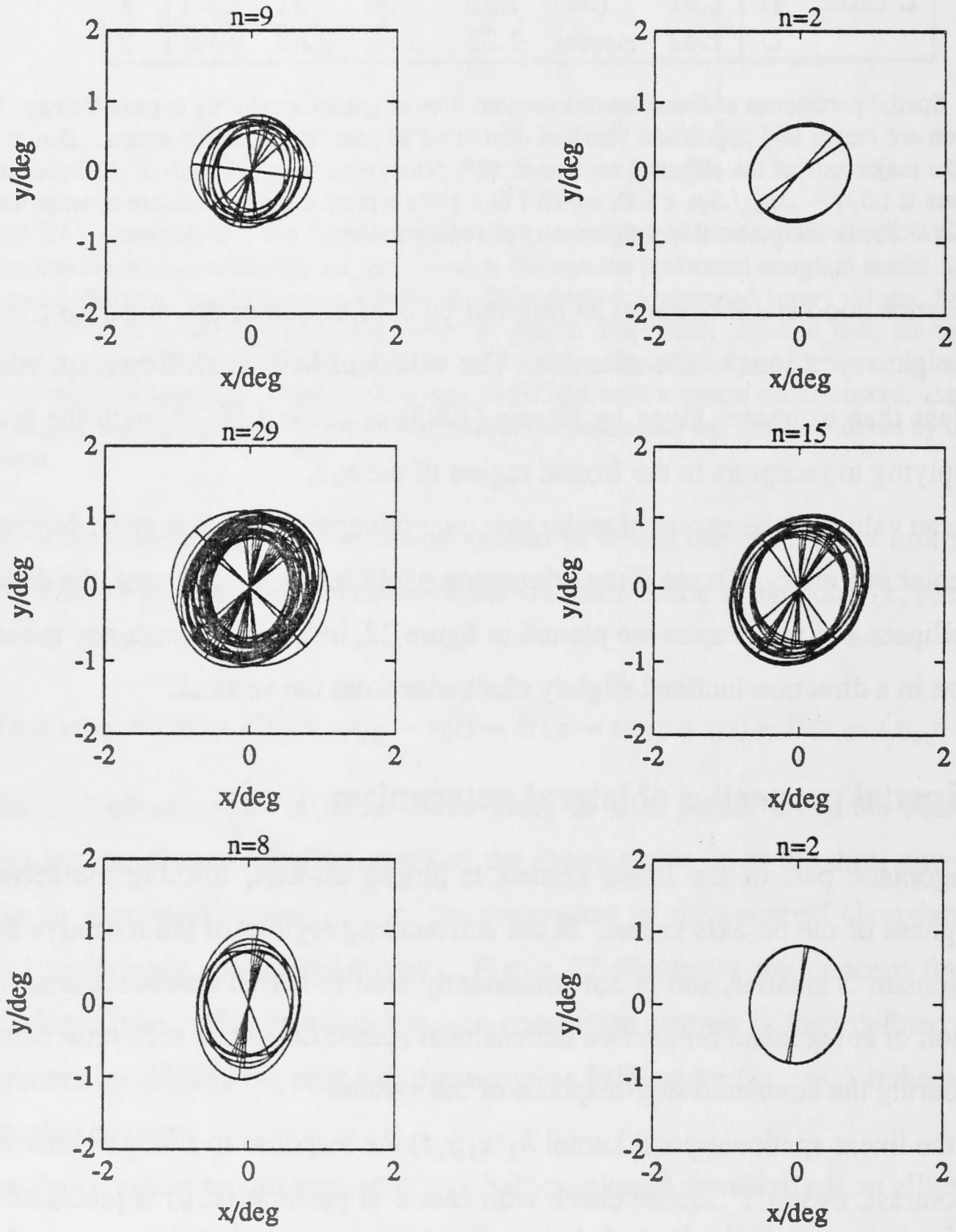

Figure 22: Ellipses of 50% sensitivity with their major axes for the Gaussian model fitted to the spatial sensitivity of the primary response. **Left**, higher mean intensity. **Right**, lower mean intensity, 2.3 log units less. **Upper**, *Eristalis* receptors. **Middle**, *Eristalis* LMCs. **Lower**, *Calliphora* LMCs.

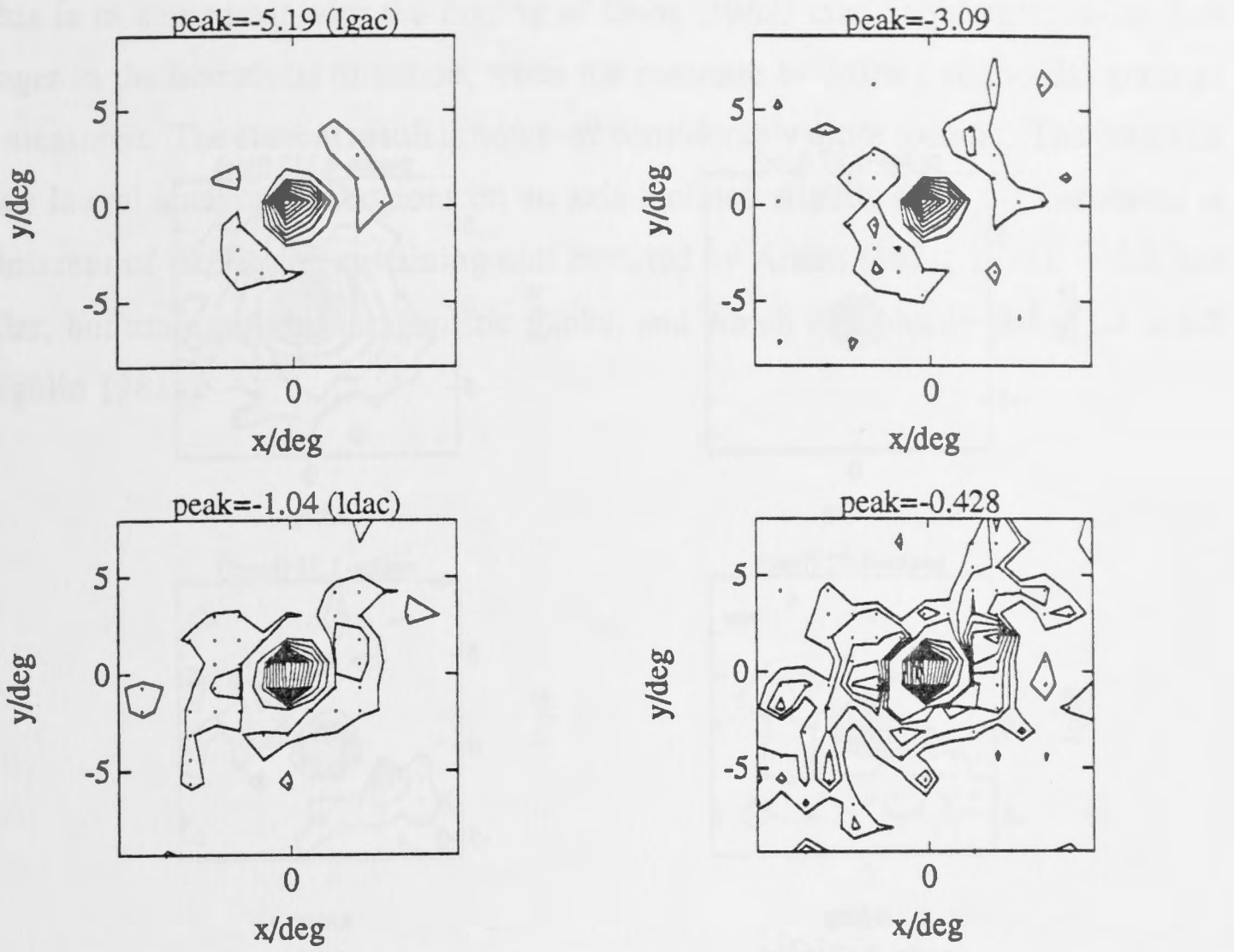

Figure 23: Peak and plateau values of simulated step-response, plotted over space. Contour step size is 5% of peak as indicated in mV, zero contour is excluded, dots indicate positive regions. **Left**, peak value. **Right**, plateau value, estimated by response at $t = 50\,ms$. Results from two *Eristalis* LMC are shown, names as indicated.

For most of the data in this study the spatiotemporal kernel value is close to zero at the longest latency considered, $50\,ms$. The step-response at $50\,ms$ is thus taken as an estimate of the plateau value. This is then another form of marginal kernel, where the kernel has been integrated over time.

Figure 23 shows some examples of simulated step-response peak and plateau values over space. In general, the two are qualitatively similar, but with the plateau value exhibiting a slightly larger region of antagonism. The peak value generally appears to be less noisy as a function of space, and is thus plotted in further examples, in figure 24.

The distribution of lateral antagonism varies, in some cases being absent (upper left), in some cases forming a complete annulus (upper right). Between the two extremes however the most interesting feature frequently occurs: the lateral antagonism appears as two regions positioned horizontally or diagonally relative to the receptive field centre, while there is a gap in the antagonistic surround above and below the centre.

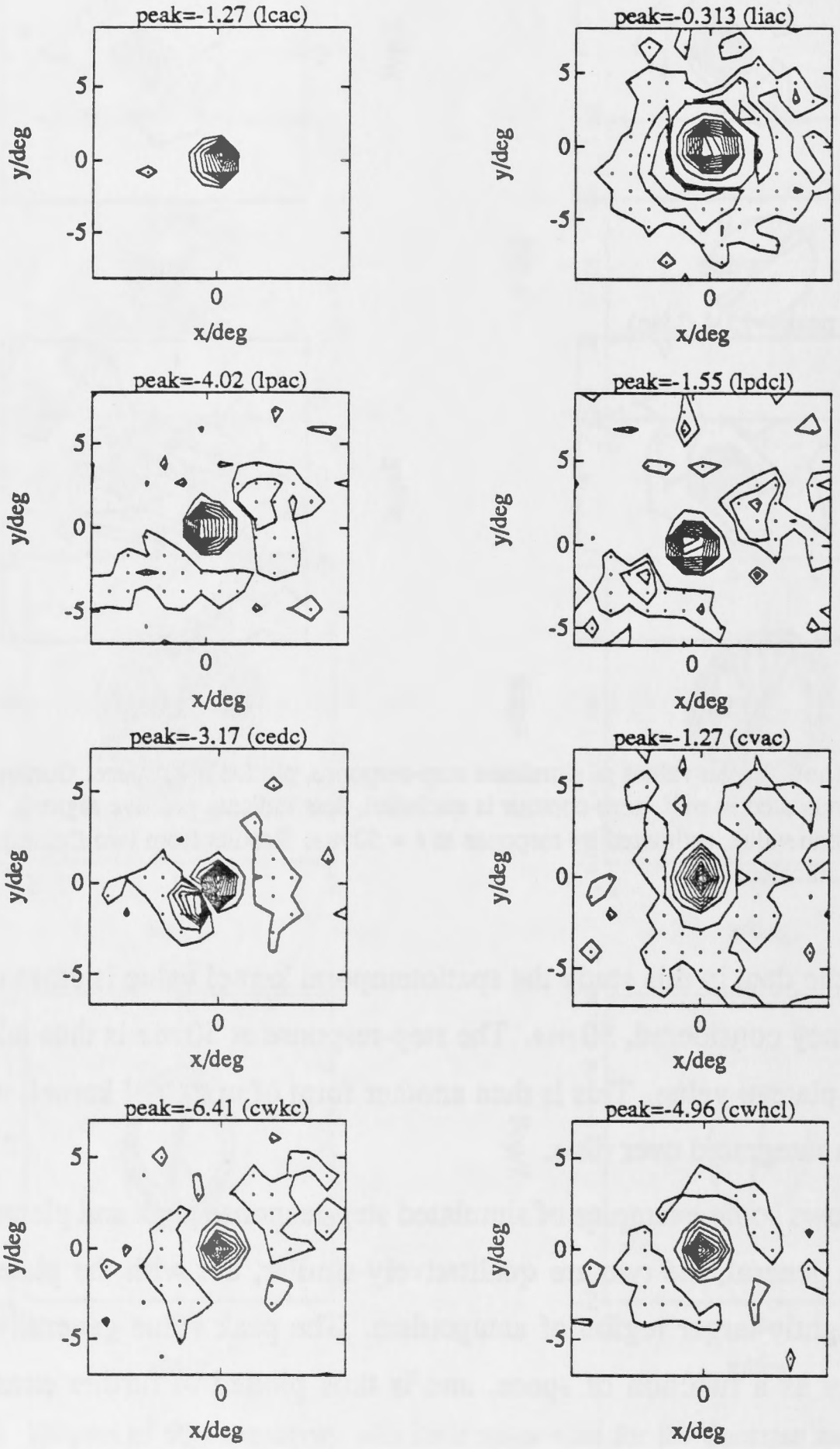

Figure 24: Peak values of simulated step-responses plotted over space. Plots as in figure 23. **First row**, two *Eristalis* LMCs, showing no antagonism (lcac) and extensive antagonism (liac). **Second row**, from an *Eristalis* LMC at high and low mean illumination. **Third row**, from two *Calliphora* LMCs. **Fourth row**, from a *Calliphora* LMC at high and low illumination.

This is in agreement with the finding of Dubs (1982) that lateral antagonism was stronger in the horizontal direction, when the response to drifting sinusoidal gratings was measured. The current result is however considerably more specific. The presence of two lateral antagonistic regions on an axis inclined slightly from the horizontal is reminiscent of the lamina sustaining unit reported by Arnett (1971, 1972), which has similar, but more potent, antagonistic flanks, and which is probably either L4 or L5 (Laughlin 1981a).

3.4 The kernels on space-time

Having examined in detail some aspects of the linear response in time and in space the kernels will now be considered on space-time, utilising the full generality of the spatiotemporal white-noise technique. The clearest view of spatiotemporal properties is generally obtained by considering the marginal kernels, reducing the dimensionality as well as accentuating the effects of lateral inhibition. The resulting view characterises the moving image processing performed as due to a composite spatiotemporal antagonism, rather than the two separate properties lateral inhibition and temporal filtering usually considered.

3.4.1 Space-time separability of the kernel

A key question to ask is whether the spatial location simply scales the amplitude of the sensitivity. The kernel may then be called separable, and is the tensor product of a spatial sensitivity function and a function of time, greatly simplifying the description of the system:

$$h(x, y, t) = h_s(x, y)\, h_t(t)$$

One form of spatial inhomogeneity was noted by Laughlin (1974), who measured peak and plateau values of the LMC step response at spatial locations across the receptive field. He found that the shape of the $V/\log I$ curves varied with location, demonstrating that the influence of spatial location on the response did not involve a simple scaling of sensitivity.

In work described below Dubs (1982) found that the shape of the modulation transfer function for LMCs varied with temporal frequency implying space-time inseparability.

The kernels derived in this thesis allow the question to be addressed directly. To give an indication of the degree of separability the temporal kernels from different spatial locations may be normalised and plotted. Figure 25 shows this done for an *Eristalis* receptor and LMC. These results are typical of almost all kernels, with the LMC kernels having additional antagonism off-axis relative to the on-axis section.

To test more carefully, the general separable model was fitted to the spatiotemporal kernels. The kernel is estimated at 15×15 spatial locations, and 23 steps of latency, giving 5175 points. The Marquardt-Levenburg algorithm is used to find the 15×15

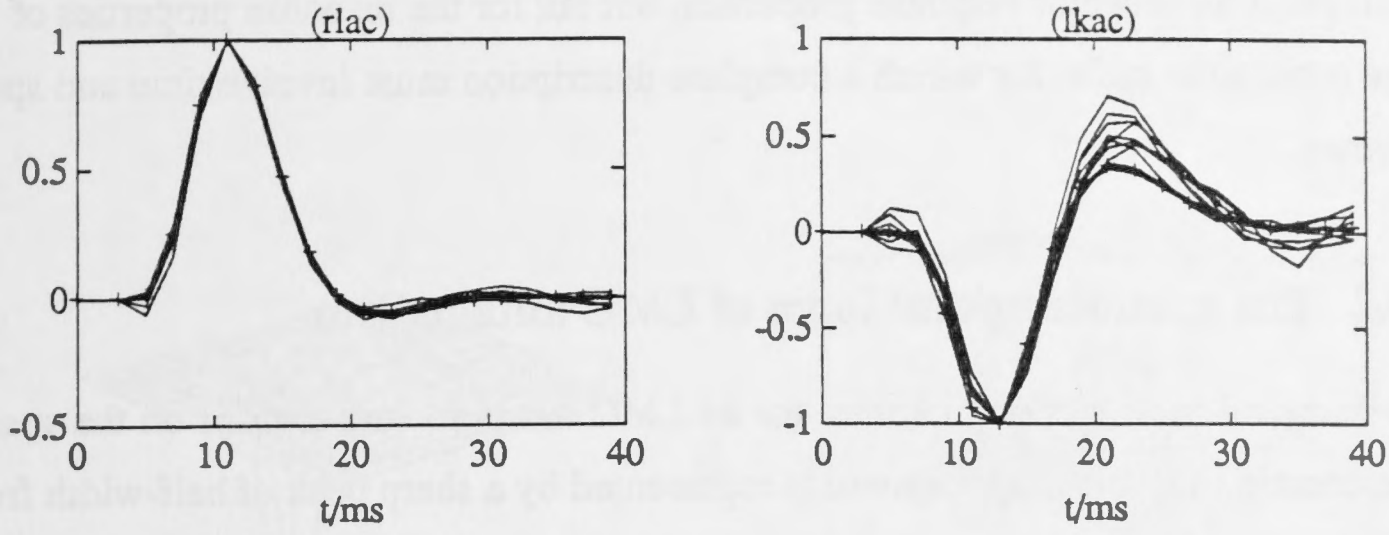

Figure 25: Test for space-time separability of the kernels. The temporal kernel sections are plotted normalised for those spatial positions where 10% of the peak kernel value was reached. The section at receptive field centre is marked with plus signs. **Left,** an *Eristalis* receptor (rlac). **Right,** an *Eristalis* LMC (lkac). This LMC is one not showing a large degree of lateral antagonism (see figure 29).

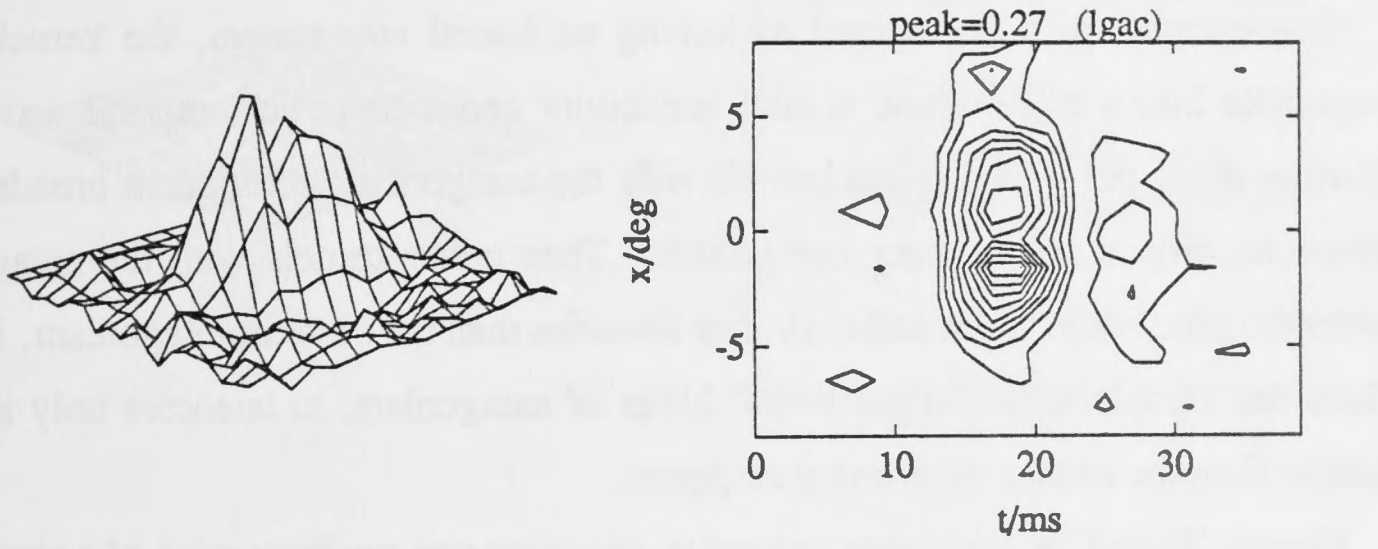

Figure 26: Residuals from the separable model fit to an *Eristalis* LMC kernel. The kernel was fitted with a tensor product model, as described in the text. The residuals were integrated over the vertical dimension, and the data plotted in the same manner as in figure 16, which shows the horizontal marginal kernel from the same experiment. The residuals reach a peak value which is 14% of the peak value of the kernel.

array of spatial sensitivity values and the 23 point temporal kernel giving the least-squares fit. The model is nonlinear, but of a particularly simple structure, with the first derivatives being of simple form. There is one degree of redundancy in the model, which is removed by setting the point of maximum spatial sensitivity to unity.

Goodness of fit is judged not only by the relative residual error, but also by the presence of any pattern in the residuals over the space-time domain. Figure 26 shows clearly the lack of fit for the LMC kernel, corresponding to the extra antagonism seen at surround locations.

These results hold for almost all LMC kernels, while for receptor kernels there is no such departure from fit, suggesting that space-time separability is a reasonable

assumption for receptor response properties, but not for the response properties of the large monopolar cells, for which a complete description must involve time and space together.

3.4.2 The spatiotemporal form of LMC antagonism

The marginal spatiotemporal kernel for an LMC has two clear regions on the space-time domain. The primary response is represented by a sharp peak of half-width from 1–2°, latency around 10 ms and temporal half-width of 5–10 ms. The second region, reflecting the antagonistic response is more variable in form. The shapes on space-time form a continuum; figure 27 shows three examples illustrating the range of forms, in perspective and contour plots.

One extreme may be defined as having no lateral antagonism, the kernel being separable into a monophasic spatial sensitivity and a biphasic temporal waveform. Further along the spectrum are kernels with the antagonistic component broadened in space relative to the primary component. Then come kernels with the antagonism extending further in space and at shorter latencies than the on-axis antagonism. Finally there are kernels with distinct lateral lobes of antagonism, at latencies only slightly longer than the latency of primary response.

Figures 28 and 29 give more examples, choosing one run from each of a number of cells.

Runs taken from the same cell had very consistent kernels, except for variation in amplitude. The plots are ordered by eye with descending extent of lateral antagonism. It is notable that all *Calliphora* LMCs recorded from had strong lateral antagonism, while the *Eristalis* LMCs varied along the rest of the spectrum.

Light adaptation between the two mean intensities used affects the time course of the kernels, more than the extent of lateral antagonism. Figure 30 shows kernels from two sample cells, an *Eristalis* LMC with a medium degree of lateral antagonism and a *Calliphora* LMC with strong lateral lobes of antagonism. The reduction of mean intensity by 2.3 log units causes a clear shift to longer latency and longer and lower antagonism in time, while causing some reduction in the degree of lateral antagonism.

Lateral antagonism in the response of fly LMCs can be an elusive property when examined in detail. We can state conclusively that it is not as apparent as the lateral inhibition found in vertebrate X-cells (Enroth-Cugell *et al* 1983), nor does the kernel

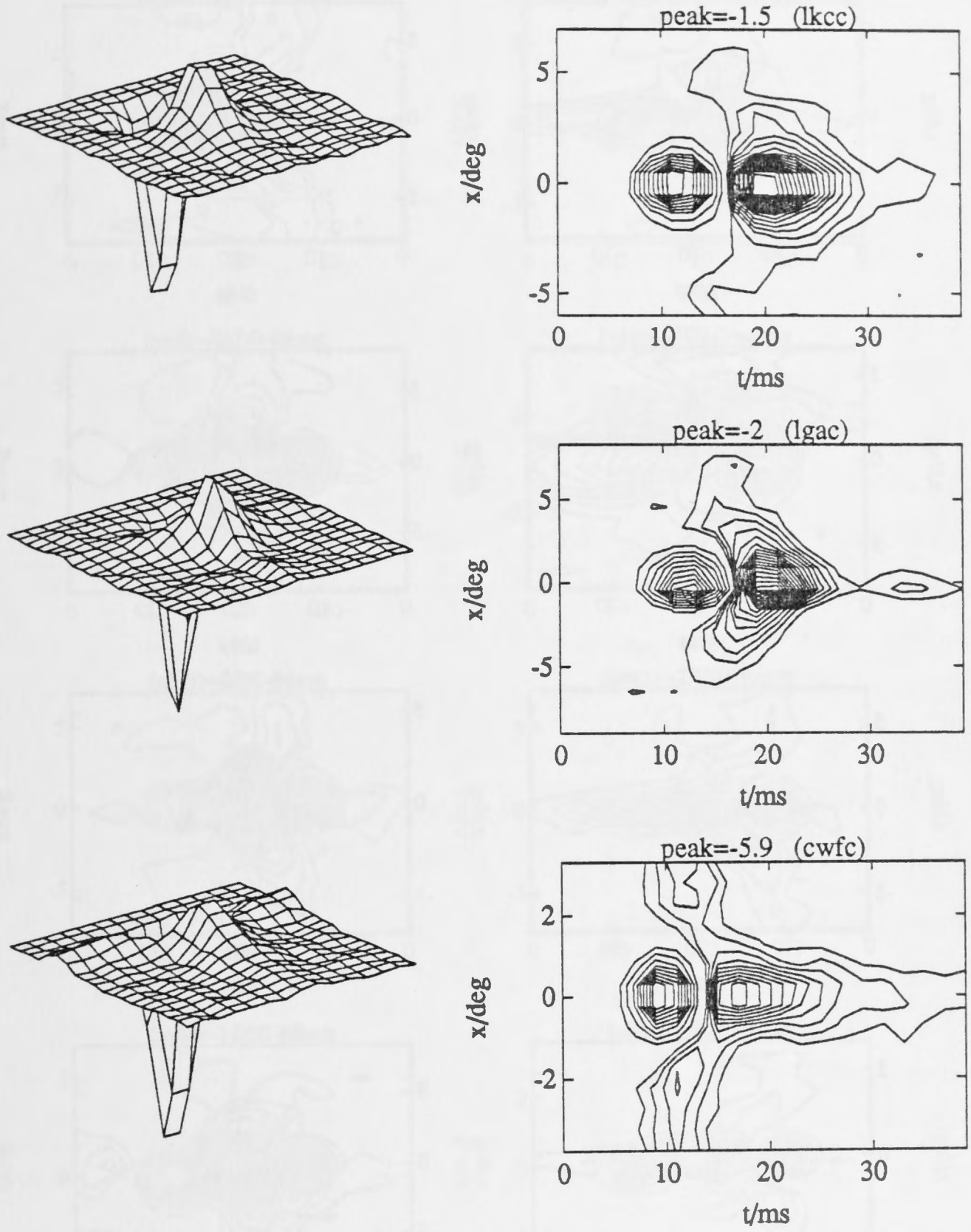

Figure 27: Examples of forms of LMC response antagonism. **Left,** perspective plots of horizontal spatiotemporal marginal kernels $h_1(x,t)$. **Right,** contour plots of same data. Peak values are as indicated, in $mV/(C\ ms\ deg^2)$. For negative range contour step size is 10% of peak value. To show the more diffuse antagonistic region the positive range has contour step size equal to 2% of the peak value. **Upper,** *Eristalis* LMC with little lateral antagonism. **Middle,** *Eristalis* LMC with more lateral antagonism. **Lower,** *Calliphora* LMC with clear lateral antagonistic lobes.

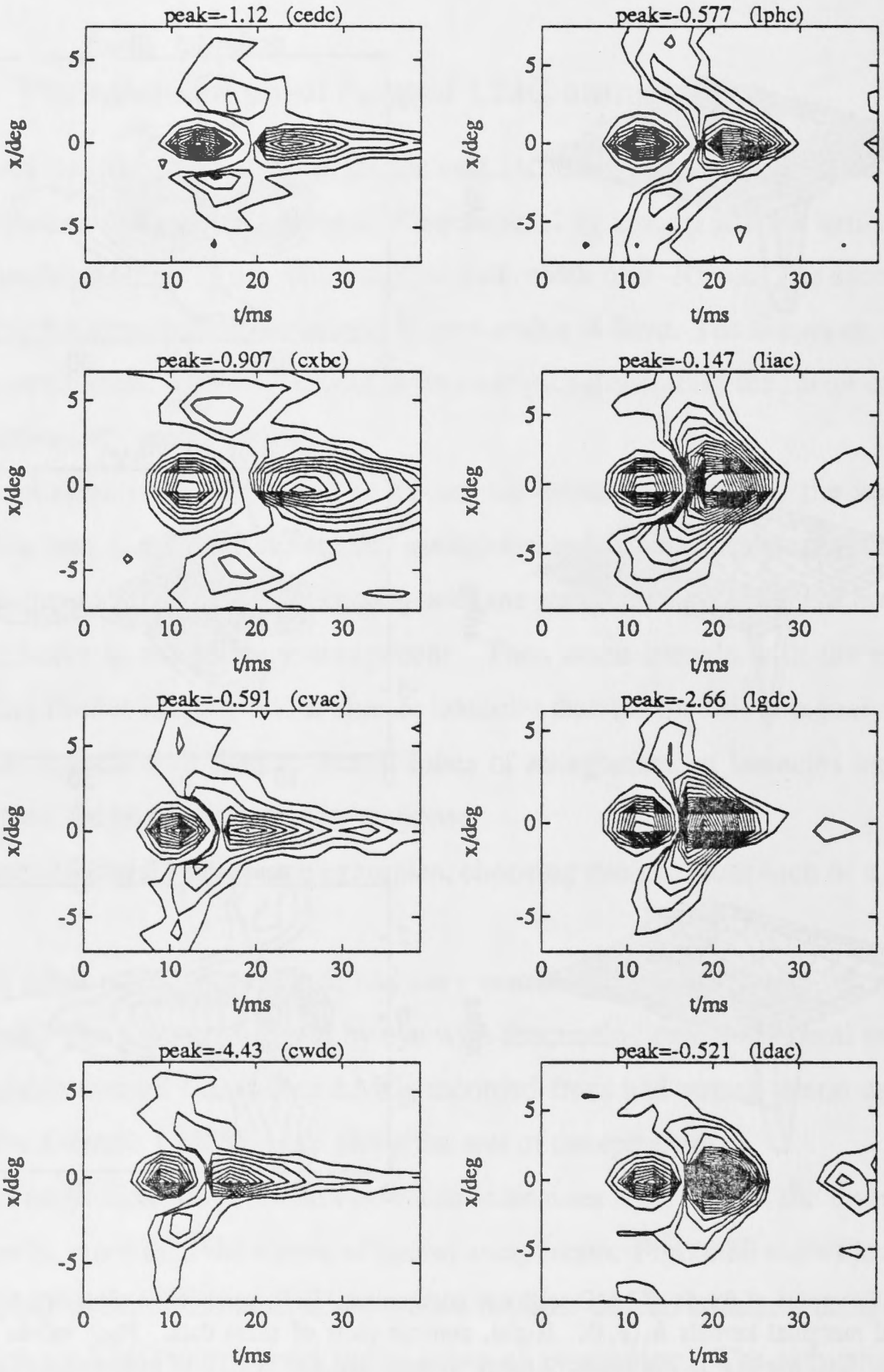

Figure 28: The range of LMC antagonism. Sample horizontal marginal kernels are shown in apparent order of decreasing lateral antagonism. **Left column**,from four *Calliphora* LMCs. **Right column**, from *Eristalis* LMCs. Format of contour plots as in figure 27.

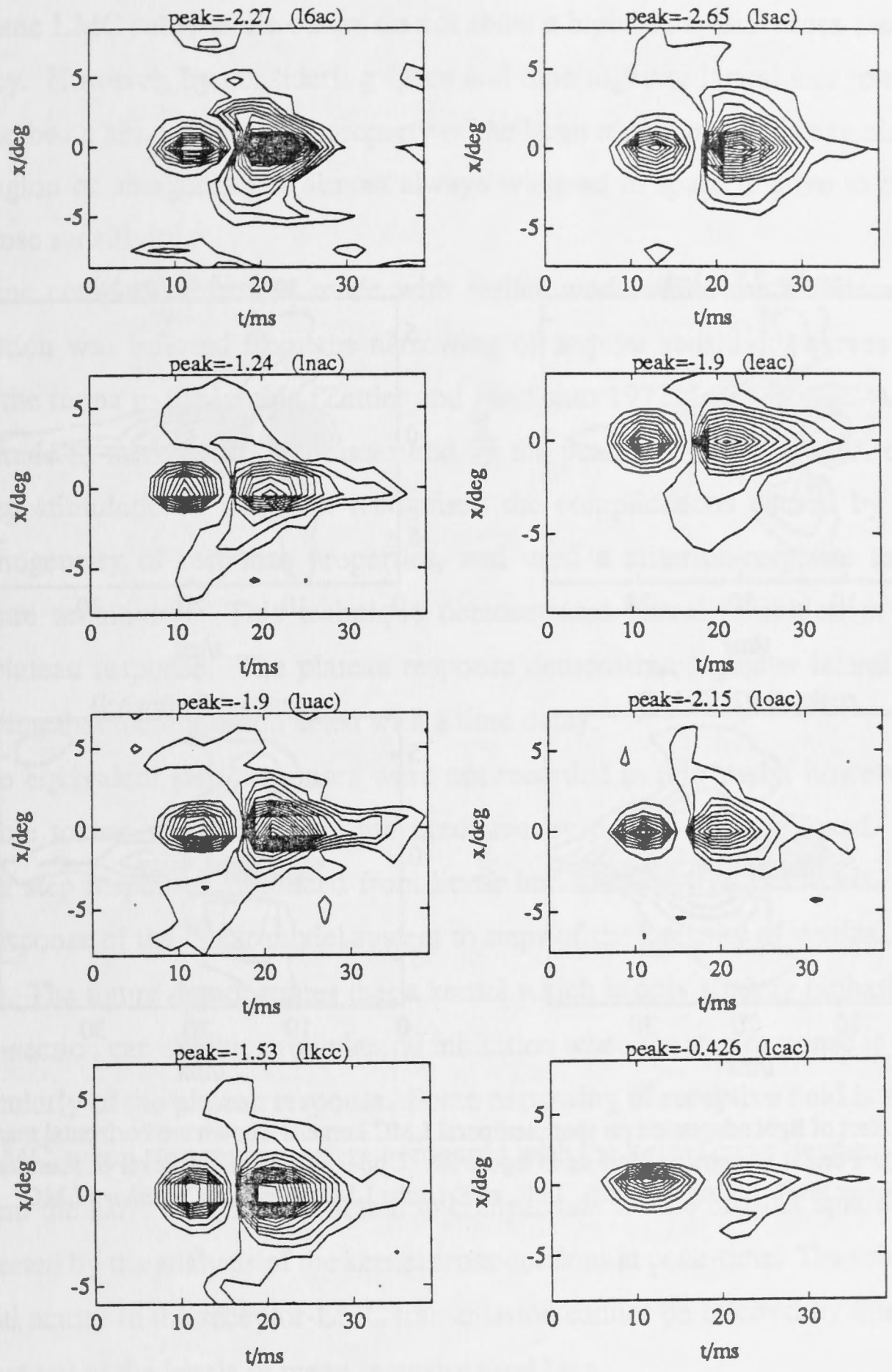

Figure 29: The range of LMC antagonism (continued). Further sample horizontal marginal kernels in apparent order of decreasing lateral antagonism, from *Eristalis* LMCs. Format of contour plots as in figure 27.

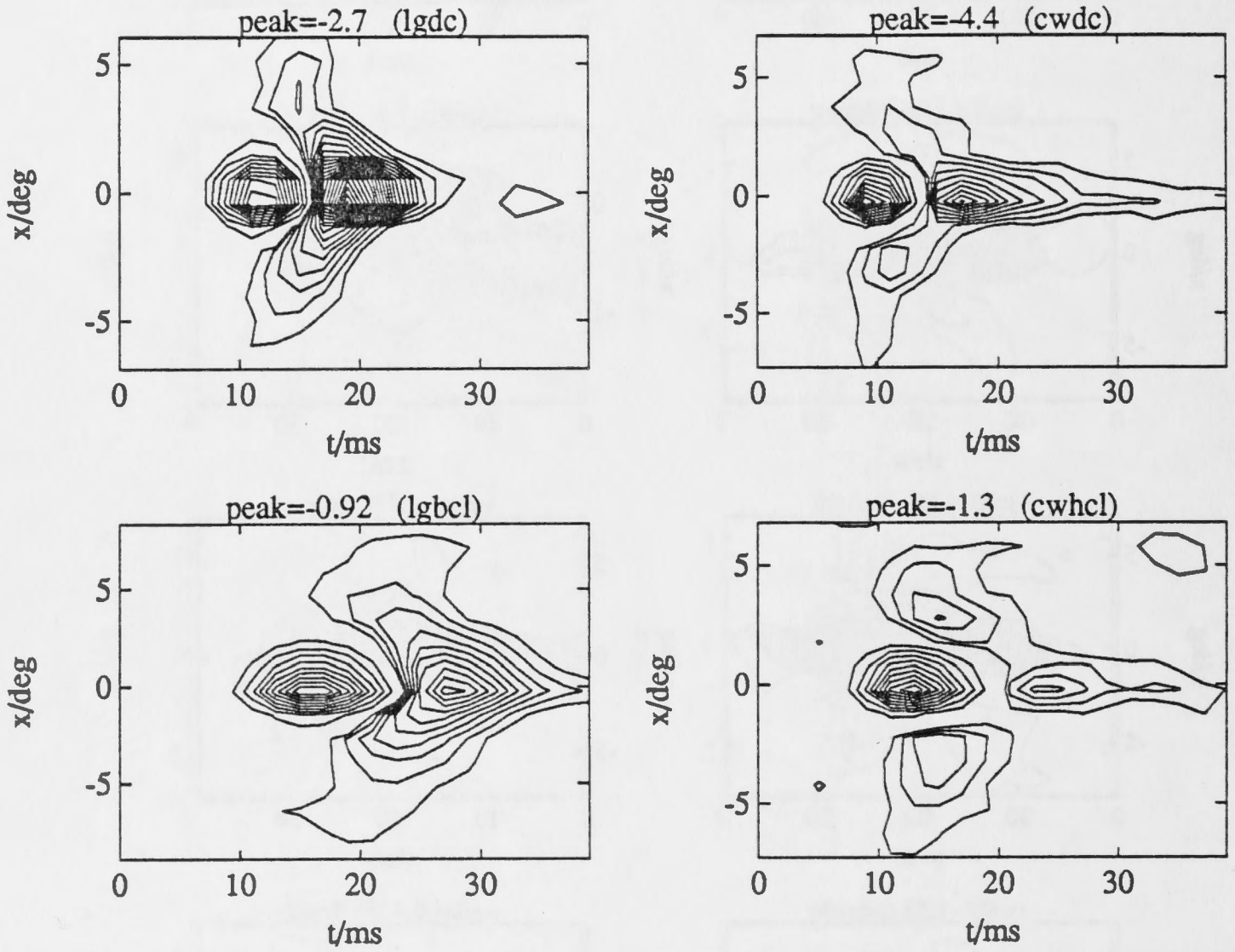

Figure 30: Effect of light adaptation on spatiotemporal LMC kernels. Shown are horizontal marginal kernels $h_1(x,t)$. Format of contour plots as in figure 27. **Upper**, at the higher level of illumination. **Lower**, at the lower level, 2.3 log units less. **Left**, an *Eristalis* LMC. **Right**, a *Calliphora* LMC.

have the spatial profile of the Laplacian of a Gaussian function, the $\nabla^2 G$ function widely adopted for computer simulation of visual processing.

Considering spatial cross-sections of kernels, diffuse lateral antagonism is apparent for some LMC cells, while others do not show a biphasic spatial cross-section at any latency. However, by considering space and time together lateral antagonism can be seen to be an almost universal property of the large monopolar cells examined, in that the region of antagonism is almost always widened in space relative to the primary response sensitivity.

Some comparison can be made with earlier work where the existence of lateral inhibition was inferred from the narrowing of angular sensitivity curves in passing from the retina to the lamina (Zettler and Järvilehto 1972, Laughlin 1974). Response amplitude in these works was measured by the peak and plateau values of response to step stimulation. Laughlin recognised the complications caused by the spatial inhomogeneity of response properties, and used a criterion-response technique to measure sensitivity. This technique demonstrated lateral inhibition of both peak and plateau response. The plateau response demonstrated greater lateral inhibition, implying that the inhibition acted with a time delay.

The equivalent step responses were not recorded in this study, however it is still possible to see what responses are predicted by the kernels measured. Figure 31 shows step responses simulated from linear horizontal marginal kernels. This gives the response of the linear model system to steps of the intensity of vertical bars across space. The figure demonstrates that a kernel which is only slightly biphasic in spatial cross-section can exhibit strong lateral inhibition when the step response is considered, particularly of the plateau response. Some narrowing of receptive field is apparent for the LMC, when step responses are compared with the kernel cross-section, however in general the narrowing is insufficient to compensate for the broader spatial sensitivity suggested by the analysis of the kernel cross-sections at peak-time. Thus sharpening of spatial acuity in the receptor-LMC transmission cannot be inferred by this technique, at least not at the levels of mean intensity used here.

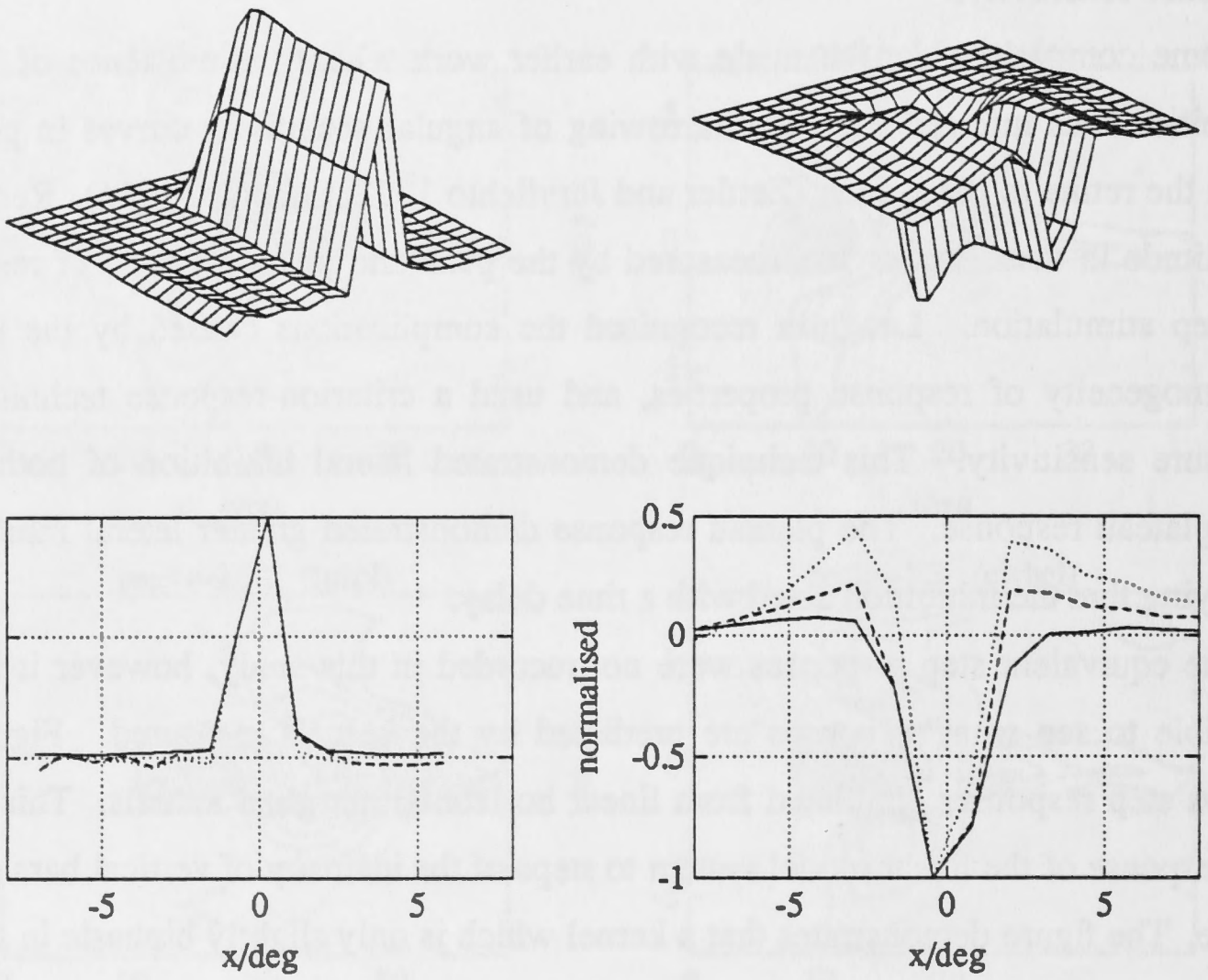

Figure 31: Simulated step responses across space. The response of linear spatiotemporal models is calculated for a step increment of intensity of a narrow vertical bar at a range of horizontal locations. **Left**, an *Eristalis* receptor (rfac). **Right**, an *Eristalis* LMC (liac). **Upper**, the step responses over time at the range of spatial locations. Grid size is $2\,ms$ for time and .9° for location. **Lower**, plotted normalised over space are: **solid line**, cross-section of the marginal kernel at the peak-time; **dashed line**, the peak value attained by the step response; **dotted line**, the step response after $40\,ms$, estimating the plateau response.

3.5 Frequency domain kernels

Although this study derives kernels using only time-domain techniques, this section considers the corresponding frequency domain results, both as a useful representation of linear systems, and to allow comparison with previous work on spatiotemporal properties of LMCs using frequency domain techniques such as modulation transfer functions (notably Dubs 1982).

For a linear system Fourier transforms of the kernel provide a representation theoretically equivalent to the time-domain representation. Fourier transforms can be taken with respect to the temporal dimension, latency, and/or with respect to spatial dimensions.

The notation for this section will be as follows: frequency coordinates are indicated by upper-case letters, thus T is temporal frequency in Hz and X is spatial frequency in cycles per degree. The Fourier transform of the kernel with respect to any dimension is indicated by the upper-case kernel symbol H_1, with frequencies as arguments in the appropriate dimensions. Thus $H_1(x, y, T)$ is the temporal frequency transfer function for stimulation at the location (x, y), while $H_1(X, T)$ is the spatiotemporal frequency transfer function for stimuli extended uniformly in the vertical dimension:

$$H_1(X,T) = \int_{-\infty}^{\infty}\int_{-\infty}^{\infty} h_1(x,t)e^{-2\pi i(xX+tT)}\,dt\,dx$$

When required, the form of transform can be made more explicit by attaching the arguments as superscripts: H_1^{xT} is thus the time-only Fourier transform of the horizontal marginal kernel.

Note that the linear Wiener kernels estimated in this study are the linear models providing least-squares fits to the data, and are influenced by system nonlinearity. The Fourier transforms are thus the frequency transfer functions of these model systems, and not necessarily the transfer functions which would be obtained by using sinusoidal stimulation. Nevertheless, as the systems are primarily linear these Fourier transforms will be presented.

3.5.1 The spatiotemporal frequency domain

For graphical tractability we will consider stimuli varying in time on one spatial dimension, uniformly extended in the other spatial dimension. The model operators

are then represented by the marginal kernels, integrated over one spatial dimension, h_1^{xt} and h_1^{yt}.

The elementary spatiotemporal frequency stimulus is a drifting sinusoidal grating, for example a vertically extended grating having a contrast on space-time of the form:

$$s(x,t) = a \sin(2\pi(xX + tT))$$

where a is the amplitude, X is the spatial frequency of the grating and T is the temporal frequency of modulation at any fixed location. The velocity of such a grating is $v = -T/X$ in degrees per second. X and T are to be considered as signed quantities; when they are positive v is negative, that is drifting backwards in space. Drifting the grating in the other direction is equivalent to reversing the direction of time, which is equivalent to changing the sign of the temporal frequency T. On the spatiotemporal frequency domain this stimulus appears as two point masses, one at (X,T), with mass $a/2i$, the other symmetrically at $(-X,-T)$, with the complex conjugate mass $-a/2i$. A grating drifting in the other direction has mass in the other two quadrants of the (X,T) plane.

The response of the linear spatiotemporal model to this stimulus is sinusoidal, and is specified by the transform kernel value $H_1(-X,T)$. The kernel is evaluated at $-X$ because our model integrates forward over the space dimension rather than convolving over space. The modulus, $|H_1(-X,T)|$, gives the gain of transmission in millivolts per unit contrast, (mV/C), while the argument, $\angle H_1(-X,T)$, gives the phase shift in radians relative to the stimulus at $x = 0$. The model output Fs is thus

$$Fs(t) = a\,|H_1(-X,T)|\,\sin(2\pi tT + \angle H_1(-X,T))$$

As the kernel $h_1(x,t)$ is real-valued, the spatiotemporal frequency kernel has conjugate symmetry with respect to X,T together,

$$H_1(-X,-T) = H_1(X,T)^*$$

where $*$ denotes the complex conjugate, but will not in general have symmetry with respect to one argument alone. If spatial symmetry is not to be assumed, the kernel must be specified on one half of the (X,T) plane; it is plotted here on positive and negative spatial frequencies. Correspondingly, to measure it with sinusoidal gratings the gratings must be drifted in both directions.

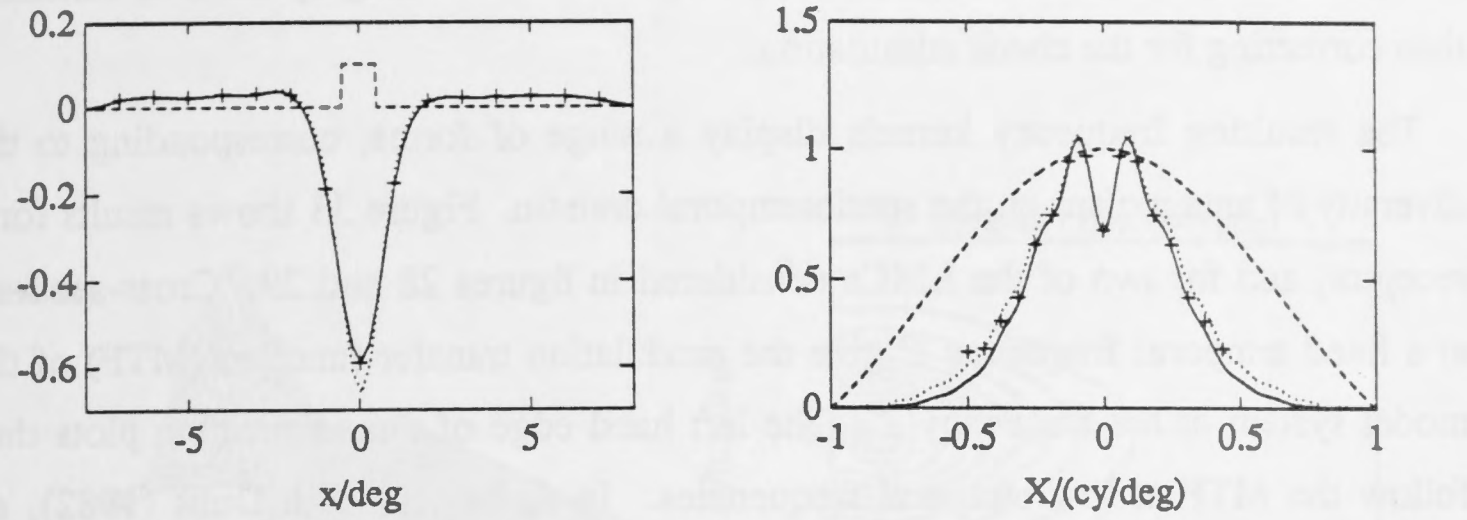

Figure 32: Example of spline interpolation, and Fourier transformation. **Left**, a cross-section is taken through the horizontal marginal kernel $h_1(x,t)$ at the peak-time, for an *Eristalis* LMC (cvac). **Plus signs**, estimated kernel points. **Solid line**, cubic spline interpolation. **Dashed line**, profile of check in checkerboard stimulus, in this case of size $\Delta x = 1°$, scaled arbitrarily in amplitude. **Right**, modulus of Fourier transforms. **Plus signs**, discrete Fourier transform of uninterpolated data. **Solid line**, transform of spline interpolation. **Dashed line**, transform of check gives sinc function. **Dotted line**, quotient of previous two gives transform of deconvolved kernel.

If the kernel is space-time separable, $h_1(x,t) = h_1^x(x)h_1^t(t)$, then the frequency kernel is similarly separable:

$$H_1(X,T) = H_1^X(X)H_1^T(T)$$

As shown above this is a reasonable assumption for receptor kernels, but not for LMC kernels; LMC response properties are thus comprehensively represented only by considering space and time together.

Consideration of discrete Fourier transforms of the measured kernels indicated that the temporal resolution of sampling was adequately fine but that the spatial resolution, given by check sizes between .6° and 1.2° was generally too coarse, leading to truncation of the spatial frequency kernel, and folding back of higher frequency components. To obtain reasonable results the kernels were interpolated with cubic splines to four times greater resolution on the spatial domain before Fourier transforming. Figure 32 shows a sample spatial cross-section of kernel, the spline interpolation and the corresponding frequency domain kernels. The figure also shows the profile of the stimulus check of size $\Delta x = 1.2°$ and the corresponding Fourier transform, $\mathrm{sinc}(2\pi X \Delta x/2)$, where sinc is the $\sin(x)/x$ function. Recall that the use of check stimulation means that the measured kernel points are effectively samples of the actual kernels convolved with the check profile. The spatial frequency composition of the kernels always reduced to negligible strength below the frequency of the first zero of the sinc function, at $X = 1/\Delta x$. Deconvolution could be achieved by truncating on

the spatial frequency domain at $X = .9/\Delta x$, and then dividing by the sinc function, thus correcting for the check stimulation.

The resulting frequency kernels display a range of forms, corresponding to the diversity of antagonism on the spatiotemporal domain. Figure 33 shows results for a receptor, and for two of the LMCs considered in figures 28 and 29. Cross-sections at a fixed temporal frequency T give the modulation transfer function (MTF) of the model system at the frequency T. The left hand edge of the perspective plots thus follow the MTF at low temporal frequencies. In agreement with Dubs (1982), all LMC cell kernels indicate a dip in the MTF at $X = 0$ for low temporal frequencies, indicating spatial high-pass filtering. Where a strong lateral antagonism is present this dip extends to high temporal frequencies, forming a valley between two peaks. For many of the cells however, with less lateral antagonism, the spatial high-pass filtering has disappeared before the peak temporal frequency is reached, leaving a single peak. The receptor kernels interestingly indicate some high-pass filtering in space as well as time.

Frequency kernels from the same cell at high and low intensities of illumination are shown in figure 34. The cell was a *Calliphora* LMC exhibiting strong lateral inhibition relative to other cells in this study. The form of the spatiotemporal frequency kernel is essentially unchanged over the 2.3 log units of illumination used, apart from a shift to lower temporal frequencies at the lower light level. This result was qualitatively true for all the LMC kernels in the study. The receptor kernels at low intensity altered in having no rolloff at low temporal frequencies, while retaining some spatial high-pass filtering. An example is shown in figure 35.

The spatiotemporal frequency kernels allow comparison to be made with the largest previous study made of LMC spatial properties, that of Dubs (1982).

Dubs measured the modulation transfer function (MTF) of receptors and LMCs in three species of fly, *Calliphora stygia, Musca domestica* and *Lucilia sericata.* The MTF was defined as the reciprocal of the contrast required to give a certain criterion amplitude of response to a moving sinusoidal grating, as a function of the spatial frequency of the grating. This was measured at 25 spatial frequencies between .0125 and 5 cycles per degree, and at temporal frequencies between 1.2 and 12 *Hz*. For a linear system this estimates points of the dual Fourier transform kernel, $H_1(X, T)$. Also, for a system performing linear spatiotemporal summation and then transforming the signal

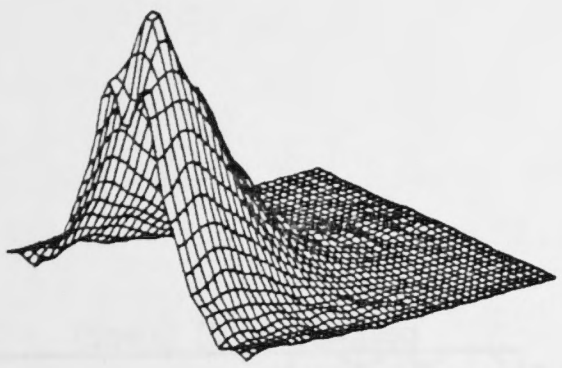

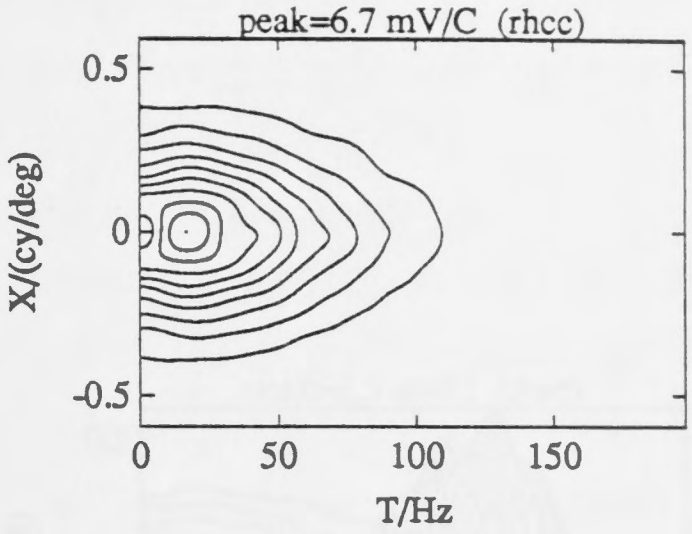

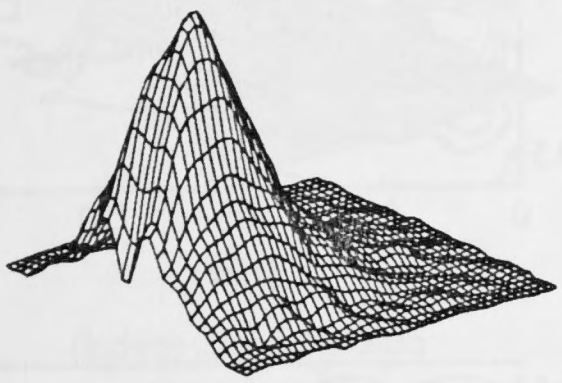

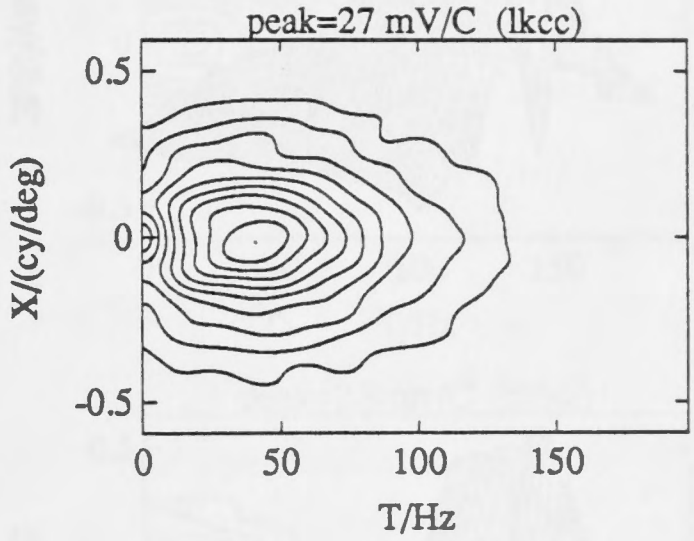

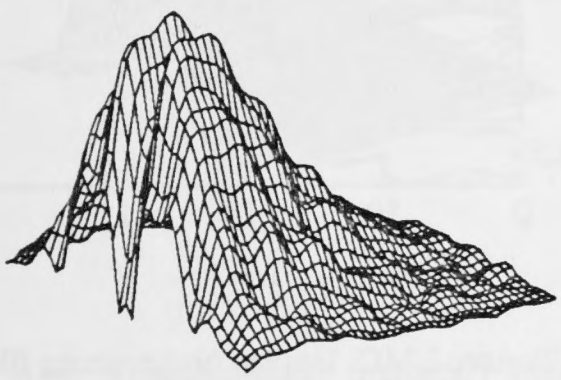

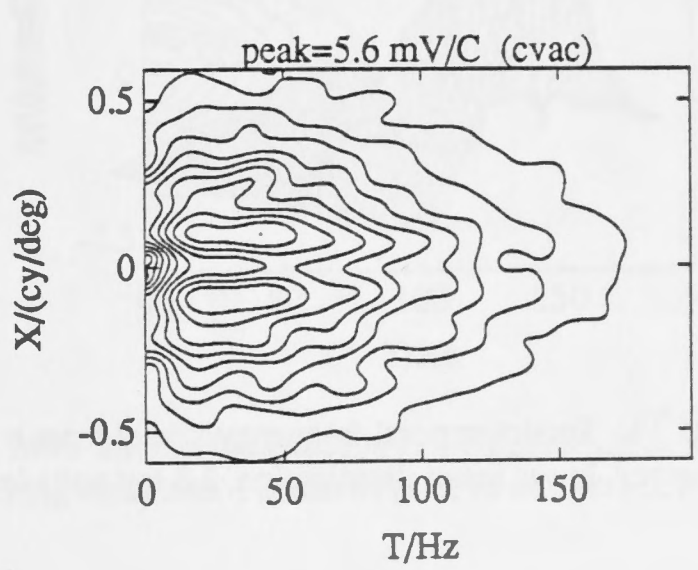

Figure 33: Spatiotemporal frequency kernels. Modulus of $H_1(X,T)$ is plotted on positive temporal frequencies, for spatial frequency from $-.6$ to .6 cycles per degree. Kernels are calculated by Fourier transformation of the horizontal marginal kernel $h_1(x,t)$, after cubic spline interpolation in the x dimension. **Left**, perspective plot, data decimated by four to reduce grid density. **Right**, 10% contours of same data. **Upper**, from an *Eristalis* receptor. **Middle**, from an *Eristalis* LMC. **Lower**, from a *Calliphora* LMC. Run identifiers, in parentheses, are described in section 2.5.3

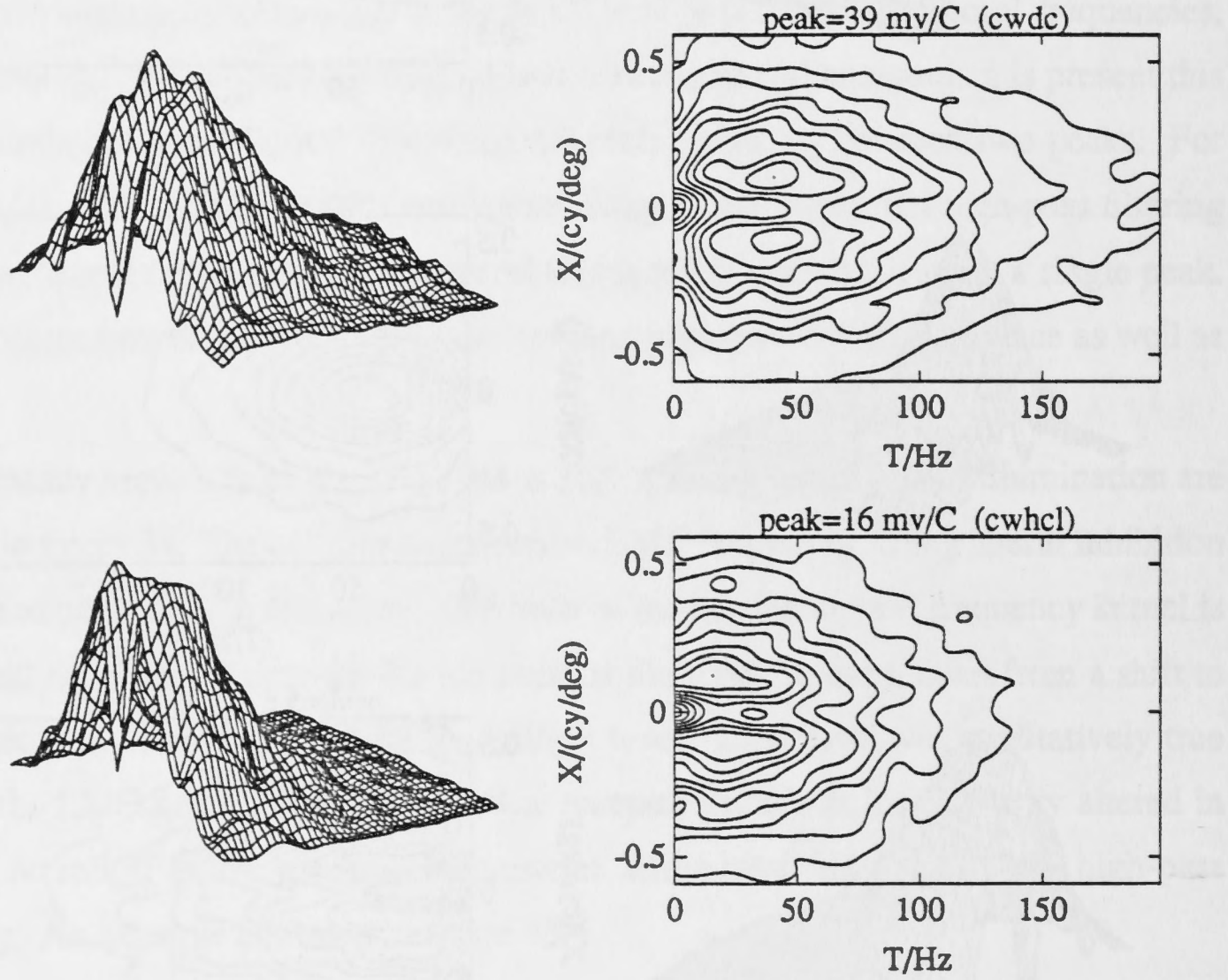

Figure 34: Spatiotemporal frequency kernel from a *Calliphora* LMC. **Upper**, higher mean illumination. **Lower**, lower mean illumination, 2.3 log units less. Format of plots as in figure 33.

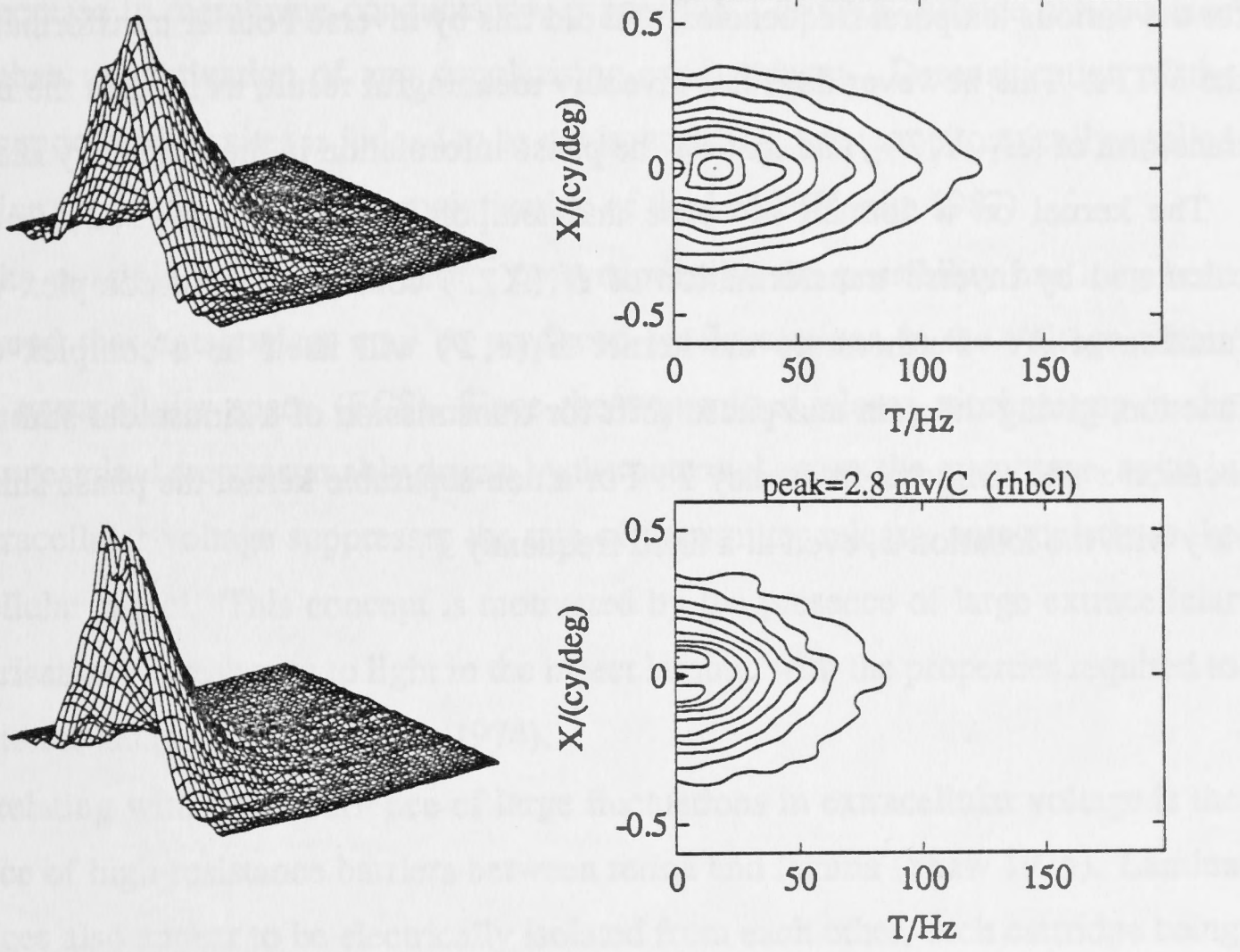

Figure 35: Spatiotemporal frequency kernel from an *Eristalis* receptor. **Upper**, higher mean illumination. **Lower**, lower mean illumination, 2.3 log units less. Format of plots as in figure 33.

by a static, monotonic nonlinear mapping, the criterion response technique eliminates dependence on the nonlinearity, and describes accurately the linear summation. The results are thus not precisely comparable with the kernels of this study, which are the least squares linear fit, and are influenced by system nonlinearity. The highest mean intensity of illumination used was estimated as $1.7 \times 10^{-6}\, W\, cm^{-2}\, sr^{-1}$ delivered by a P31 phosphor, and thus comparable to the lower intensity used here.

In his study Dubs noted that for the LMCs the spatial frequency transfer functions varied with the temporal frequency of the moving grating, thus implying a kernel which is not space-time separable. He wished to present angular sensitivity functions for the various temporal frequencies, and did this by inverse Fourier transformation of the MTFs. This however does not give any meaningful result, as it takes the inverse transform of $|H_1(X,T)|$, and ignores the phase information in the frequency kernel.

The kernel on a domain of space and temporal frequency, $H_1(x,T)$, must be calculated by inverse transformation of $H_1(X,T)$ considered as a complex-valued function of X. Furthermore the kernel $H_1(x,T)$ will itself be a complex-valued function, giving the gain and phase shift for transmission of a sinusoidal stimulus at location x and temporal frequency T. For a non-separable kernel the phase shift will vary with the location x, even at a fixed frequency T.

3.6 Mechanisms of antagonism

It now seems that the transmission from receptor to lamina is primarily by way of a synapse involving the transmitter histamine (Hardie 1987), which increases the chloride conductance of the LMC membrane, leading to the hyperpolarising response to light increments (Zettler and Straka 1987, Hardie 1987, 1989).

Possible mechanisms producing antagonism in receptor–lamina transmission have recently been discussed in Laughlin and Osorio (1989). In that paper evidence is presented that the decay of the LMC response to a step increment of light is accompanied by a decrease in membrane conductance, suggesting a drop in chloride conductance rather than the activation of any depolarising conductances. Desensitisation of the postsynaptic binding sites is judged to be not important, since ionophoretically applied histamine produces a tonic hyperpolarisation of the LMC (Hardie 1987).

Of the possible mechanisms acting presynaptically, the possibility has long been considered that antagonism may be produced by fluctuations in the voltage within lamina extracellular space (ECS). Since the transmitter release mechanisms in the receptor terminal are presumably driven by the potential across the membrane, a rise in the extracellular voltage suppresses the rate of transmitter release, antagonistic to the intracellular signal. This concept is motivated by the presence of large extracellular depolarisations in response to light in the insect lamina, with the properties required to generate the antagonism (Laughlin 1974).

Correlating with the occurrence of large fluctuations in extracellular voltage is the presence of high-resistance barriers between retina and lamina (Shaw 1975). Lamina cartridges also appear to be electrically isolated from each other, each cartridge being surrounded by three epithelial glial cells between which are tight junctions (Shaw 1984). The hexagonal array of lamina cartridges is thus embedded in a matrix of epithelial glial cells. Gap junctions exist between epithelial glial cells, allowing current to flow across the lamina within the glial cell matrix.

3.6.1 A model of current flow in the retina-lamina array

An electrical circuit has been proposed to represent the process of electrical lateral inhibition in the insect lamina (Shaw 1975). This section develops that concept into a quantitative model of current flow within the lamina array that produces model kernels

that can be compared with the observed spatiotemporal kernels.

The original Shaw model is reproduced in figure 36. Stimulation of a receptor is equivalent to an injection of current into the cell body. Part of that current flows to the receptor terminal and out into the surrounding extracellular space (ECS). As the normal return path is blocked by a high resistance barrier, current returns through neighbouring receptors, producing a hyperpolarisation of the terminal membranes of these neighbours, thus suppressing their transmitter release. The voltages that will be recorded elecrophysiologically depend on the position of the indifferent electrode. If it is positioned in the haemolymph, then their are ground points between retina and lamina ECS, due to the presence here of blood vessels. There are thus virtual ground points along each resistive path between retina and lamina, as depicted in the circuit.

The model in this section elaborates Shaw's scheme in the following ways.

1. Temporal dynamics are modelled by taking the capacitance of components into account.

2. The role of glial cells in separating lamina cartridges is taken into account.

3. An array of units is considered, extended in one dimension.

It has been suggested that extracellular potentials contribute not only to lateral antagonism but also to the temporal high-pass filtering in receptor–lamina transmission. In order to produce the temporal filtering the rise in extracellular voltage in the stimulated cartridge must be delayed relative to the receptor response. Mechanisms which might produce that delay have not been clearly proposed in the literature.

An underlying idea in the present modelling is that the capacitance of the glial cell membrane may provide the delay required. Glial cells present a considerable area of membrane to the extracellular space of a lamina cartridge. They also have extensive invaginations, which will add to their capacitance if the membrane involved is electrically connected with the ECS. It is proposed here that current flowing out of a stimulated receptors terminal spreads laterally in the lamina crossing glial cell membranes largely as capacitive current, with the glial cell membranes having high resistivity. As the response to stimulation declines, charge accumulated on the glial cell membrane discharges not through the membrane itself, but largely back through the stimulated receptor, hyperpolarising the terminal membrane and suppressing transmitter release. We will thus wish to see whether a model of current flow in the

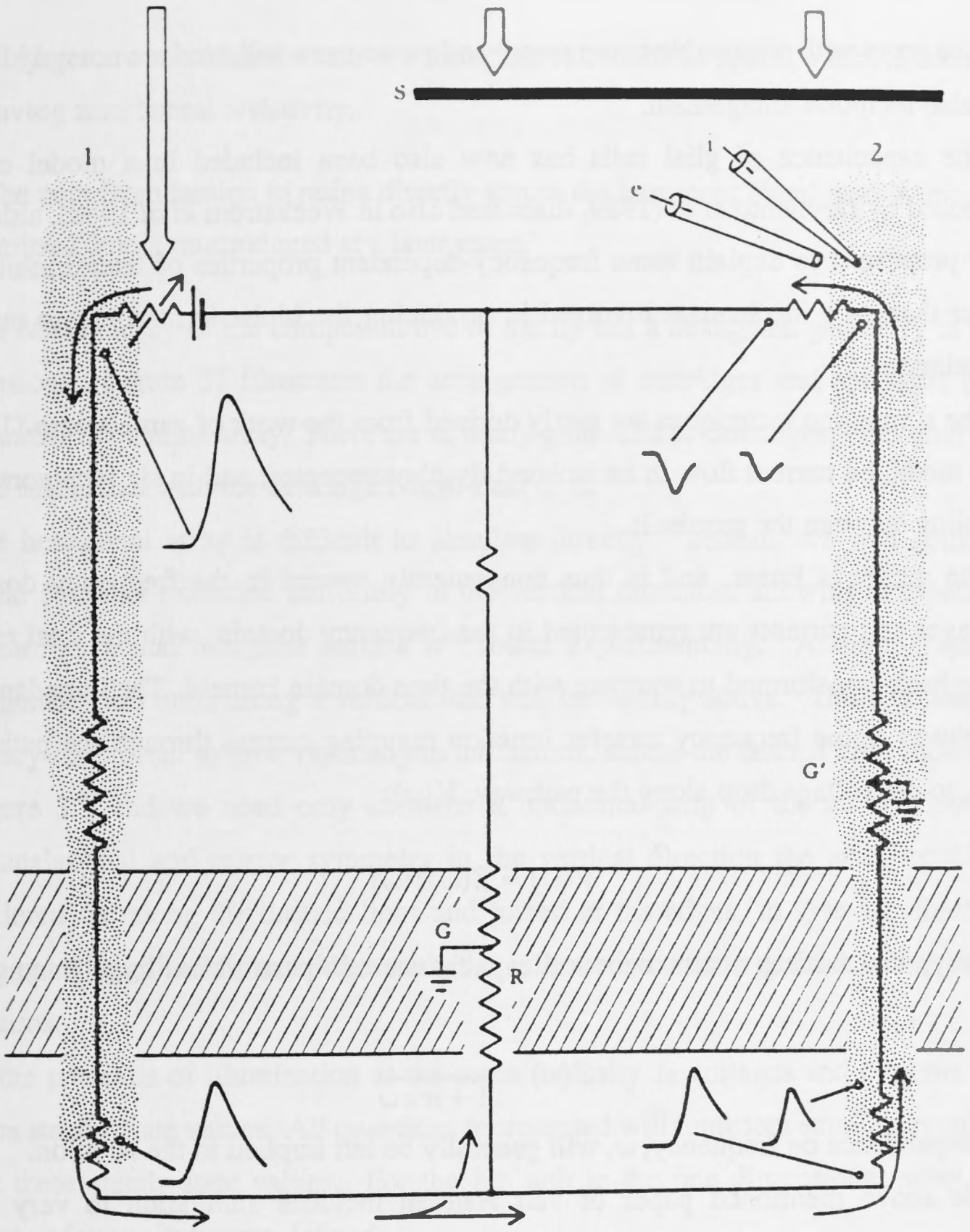

Fig. 9. The scheme originally developed for the locust, to explain current flow during electrical presynaptic inhibition (Shaw, 1975). Photocurrent issuing from the terminal of an illuminated photoreceptor (1), spreads laterally amongst the cartridges. Because the more direct return circuit is blocked by an extracellular barrier, R, some of the current enters and travels inside other less stimulated receptors, such as 2. Entry concentrated at the terminal will hyperpolarize the membrane there, reducing any existing transmitter release. The parasitic current has to leave receptor 2 again, but does this over a wide area of soma, producing only a small depolarization there. The actual recorded wave shapes are incidental, and will depend on the position of the reference electrode and the presence of blood channels in the eye at G. Similar circuits explain extracellular current flow in the butterfly (Matič, 1983) and in the Mauthner cell's electrical interaction. G', a null-point (virtual ground) that exists at some point along the intracellular pathway 2, because the latter forms an external potentiometric loop in parallel with the real ground at G, the effective position of the reference electrode here. e, extracellular recording micropipette, set about 20 μm back from intracellular recording pipette, i. S, stop, preventing a light flash from falling on photoreceptor 2.

Figure 36: Reproduction of figure showing proposed circuit underlying electrical lateral inhibition in the insect lamina, from Shaw (1975).

lamina array with reasonable components and parameters will produce not only lateral but also temporal antagonism.

The capacitance of glial cells has now also been included in a model circuit proposed by Järvilehto *et al* (1989, discussed also in Weckström *et al* 1988), although they propose it to explain some frequency-dependent properties of lateral inhibition rather than as a mechanism involved in producing the biphasic response to on-axis stimulation.

The simulation techniques are partly derived from the work of van Hateren (1986), who modelled current flow in an isolated fly photoreceptor, and in six receptors with coupling between the terminals.

The model is linear, and is thus conveniently treated in the frequency domain. Voltages and currents are represented in the frequency domain, with the final results being back-transformed to compare with the time domain kernels. The impedance of a pathway is the frequency transfer function mapping current through the pathway, $I(\omega)$, to the voltage drop along the pathway, $V(\omega)$:

$$V(\omega) = Z(\omega)I(\omega)$$

A component having resistance r and capacitance c in parallel has impedance given by:

$$Z(\omega) = \frac{r}{1 + irc\omega}$$

The dependence on frequency, ω, will generally be left implicit in the notation.

The above mentioned paper of van Hateren includes simulation to very high frequency, $10\,KHz$, allowing description of behaviour if high-bandwidth injection of current is considered. Here, we wish only to model responses to light, so that the input is already low-pass filtered by the transduction process, with little power above $200\,Hz$. In particular this justifies greater 'lumping' whereby extended structures are modelled as being isopotential components.

The following simplifications are made, relative to Shaw's diagram:

1. The impedance between receptor body and terminal is ignored, taking the receptor as isopotential. The simulation of van Hateren suggests almost constant gain of voltage transfer from receptor body to terminal over the bandwidth of interest.

2. Complications caused by the position of the indifferent electrode are ignored.

Voltages are considered relative to the retina extracellular space, which is taken as having zero lateral resistivity.

3. The path from lamina to retina directly across the basement membrane is initially omitted, but is reintroduced at a later stage.

The lamina array of the compound eye of the fly has a hexagonal geometry in two dimensions. Figure 37 illustrates the arrangement of cartridges and epithelial glial cells across the lamina array. There are as many glial cells as cartridges; each glial cell can be associated with the cartridge North-East of it.

The hexagonal array is difficult to simulate directly. Instead, we will consider a visual stimulus extended uniformly in the vertical direction, allowing comparison with the horizontal marginal kernels h^{xt} found experimentally. Assuming spatial homogeneity, all units along a vertical line will be equally active. There is thus no tendency for current to flow vertically in the lamina, across the dashed lines indicated in figure 37, and we need only consider a horizontal strip of the array. Due to the translational and mirror symmetry in the vertical direction the array could be considered cut along the dashed lines and joined at the edges, to give a cylindrical topology. Along the strip cartridges and glial cells are indexed in positive and negative directions.

In the presence of illumination at the mean intensity I_0 voltages and currents will take on steady-state values. All quantities represented will represent small fluctuations about these steady-state values. For the kth unit in the one dimensional array, the following four voltages are defined:

R_k, receptor intracellular voltage.

E_k, extracellular voltage in lamina cartridge.

$M_k = R_k - E_k$, retina terminal membrane potential.

G_k, epithelial glial cell intracellular voltage.

Voltages are relative to retina ECS, except retina terminal membrane potential, M_k. The following impedances to current flow across membranes are defined:

Z_b, from receptor body to retina ECS.

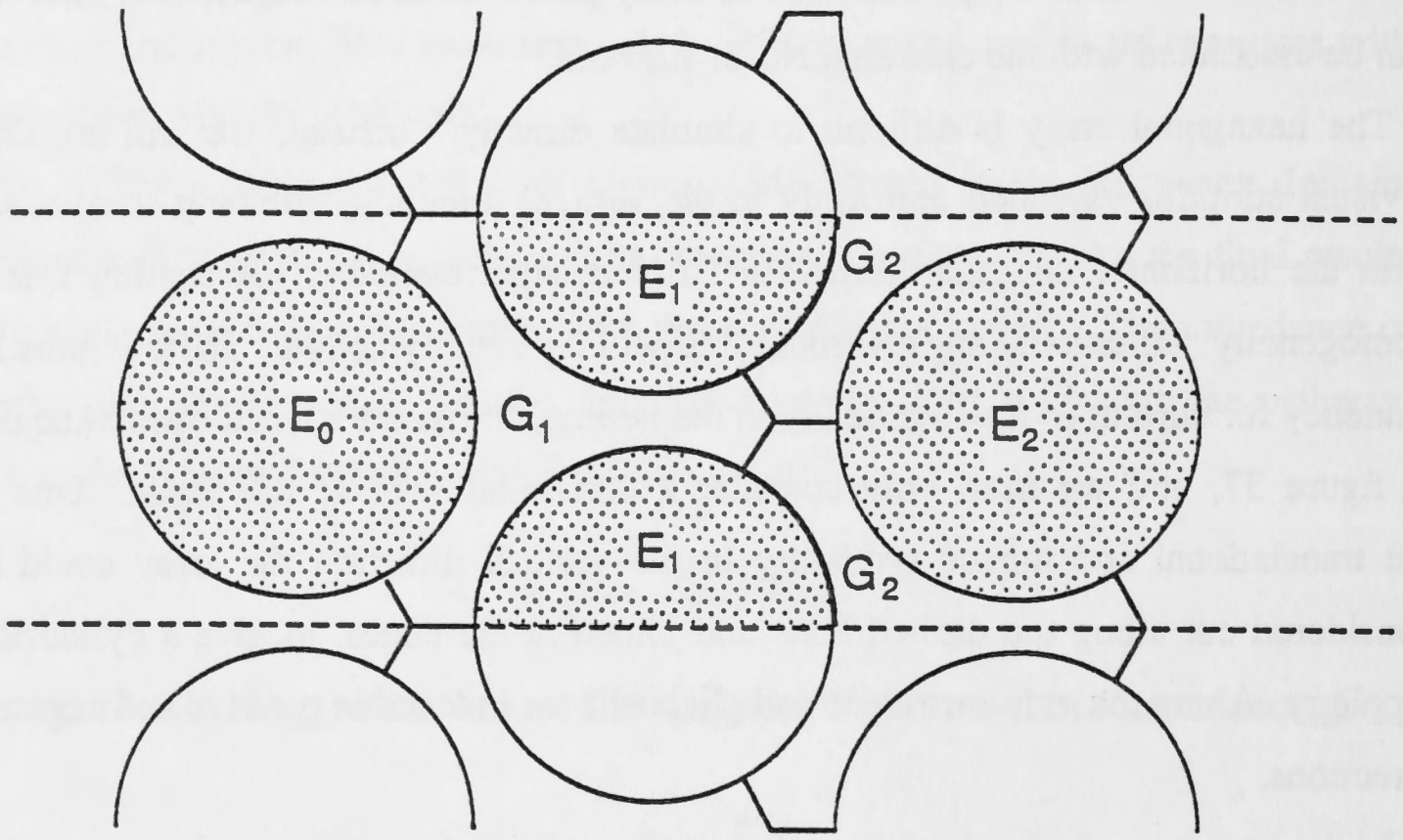

Figure 37: A schematic representation of the hexagonal arrangement of lamina cartridges, E_k, and epithelial glial cells, G_k, in the fly lamina. The figure is adapted from the figure of Shaw (1984) reproduced in chapter 1 as figure 6. That figure is adapted from Boschek (1971). In copying I have rotated the array through 90° and reduced the relative volume of the glial cells. One spatial period of the array in the vertical dimension is contained between the dashed lines.

Z_t, from receptor terminal to lamina ECS.

Z_g, from lamina ECS to a glial cell, over a 120° arc, thus between points E_0 and G_1 in figure 37. From G_1 to E_1 there are two such paths, hence the impedance is $Z_g/2$.

Z_j, from glial cell to glial cell, such as G_1 to G_2. Gap junctions contribute to this pathway, which we assume to be purely resistive.

The connectivity of the circuit array is shown in figure 38 (upper). Analysis is simplified by performing a 'delta–star' transformation, whereby each delta shaped section such as $E_1G_1G_2$ is replaced by an equivalent star network, having at its centre a virtual point Y_k. The equivalent array is displayed in figure 38 (lower). The impedance from E_k to Y_k is

$$Z_{EY} = Z_g^2/(3Z_g + 2Z_j)$$

and the lateral impedance, Z_l, between Y_k and Y_{k+1} is given by:

$$Z_l = \frac{3}{2}Z_gZ_j/(\frac{3}{2}Z_g + Z_j)$$

The model circuit is now fully defined, and a solution can be sought, giving the required relationships between the voltages. We will be seeking the receptor terminal membrane voltages, M_k, in terms of the receptor intracellular voltages, R_k, for which we have data.

3.6.2 Solution of the circuit

As with most linear electrical circuits there are many ways to find an analytical solution, and the main problem is in choosing which to use. Most electronics textbooks suggest defining variables for all quantities, and solving the myriad resulting equations. I have found the following methodology to be effective and simpler: to reduce the number of variables defined we will avoid explicitly representing currents at any stage, and deal only with voltages and impedances.

Three rules are then required for solving the circuit.

1. Impedances in series add.

2. Impedances in parallel are combined with the 'parallel' operation:

$$Z_a \| Z_b = (Z_a^{-1} + Z_b^{-1})^{-1}$$

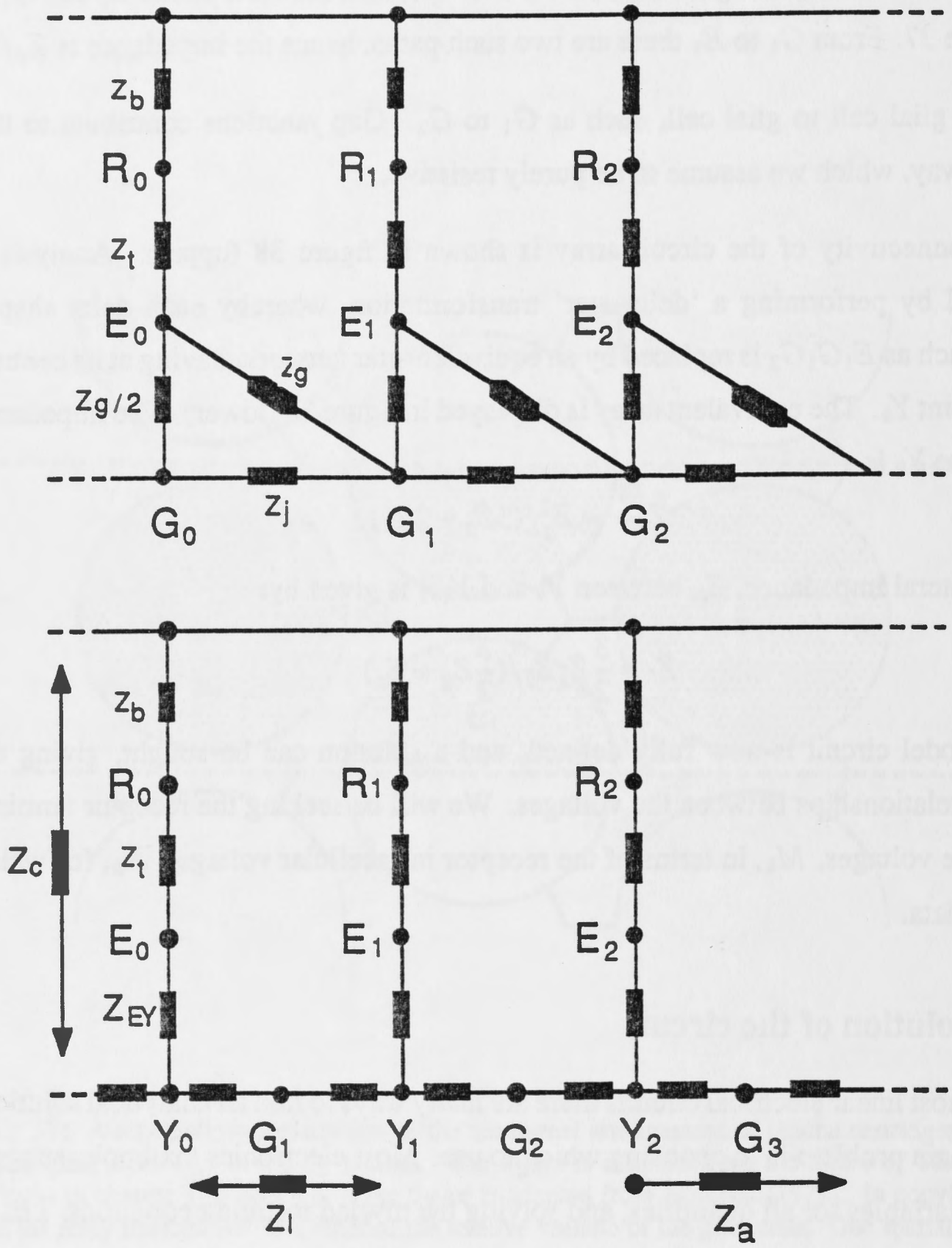

Figure 38: Model electrical circuits of the one dimensional lamina array. Along the top is the retina ECS. The points R, E,G and Y are as defined in text. The thick black elements represent impedances, also defined in text. The array extends to the left, with negative indices. **Upper**, reflecting directly the connectivity apparent in the schematic in figure 37. **Lower**, after replacing the delta shaped circuits above with equivalent star networks, introducing the virtual points Y_k.

3. In a series circuit, voltage divides in proportion to impedance.

The circuit has lateral impedance Z_l between cartridges. Let Z_c be the centrifugal impedance, from the virtual point Y back to ground in the retina ECS, within one facet unit:

$$Z_c = Z_b + Z_t + Z_{EY}$$

It can be noted parenthetically that this circuit is the discrete analog of the cable equation (Jack *et al* 1975), in which the axial resistance corresponds to Z_l and the membrane impedance corresponds to Z_c. In the limit as Z_l tends to zero but the product $Z_l Z_c$ remains finite, our circuit becomes that of a leaky cable.

The circuit array has translational symmetry. Let Z_a be the impedance of one arm of the array, that is, the impedance of the path from any point Y_k back to the retina ECS through the facet units to the right of unit k. Since this is the same for k and $k+1$, the following holds:

$$Z_a = Z_l + (Z_a \| Z_c)$$

This is a quadratic equation with the solution

$$Z_a = Z_l/2 + \sqrt{(Z_l/2)^2 + Z_c Z_l}$$

The impedance from the point Y_0 back through the two arms on either side is then $Z_a/2$. Note again the correspondence with the continuous-space case: in the limit as Z_l tends to zero, the impedance of the arm becomes $Z_a = \sqrt{Z_c Z_l}$, as in the leaky cable.

Now consider the voltages. Assume first that only the central receptor, indexed by zero, is stimulated. Stimulation of the receptor is equivalent to the injection of a current at the point R_0 from the retina ECS, which we term the photocurrent. The response in this receptor, R_0, we assume to be according to the measured receptor kernels, which we model by the double log-normal time course and a Gaussian spatial sensitivity. The photocurrent flows from this point back to the retina ECS through the receptor body, or around a return path comprising the points E_0, Y_0 and the two arms of the circuit. The voltage divides in proportion to impedance, hence the membrane voltage across the terminal of the stimulated receptor is

$$M_0 = R_0 \frac{Z_t}{Z_t + Z_{EY} + Z_a/2}$$

and the voltage at the point Y_0 is:

$$Y_0 = R_0 \frac{Z_a/2}{Z_t + Z_{EY} + Z_a/2}$$

From a point Y_k, $k > 0$, consider current flowing to the retina ECS through the arm to the right of unit k. The voltage Y_k will divide such that the potential drop between Y_k and Y_{k+1} is

$$Y_k - Y_{K+1} = Y_k \frac{Z_l}{Z_a}$$

so that the voltage at Y_{K+1} is:

$$Y_{k+1} = Y_k(1 - Z_l/Z_a)$$

The voltages at the Y points along the array thus fall off according to a geometric series. To the left of the stimulated receptor the voltages similarly decay geometrically, so that in general:

$$Y_k = Y_0(1 - Z_l/Z_a)^{|k|}$$

In each unit this voltage divides along the centrifugal path, so that the voltage across the receptor terminal membrane, M_k, for $K \neq 0$ is

$$M_k = -Y_k \frac{Z_t}{Z_c}$$

with the negation to give the correct sign, so that $M_k = R_k - E_k$.

These equations allow the model receptor terminal membrane voltage to be calculated across the entire array, given the response of the stimulated receptor. Conversely, when the entire array is stimulated, the model receptor terminal membrane voltage of a given unit can be calculated by superposition of components from each stimulated unit, due to the linearity of the model.

Transmission from the receptor membrane potential to the LMC is high-bandwidth relative to the receptor signal, with a gain of around six (Laughlin *et al* 1987). For small amplitude signals we can assume that the map $M \rightarrow L$ is a static, linear mapping involving multiplication by -6. Combining the model receptor response, the mapping from receptor potentials R_k to the receptor terminal membrane potential M_0 and the static transmission to the LMC produces a model spatiotemporal marginal kernel, h^{xt}, for the LMC.

3.6.3 Simulation results

The system was simulated with various values of parameters, while comparing the resulting model LMC kernel with observed LMC horizontal marginal kernels. To

simplify the exploration of the parameter space, as many parameters as possible were set to values derived from published data, as given in the caption of figure 39. A common value of the half-width of receptor angular sensitivity, $\Delta\rho$, was used in the three illustrated fits. The following four nonlinear parameters were allowed to vary while a least-squares fit to the observed LMC kernel was sought: the peak-time of the receptor response, the resistivities of the receptor terminal and glial cell and the resistance between glial cell through gap junctions. The amplitude of the receptor kernel is a linear parameter which was estimated by linear regression for each choice of the nonlinear parameters.

This nonlinear optimisation was performed using the Nelder-Meade algorithm (Press *et al* 1988, p305). This is a slow algorithm which does not use derivatives, however it is useful to watch the evolution of the fit as the parameter space is searched, giving an insight into the effect of the various parameters on the simulated behaviour. The algorithm was stopped when a reasonable fit was obtained with realistic values of the parameters. Note that it is not proposed that the model describes precisely all the processes at work, hence what is of interest is to see if the simulation can provide a fit with realistic parameter values, rather than to find the optimum values.

Figure 39 shows the fit obtained to an LMC exhibiting wide antagonistic flanks. The simulation produces a kernel with three parts, the negative primary, an antagonistic part on-axis and a pair of lateral antagonistic flanks. These parts are produced by wide ranges of parameter values; the main effects of the parameters are as follows. The peak-time, t_{p1}, and half-width, $\Delta\rho$, of the receptor kernel determine the negative primary part of the model LMC kernel. The antagonistic part on-axis is produced mainly by the discharge of the glial capacitances back through the central receptor. The time course of this discharge depends on the glial capacitance and the resistance of receptor terminal and body. The amplitude of this antagonistic part is reduced if glial cell resistance is reduced, so that photocurrent leaks through the glial cell membrane rather than charging the membrane. The lateral flanks become broader and smaller if the gap junction resistance is reduced, causing current to flow further laterally before passing back to the retina.

The model has enough range to fit the on-axis time course well, but has two restrictions. Firstly, the on-axis antagonistic part always has the same width as the negative primary, whereas we have seen that lateral antagonism is in many cells a

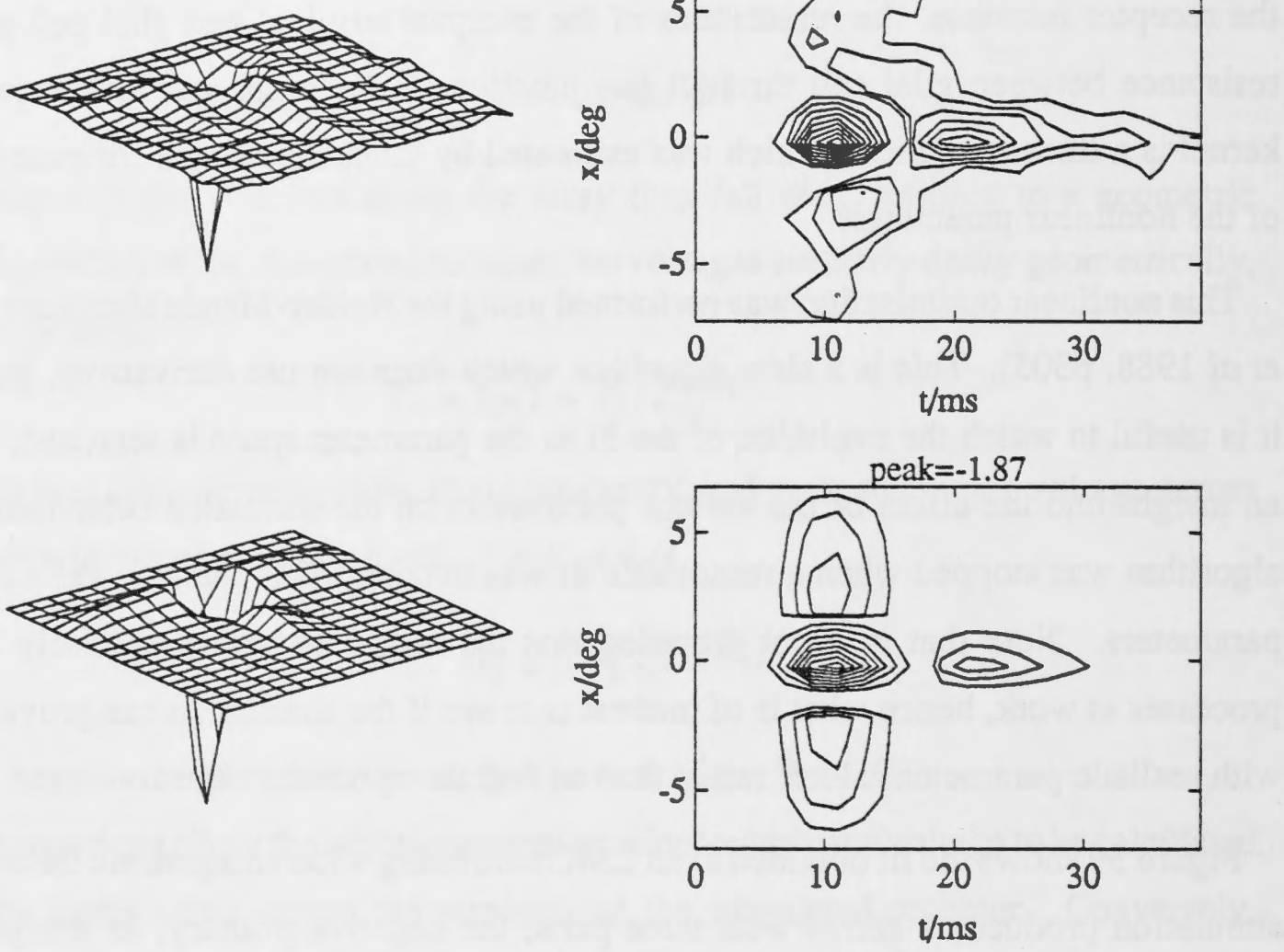

Figure 39: Fit of the model described to the horizontal marginal kernel of a *Calliphora* LMC (cwkc). **Upper**, the observed kernel in perspective and contour plot as in figure 27; contour step size is 10% of peak for negative range and 2% of peak for positive range, zero contour excluded. **Lower**, the least-squares fit found, with the same contour values as above. The RMS error of fit was 2.6% of the peak value.

The following parameters were fixed. From van Hateren (1986): receptor body length 250 μm, diameter 5 μm, microvilli contribute 40 μm^2 to membrane area per μm of receptor body length, membrane capacitance of receptor $1 \mu F/cm^2$, this figure also used for all other membranes. Derived from Strausfeld (1971): length of lamina cartridge 50 μm, diameter of receptor terminals 2 μm, diameter of cartridge 8 μm. The area of membrane between one glial cell and one cartridge ECS is taken as a third of a cylinder of this diameter. This may underestimate the capacitance of this path as any invaginations are ignored. From Hardie (1985): interommatidial angle, $\Delta\phi$ = .6° (in frontal region), receptor body membrane resistivity R_b = .03 ΩM^2, this is the figure .3 ΩM^2 divided by 10 to allow for light adaptation.

The following parameters were produced while running the optimization procedure: t_{p1} = 11.4 ms, $\Delta\rho$ = 1.47°, resistivities in ΩM^2 R_t = .011, R_g = .05, resistance between glial cells .46 $M\Omega$.

broadening of the width of this part. Second, the lateral parts are at the same latency as the negative primary, whereas when found in observed kernels the lateral flanks are always delayed, by an amount between 1 ms and 5 ms.

In order to delay the lateral flanks another element was added to the model circuit, representing a direct return path from the lamina ECS to the retina ECS. If this path has capacitance, delay can be produced, as the laterally flowing photocurrent is initially shunted through the capacitance and then later flows through the surround receptors. The modified circuit is easily solved by following the methodology above. This modification is an *ad hoc* addition to the model, and large values of capacitance were required to delay the antagonism sufficiently. The value was set at 100 pF for the fits illustrated, comparable with the receptor body capacitance, 140 pF. This value may be unreasonable; we conclude merely that some mechanism beyond the basic model is required to produce the delay observed in lateral antagonism. A fit obtained with this model is shown in figure 40.

Modifications of this model thus seem to be able to produce a wide range of behaviour, corresponding to many properties seen in the LMC response. Adaptation of properties with level of illumination can also be produced with the model. Presumably membrane areas and capacitances remain constant, but the resistivities of the elements could all conceivably adapt, under the control of the neural mechanisms known to exist in the lamina. Figure 41 shows the fit to a kernel from the same cell as previously, at the lower light level. Besides the increase in peak-time, the changes required are increases in the resistance of the glial cell membrane and in the resistance between glial cells.

Further evaluation of models such as this would be possible given more data on the resistances and time constants of the units present, and their variation with intensity of illumination. It is interesting to see that both lateral antagonism and temporal high-pass filtering can be produced by a model circuit involving extracellular potential, when capacitances are included. Thus it is conceivable that the basic mechanisms of antagonism lie in the passive electrical properties of the neuronal-glial network, while the other cell classes of the lamina may contribute additional synaptic effects to produce the overall observed behaviour.

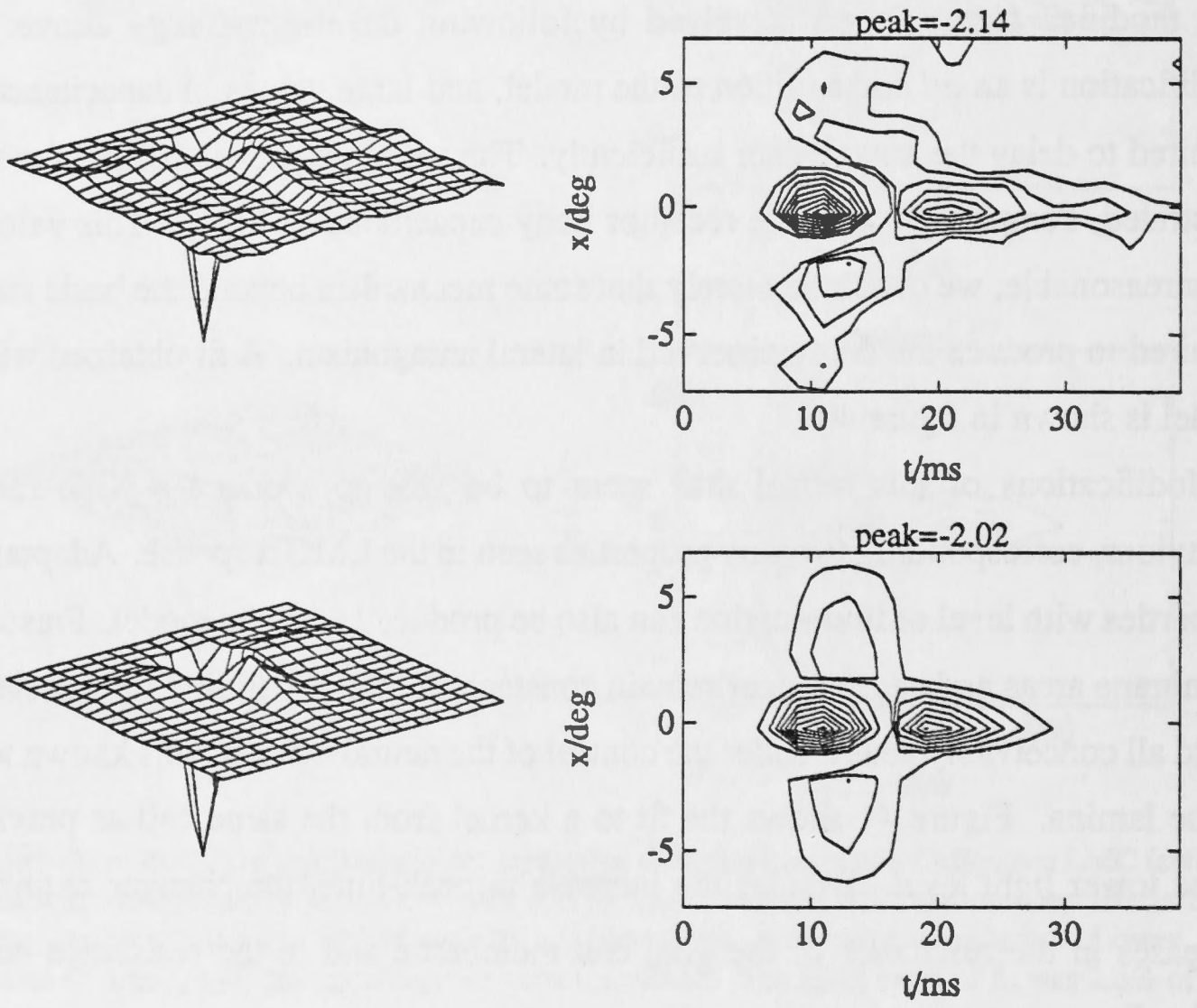

Figure 40: Fit of modified model to the horizontal marginal kernel of the same *Calliphora* LMC as previously, at high illumination (cwkc). The circuit is modified by the addition of a capacitive pathway from each lamina ECS, E_k, to the retina ECS (ground) with capacitance $100\,pF$. Plots and fixed parameters are as in figure 39. RMS error of fit is 1.5% of peak value. Half-width is held at the previous value, $\Delta\rho$ = 1.47°. Other parameters are: t_{p1} = $11.3\,ms$, resistivities in ΩM^2 R_i = .010, R_g = .046, resistance between glial cells .47 $M\Omega$.

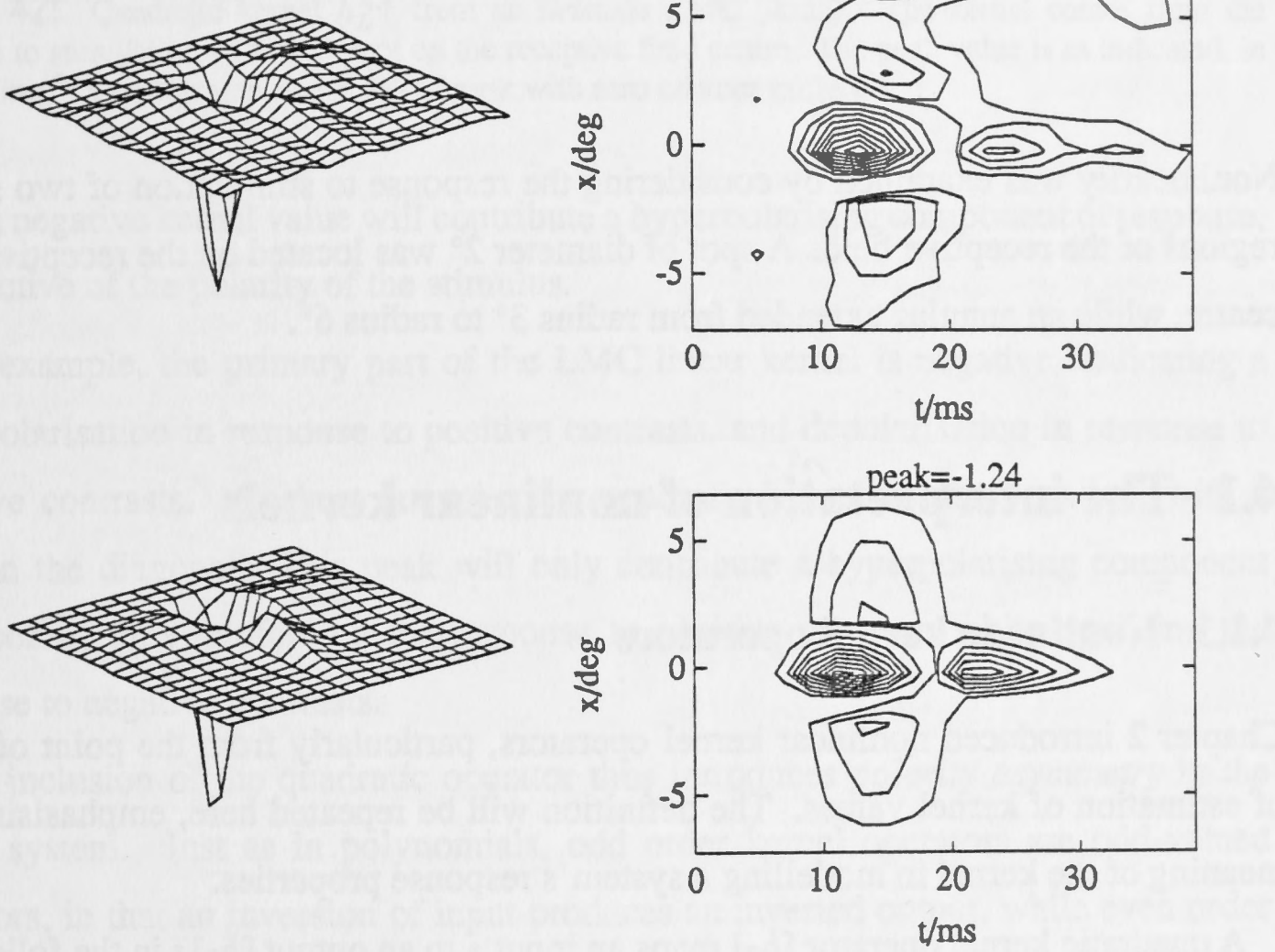

Figure 41: Fit of modified model to the horizontal marginal kernel of the *Calliphora* LMC of figure 40 at low illumination (cwgc6). Plots and fixed parameters are as in figure 39. RMS error of fit is 3.5% of peak value.
Half-width, $\Delta\rho$ = 1.47°, is held constant from previous fits. Other parameters are: t_{p1} = 15.8 ms, resistivities in ΩM^2 R_t = .013, R_g = .10, resistance between glial cells 1.2 $M\Omega$.

Chapter 4

Nonlinear Components of Response

Nonlinearity was examined by considering the response to stimulation of two spatial regions of the receptive field. A spot of diameter 2° was located on the receptive field centre, while an annulus extended from radius 3° to radius 6°.

4.1 The interpretation of nonlinear kernels

4.1.1 Nonlinear kernel operators

Chapter 2 introduced nonlinear kernel operators, particularly from the point of view of estimation of kernel values. The definition will be repeated here, emphasising the meaning of the kernel in modelling a system's response properties.

A quadratic kernel operator $[h_2]$ maps an input s to an output $[h_2]s$ in the following way,

$$[h_2]s(t) = \int_0^m \int_0^m h_2(t_1, t_2)\, s(t - t_1)\, s(t - t_2)\, dt_1\, dt_2$$

where h_2 is the quadratic kernel and m is the memory length of the model. In our case the input is the contrast of a visual stimulus relative to a mean level of illumination, and the output is an intracellular response in millivolts. Figure 42 shows a sample quadratic kernel from an *Eristalis* LMC, describing response to stimulation by a 2° spot on axis. Taking one element of this integral, the output at time t is influenced by the product of the input at latencies t_1 and t_2, $s(t - t_1)s(t - t_2)$, with weighting $h_2(t_1, t_2)$. Along the diagonal $t_1 = t_2$ the product is non-negative, hence we can say that a positive kernel value will contribute a depolarising component of response,

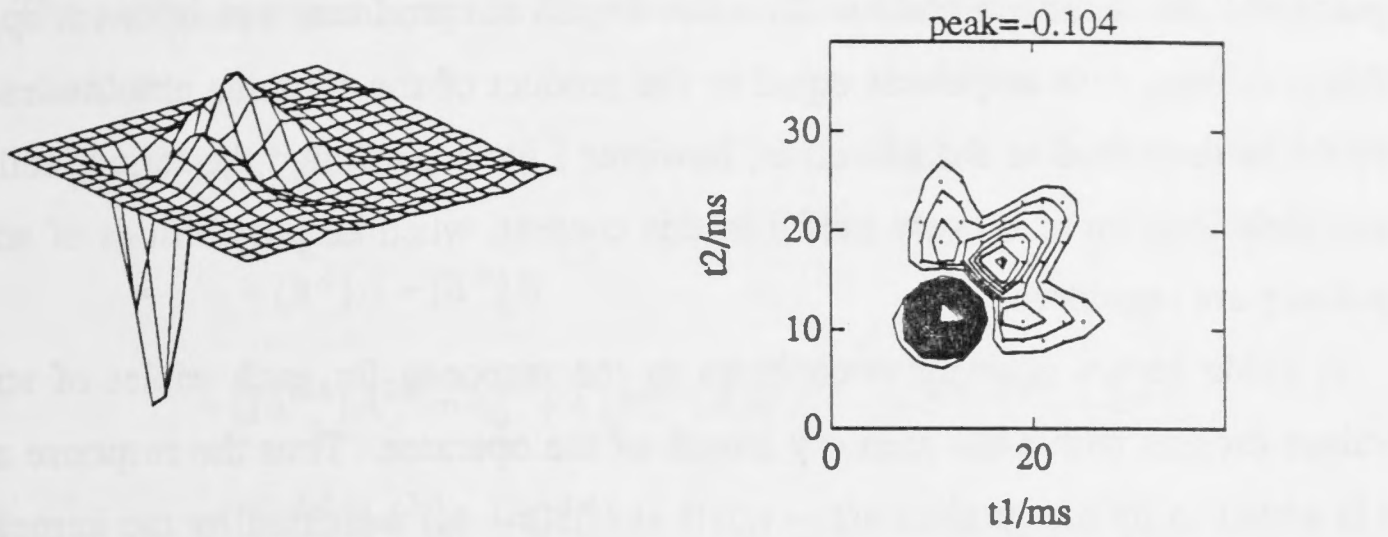

Figure 42: Quadratic kernel h_L^{AA} from an *Eristalis* LMC (lkma). The kernel comes from the response to stimulation with a 2° spot on the receptive field centre. The peak value is as indicated, in $mV/(C\,ms)^2$. Contour step size is 5% of peak with zero contour excluded.

while a negative kernel value will contribute a hyperpolarising component of response, irrespective of the polarity of the stimulus.

For example, the primary part of the LMC linear kernel is negative, indicating a hyperpolarisation in response to positive contrasts, and depolarisation in response to negative contrasts. At short latencies the quadratic kernel is also negative, with a peak on the diagonal. This peak will only contribute a hyperpolarising component of response, thus reinforcing the response to positive contrast, while opposing the response to negative contrasts.

The inclusion of the quadratic operator thus introduces *polarity asymmetry* in the model system. Just as in polynomials, odd order kernel operators are odd-valued operators, in that an inversion of input produces an inverted output, while even order kernel operators are even-valued mappings. The linear Wiener kernel provides the best linear model of the system, in the least squares sense for the white-noise input, and thus is a compromise, attempting to describe the response to positive and negative stimuli. The quadratic kernel can be studied to account for asymmetry observed in response to increment and decrement light stimuli.

Off the leading diagonal, or when the kernel combines two different channels of stimulation, the sign of the response component depends on the polarity of the two stimuli involved. The kernel in figure 42 has positive parts parallel to the axes, where one latency equals the peak-time, around $10\,ms$, extending from $16\,ms$ to $28\,ms$ in the other dimension. A pulse of light at time $t - 10\,ms$ generates a hyperpolarisation in the LMC at time t. The presence of the positive region just mentioned means that a

pulse of light in the interval $t - 28\,ms$ to $t - 16\,ms$ produces a component opposing this response, with amplitude equal to the product of the stimulus amplitudes. This could be described as defacilitation, however I have not found the terms facilitation and defacilitation to be very useful in this context, when all possibilities of stimulus polarity are considered.

A cubic kernel operator contributes to the response for each triplet of stimulus values present within the memory length of the operator. Thus the response at time t is added to by the product $s(t - t_1)s(t - t_2)s(t - t_3)$ weighted by the kernel value $h_3(t_1, t_2, t_3)$. Integrating over the three dimensional domain of latencies, this produces the following:

$$[h_3]s(t) = \int_0^m \int_0^m \int_0^m h_3(t_1, t_2, t_3)\, s(t - t_1)\, s(t - t_2)\, s(t - t_3)\, dt_1\, dt_2\, dt_3$$

We now review the more compact notation developed in chapter 2, which will allow fluency in dealing with networks of operators. The output of the quadratic kernel operator is a bilinear function of the input s, or, equivalently, a linear function of the tensor product $s \otimes s$. This tensor product is denoted by tensor exponentiation as $s^{2\otimes}$. The output over time is the leading diagonal of the two-dimensional convolution of the kernel with this tensor product.

It is useful to be able to associate a kernel, h_n for example, with the operator involving that kernel, hence we denote that operator in square brackets as $[h_n]$. The input to such an operator is a function of n variables, produced by the tensor product of n input signals, or a single input raised to the tensor power n. The tensor exponentiation can be left implicit, thus $[h_n]s$ and $[h_n]s^{n\otimes}$ are equivalent. This notation can equally represent continuous-time or discrete-time systems, depending on the context.

Where a network of operators between quantities is considered, an operator has its inputs denoted by superscripting and its output denoted by subscripting. A network may indicate a number of operators having outputs summed to give a quantity. Kernels describing mappings are similarly denoted, with the degree of the kernel denoted by repetition of the input superscripts, or occasionally by the presence of a subscript index. This leads to somewhat elaborate looking equations, but it does generate a systematic notation, rather than requiring the introduction of large numbers of arbitrary identifiers.

The kernel operator model describing the response to the spot-annulus stimulus is as follows. The spot channel of the stimulus is denoted by A and the annulus channel

by B. The model contains terms to degree two in channels A and B and to degree three in A alone:

$$\begin{aligned} r &= F(A,B) \\ &= h_0 + [h^A]A + [h^B]B \\ &\quad + ([h^{AA}]A^{2\otimes} + h_0^{AA}) + [h^{AB}]A \otimes B + ([h^{BB}]B^{2\otimes} + h_0^{BB}) \\ &\quad + ([h^{AAA}]A^{3\otimes} + [h_1^{AAA}]A) \end{aligned}$$

The kernels h_0^{AA} and h_0^{BB} are the zero degree kernels associated with h^{AA} and h^{BB} respectively, and h_1^{AAA} is the linear kernel associated with h^{AAA}. These terms achieve the orthogonalisation of the series with respect to the binary white-noise input, as derived in section 2.3.3. Briefly, the orthogonalisation cancels the contribution of all elements of the kernels having a repeated index, when the stimulus consists of values ± 1 only.

4.1.2 Kernels parts and components

A distinction will be made between the parts of a kernel and the components of a kernel. The *parts* of a kernel will mean the kernel on non-overlapping regions of its domain, the parts generally being delineated by the polarity of the kernel. For example the linear LMC kernel has two parts, the primary negative part, of large amplitude and short duration, and the positive secondary part of smaller amplitude and longer duration. Parts of the quadratic kernels are defined on two dimensional regions of the domain, and so on. The parts of a kernel can be identified by direct inspection of the kernel by itself.

The *components* of a kernel, in contrast, are defined with reference to some proposed structural model of the system. The components of the structural model produce component kernels, which when added produce the overall model kernel, attempting to reconstruct the experimentally derived kernel.

A given kernel component may be largely associated with some kernel parts, but in general components will be nonzero on overlapping regions of the domain. The components are then confounded, and decomposition into components is ambiguous. One use of the nonlinear kernels is to distinguish components which are confounded in the linear kernels, as will be seen below.

4.2 The observed nonlinear kernels

4.2.1 Quadratic kernels from LMCs

Figure 43 shows a set of linear and quadratic kernels for an *Eristalis* LMC. The linear kernels have the two parts previously described, with the surround kernel h^B having relatively less amplitude in the primary part.

In the self-quadratic kernel for the centre, h^{AA}, we will distinguish four parts. The primary part is a compact negative region centred on the diagonal at latency slightly less than the primary peak of the linear kernel. There is a positive secondary part extending parallel to the axes, along a line through the primary peak. This part appears as two mirror images due to the symmetrisation. These will be called the axial extensions. A positive diagonal peak appears at a latency ahead of the positive peak of the linear kernel. Lastly we will distinguish a positive diagonal extension, at latencies beyond the positive diagonal peak.

These four parts, with varying amplitudes and timings, can describe the features of most of the observed LMC h^{AA} kernels. The other part sometimes seen is a negative tertiary part appearing on each side of the diagonal extension, as in figure 45. The greatest variability in the kernels lies in the relative amplitude of the two diagonal peaks. To give extremes, figure 46 shows a kernel with the positive diagonal peak entirely absent, while figure 47 has the positive peak larger than the negative primary peak. Note here also that when the positive peak is large, the negative tertiary parts appear clearly, along vertical and horizontal lines through the positive peak.

The quadratic cross-kernel h^{AB} in some cases has a negative primary part corresponding in latency to the negative primary part of h^{AA}, however this part is not generally the largest in amplitude and is sometimes absent. The most consistent part is a positive part at latency t_1 corresponding to the negative primary peak of h^{AA}, and t_2 corresponding to the positive diagonal peak of h^{AA}. Thus in this case the peak would give a depolarising contribution at time t in response to a pulse of stimulus in the surround at $t - 19\,ms$ followed by a pulse on centre at $t - 11\,ms$.

Other parts occur in some cross-kernels, the next most common being a negative peak located along the same off-diagonal as the positive peak, at a greater latency, such as in figure 45.

The self-quadratic kernel for the surround, h^{BB}, is very variable between cells,

and generally small in amplitude relative to the other two quadratic kernels. The most consistent feature is a positive peak, and sometimes extension, on the diagonal, corresponding in latency to the positive diagonal parts of h^{AA}. This is seen in figure 43.

The *Calliphora* quadratic kernels have the same features, with the same variability in relative peak size, as in figures 48 and figure 50.

At the lower light level, the quadratic kernels are slowed, in correspondence with the linear kernels, see figures 44 and 49. The other consistent change is the disappearance of the positive axial extensions, leaving only diagonal positive parts.

4.2.2 LMC cubic kernels

A typical LMC cubic kernel, h_L^{AAA}, is displayed as a sequence of sections in figure 53. These sections can be reassembled mentally to imagine the kernel on its three dimensional domain. To facilitate visualisation, the kernel can be considered as the three dimensional analog of the typical quadratic kernel, h_L^{AA}, but inverted in sign and slower in timing. The primary feature is a positive part on the diagonal coinciding in latency with the primary part of the linear kernel. Negative axial parts extend from the primary part parallel to each of the three time axes, at latencies corresponding to the secondary part of the linear kernel. There can be a small positive peak on the diagonal after the positive primary part, and a negative extension along the triple diagonal $t_1 = t_2 = t_3$.

Figures 43 to 52 include one dimensional sections of the cubic kernels through the primary peak parallel to the axes. The sections are shown normalised in the upper right plots allowing comparison with other kernels and sections. The close agreement with the linear kernel time-course can be seen, contrasting with the faster time-course of the quadratic kernel sections.

4.2.3 Receptor kernels

The kernels for photoreceptors are relatively simple. An example is shown in figure 51. Other cases are equivalent, with those at the lower mean light level being slowed and monophasic, in correspondence with the linear kernels. The linear kernels are slightly biphasic, with the surround kernel h_R^B having a peak corresponding to the peak of h_R^A, suggesting that the annulus in these experiments did produce a response in the

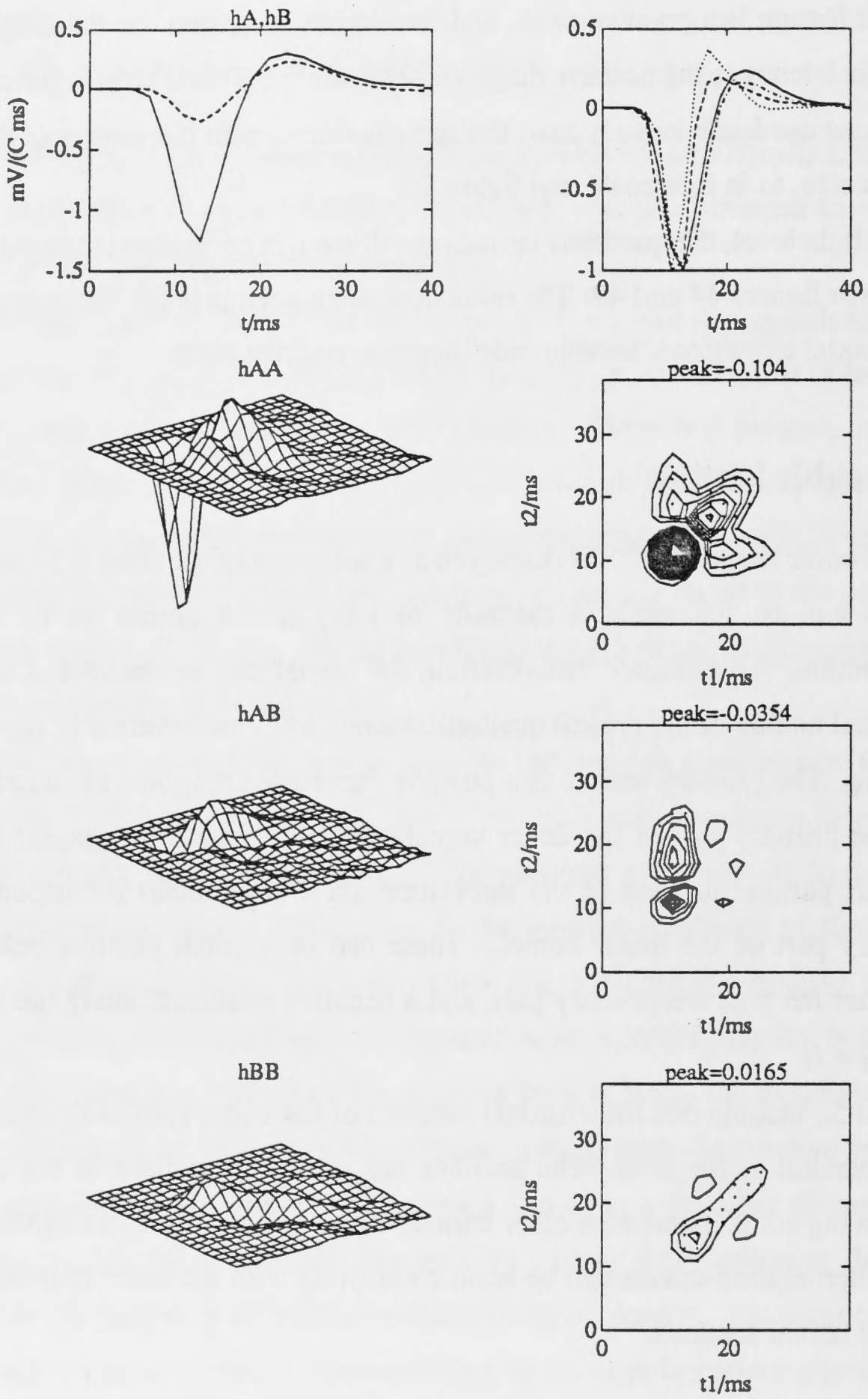

Figure 43: Linear and quadratic kernels for an *Eristalis* LMC (lkma). **Upper left**, the linear kernels for centre and surround, h^A and h^B in units $mV/(C\,ms)$. **Upper right**, normalised kernels and sections as follows: **solid line**, centre kernel h^A; **dashed line**, section through h^{AA} primary peak parallel to an axis; **dotted line**, diagonal of h^{AA}; **dot-dash**, section through h^{AAA} primary peak parallel to an axis, inverted for LMC data to allow comparison with other kernels.
Lower three, the quadratic kernels h^{AA}, h^{AB} and h^{BB}. Perspective plots are to same scale, peak values are indicated above contour plots in units $mV/(C\,ms)^2$. Contour step size is 5% of the peak over all three kernels, zero contour is excluded, dots indicate positive regions.
Note the difference in timing between linear and quadratic kernels.

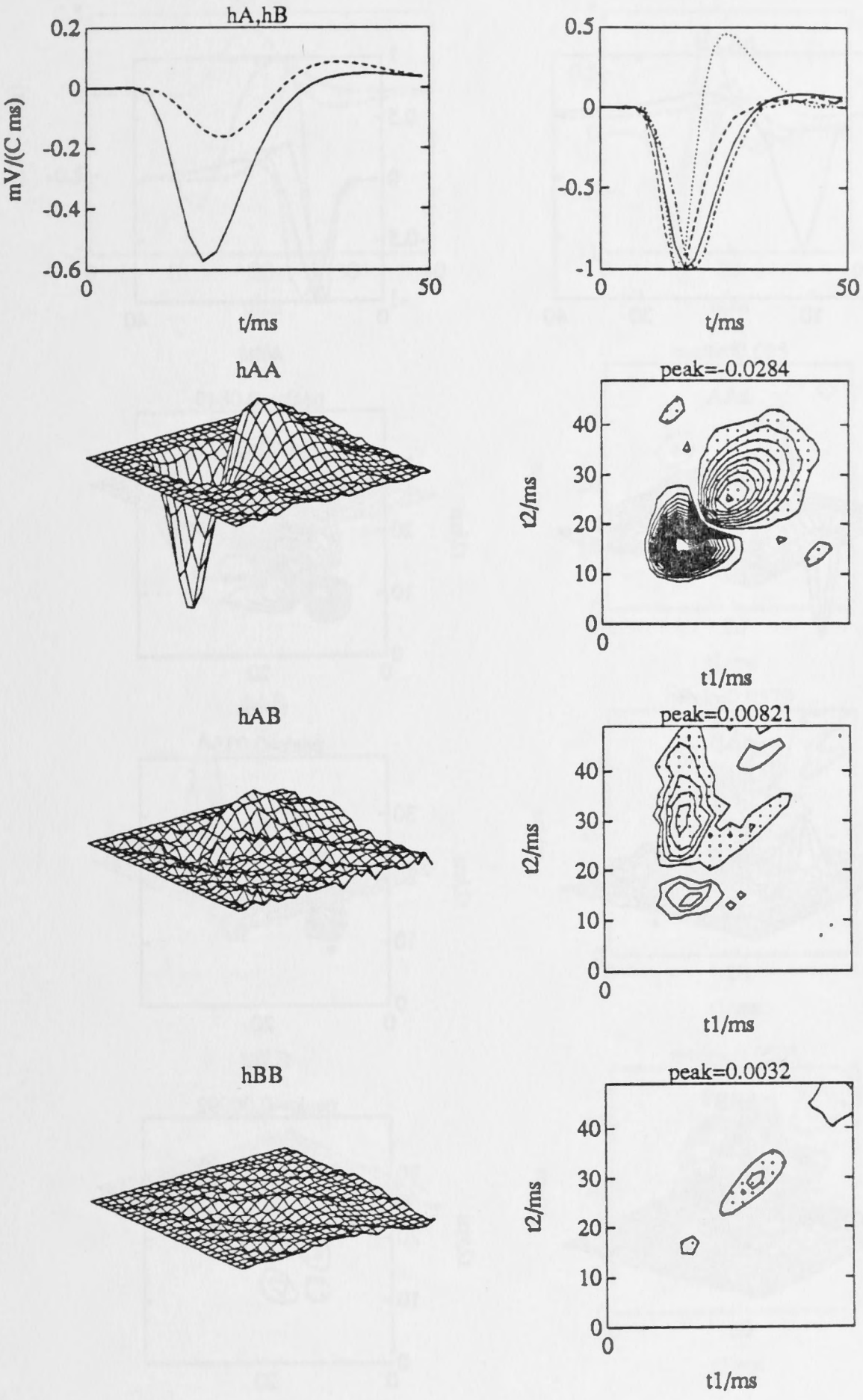

Figure 44: Linear and quadratic kernels for the same cell as previous figure, at the lower mean intensity (lkial). Plots as in figure 43. Note the longer latencies and loss of the axial secondary parts. The positive diagonal part intrudes into the negative primary part, suggesting the presence of opposing components.

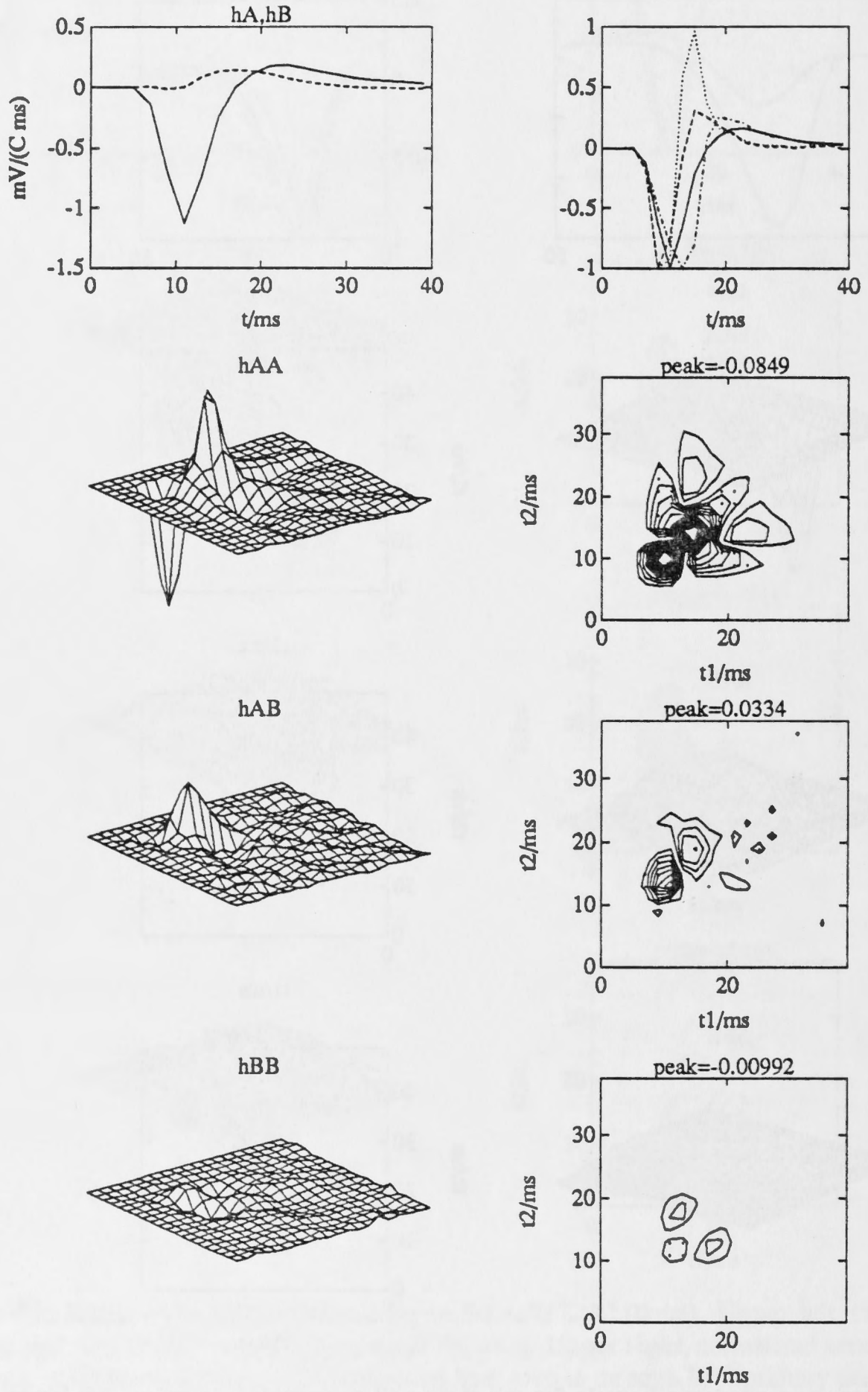

Figure 45: Linear and quadratic kernels for an *Eristalis* LMC (lnba). Plots as in figure 43. Note absence of significant negative part in surround kernel h^B, indicating low optical cross-talk.

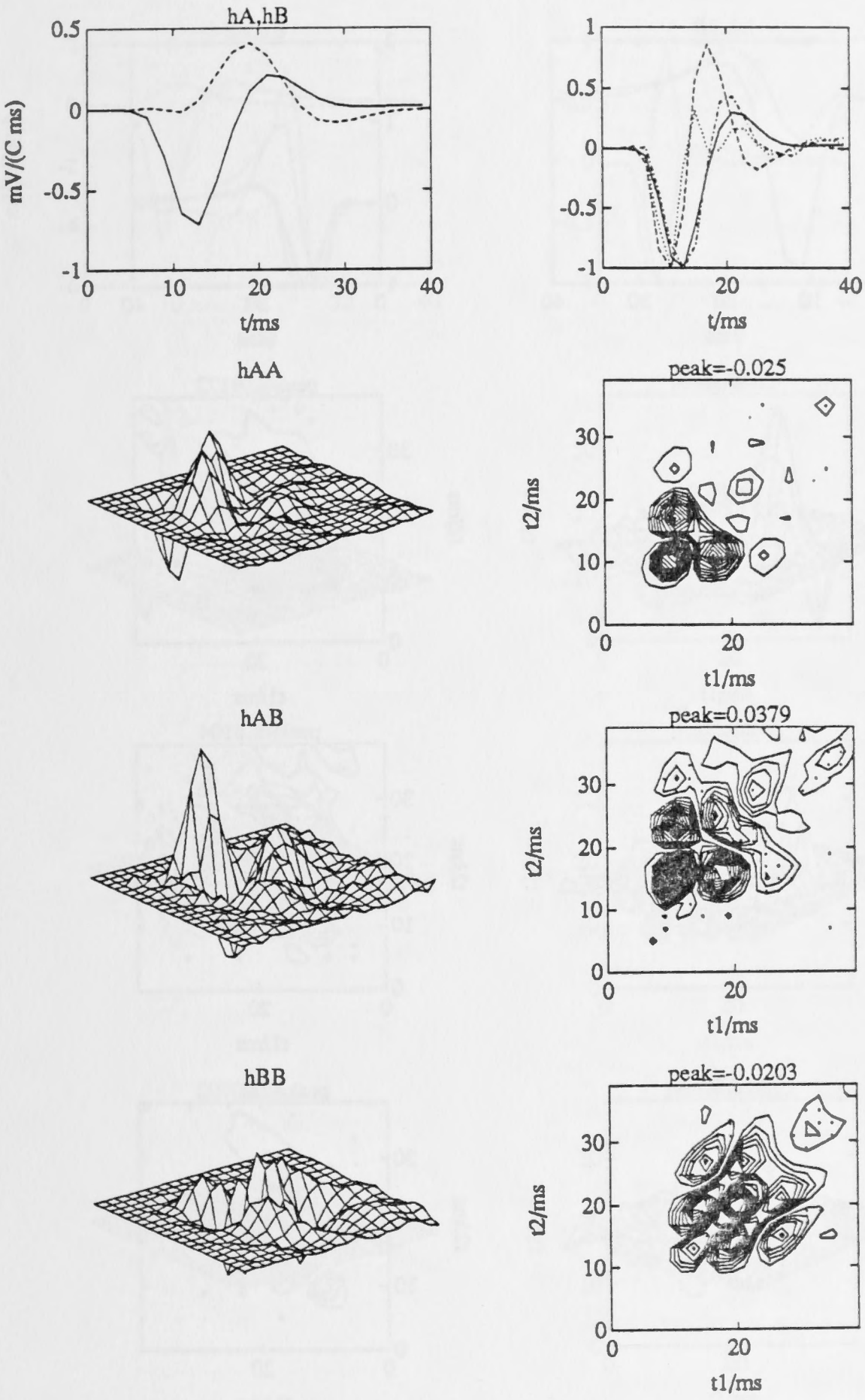

Figure 46: Linear and quadratic kernels for an *Eristalis* LMC (lpba). Plots as in figure 43. This cell has a number of distinctive features. The optical cross-talk is low, while lateral antagonism is high. The h^{AA} kernel lacks entirely the positive diagonal peak, while showing additional parts at longer latencies. The cross-kernel h^{AB} reproduces the self-kernel h^{AA} in great detail, but inverted and delayed along the t_2 axis.

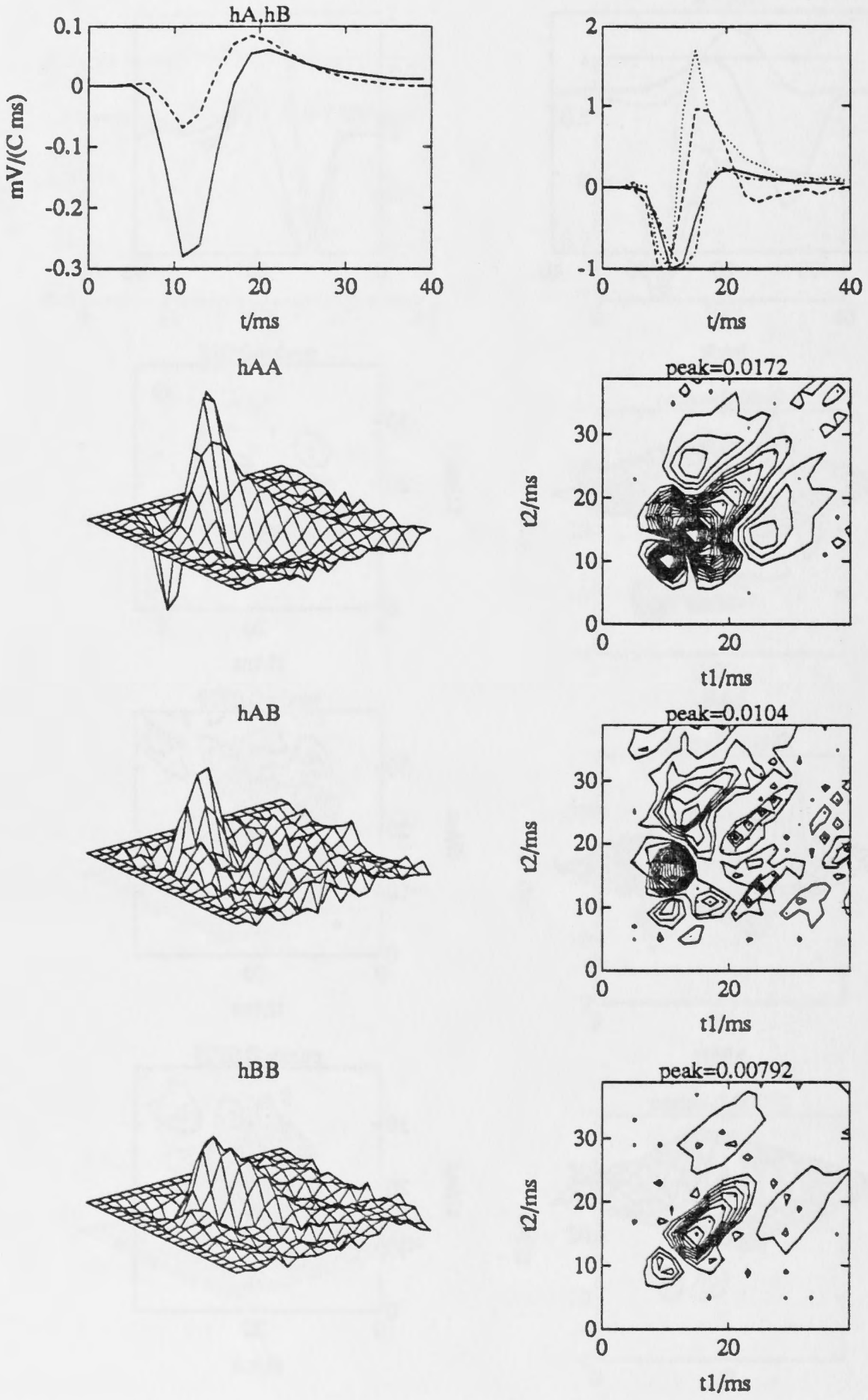

Figure 47: Linear and quadratic kernels for an *Eristalis* LMC (lsba). Plots as in figure 43. The h^{AA} kernel has a positive diagonal peak of greater amplitude than the negative primary, and has negative regions flanking the diagonal extension. The strong positive diagonal parts appear to be reproduced in the surround kernel h^{BB}.

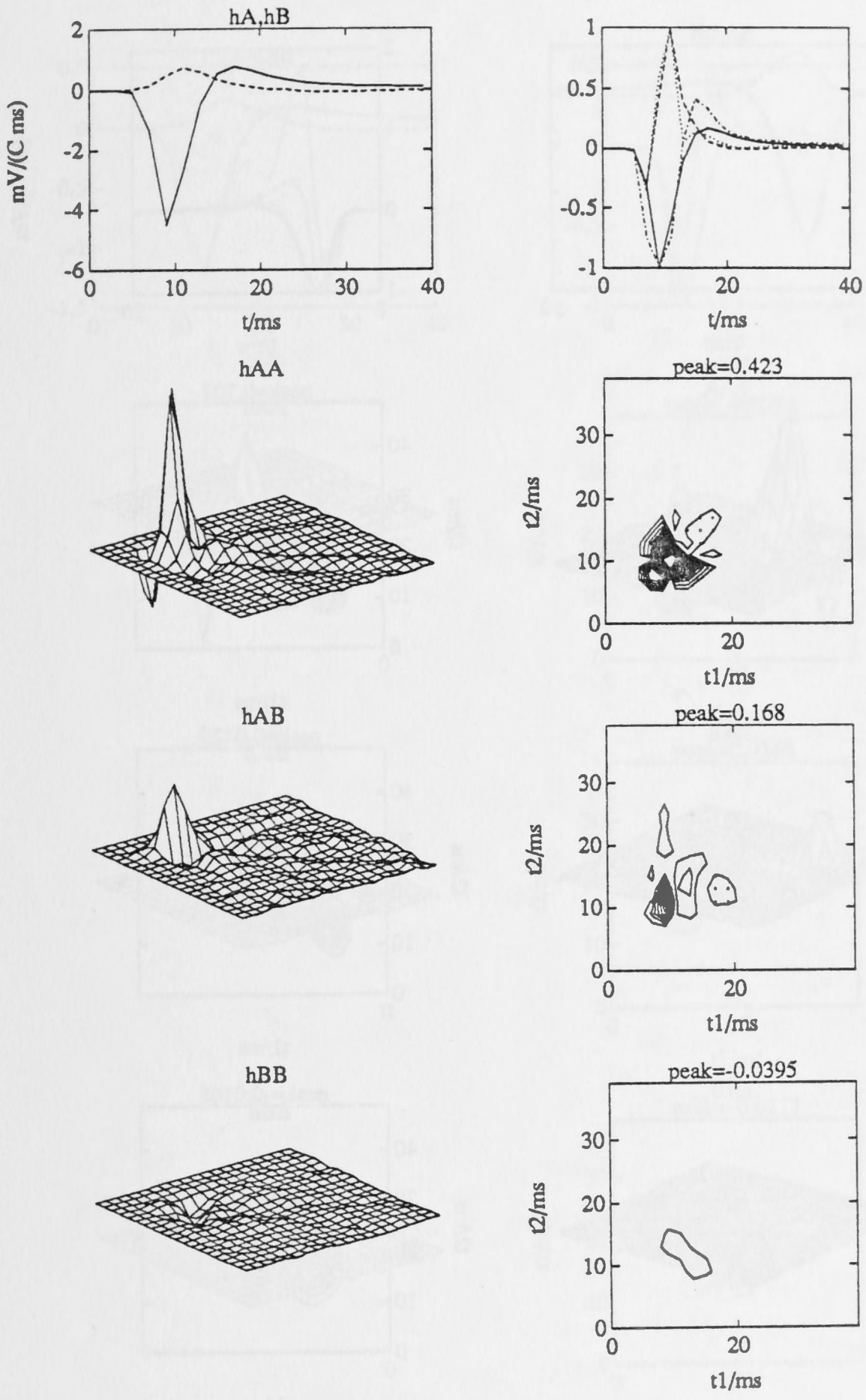

Figure 48: Linear and quadratic kernels for a *Calliphora* LMC (cwca). Plots as in figure 43. This experiment produced the largest amplitude kernels found. Optical cross-talk is low. The h^{AA} kernel has positive diagonal peak larger than negative primary. In the cross-kernel h^{AB} however the earlier part is the larger, as normal.

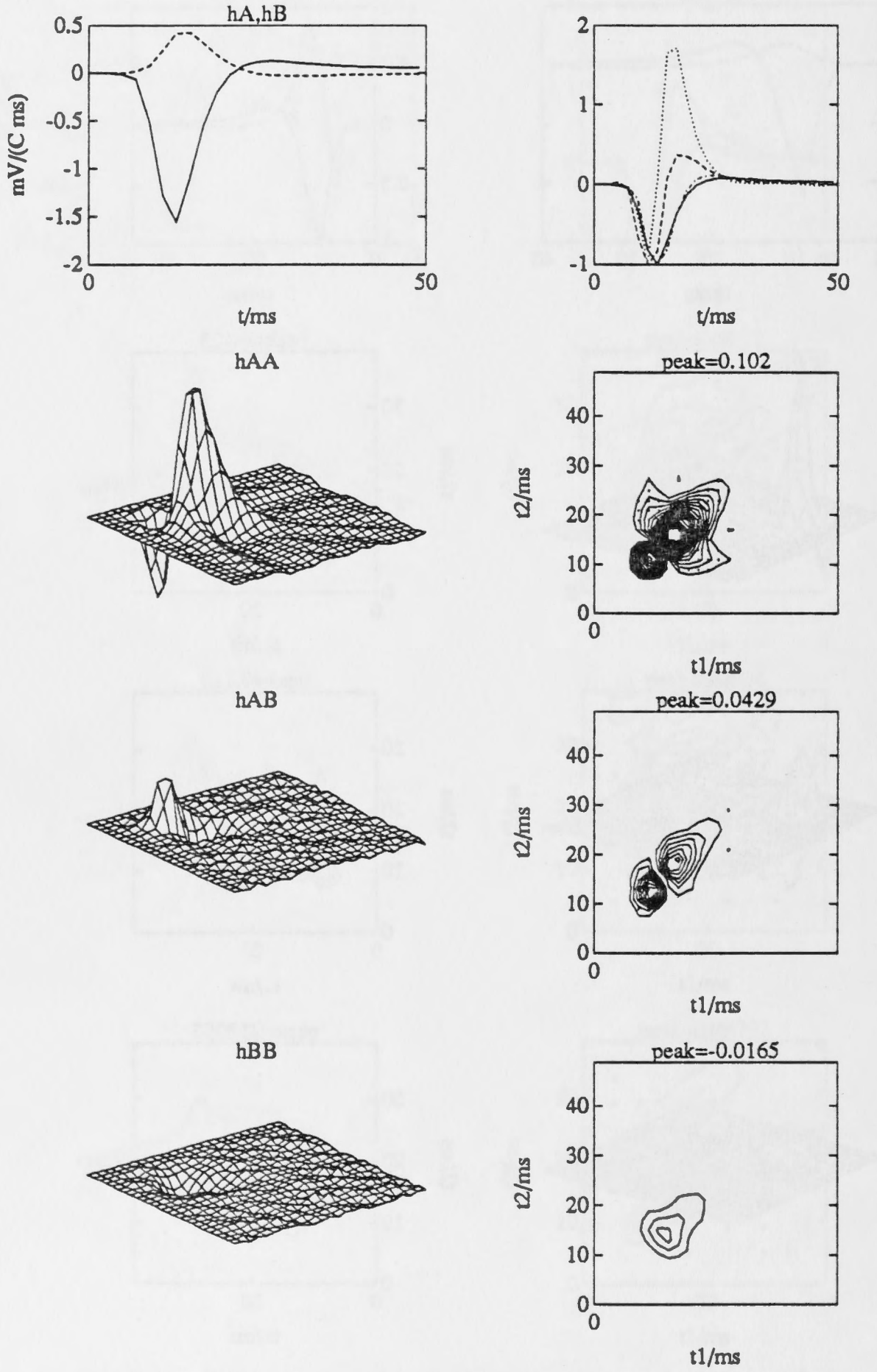

Figure 49: Linear and quadratic kernels for the same *Calliphora* LMC as previously, at the lower light level (cwjal). Plots as in figure 43. Note latency of surround effect is very close to latency at centre.

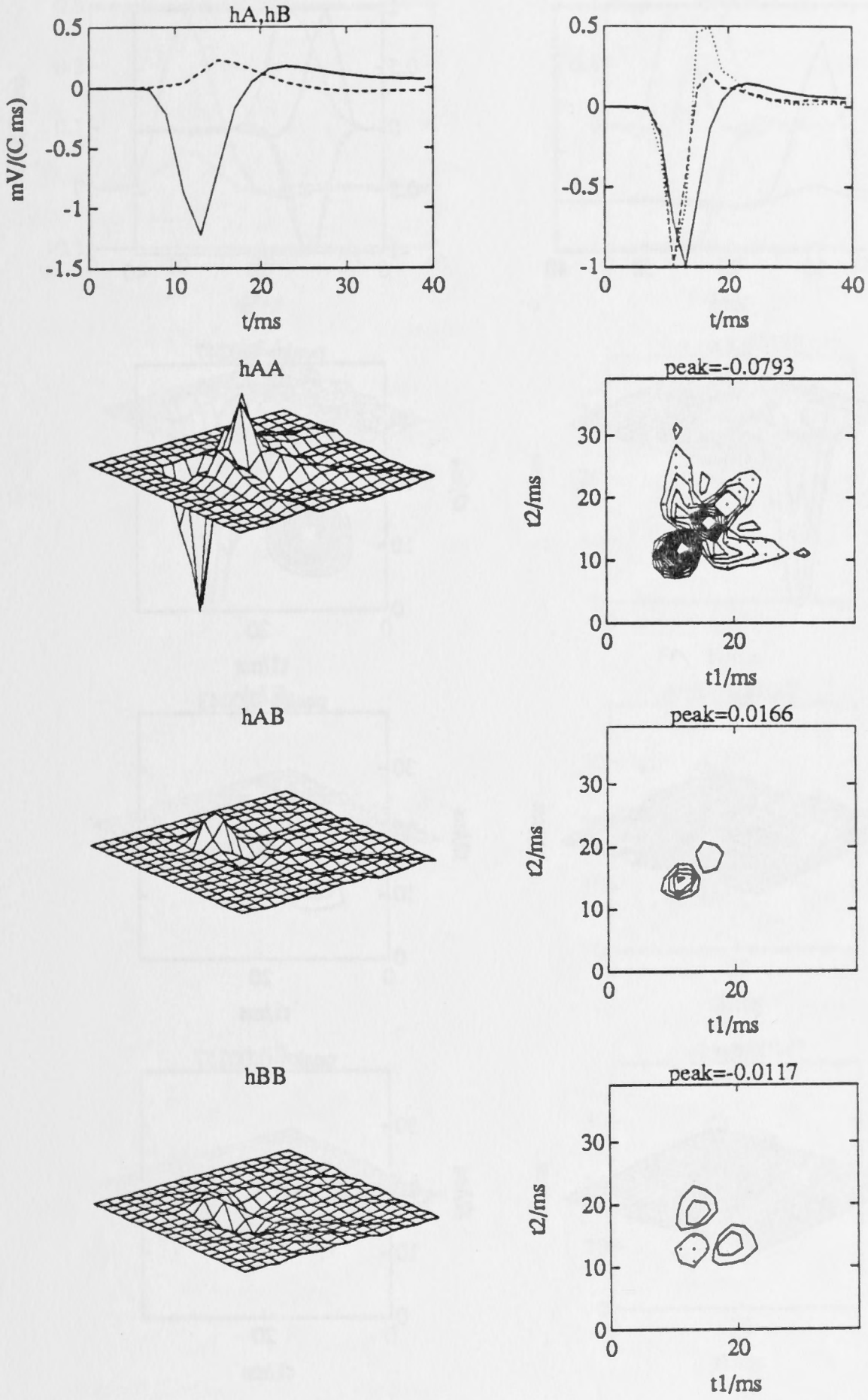

Figure 50: Linear and quadratic kernels for a *Calliphora* LMC (ceca). Plots as in figure 43. Optical cross-talk is low, positive diagonal peak of h^{AA} is smaller in amplitude than negative primary peak.

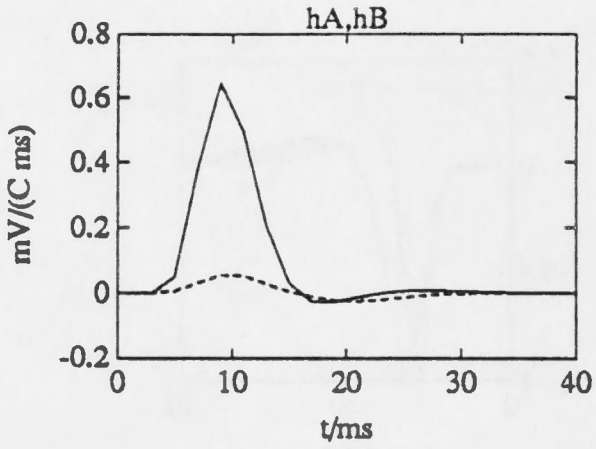

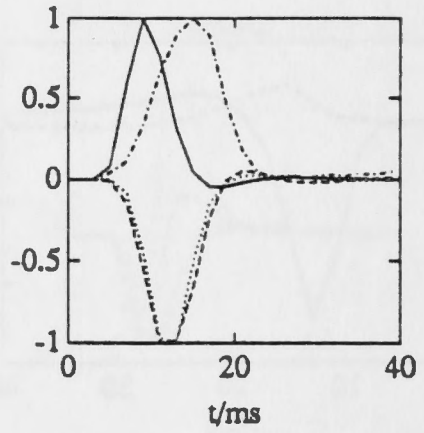

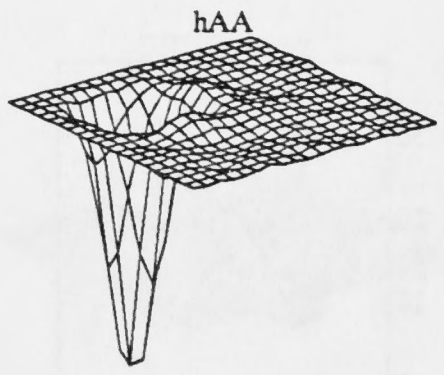

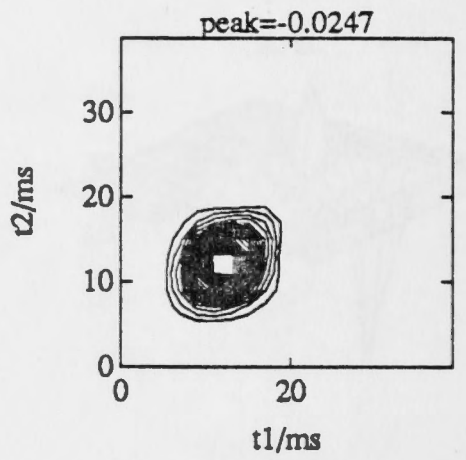

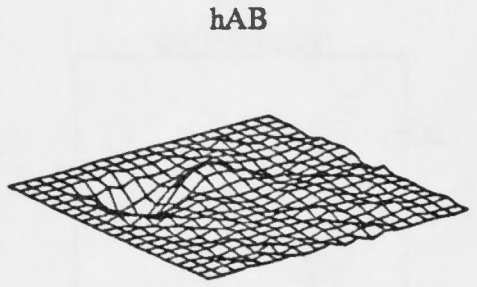

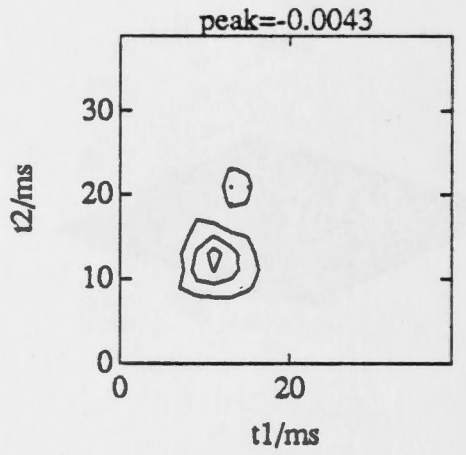

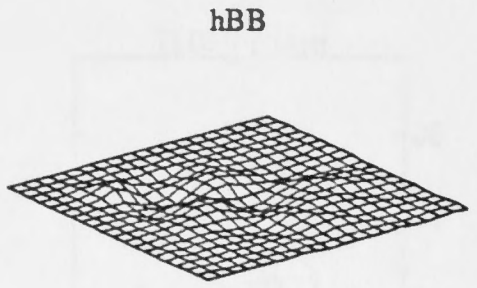

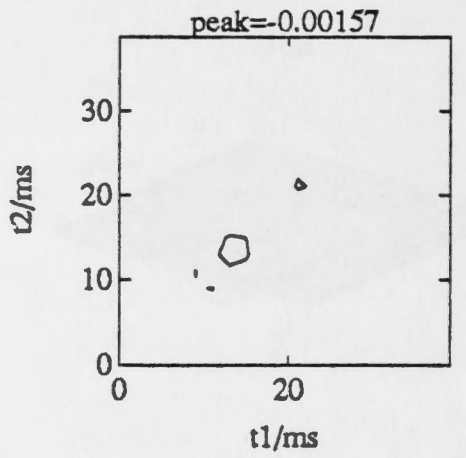

Figure 51: Linear and quadratic kernels of an *Eristalis* photoreceptor (rqba). Plots as in figure 43, but section of h^{AAA} in upper right is not inverted. Note presence of a small optical cross-talk, and some lack of space-time inseparability. The kernel h^{AA} is close to a tensor product, $-p^{2\otimes}$.

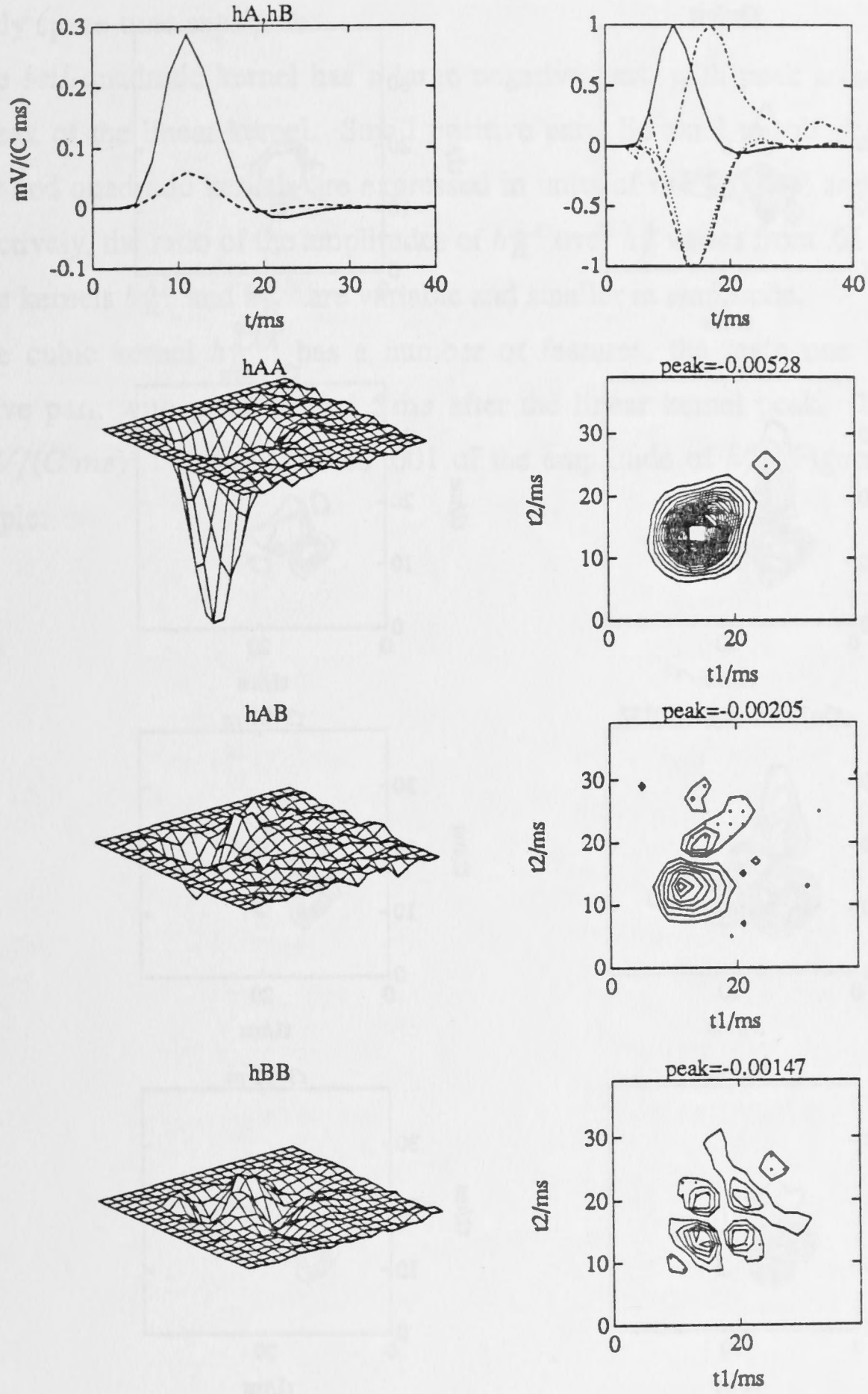

Figure 52: Linear and quadratic kernels of an *Eristalis* photoreceptor (rlca). Plots as in figure 43, but section of h^{AAA} in upper right is not inverted. Optical cross-talk is higher than in previous figure. The kernel h^{AA} suggests some 'filtering along the diagonals.'

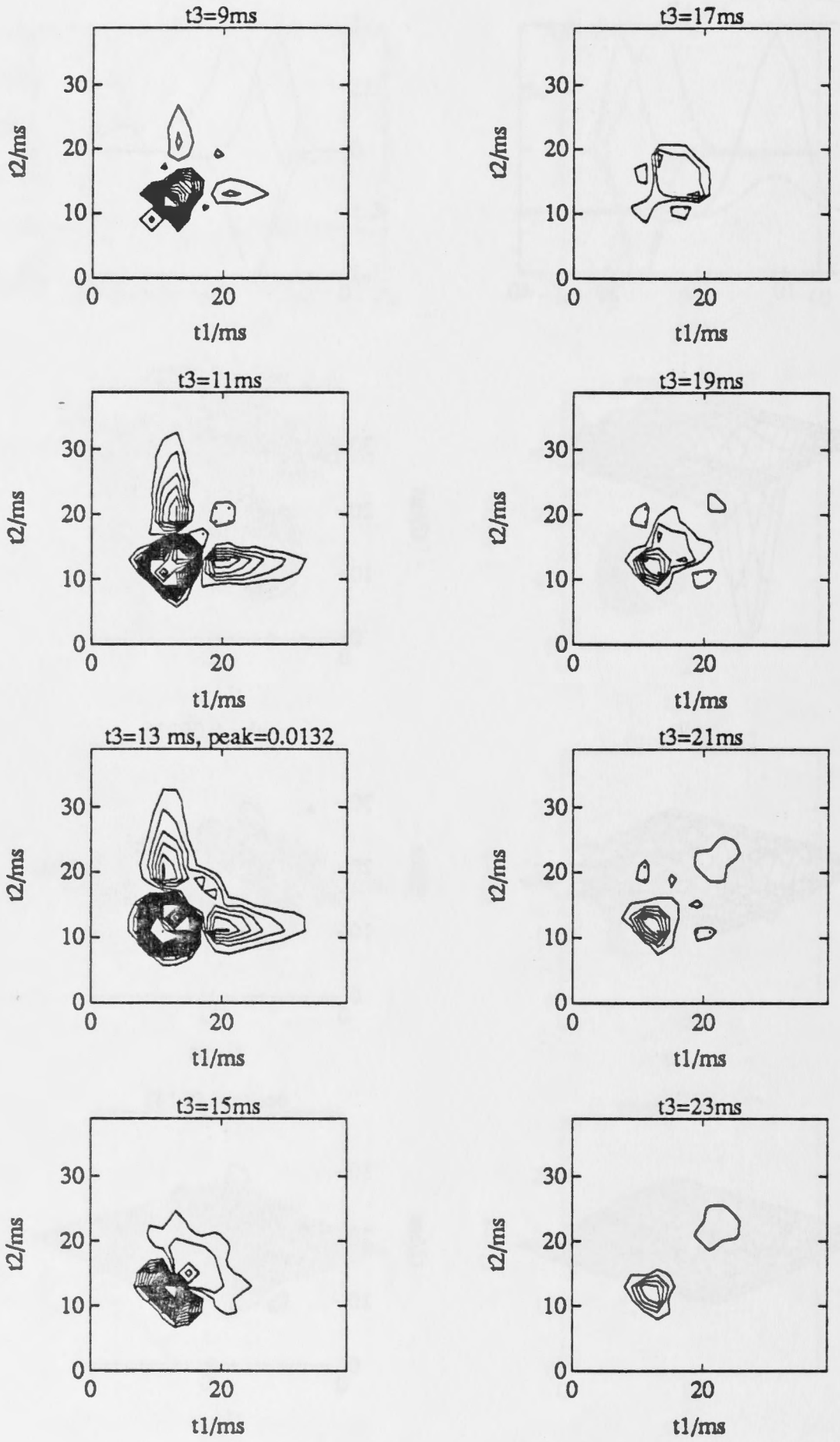

Figure 53: The cubic kernel h^{AAA} from the *Eristalis* LMC of figure 45 (lnba). Plotted are sections of the kernel at the latencies t_3 as indicated. Contour step size is 5% of the overall peak as indicated. Regions of positive values are marked with dots.

axial photoreceptors through optical cross-talk. The amplitude of h_R^B varied up to a maximum of one fifth of the amplitude of h_R^A. When normalised, h_R^B can be seen to have a larger negative peak relative to h_R^A, indicating that the receptor response is not entirely space-time separable.

The self-quadratic kernel has a large negative part, with peak around $3\,ms$ after the peak of the linear kernel. Small positive parts lie axial to this peak. When the linear and quadratic kernels are expressed in units of $mV/(C\,ms)$ and $mV/(C\,ms)^2$ respectively, the ratio of the amplitudes of h_R^{AA} over h_R^A varies from .01 to .04.

The kernels h_R^{AB} and h_R^{BB} are variable and smaller in amplitude.

The cubic kernel h_R^{AAA} has a number of features, the main one being a broad positive part, with peak around $5\,ms$ after the linear kernel peak. The amplitude, in $mV/(C\,ms)^3$ is from .0005 to .001 of the amplitude of h_R^A. Figure 54 shows an example.

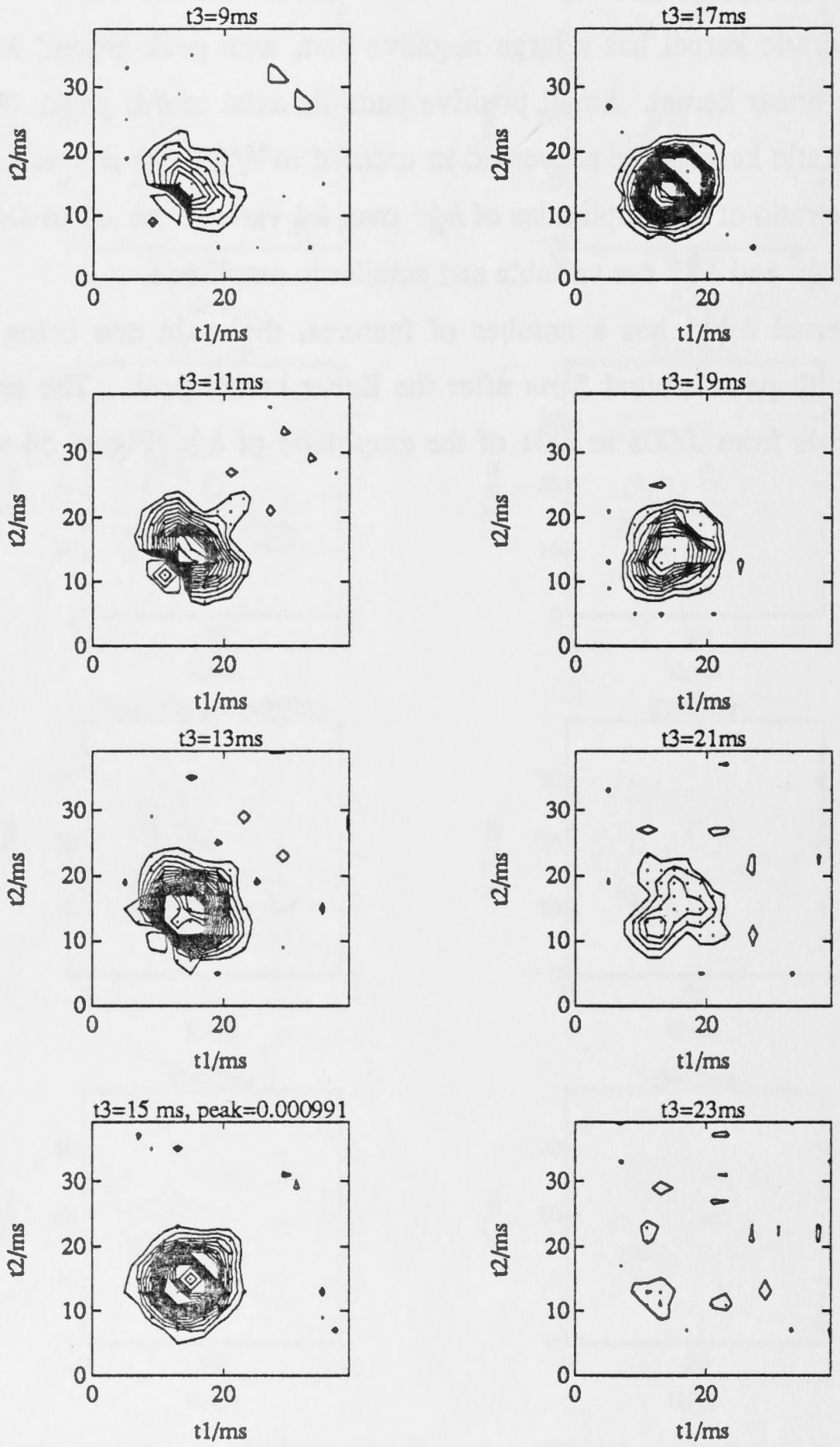

Figure 54: Cubic kernel h^{AAA} from the *Eristalis* receptor of figure 51. Plots as in figure 53.

4.3 Structural modelling of nonlinear systems

Having studied the empirical form of the kernels derived from experimentation we now consider what structural models can be constructed, consisting of simpler components which when connected produce overall kernels in agreement with the observed kernels. Structural modelling has as a goal the association of the structural components with biophysical mechanisms, and proceeds in concert with the consideration of data from other sources elucidating the mechanisms present. The association of components with mechanisms is however a further inferential step, and is tentative and in some cases incomplete.

The structural modelling of the early visual system studied here is basically to factorise the mapping from stimulus to LMC response into a transduction step, from stimulus to receptor response, and a transmission step or steps, describing the transformation of neural image taking place between receptor and LMC. For linear systems this would amount to a deconvolution; for the nonlinear system found here it is a more involved procedure.

4.3.1 Cascading of kernel operators

Some further theoretical results are required, concerning the operation of composing, or cascading, kernel operators. As is well-known, the cascading of two linear kernel-operators, $[p]$ and $[q]$ produces an overall mapping which is a linear kernel-operator, with kernel given by the convolution of the two component kernels:

$$[q][p] = [q * p]$$

The composition of a degree n operator with a degree m operator produces an operator of degree mn, just as squaring followed by cubing produces a sixth power, when monomial functions are considered. Thus if

$$[h] = [g_n][f_m]$$

then $[h]$ is of degree mn. The form of the kernel is complicated, although it follows easily from the definitions. It can be represented as follows. Let the mn arguments of h be written as an $m \times n$ array t and let $t_{.j}$ be column j of the array. If the n arguments

of g_n are written as a vector v with elements v_j then

$$h(t) = \int g_n(v) \prod_{j=1}^{n} f_m(t_{.j} - v_j)\, dv$$

with integration taken over the n variables v_j, up to the memory length of the operator $[g_n]$.

The following special cases will be of use in this chapter. First, consider the case where a linear operator with kernel p is followed by a degree n operator with kernel g_n:

$$s \xrightarrow{[p]} X \xrightarrow{[g_n]} Y$$

The function $X(t)$ represents the intermediate signal, and $Y(t)$ the final output. Algebraically, we have the following

$$\begin{aligned} X(t) &= \int p(u)\, s(t-u)\, du \\ Y(t) &= \int g_n(t_1, \ldots, t_n) X(t-t_1) \ldots X(t-t_n)\, dt_1 \ldots dt_n \end{aligned}$$

where integrals are taken over the relevant memory lengths. Substitution and a change of variables of integration shows that the mapping from s to Y is a degree n kernel operator, with the following kernel:

$$\int g_n(t_1, \ldots, t_n) p(v_1 - t_1) \ldots p(v_n - t_n)\, dv_1 \ldots dv_n$$

This integral is a convolution, and the result can thus be summarised in terms of compact notation as

$$[g_n][p] = [g_n * p^{n\otimes}]$$

where $*$ is an n-dimensional convolution and $p^{n\otimes}$ is the n-fold tensor product of the linear kernel p.

A special case of this occurs when the nonlinear operator $[g_n]$ is an *instantaneous*, or *static*, nonlinearity, whereby the value of X at each time t is raised to the power n and scaled by a coefficient:

$$Y(t) = \gamma_n X(t)^n$$

In this case the overall relationship is:

$$Y = [\gamma_n p^{n\otimes}] s$$

If the static nonlinearity is a polynomial or Taylor series with coefficients γ_n, this can be generalised to

$$\begin{aligned} Y(t) &= \sum_{n=0}^{\infty} \gamma_n X(t)^n \\ &= \sum_{n=0}^{\infty} [\gamma_n p^{n\otimes}] s(t) \end{aligned}$$

This is a Volterra series, with the kernel of degree n being $\gamma_n p^{n\otimes}$. The presence of a tensor product structure in a set of kernels thus suggests the possibility of fitting this type of model, which has been termed the *Wiener model.*

The other case we will consider is when the nonlinear operator is followed by a linear operator $[q]$

$$X \xrightarrow{[g_n]} Y \xrightarrow{[q]} Z$$

producing a final output $Z(t)$. Substitution of the definitions and change of variable in this case shows that the resulting mapping is a kernel operator of degree n with kernel k_n such that:

$$k_n(t_1, \ldots, t_n) = \int q(u)\, g_n(t_1 - u, \ldots, t_n - u)\, du$$

This combination can be thought of as 'filtering along each diagonal' of the kernel g_n. The term 'diagonal' here means any one-dimensional section of the form $g_n(t_1 - u, \ldots, t_n - u)$ for fixed $t_1, \ldots, t_n$ and varying u. In this sense, each diagonal of k_n is the corresponding diagonal of g_n convolved with the linear kernel q. This structure can sometimes be suggested by visual inspection of a kernel, where mass appears to be spread diagonally across the domain.

4.3.2 Linear-Nonlinear-Linear cascade models

A subset of the space of nonlinear operators is formed by those termed sandwich systems. The most general form which has tractable mathematical properties is a cascade combining two of the above structures, termed an LNL system. It consists of a cascade of a linear system and a static nonlinear mapping, as in the Wiener model, then followed by a further linear system. This form of cascade is analysed in Korenberg and Hunter (1986), which includes an elaborate procedure for fitting the model, given the kernels of a system. Some results apparently date from an earlier conference proceedings (Korenberg 1973).

The model thus has the following structure:

$$s \xrightarrow{[p]} X \xrightarrow{N} Y \xrightarrow{[q]} Z$$

Between the linear systems $[p]$ and $[q]$ is a static nonlinearity N. If the function N has a Taylor series with coefficients γ_n then the mapping from s to Y is a Volterra series with kernels $\gamma_n p^{n\otimes}$, as we have seen above. The subsequent linear operator $[q]$ 'filters these kernels along each diagonal', to produce the resulting overall Volterra kernel of degree n

$$k_n(t_1, \ldots, t_n) = \gamma_n \int q(v)p(t_1 - v)\ldots p(t_n - v)\, dv$$

as shown by Billings and Fakhouri (1978).

To fit such a model is difficult, being akin to a deconvolution, but involving nonlinear operators. Note that the Volterra kernel k_n is a linear function of the kernel q, but involves the kernel p to degree n. It is worth testing if the model is likely to provide a fit before proceeding, by seeing if some necessary conditions are satisfied. A particularly simple test is described in Chen *et al* (1986). They arrive at the test by means of a complicated argument via the frequency domain; in fact, the result can be derived easily by considering the time domain Volterra kernels of degree one and two. From the above, these are:

$$\begin{aligned} k_1(t_1) &= \gamma_1 \int q(v)p(t_1 - v)\, dv \\ k_2(t_1, t_2) &= \gamma_2 \int q(v)p(t_1 - v)p(t_2 - v)\, dv \end{aligned}$$

Consider the function obtained by taking a marginal integral of k_2, that is, integrating over one of the latency dimensions. Exchanging the order of integration, and then substituting $w = t_2 - v$, this becomes:

$$\begin{aligned} \int k_2(t_1, t_2)\, dt_2 &= \gamma_2 \int q(v)p(t_1 - v) \left(\int p(t_2 - v)\, dt_2 \right) dv \\ &= \gamma_2 \left(\int p(w)\, dw \right) \int q(v)p(t_1 - v)\, dt_1 \\ &= \gamma_2 \left(\int p(w)\, dw \right) \gamma_1^{-1}\, k_1(t_1) \end{aligned}$$

In short, the marginal integral of the second degree kernel is proportional, as a function of latency, to the first degree kernel (Chen *et al* 1986). This test will be robust unless the operator $[p]$ is high-pass, making the integral of p small, or the coefficient γ_1 is small.

This result immediately generalises to degree n, whereby the marginal integral of the kernel k_n, integrated over $n-1$ dimensions, must be proportional to the linear kernel k_1.

The test can be applied to Wiener kernels due to the following very useful result: for a system with LNL structure, the Wiener kernel of each degree is proportional to the corresponding Volterra kernel (Korenberg 1973; Korenberg and Hunter 1986). Wiener kernels must thus also satisfy the proportionality constraints to represent an LNL system.

This result does not hold precisely for Wiener kernels corresponding to binary white-noise, where the equations are complicated by additional terms due to the difference in correlation properties relative to Gaussian white-noise (see section 2.3.3). This difference is small however, and tends to zero as the time-discretisation becomes finer. Note that the marginal integrals of the higher degree kernels involve all elements of the kernels, so that the interpolated diagonal elements receive little weight in the result. The test is thus more robust than considering kernel diagonals alone.

To check for proportionality, figure 55 shows the linear kernels and marginal integrals of second and third degree kernels for a variety of experiments in this study. The curves are normalised, and inverted where necessary, to have unit maximum value. It is clear that proportionality does not hold, with the time courses of the components of different degree being distinctly different.

Chen *et al* suggest illustrating the proportionality of two time courses graphically by plotting their ratio as a function of time. This will give unstable results where the denominator is small in amplitude. As an alternative, the values of the two functions can be plotted against each other, defining a trajectory on the plane. If they are proportional, the curve will be a straight line through the origin. The entire database of nonlinear kernels is plotted in this way in figure 56, showing clearly the lack of proportionality.

It can thus be concluded that neither the LNL model, nor any submodel, such as the LN (Wiener) or NL (Hassenstein) models, is likely to give a useful fit to this data. It is necessary to look at more complex structural models, whereby the kernels of different orders may follow different time courses, and possibly where parallel pathways may contribute different components to the same kernel.

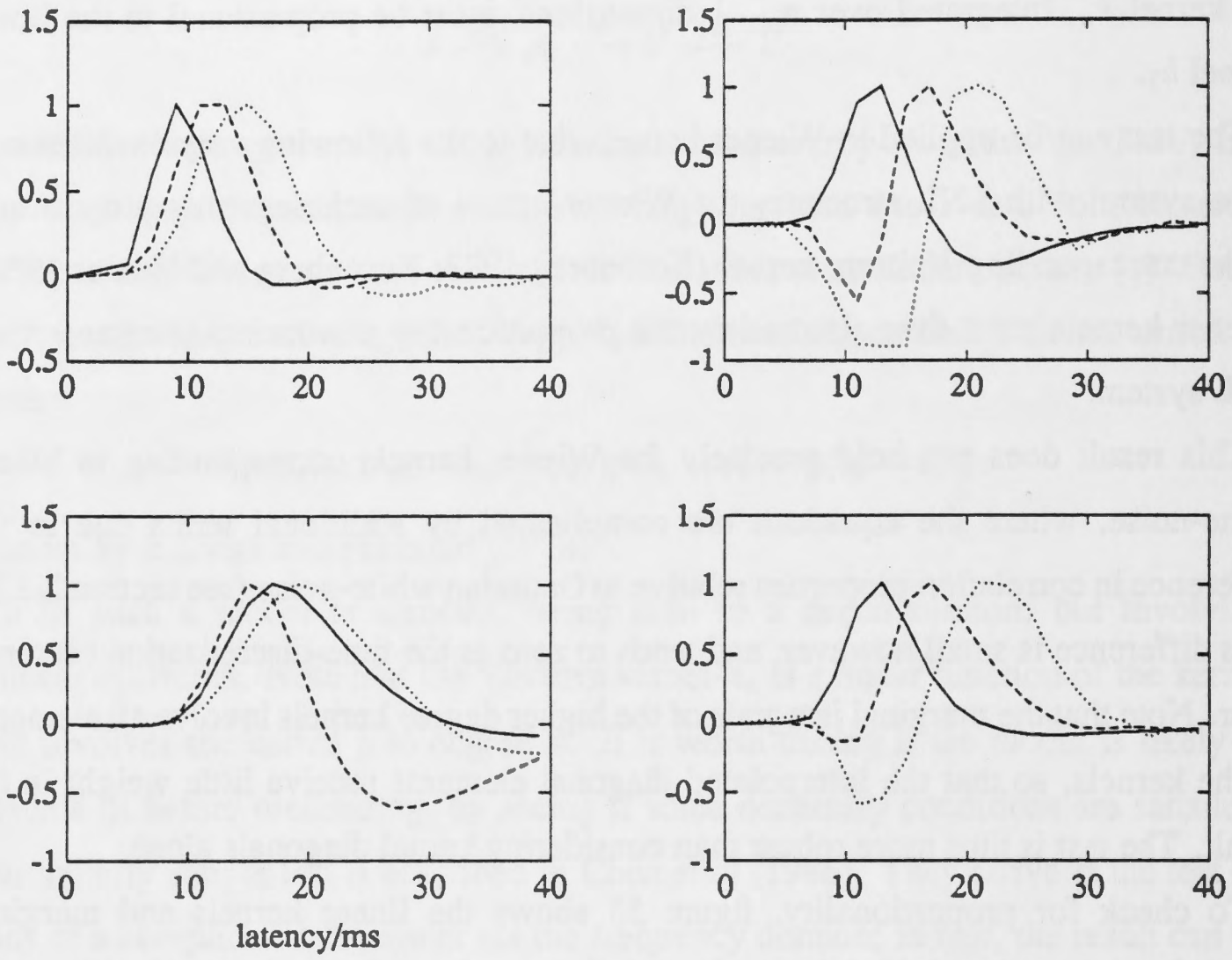

Figure 55: Test for LNL structure by comparing proportionality of time courses. **Solid line** linear kernel, **dashed line** marginal integral of second degree kernel, **dotted line** marginal integral of third degree kernel. All curves normalised, and possibly inverted, to give unit maximum value. **Upper left** *Eristalis* receptor, high intensity. **Upper right**, *Eristalis* LMC, high intensity. **Lower left**, the same *Eristalis* LMC, at low intensity. **Lower right**, *Calliphora* LMC, low intensity.

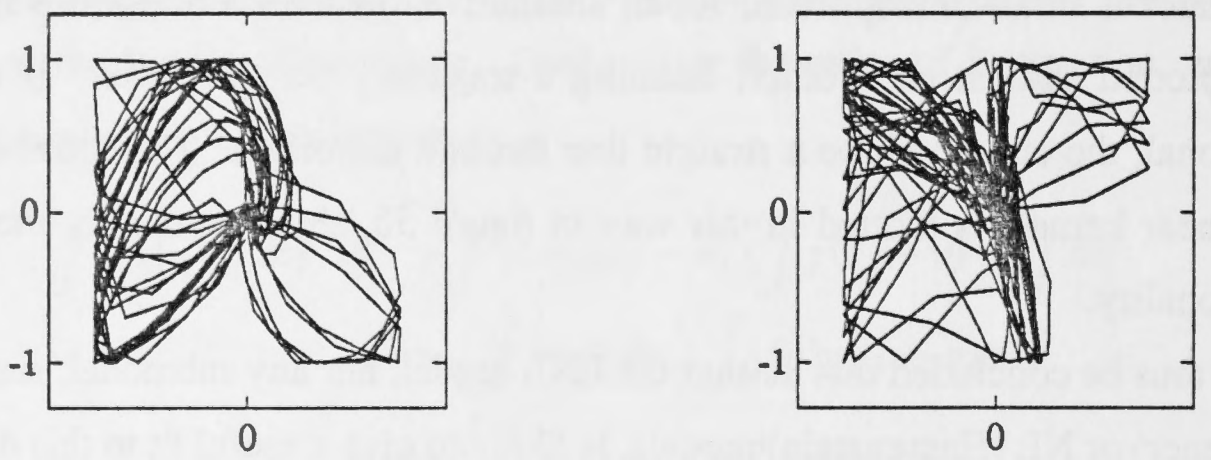

Figure 56: Trajectories testing the LNL model for the database of nonlinear kernels. **Left**, For each experiment, the marginal integral of the second degree kernel is plotted against the linear kernel, as a trajectory over time. **Right**, The marginal integrals of the third degree kernels are plotted against the linear kernels. All data is normalised to unit amplitude.

4.4 Photoreceptor nonlinearities

Figure 51 shows a typical receptor kernel, h_R^{AA}. From the marginal integral test we see that the receptor kernels of all degrees cannot be modelled by a single LNL cascade. Nevertheless, inspection of the kernel h_R^{AA} suggests that it is close to having tensor product form, having cross-sections of constant profile. The kernel is symmetric, but is negative along the main diagonal. We can attempt to fit it with the negative of a tensor square, $-p^{2\otimes}$, for some p a function of time. Interestingly, the function p is then the tensor square root of $-h_R^{AA}$.

The fitting can be done by the procedure which fitted the space-time separable model to the linear spatiotemporal kernels. Figure 57 shows the resulting function p along with the linear kernel h_R^A. The quadratic kernel could thus be produced by a structural model of the Wiener form

$$A \xrightarrow{[p]} X \xrightarrow{N} R$$

where the nonlinearity, N, is $R(t) = -X(t)^2$. For some receptor data the presence of a final linear filter $[q]$ is necessary to produce a very good fit, giving a small amount of 'smoothing along the diagonal.'

The receptor can thus be modelled as a linear operator in parallel with an LNL cascade with slower time course. The effect of the quadratic component on the light adaptation of the linear kernel will be discussed below, and is illustrated in figure 68. The intensity kernel decreases in amplitude with increasing I_0. The $3\,ms$ delay in the quadratic dynamics relative to the linear response introduces a polarity asymmetry in the timing, pushing the peak forward for increments in I_0 and bringing it back for decrements. These asymmetries reflect the reduction in intensity gain and quickening of response well-known in the light adaptation of receptors. Structural models involving feedback pathways may be required to adequately explain these processes, as will be discussed in the conclusion.

4.5 Components of the LMC centre response

In this section we examine some structural models describing the transmission from receptor to LMC, attempting to fit the observed LMC kernels.

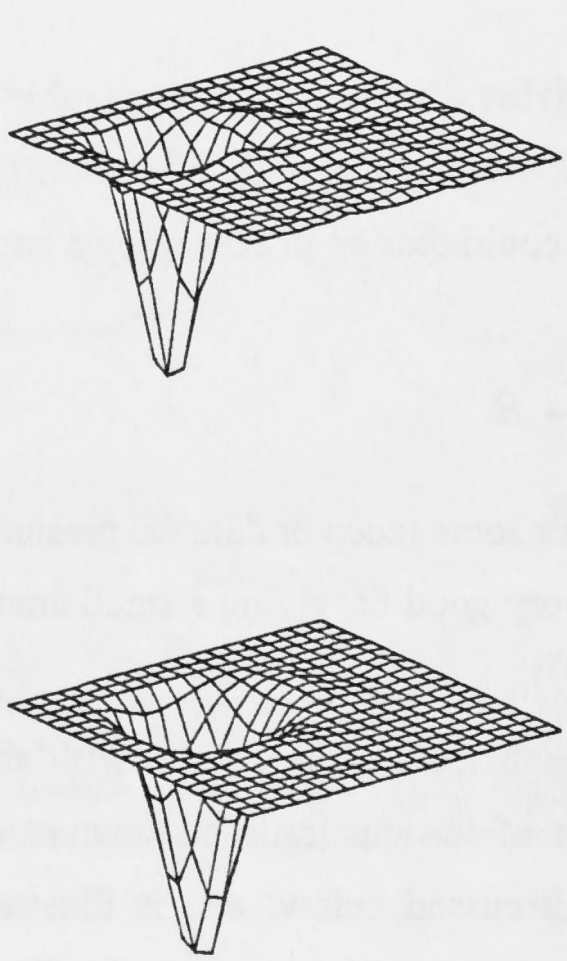

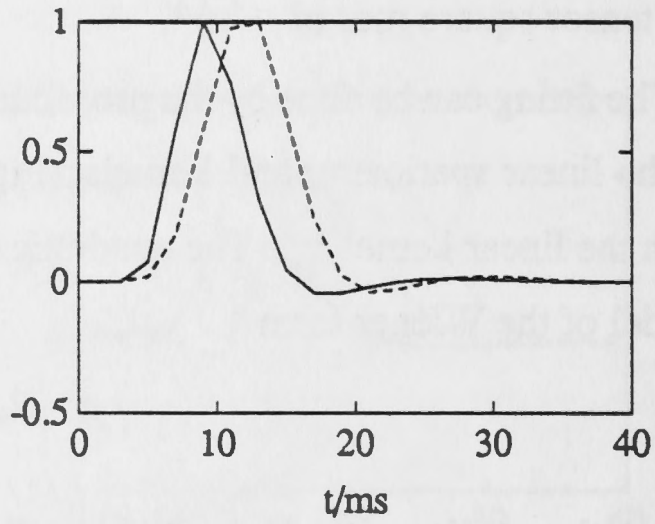

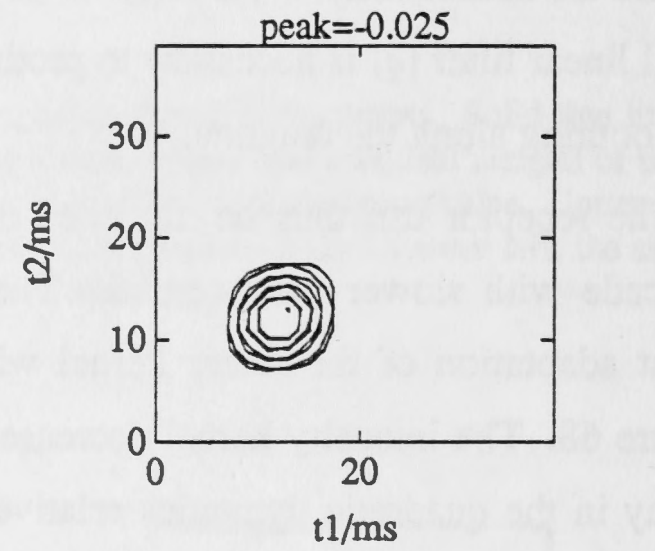

Figure 57: Fit of a receptor quadratic kernel h_R^{AA} by a tensor square $-p^{2\otimes}$. **Upper left,** the kernel h^{AA} for an *Eristalis* receptor (rqba). **Upper right,** the linear kernel h^A (solid line) and the tensor square root p of $-h^{AA}$ (dashed line), normalised in amplitude. **Lower left,** the fitted kernel, $-p^{2\otimes}$. **Lower right,** observed and fitted kernel, 20% contours superimposed.

4.5.1 The primary transmission pathway

It now appears that the principal transmission pathway from receptor to LMC involves the neurotransmitter Histamine (Hardie 1987), producing an increase in chloride conductance in the LMC membrane (Zettler and Straka 1987), thus leading to the inversion of the signal. The signal is amplified at this synapse, with the gain being estimated at around 6 (Laughlin *et al* 1987). A synapse acting at this high gain is likely to introduce considerable nonlinearity of response, both due to nonlinearity between presynaptic voltage and the rate of transmitter release, and to self-shunting of the response in the postsynaptic cell.

The rate of transmitter release is dependent on the presynaptic membrane potential, and as we have seen, it is likely that antagonism acts presynaptically, making this membrane voltage high-pass filtered relative to the receptor response. The receptor terminal membrane voltage will be represented by $M(t)$, and the kernel h_M^A relating stimulus to M is likely to be more biphasic than the receptor kernel h_R^A.

The postsynaptic response of the LMC to the transmitter appears to be rapid. Impulse response data suggests a time constant of .5 to 1 ms, with a delay of 0 to .5 ms at some point in the transmission (Laughlin *et al* 1987). Estimates of the time constant of the LMC membrane are similar, at .5 to 1 ms (Laughlin and Osorio 1989). Given the high bandwidth of the transmission from receptor membrane potential to LMC response, relative to the transduction process, we will simplify the subsequent modelling by ignoring the temporal dynamics of the map $M \rightarrow L$ and assuming that it is a static nonlinearity. Transmission through the histamine pathway is thus modelled as a Wiener system

$$R \xrightarrow{[h_M^R]} M \xrightarrow{N} L$$

whereby the linear high-pass filter $[h_M^R]$ is followed by a static nonlinearity N. In some models a pure delay of 1 ms is included to represent the synaptic transmission dynamics.

The synaptic transfer was modelled as a static nonlinear mapping by Laughlin *et al* (1987) in order to fit the characteristic curve relating the amplitude of step-responses measured intracellularly in receptors and LMCs. The model is similar to the model of Falk and Fatt (1972) for vertebrate photoreceptor synapses.

The number, T, of postsynaptic conductance channels activated by the transmitter

is assumed to increase exponentially with the receptor membrane voltage M:

$$T = a \exp(bM)$$

The postsynaptic voltage L is related hyperbolically to the number of activated conductances, due to the finite reversal potential, L_m, for the response, which is negative for chloride. If L is defined to be zero when T is zero, the relationship is of the form:

$$L = L_m \frac{kT}{kT + 1}$$

Combining these two gives the relation

$$L = L_m \frac{ka \exp(bM)}{ka \exp(bM) + 1}$$

as in Laughlin *et al* (1987).

If M is defined so that it is zero when $kT = 1$, this simplifies further to

$$L = \frac{L_m}{1 + \exp(-bM)}$$

involving only the reversal potential L_m and the sensitivity b. An example of the curve can be found in figure 58 (lower).

If the presynaptic voltage fluctuates about some set level M_0, so that $M = M_0 + \Delta M$, the postsynaptic voltage is then:

$$L = \frac{L_m}{1 + \exp(-b(M_0 + \Delta M))}$$

By differentiation of this expression the coefficients of the Taylor series can be derived, as a function of the set point M_0. These are illustrated in figure 58 (upper right).

From the Taylor series coefficients and initial and final linear kernels, the Volterra kernels of the LNL cascade can be calculated, as shown above. Truncated Taylor and Volterra series are the appropriate means of approximation in the limit for small fluctuations of signal amplitude. The observed Wiener kernels however relate to signals with significant amplitude. If the receptor is assumed to be a linear transducer, integrating the stimulus over an interval covering several frames, then the receptor voltage will have an amplitude distribution close to Gaussian, by the central limit theorem. Histograms of recorded receptor voltages in section 4.7.2 are in agreement. The static nonlinear mapping N is then best approximated by a truncated Hermite series, giving the least-squares-error approximation. Combining the coefficients of

this Hermite series with the initial linear kernel produces the overall Wiener kernels for the LN cascade model. Thus if $[h_M^A]$ represents the linear mapping from stimulus A to the receptor membrane potential M, transmission through the nonlinear synapse produces a component of the degree n Wiener kernel of the mapping $A \rightarrow L$ given by

$$\gamma_n (h_M^A)^{n\otimes}$$

where γ_n is the Hermite coefficient of degree n.

The values of the Hermite coefficients depend on the set point, M_0, about which the membrane potential fluctuates. An illustration of this dependence is given in figure 58 (upper right). The primary part of the observed LMC linear kernel h_L^A is negative. The quadratic kernel h_L^{AA} also has negative primary part, while the cubic kernel h_L^{AAA} has positive primary part. This pattern of signs is in correspondence with the Hermite coefficients for values of M_0 in an interval immediately to the left of zero, suggesting that the receptor–LMC synapse is operating around a point slightly less than halfway down its characteristic curve. Note that in near $M_0 = 0$ the quadratic coefficient γ_2 is changing rapidly with M_0, and so variability in the size of the quadratic component is to be expected. Figure 58 (lower) shows the fit of the Taylor and Hermite series to the example characteristic curve for a steady state value in this interval.

We can test the adequacy of this model in the following way. We assume the estimate $\gamma_1 = -6$ (dimensionless). For a given set of LMC kernels, we then have:

$$h_M^A = 1/\gamma_1 h_L^A$$

The higher degree kernels are then fitted by linear regression, according to the models:

$$\begin{aligned} h_L^{AA} &= \gamma_2 (h_M^A)^{2\otimes} \\ h_L^{AAA} &= \gamma_3 (h_M^A)^{3\otimes} \end{aligned}$$

Figure 59 shows a typical example of the fit obtained.

The primary part and axial extensions of the cubic kernel are well fitted by the model, with a value of γ_3 which is close to compatible with the values predicted by the Hermite coefficients calculated in figure 58. As expected, the quadratic kernel deviates from the fit both due to the presence of the diagonal parts and due to the faster time-course of the primary and axial secondary parts. This is a general result, which is reflected in the plots of normalised kernel sections in figures 43 to 50. In all cases

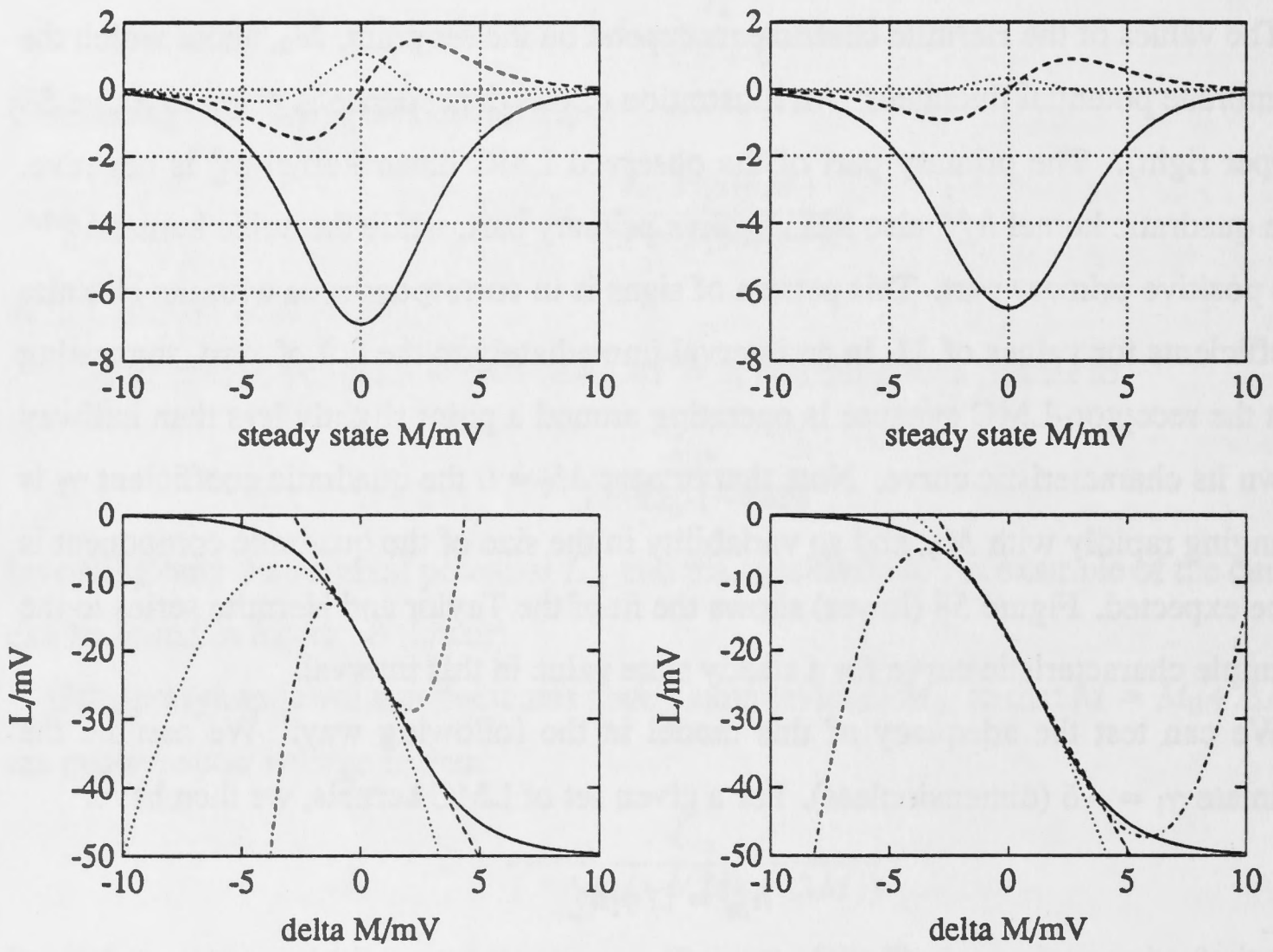

Figure 58: Series approximations to a model characteristic curve for the receptor–LMC synapse given in the text. The parameters of the curve are: $L_m = -50\,mV$, $b = .55\,mV^{-1}$. **Left**, Taylor series. **Right**, Hermite series when receptor membrane voltage fluctuation has standard deviation $1\,mV$. **Upper**, the first, second and third degree coefficients of the series as a function of steady state value M_0, (solid, dashed and dotted lines respectively). **Lower**, model characteristic curve (solid line) and first, second and third degree approximations for fluctuations about a steady state value $M_0 = -1\,mV$ (dashed, dotted and dot-dash respectively).

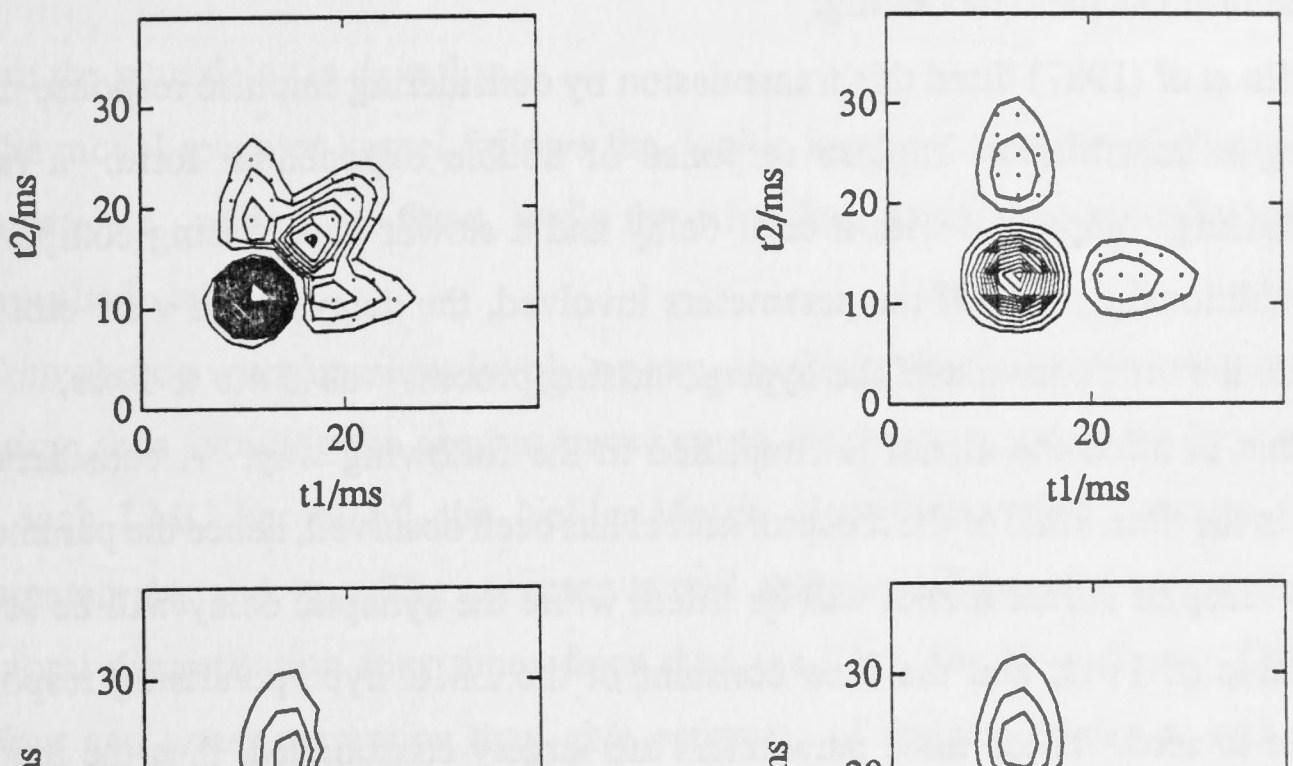

Figure 59: Fit of the LN cascade model of the primary transmission pathway to the kernels of the *Eristalis* LMC of figure 43 (lkma). **Upper left,** observed quadratic kernel h_L^{AA}. Contours step size is 5% of peak as indicated. **Upper right,** fit of form $\gamma_2(h_M^A)^{2\otimes}$ where h_M^A is estimated from linear kernel and $\gamma_2 = -1.5\,mV^{-1}$, from regression. Contour levels as in upper left. **Lower left,** axial cross-section through peak point of the cubic kernel h_L^{AAA}. Contour step size is 5% of peak value as indicated. **Lower right,** fit of form $\gamma_3(h_M^A)^{3\otimes}$, where $\gamma_3 = 1.1\,mV^{-2}$ from regression. Note fit to cubic kernel is reasonable while even the primary and axial parts of the quadratic are not fitted.

we see that the axial section through the peak of the cubic kernel is in good agreement with the linear kernel, while the axial section of the quadratic kernel is consistently different in waveform.

4.5.2 Dynamics of receptor-LMC transmission

This section will present a simple parametric model for the receptor-LMC linear kernel h_L^R for use in subsequent modelling.

Laughlin *et al* (1987) fitted this transmission by considering impulse response data, and fitting a transmission impulse response of double exponential form: a rapid hyperpolarising component with a brief delay and a slower depolarising component with an additional delay. Of the parameters involved, the delays fitted were close to zero, while the time constant of the hyperpolarising process was .5 ms to 1 ms.

With this in mind the model is simplified in the following way. A considerable variation in the time-scale of the receptor kernel has been observed, hence the parameter t_{p1} of the receptor kernel model will be fitted, while the synaptic delay will be set to a fixed value of $1\,ms$, and the time constant of the LMC hyperpolarising response will be set to zero. These three parameters are largely confounded, thus the precise optimum values for the fit are not of interest.

No additional delay will be included in the antagonistic component. This component is assumed to be due to fluctuation in the extracellular voltage within the lamina cartridge, denoted by E. If E is dependent on R according to first order linear dynamics, then the kernel h_E^R is a decaying exponential starting at $t = 0$. There seems to be no established notation for this useful function, so we define the function $\exp_0$ as follows:

$$\exp_0(x) = \begin{cases} \exp(x) & \text{if } x < 0 \\ 1/2 & \text{if } x = 0 \\ 0 & \text{if } x > 0 \end{cases}$$

In the form $h(t) = a \exp_0(-t/\tau)$, this is then the required kernel. The value $1/2$ at $x = 0$ ensures that the kernel $h(t)$ and the function

$$H(T) = \frac{a\tau}{1 + 2\pi i \tau T}$$

are precisely related as a Fourier transform pair.

The model kernel for the mapping $R \rightarrow M$ is thus

$$h_M^R(t) = \delta(t) - a_E \exp_0(-t/\tau_E)$$

where the dirac δ function produces the identity operator, $[\delta]$, and the kernel for the overall transmission $R \rightarrow L$ is

$$h_L^R(t) = \gamma_1 \left(\delta(t - d_L) - a_E \exp_0(-(t - d_L)/\tau_E)\right)$$

where the pure delay is $d_L = 1\,ms$.

The model receptor kernel follows the double log-normal curve of chapter 3. The parameters t_{p1} and a_1 are fitted, while the other four parameters are calculated using the results in table 3.

Convolution with functions involving $\exp_0$ is efficiently done using recursive digital filtering, thus avoiding the need to transform to the frequency domain for simulation. For each LMC kernel h_L^A the Nelder-Meade algorithm varied the two nonlinear parameters t_{p1} and τ_E. The receptor kernel and convolution are calculated with a temporal discretisation four times finer than the data, so $\Delta t = .5\,ms$. Decimation by four and linear regression then give estimates of the amplitudes a_1 and a_E. The coefficient of synaptic transmission is again taken as $\gamma_1 = -6$.

The model fits all LMC kernel data with an RMS error of less than 4% of peak value. Figure 60 shows examples of the fit, with the constituent components, at the high and the low mean intensity.

4.5.3 Transmission of receptor nonlinearity

In factoring the LMC response into transduction and transmission, we must consider not only the nonlinearities introduced in the transmission, but also the nonlinear components in transduction, which are transmitted to the LMC. Although the receptor nonlinearities are smaller than those of the LMC response, the quadratic kernel h_R^{AA} appears to be large enough to make a significant contribution to the LMC kernel h_L^{AA}.

The composition of polynomial operators can be expanded in the same way as a composition of polynomial functions. It is probably helpful to consider this simpler case first. Assume that the mappings from stimulus A to receptor voltage R to LMC voltage L were static functions, equal to the following polynomials, omitting terms of

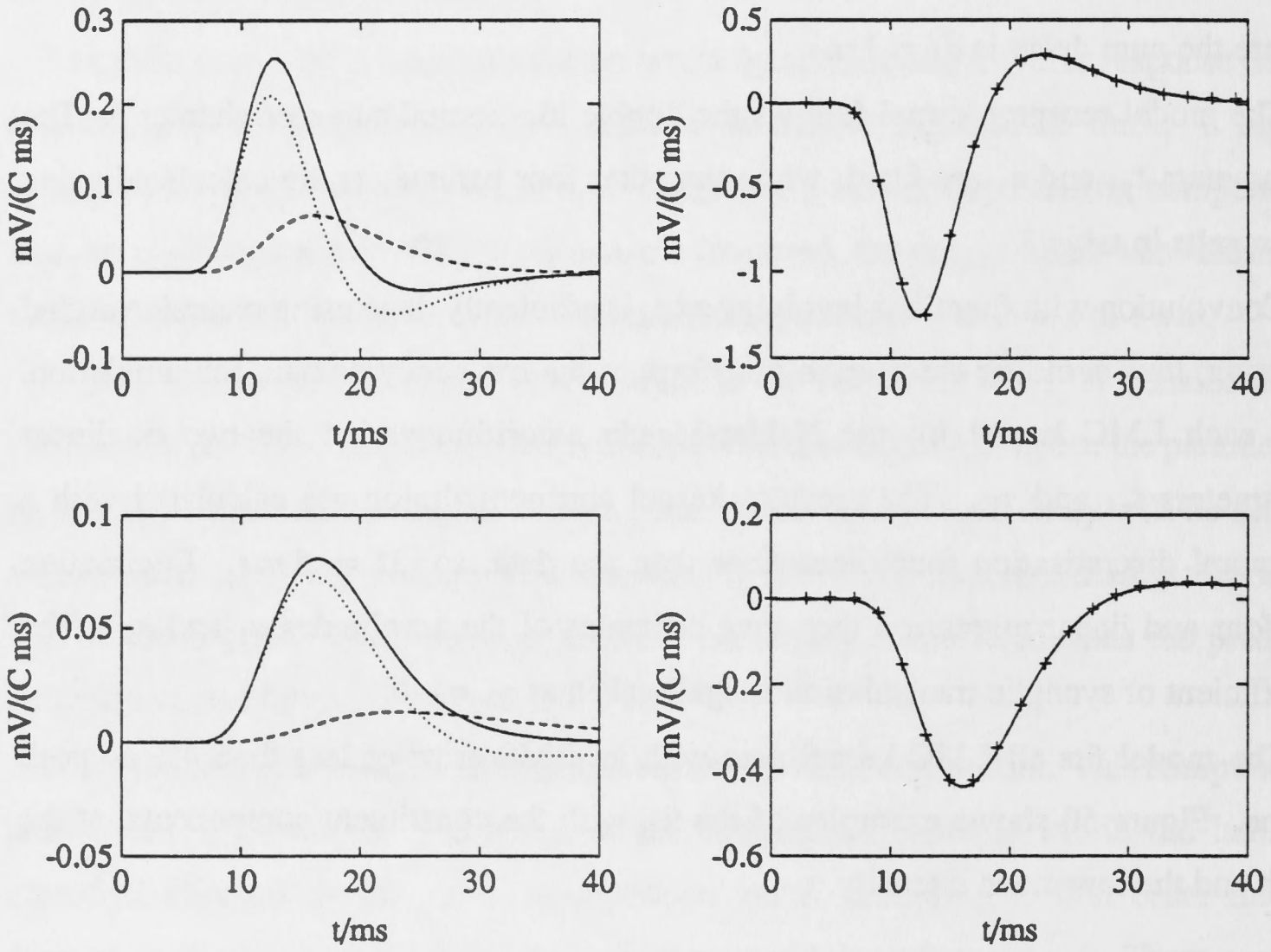

Figure 60: Parametric fit for linear transmission kernel h_L^R. **Left**, solid line is fitted receptor kernel; dashed line is fitted kernel describing extracellular response, h_E^A; dotted line is fitted kernel describing membrane potential, $h_M^A = h_R^A - h_E^A$. **Right**, plus signs are observed LMC kernel, h_L^A; solid line is fitted kernel. **Upper**, at the high mean intensity (lkma): $t_{p1} = 11.8\,ms$, $\tau_E = 6.9\,ms$, $a_1 = .24\,mV/(C\,ms)$, $a_E = .068\,ms^{-1}$. **Lower**, at the low mean intensity (lknal): $t_{p1} = 15.4\,ms$, $\tau_E = 15\,ms$, $a_1 = .081\,mV/(C\,ms)$, $a_E = .025\,ms^{-1}$

zero degree and noting only terms to degree three:

$$\begin{aligned} R &= \alpha_1 A + \alpha_2 A^2 + \alpha_3 A^3 + \ldots \\ L &= \beta_1 R + \beta_2 R^2 + \beta_3 R^3 + \ldots \end{aligned}$$

Substituting and noting only terms to degree three we have:

$$\begin{aligned} L = \beta_1\alpha_1 A \quad &+ \beta_1\alpha_2 A^2 \quad + \beta_1\alpha_3 A^3 + \ldots \\ &+ \beta_2(\alpha_1 A)^2 \quad + 2\beta_2(\alpha_1 A)(\alpha_2 A^2) + \ldots \\ &\qquad\qquad + \beta_3(\alpha_1 A)^3 + \ldots \end{aligned}$$

The formulation for kernel operators is analogous, and can be readily written down using the notational conventions developed. We will consider cascaded Volterra systems for simplicity. If stimulus, receptor and LMC signals have the following relationships

$$\begin{aligned} R &= [k_R^A]A + [k_R^{AA}]A^{2\otimes} + [k_R^{AAA}]A^{3\otimes} + \ldots \\ L &= [k_L^R]R + [k_L^{RR}]R^{2\otimes} + [k_L^{RRR}]R^{3\otimes} + \ldots \end{aligned}$$

then the overall mapping from stimulus to LMC response is:

$$\begin{aligned} L = [k_L^R][k_R^A]A \;+\; &[k_L^R][k_R^{AA}]A^{2\otimes} \;+\; [k_L^R][k_R^{AAA}]A^{3\otimes} \;+\; \ldots \\ + \;&[k_L^{RR}]([k_R^A]A)^{2\otimes} \;+\; 2[k_L^{RR}]([k_R^A]A)\otimes([k_R^{AA}]A^{2\otimes}) \;+\; \ldots \\ + \;&[k_L^{RRR}]([k_R^A]A)^{3\otimes} \;+\; \ldots \end{aligned}$$

The leading terms of these lines have already been discussed, as the transmission of the linear receptor component through the nonlinear synaptic mechanisms.

The second term of the first line represents the linear transmission of the receptor quadratic component. For a given LMC kernel set this component can be fitted as follows. The linear kernel is decomposed into transduction and transmission steps as described in the previous section. From the estimated peak-time and amplitude of the fitted transduction kernel h_R^A, an estimate of the receptor kernel h_R^{AA} is made. This is then 'filtered along each diagonal' by the linear transmission operator $[h_L^R]$, which can be done efficiently by recursive digital filtering techniques. The observed kernel h_L^{AA} is regressed on the resulting component along with the quadratic transmission

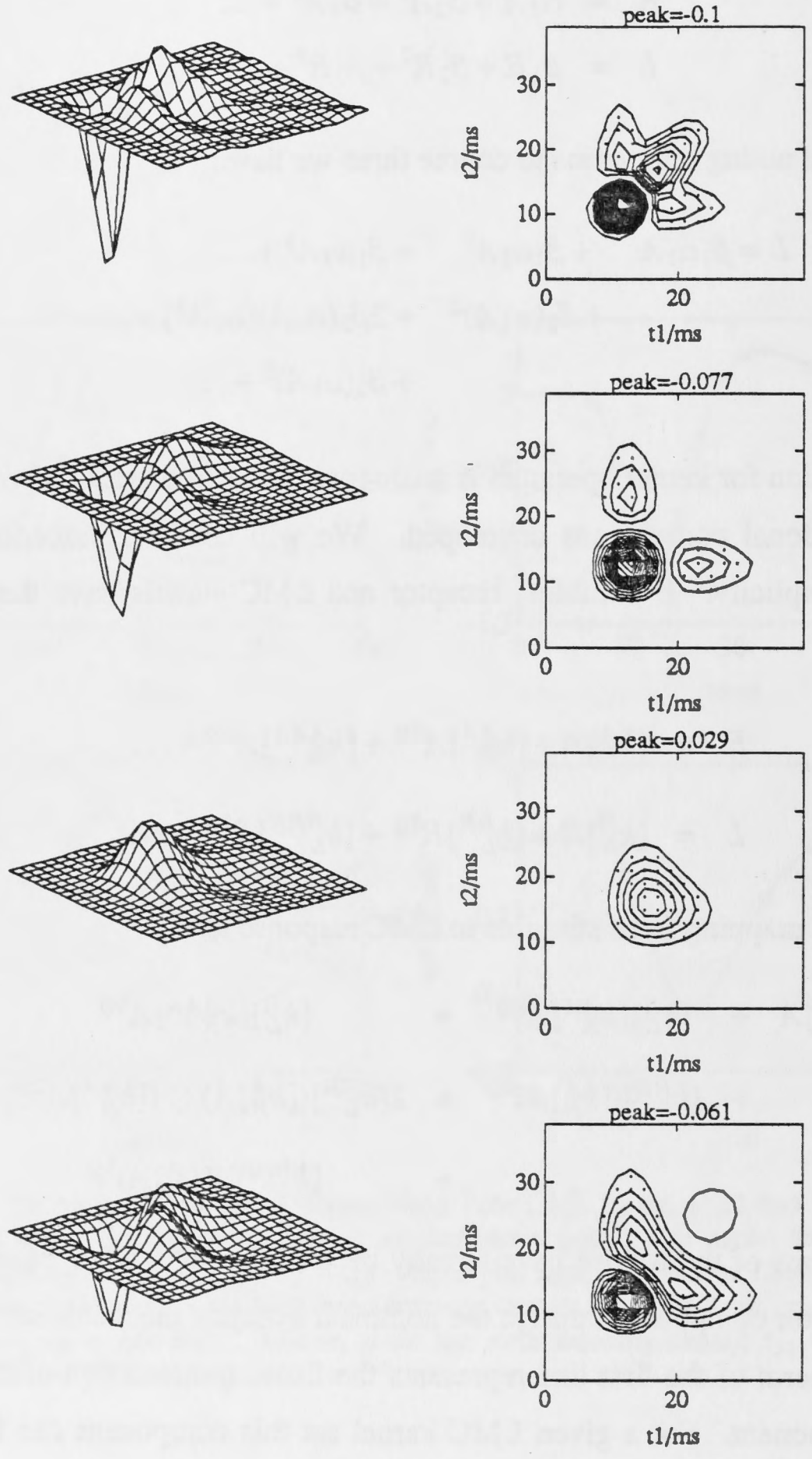

Figure 61: The effect of the receptor quadratic kernel h_R^{AA} transmitted to the LMC. **Upper**, the kernel h_L^{AA} from an *Eristalis* LMC (lkma). **Second row**, the estimated component from quadratic transmission, $\gamma_2(h_M^{AA})^{2\otimes}$. The coefficient is estimated as $\gamma_2 = -1.7\,mV^{-1}$. **Third row**, the estimated component due to linear transmission of the receptor kernel h_R^{AA}. Regression produces an estimate of $-.025$ for the ratio of h_R^{AA} peak to h_R^A peak, which is within the observed range. **Lower**, the total fitted kernel, which is significantly different from the data, h_L^{AA}.

component $(h_M^{AA})^{2\otimes}$. The regression coefficients produce estimates of the coefficient γ_2 and an adjustment to the amplitude of h_R^{AA}.

Figure 61 shows an example of these fits.

The kernel h_R^{AA} has a large negative part, with peak around $3\,ms$ after the linear peak. When transmitted this produces a positive diagonal part with a smaller negative part at longer latencies. The amplitude of receptor quadratic kernels varied from .01 to .04 times the amplitude of the linear kernels, in their respective units. The ratio produced by this fitting procedure lies in this range. This component partly accounts for the positive diagonal peak seen in LMC quadratic kernels, however we see that the kernel h_L^{AA} is still not well fitted.

The other two terms, of degree three, representing transmission of receptor non-linearities were found to be of insignificant amplitude and are excluded from further modelling.

It might be of theoretical interest to note the second term on line two of the expansion, indicating that when the sum of a linear term and a quadratic term undergoes quadratic transmission a cubic term is produced, among others. This is of course obvious when polynomial functions are considered, illustrating the utility of the analogy.

4.5.4 Parallel LNL models

The structural models considered so far have failed to adequately account for the quadratic LMC kernel h_L^{AA}. If the system is to be fitted by a structural model involving LNL cascades then at least one additional pathway must be added in parallel to those already considered.

A parallel LNL or 'parallel sandwich' model has the form

$$[q]N[p] + [q']N'[p']$$

where p, p', q, q' are linear kernels and N, N' are static nonlinear mappings. The first point to note is that at least two of the pairs $p, p'; q, q'$ and N, N' must consist of distinct elements, otherwise the model can be factored into a single LNL cascade. For example, if the corresponding linear kernels are equal then

$$[q]N[p] + [q]N'[p] = [q](N + N')[p]$$

and a single cascade results.

Consideration of the range of observed kernels h_L^{AA} suggests that there are two components present, with large variation in their relative amplitudes between cells. One component produces the negative primary and positive axial extensions. This is a good example of the kernel produced by an LN model, in which a linear operator with a biphasic kernel is followed by a nonlinearity with a negative second degree coefficient. We have seen such a component in figure 59, but to fit the observed kernel the biphasic kernel must be faster in time-course.

The other component produces the positive diagonal peak and extension. This suggests a significant final linear filter, which 'filters each diagonal', thus spreading the diagonal peak along the main diagonal to produce the extension. A delay is also incurred somewhere along the pathway, but due to commutativity this may be before or after the nonlinearity. The second degree coefficient for this component is positive. If the first degree coefficient is negative then this component reinforces the primary component of the linear kernel. The delay and smoothing mean that this component adds to the linear kernel at longer latencies. We thus have the possibility that the histamine pathway generates a fast component of response, following the time-course of the axial section of the quadratic kernel, while the second pathway generates a slightly slower response, adding to the histamine component in the linear kernel to produce the broader primary part, while opposing the histamine component in the quadratic kernel, producing the positive diagonal peak and extension.

If the second pathway is driven by the receptor membrane potential M, which we have modelled with a biphasic response to stimulation, then this component will in addition generate negative parts in the quadratic kernel in regions extended axially from the positive peak. These parts are in fact observed in several cases, such as in figures 45, 47 and 50.

A mechanism which would produce a component like this is suggested by the results of Laughlin and Osorio (1989) and Weckström *et al* (1989). In these studies current-clamp techniques were used to analyse the response to step stimulation. The first paper finds that polarising conductances with positive reversal potentials contribute to large-amplitude responses to negative contrasts, adding to the reduction in chloride conductance driven by the histamine pathway. As this effect contributes to depolarisation when the stimulus is negative, and seems to be less important when the stimulus is positive, the characteristic curve for the transmission is positive when the

stimulus is negative and small when the stimulus is positive. The Hermite series for such a curve has negative linear coefficient and positive quadratic coefficient. Without knowing more about the shape of the curve it is not possible to predict the sign of the cubic coefficient. The depolarising conductance pathway also appears to operate with slightly longer latency than the histamine pathway. The reported depolarising pathway thus has properties in agreement with the proposed second LNL cascade.

Association of the second LNL cascade with the reported depolarising input is hypothetical, and the neural components generating the depolarising input are at present also uncertain. Let us in this section simply propose a hypothetical quantity Z which is driven by the membrane potential M and which effects the LMC voltage L.

The parallel LNL model is represented by the following mapping network:

$$\begin{array}{ccc} & A & \\ & \downarrow & \\ & R & \\ & \downarrow & \\ & M & \\ \downarrow\downarrow & & \searrow\searrow \\ L & \leftarrow & Z \end{array}$$

It was fitted to sets of LMC kernels, with the primary transmission pathway being modelled as before: the map $A \rightarrow R$ has as linear kernel a double log-normal curve with variable parameter t_{p1} and amplitude, the receptor-LMC primary transmission has a high-pass filter followed by a static nonlinearity with linear coefficient $\gamma_1 = -6$.

The second pathway is also driven by the receptor membrane potential, M. It then has a static nonlinear mapping, N_Z, and a final linear operator $[h_L^Z]$.

$$M \xrightarrow{N_Z} Z \xrightarrow{[h_L^Z]} L$$

We let the kernel h_L^Z embody a delay followed by an exponentially decaying response:

$$h_L^Z(t) = a_Z \exp_0(-(t - d_Z)/\tau_Z)$$

A component due to transmission of the receptor quadratic nonlinearity is also included.

Linear and quadratic kernels were fitted simultaneously using the Nelder-Meade algorithm to vary five nonlinear parameters and linear regression to fit amplitudes. Figure 62 shows the fit that can be obtained.

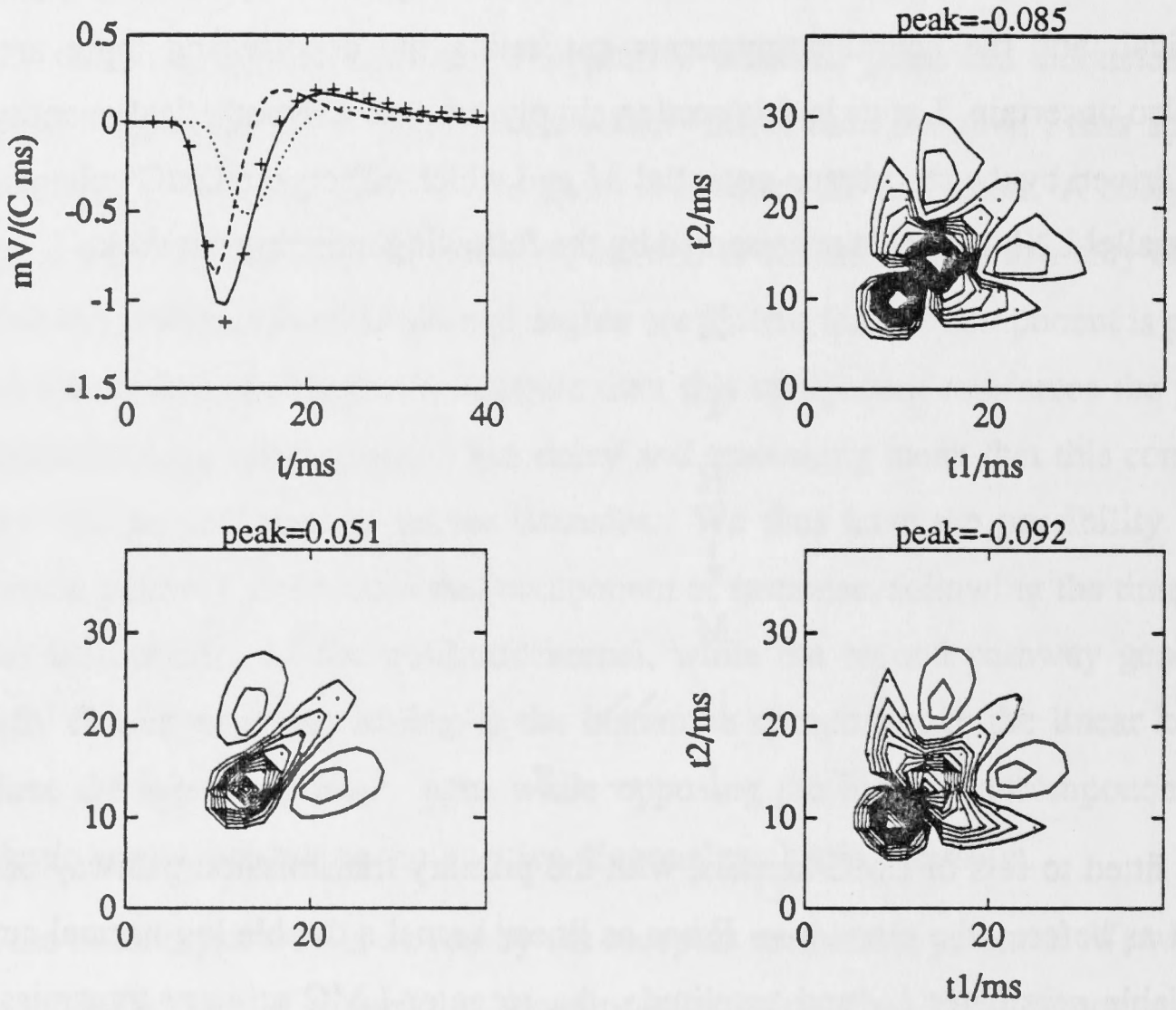

Figure 62: Fit of parallel LNL model, as described in text. Data is from an *Eristalis* LMC (lnba). Contour step size is 5% of peak value of kernel h_L^{AA} (upper right). bf Upper left, fit to linear kernel: plus signs, observed kernel h_L^A; solid line, total fitted kernel; dashed line, component transmitted through histamine pathway; dot-dash, component transmitted through second pathway, $M \rightarrow Z \rightarrow L$. **Upper right,** observed kernel h_L^{AA}. **Lower left,** component transmitted through second pathway. The final linear filter $[h_L^Z]$ creates the diagonal extension. **Lower right,** total fit to h_L^{AA}. The nonlinear parameters used are: $t_{p1} = 8.0\,ms$, $a_E = .061\,ms^{-1}$, $\tau_E = 7.5\,ms$, $\tau_Z = 3.6\,ms$, $d_Z = 2.6\,ms$.

Consideration of the quadratic kernel has thus suggested a second pathway of transmission from receptor to LMC, which corresponds in many properties with a pathway suggested by current-clamp results. This raises an interesting parallel; in neural systems there are often multiple mechanisms contributing to an observed behaviour, and one aim of neurophysiological investigation is to distinguish components which are normally confounded. Just as the use of current and voltage clamp techniques can separate the roles of contributing mechanisms, consideration of the higher degree kernels can also isolate components.

4.6 Surround effects

The effect of stimulation in the surround of the receptive field was tested by an annular region of stimulus extending from 3° to 6°, modulating in contrast according to a binary white-noise signal $B(t)$ independently of the central spot. We now consider what structural models are suggested by the kernels involving the surround channel.

4.6.1 Optical cross-talk component

The linear surround kernel for receptors, h_R^B, has a positive primary part which corresponds closely with the positive part of the centre kernel h_R^A, but with smaller amplitude. This suggests that light from the annulus is being absorbed in the recorded receptor and is transduced in an equivalent manner to light from the spot. This pathway will be referred to as optical cross-talk, and an optical cross-talk coefficient η can be estimated for each experiment, giving the effectiveness of the annulus on the central receptors relative to the effectiveness of the spot. An example of receptor linear kernels is shown in figure 51, with h_R^B also plotted with peak normalised to h_R^A. This shows the surround kernel to be relatively more phasic; hence the receptor spatiotemporal response is not precisely separable in this case. An additional component adding to the negative second phase is indicated, but this is small in absolute terms and will not be included in subsequent modelling.

Receptor linear response is thus modelled as

$$R = [h_R^A]A + [h_R^B]B$$

where the surround kernel is

$$h_R^B = \eta h_R^A$$

for some η. The coefficient η was estimated by considering kernel values up to and including the peak of the primary part, and regressing the surround values on the centre values. The receptor data gave values of η from .08 to .4.

This optical cross-talk component is transmitted to LMCs, influencing the linear and quadratic kernels involving surround. Many of the kernels h_L^B have a negative primary part, whose leading edge corresponds closely in latency and waveform with the leading edge of the centre kernel h_L^A. For these experiments the parameter η is estimated as above, yielding estimates from zero to .5.

To predict the effect of optical cross-talk on the quadratic LMC kernel, we consider the LMC response to second degree in the receptor response; the mappings involved can be summarised by the following diagram:

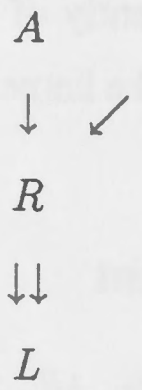

Algebraically, we write R in terms of L, and substitute the above expression for R to get:

$$\begin{aligned} L &= [h_L^R]R + [h_L^{RR}]R^{2\otimes} \\ &= [h_L^R * h_R^A]A + [h_L^R * h_R^B]B \\ &\quad + [h_L^{RR} * (h_R^A)^{2\otimes}]A^{2\otimes} + [2h_L^{RR} * (h_R^A \otimes h_R^B)]A \otimes B + [h_L^{RR} * (h_R^B)^{2\otimes}]B^{2\otimes} \end{aligned}$$

If the cross-talk gives the relationship $h_R^B = \eta h_R^A$ then the linear component for surround effect becomes

$$\begin{aligned} h_L^R * h_R^B &= \eta h_L^R h_R^A \\ &= \eta h_R^A \end{aligned}$$

as expected.

The quadratic cross-kernel above, operating on $A \otimes B$, becomes equal to:

$$\begin{aligned} 2h_L^{RR} * (h_R^A \otimes h_R^B) &= 2\eta h_L^{RR} * (h_R^A)^{2\otimes} \\ &= 2\eta h_L^{AA} \end{aligned}$$

We would thus expect a component in the interaction kernel h_L^{AB} with the same form as h_L^{AA} but scaled by 2η. Inspection of the cross-kernels reveals that in every case where the linear kernels indicate nonzero optical cross-talk there is a negative part in the kernel h_L^{AB} at latencies corresponding to the negative primary part of h_L^{AA}, and when cross-talk is absent this part is absent. Note however that the positive diagonal peak of h_L^{AA}, which in some cases is larger than the negative primary, is not always reflected in the cross-kernel, as in figure 47. Possibly the positive diagonal peak is due to pathways other than the central receptors, since the spot will stimulate nearest neighbours to a considerable degree.

The self-quadratic kernel for surround, h_L^{BB}, has a component proportional to η^2, which is not consistently observed.

The space-time inseparability of the LMC response properties means that optical cross-talk only produces a component of the surround kernels as has been seen, and other pathways must now be considered.

4.6.2 Lateral antagonism

The annulus stimulates a large number of receptors surrounding the central ommatidium, and as the linear spatiotemporal kernels have shown there is a range of forms of lateral antagonism from these receptors. Consideration of the nonlinear components of lateral antagonism is simplified by looking at those cells for which the optical cross-talk appears to be absent, of which fortunately there are six. The other cells presumably combine components for optical cross-talk and lateral antagonism. This section is thus primarily applicable to those cells exhibiting extended lateral antagonistic flanks, as illustrated in the spatiotemporal plots of chapter 3.

The network of mappings must be expanded, and we introduce a signal $S(t)$ representing the strength of response in the surround receptors stimulated by the annulus. The mapping from spot to central receptors is presumably similar to the mapping from annulus to surround receptors, thus $A \rightarrow R$ and $B \rightarrow S$ will be taken as equivalent.

Comparison of centre and surround linear kernels where optical cross-talk is absent suggests that the surround kernel could be obtained from the centre kernel by inversion, attenuation, delay and smoothing. Comparison of the kernels h_L^{AA} and h_L^{AB} in these case also suggests a relationship, where inversion and attenuation have occurred, and where delay and smoothing has occurred along the t_2 dimension. The most remarkable case appears in figure 46, where the cross-kernel reproduces in inverted and delayed form every detail of the centre quadratic kernel. From chapter 3 it can be noted that this cell was the *Eristalis* LMC exhibiting the strongest degree of lateral antagonism.

The modelling of the primary transmission pathway has suggested that the main source of nonlinearity is the synapse between receptor and LMC. The results noted here can be accounted for assuming that the lateral antagonism acts presynaptically, before the nonlinearity. This could possibly be by the surround receptors signal S contributing to the extracellular potential in the recorded cartridge, and thus adding a negative component to the potential across the receptor membrane, M.

This leads to the following model network

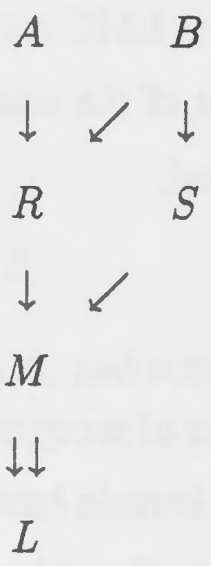

where the mapping $S \rightarrow M$ gives a component antagonistic to the central pathway. Consider the case when the optical cross-talk is zero, eliminating the upper diagonal mapping, $B \rightarrow R$. Rather than giving the full expression for this network, let us consider just the terms of interest.

The linear components of LMC response are

$$[h_L^M * h_M^R * h_R^A]A$$

$$[h_L^M * h_M^S * h_S^B]B$$

for centre and surround respectively. Assuming that $h_R^A = h_S^B$, the only difference is the replacement of h_M^R by h_M^S. The kernel h_M^R reflects the presynaptic high-pass

filtering assumed along the primary transmission pathway. The lateral antagonism is represented by the kernel h_M^S, which contributes an inverted, attenuated, delayed and smoothed surround signal to M.

The centre self-quadratic and the cross terms produced are

$$[h_L^{MM} * (h_M^R * h_R^A \otimes h_M^R * h_R^A)]A \otimes A$$

$$[2h_L^{MM} * (h_M^R * h_R^A \otimes h_M^S * h_S^B)]A \otimes B$$

where convolution, $*$, has higher precedence than tensor multiplication. Note that with $h_R^A = h_S^B$ the kernels will be the same except that h_M^R is replaced by $2h_M^S$ in the cross-kernel. The difference between these two is equivalent to applying different filtering along the t_2 dimension to generate the overall quadratic kernels, reflecting the inversion, attenuation, delay and smoothing along the t_2 axis of the cross-kernel relative to the centre kernel. The factor 2 in the cross-kernel accounts for a strange feature of the kernels in figure 46, that the cross-kernel has larger amplitude than the self-quadratic kernel.

The model was fitted in the following way to kernels showing no optical cross-talk. We assume that the surround linear kernel might be derived from the centre kernel filtering with an operator $[f]$ with a delayed exponential as kernel. This assumes the relationship

$$h_M^S = h_M^R * f$$

where f is defined by

$$f(t) = a_S \exp_0(-(t - d_S)/\tau_S)$$

The kernel f is estimated using the Nelder-Meade algorithm. The centre quadratic kernel h_L^{AA} is then filtered along the t_2 dimension with the operator $[2f]$ to produce a predicted kernel h_L^{AB} due to lateral antagonism.

The fit obtained to the kernels of figure 46 with this structural model is illustrated in figure 63.

As with the optical cross-talk component, the positive diagonal peak of h_L^{AA} is sometimes not reflected fully in the cross-kernel, as in figure 48.

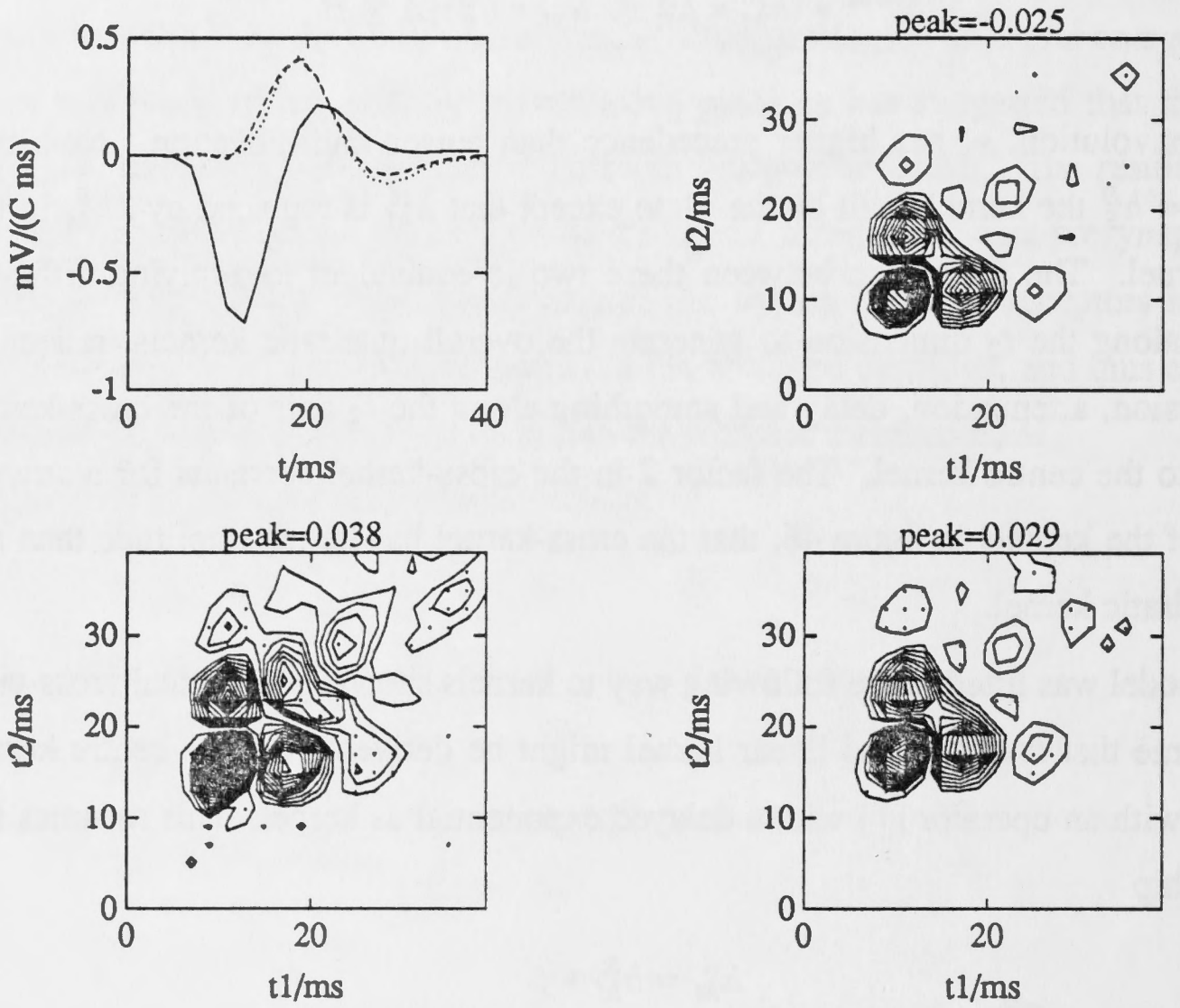

Figure 63: Fit of linear and quadratic kernels according to lateral antagonism structural model described in text. The kernels are from an *Eristalis* LMC (lpba). Contour step size is 5% of peak value of kernel h_L^{AB} (lower left). **Upper left**, linear kernels: solid line, centre kernel h_L^A; dashed line, surround kernel h_L^B; dotted line, centre kernel filtered by $[f]$. Parameters of f are: $a_S = -.23\,ms^{-1}$, $\tau_S = 1.7\,ms$, $d_S = 6.4\,ms$. **Upper right**, observed centre quadratic kernel h_L^{AA}. **Lower right**, observed cross-kernel h_L^{AB}. **Lower right**, kernel h_L^{AA} filtered along t_2 dimension by $[2f]$.

4.7 Statistical properties of response components

In this section we examine the statistical properties of some aspects of the response: the size of the contributions of components to the total response, the amplitude distribution of signal values, and the additivity of the noise component.

4.7.1 Components of response power

The size of an intracellular response can be measured by the *root mean square* (RMS) value in millivolts. When the response is modelled as a stationary stochastic process the mean can be taken as the ensemble-average, and the RMS value then corresponds to the norm induced by the response distribution

$$\text{RMS}\, r = \sqrt{E[r(t)^2]}$$

where stationarity ensures the value is independent of t. For a sampled response this is estimated by taking a time-average:

$$\text{RMS}\, r = \sqrt{\overline{r(t)^2}}$$

Ergodicity ensures the convergence of the time-average to the ensemble-average as the run length increases.

The square of this measure, the mean square response, is called the *power* of the response, by analogy with electrical circuits, in which the power dissipated across a resistance is proportional to the square of the voltage applied. Power may not be of such direct relevance in neurobiology, but it has a mathematical utility as, by Pythagoras' theorem, the power in orthogonal components adds to give the total power. We will thus look at the relative contributions of the signal components in terms of the percentages of the total power.

In this study each experiment involved 8.3 repeats of a stimulus of period $n_t = 32768$ frames. The resulting response was filtered to remove low frequency components, which are regarded as experimental artifact due to drifts and jumps in the baseline of the response. The *averaged response* is then calculated over a section of eight stimulus periods, and the *deviance* is defined as the difference between filtered and averaged response:

$$\text{filtered} = \text{averaged} \oplus \text{deviance}$$

This is an orthogonal sum with respect to time-averaging, indicated by $\oplus$.

If the response is modelled as the sum of a deterministic signal component dependent on the stimulus and an additive noise component with power P_{noise}, then the averaged response is an unbiassed estimate of the signal, although it is still contaminated with a noise component with power $\frac{1}{8}P_{\text{noise}}$. Conversely the deviance power under-estimates the power of the noise, as the deviance has $7n_t$ degrees of freedom rather than $8n_t$. Just as the denominator in the unbiassed estimator for a population variance is $n-1$ rather than n, the unbiassed estimator for noise power is:

$$\text{estimated } P_{\text{noise}} = \tfrac{8}{7}P_{\text{deviance}}$$

The signal to noise power ratio is thus estimated by:

$$\text{estimated } \frac{P_{\text{signal}}}{P_{\text{noise}}} = \tfrac{7}{8}\frac{P_{\text{averaged}}}{P_{\text{deviance}}} - \tfrac{1}{8}$$

The square root of this measure, the signal to noise RMS ratio, has been often quoted in publications.

Figure 64 shows RMS deviance plotted against RMS averaged response for four classes of experiments. *Eristalis* and *Calliphora* LMCs seem to form a homogeneous population with respect to these results, and are thus pooled throughout this section. The four classes thus comprise receptors and LMCs at the two levels of mean illumination.

There is considerable variation of noise levels even at a given signal power, however the scatter-plot appears to exhibit a clear barrier representing the maximum signal to noise ratio obtainable with this experimental design. This is plotted as a line, corresponding to a ratio of averaged to deviance RMS of 7.0. When corrected as explained above this gives an optimum signal to noise RMS ratio of 6.0. We note that although the maximum value occurs in the experiment with the largest signal power, experiments with less signal power also approach the maximum ratio, suggesting that signal and noise may be attenuated together.

Since noise power is variable, even at a given signal strength, we consider the other components relative to the RMS averaged response, rather than relative to the RMS total response. For the spot-annulus experiments the averaged response is fitted by model components of degrees zero to three. The zero degree component is insignificant, due to the removal of low frequency components and is thus omitted from the following. Components relating to spot and annulus are pooled according

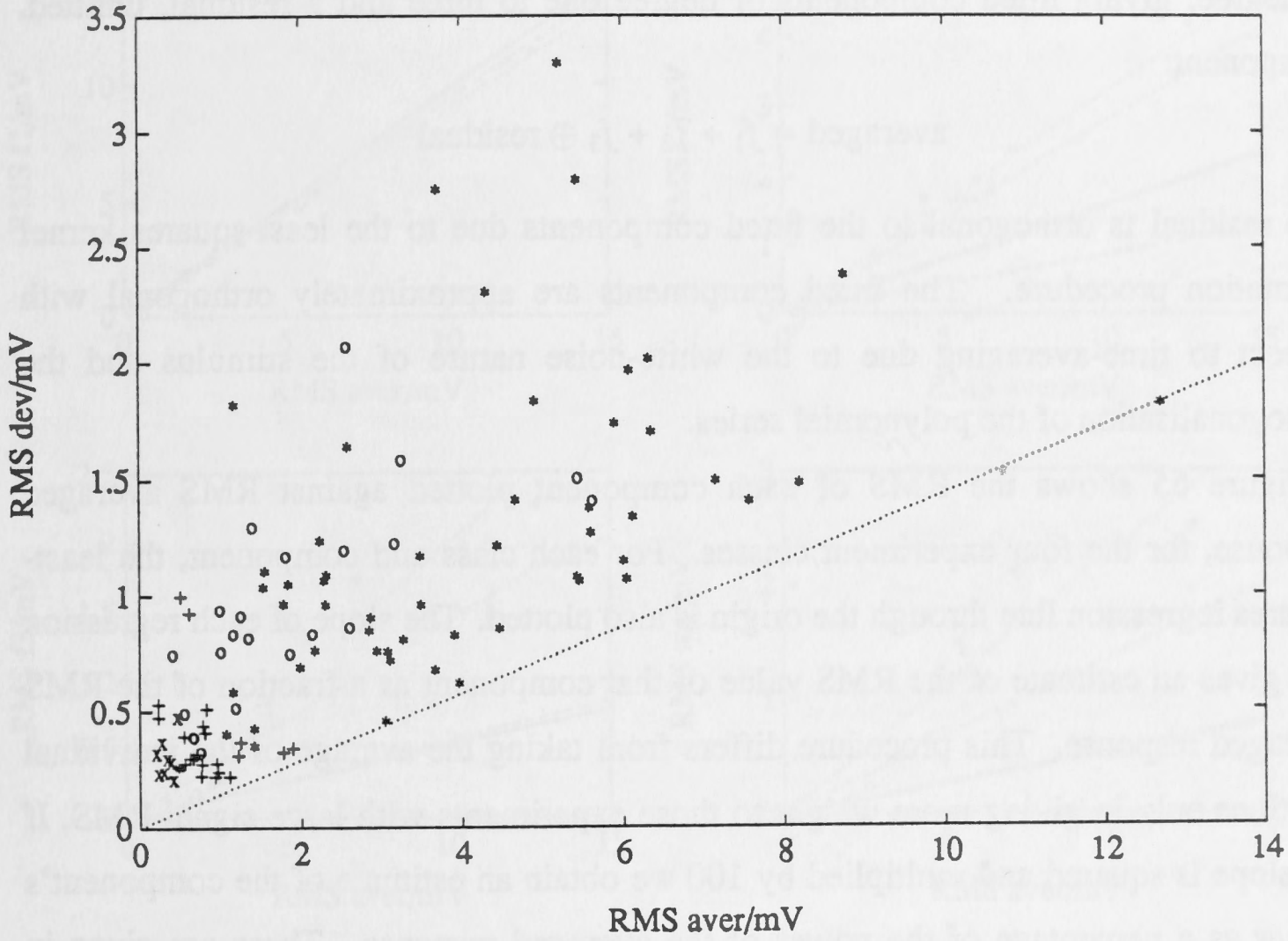

Figure 64: RMS deviance plotted against RMS averaged response, for four classes of experiments: receptors at high intensity (+); receptors at low intensity (x); LMCs at high intensity (*); LMCs at low intensity (o). The dotted line indicates the maximum signal to noise ratio obtained, equal to a averaged response to deviance RMS ratio of 7.0, equivalent to a signal to noise RMS ratio of 6.0.

celltype	I_0	f_1		f_2		f_3		residual		n
rec	H	95.2	(1.00)	2.5	(0.98)	0.3	(0.96)	0.3	(0.61)	4
	L	95.2	(1.00)	0.7	(1.00)	0.3	(1.00)	0.3	(1.00)	1
LMC	H	79.4	(1.00)	10.2	(1.00)	4.0	(0.98)	5.0	(0.96)	12
	L	86.9	(1.00)	7.7	(0.99)	2.0	(0.97)	1.8	(0.95)	5

Table 5: Power of components as a percentage of power of averaged response, for the three model components and the residual, for each of the four experiment classes. The values are obtained by squaring the regression coefficients from the fits in figure 65 and multiplying by 100. The correlation coefficients from the regressions are given in parentheses. The percentage contributions were also calculated by fitting regression lines through the estimates of power, producing very similar results.

to degree, giving fitted components of degree one to three and a residual, unfitted, component:

$$\text{averaged} = f_1 + f_2 + f_3 \oplus \text{residual}$$

The residual is orthogonal to the fitted components due to the least-squares kernel estimation procedure. The fitted components are approximately orthogonal with respect to time-averaging due to the white-noise nature of the stimulus and the orthogonalisation of the polynomial series.

Figure 65 shows the RMS of each component plotted against RMS averaged response, for the four experiment classes. For each class and component, the least-squares regression line through the origin is also plotted. The slope of each regression line gives an estimate of the RMS value of that component as a fraction of the RMS averaged response. This procedure differs from taking the average of the individual fractions only in giving more weight to those experiments with large signal RMS. If the slope is squared and multiplied by 100 we obtain an estimate of the component's power as a percentage of the power of the averaged response. These are given in table 5, along with the correlation coefficients for the regression lines.

We see that responses for this experimental design are primarily linear, with the linear component accounting for 95% of receptor response power and 80% of LMC response power at high level of illumination. The quadratic component has RMS values highly correlated with signal RMS, and contributes 2.5% to receptor averaged response power and 10% to LMC averaged response power at the high level of illumination.

The cubic component RMS is also correlated with RMS averaged response, although there is an indication that it may become relatively larger as the averaged response increases. This suggests that there may be a variable attenuation present before a

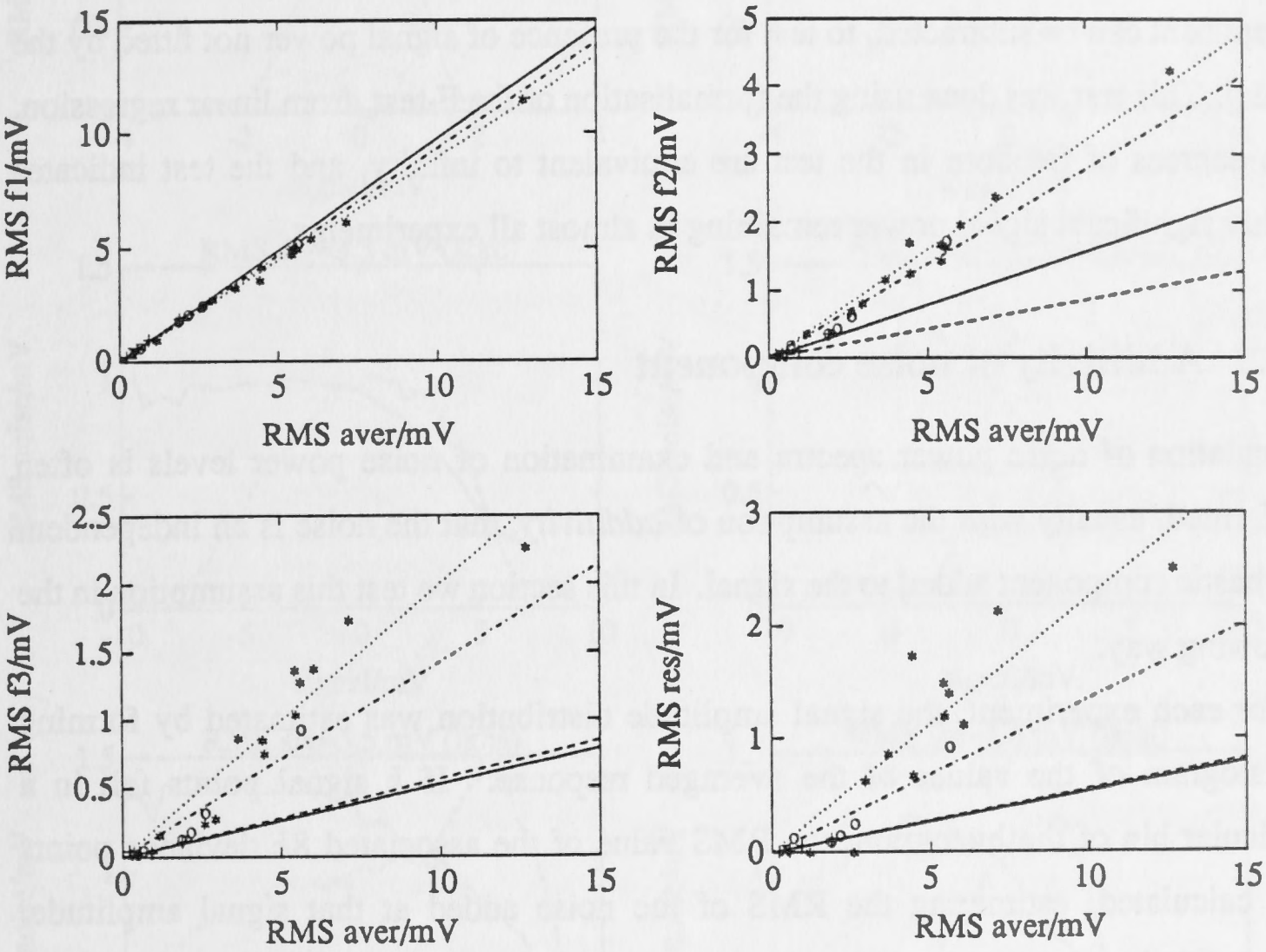

Figure 65: RMS of signal components against RMS averaged response, for the three model components and the residual, as indicated on ordinate axes. For each component the four experimental classes are plotted using symbols as in figure 64, and the least-squares regression line through the origin is plotted as follows: receptors at high intensity (solid line); receptors at low intensity (dashed line); LMCs at high intensity (dotted line); LMCs at low intensity (dot-dash).

nonlinearity in the system.

At the lower level of mean illumination, the size of all nonlinear contributions is reduced relative to the higher level.

Lastly, the residual still includes significant power, accounting for 5% in the case of LMCs at high intensity. This power comes from two components: a noise component of power $\frac{1}{8}P_{\text{noise}}$, and a signal component due to signal power not fitted by the model. This is due to the omission of significant kernel points, either of higher degree terms or at latencies beyond the memory lengths considered. An estimate of the noise component can be subtracted, to test for the presence of signal power not fitted by the model. This test was done using the formalisation of the F-test, from linear regression. The degrees of freedom in the test are equivalent to infinity, and the test indicates highly significant signal power remaining in almost all experiments.

4.7.2 Additivity of noise component

Calculation of noise power spectra and examination of noise power levels is often performed, usually with the assumption of *additivity*, that the noise is an independent stochastic component added to the signal. In this section we test this assumption in the following way.

For each experiment, the signal amplitude distribution was estimated by forming a histogram of the values of the averaged response. If k signal points fell in a particular bin of the histogram, the RMS value of the associated $8k$ deviance points was calculated, estimating the RMS of the noise added at that signal amplitude. Figure 66 shows the estimated noise RMS and normalised signal amplitude density plotted against signal amplitude for an *Eristalis* receptor and LMC.

The receptor data is unremarkable, having a constant noise RMS and a symmetric distribution of signal amplitudes. The LMC data however shows a marked dependence of noise RMS on signal amplitude, with the RMS reduced by 50% at large positive values of the signal amplitude. The spot-annulus stimulus generated greater response RMS, as shown in the lower row. With these experiments the signal amplitude distribution shows a marked skewness towards positive values. Results at high and low mean intensity are similar, but with less response RMS at low intensities.

The dependence of noise RMS on signal amplitude was a general result, illustrated by further examples in figure 67. We must conclude that noise in LMCs is nonadditive,

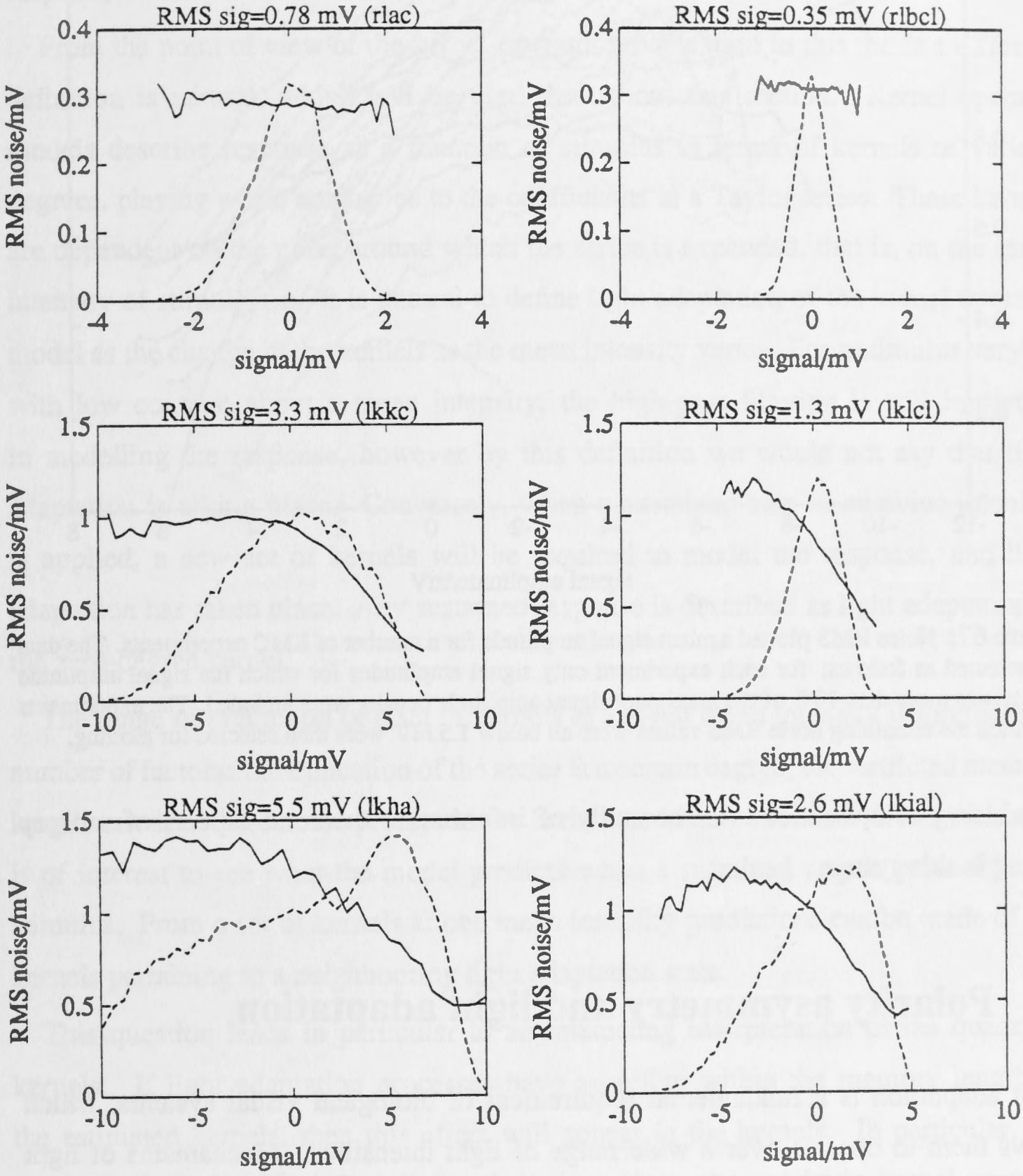

Figure 66: Noise RMS and signal amplitude density as a function of signal amplitude. The noise RMS is plotted as mV (solid lines); the density of signal amplitudes is plotted with arbitrary scale (dashed lines). RMS signal value and run identifiers are as indicated. **Left,** at high mean intensity. **Right,** at low mean intensity. **Upper row,** an *Eristalis* receptor. **Middle row,** an *Eristalis* LMC in response to checkerboard stimulus. **Lower row,** the same LMC in response to spot-annulus stimulus.

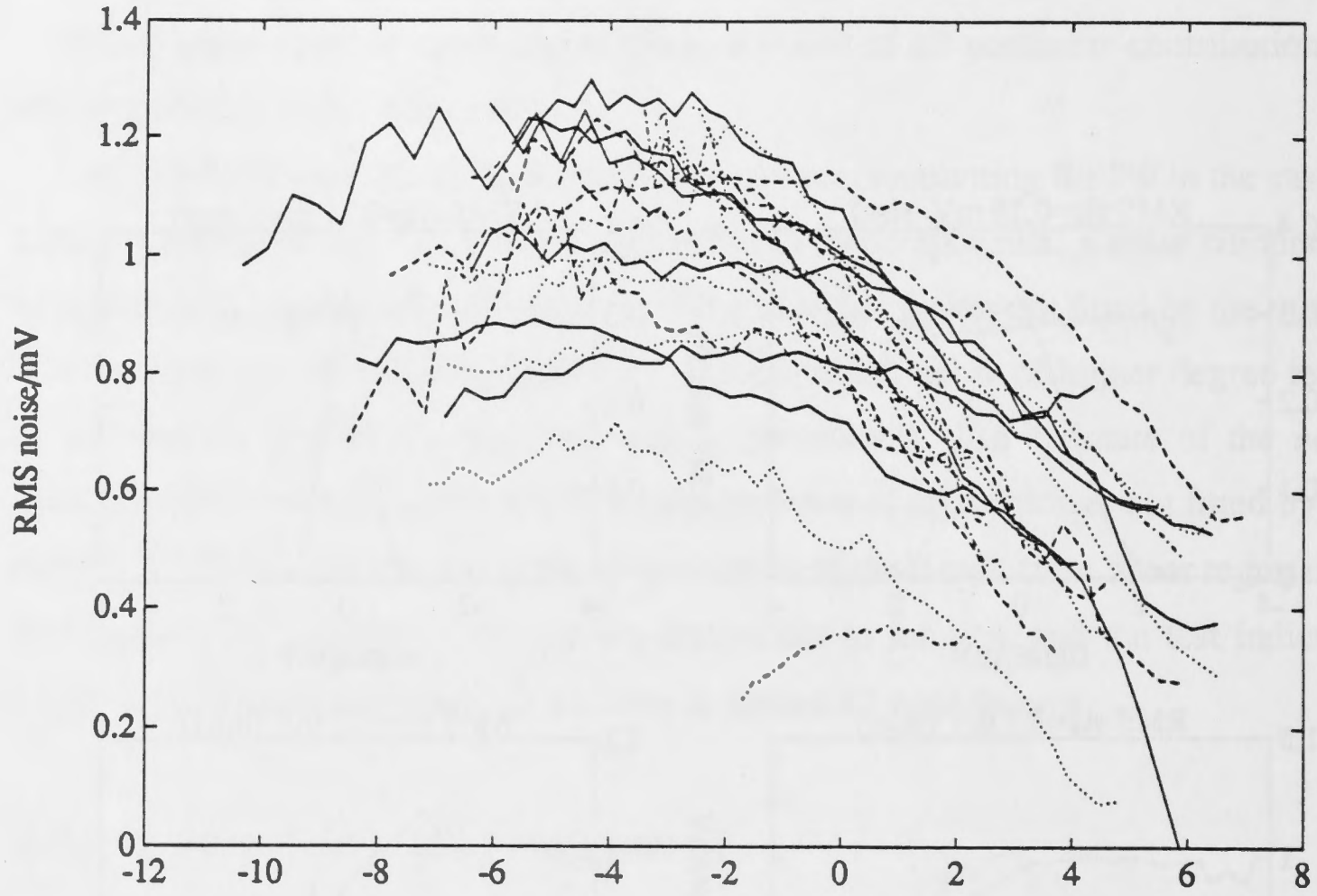

Figure 67: Noise RMS plotted against signal amplitude for a number of LMC experiments. The data was selected as follows: for each experiment only signal amplitudes for which the signal amplitude density was more than 10% of the maximum signal amplitude density were included. The experiments for which the remaining noise RMS values were all below 1.5 mV were then selected for plotting.

introducing complexities into the study of information-theoretic aspects of sensory coding in this system.

4.8 Polarity asymmetry and light adaptation

Light adaptation is a fundamental requirement of biological visual systems, which allows them to operate over a wide range of light intensities. Mechanisms of light adaptation act at a number of levels in the early visual system. In the receptor there is optical attenuation by migration of screening pigment (Howard *et al* 1987), and there is control of the gain of the biochemical transduction pathway linking photon absorption to receptor membrane sodium conductance. Changes in other receptor membrane conductivities affect the voltage response for a given sodium conductance (Muijser 1979, Weckström *et al* in press). There are also changes in the properties of transmission from receptor to LMC (Laughlin *et al* 1987).

Light adaptation can be defined broadly as a change in the response to a sustained stimulus (Laughlin 1989b). This definition includes the high-pass filtering of the visual signal in transmission to the LMC cells, since a step in stimulus intensity produces a response which peaks and then declines.

From the point of view of the kernel-operator models used in this thesis a different definition is natural, which will be used throughout this section. Kernel-operator models describe response as a function of stimulus in terms of kernels of various degrees, playing a role analogous to the coefficients in a Taylor series. These kernels are dependent on the point around which the series is expanded, that is, on the mean intensity of stimulation. It is natural to define light adaptation of the kernel-operator model as the change in the kernels as the mean intensity varies. For a stimulus varying with low contrast about a mean intensity, the high-pass filtering is still important in modelling the response, however by this definition we would not say that light adaptation is taking place. Conversely, when a sustained step in stimulus intensity is applied, a new set of kernels will be required to model the response, and light adaptation has taken place. Any sustained response is described as light adaptation of the zero-degree kernel.

The range of prediction of a set of kernels at a given mean intensity is limited by a number of factors: the truncation of the series at a certain degree, the restricted memory lengths used, and the noise present in the kernel elements estimated. Nevertheless, it is of interest to see what the model predicts when a sustained step is present in the stimulus. From a set of kernels at one mean intensity predictions can be made of the kernels pertaining to a neighbouring light adaptation state.

This question leads in particular to an interesting interpretation of the quadratic kernels. If light adaptation processes have an effect within the memory length of the estimated kernels, then this effect will appear in the kernels. In particular, the quadratic kernels will reflect light adaptation, since the quadratic kernel-operator introduces polarity asymmetry into the model, so that the response to an increment of light intensity is not the negative of the response to a decrement.

Let us deal initially with intensity kernels, as defined in section 2.1.4, and denoted throughout this section by capital H. When the stimulus is represented by fluctuation in intensity about a mean level

$$I(t) = I_0 + \Delta I(t)$$

the intensity kernels define a model mapping in terms of monomial operators in ΔI. Noting terms to degree two this is:

$$r = H_0 + [H_1]\Delta I + [H_2]\Delta I^{2\otimes} + \ldots$$

Consider a change in mean intensity, to a new level I_0', where

$$I_0' = I_0 + \Delta I_0$$

If the intensity fluctuates about this new value such that

$$I(t) = I_0' + \Delta I'(T)$$

then the input to the above polynomial model is:

$$\Delta I(t) = \Delta I_0 + \Delta I'(t)$$

The model response can then be expanded as follows, assuming the symmetric form for the quadratic kernel:

$$\begin{aligned} r &= H_0 + [H_1](\Delta I_0 + \Delta I') + [H_2](\Delta I_0 + \Delta I')^{2\otimes} + \ldots \\ &= H_0 + \\ &\quad [H_1]\Delta I_0 + [H_1]\Delta I' + \\ &\quad [H_2]\Delta I_0^{2\otimes} + 2[H_2]\Delta I_0 \otimes \Delta I' + [H_2](\Delta I')^{2\otimes} + \\ &\quad \ldots \end{aligned}$$

Since ΔI_0 is constant with time, the terms in the first column of the expansion evaluate to constants, and form part of the zero degree kernel at the new mean intensity. The terms in the second column are linear in $\Delta I'$. The second term of the expansion of the quadratic monomial evaluated at time t is:

$$\begin{aligned} 2[H_2]\Delta I_0 \otimes \Delta I'(t) &= 2\int_0^m \int_0^m H_2(t_1, t_2)\, \Delta I_0\, \Delta I'(t - t_2)\, dt_1\, dt_2 \\ &= \int_0^m \left(2\Delta I_0 \int_0^m H_2(t_1, t_2)\, dt_1\right) \Delta I'(t - t_2)\, dt_2 \end{aligned}$$

This is a linear kernel-operator mapping of $\Delta I'$, with the kernel as shown in parentheses.

If the linear kernel at the new mean intensity is denoted by H_1', then we have:

$$H_1'(t) = H_1(t) + 2\Delta I_0 \int_0^m H_2(t_1, t)\, dt_1 + \ldots$$

The linear kernel has thus been incremented by a scalar multiple of the marginal integral of the quadratic kernel. Similar terms can be added for the influence of higher

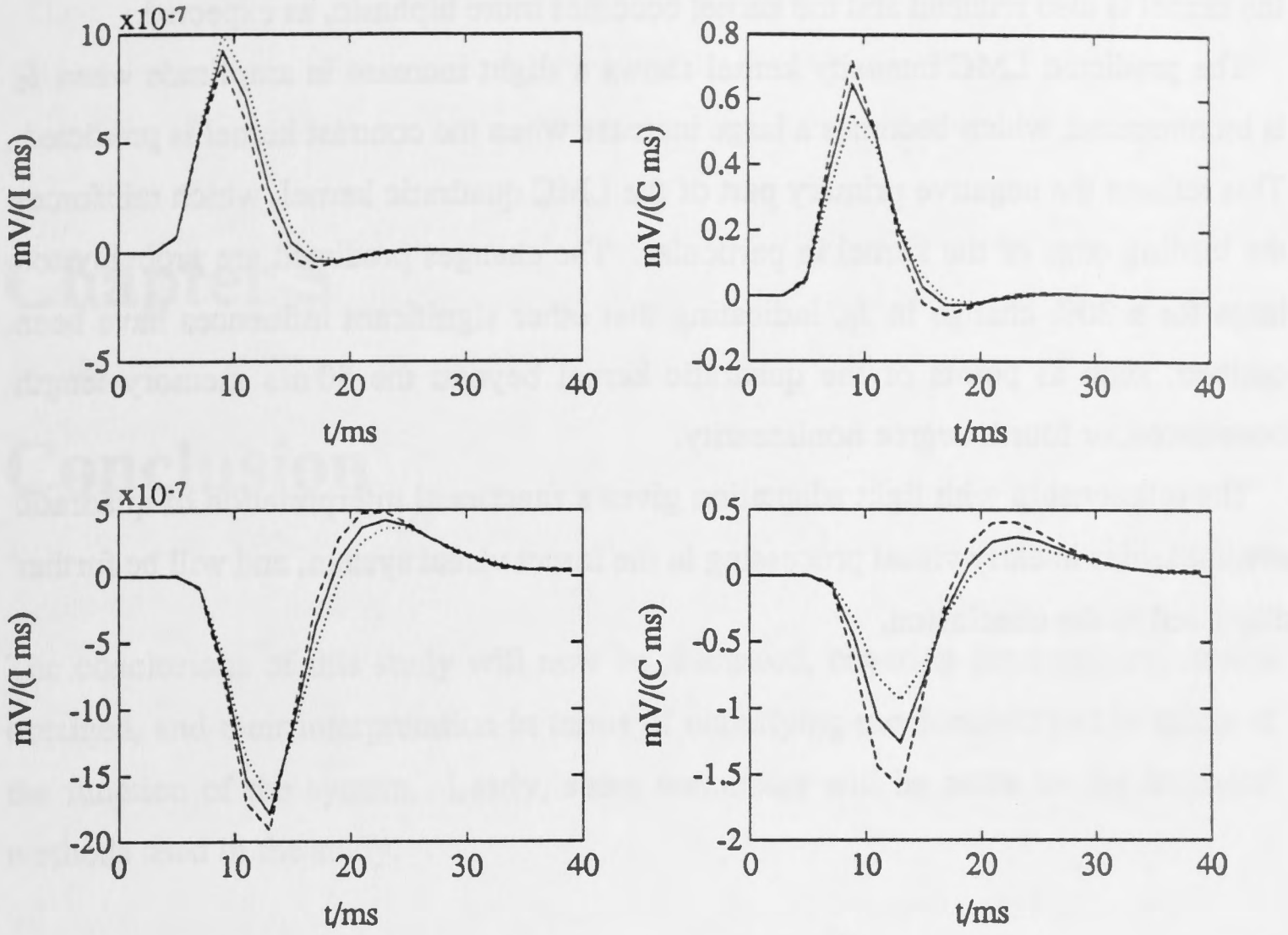

Figure 68: Predicted linear kernels at neighbouring adaptation states, taking into account the quadratic kernel, as described in text. Each plot shows the measured linear kernel (solid line), the predicted linear kernel when I_0 is incremented by 20% (dashed line), and when I_0 is decremented by 20% (dotted line). **Left**, intensity kernels, in units $mV/(I\,ms)$, where I is the unit of intensity, $ph\,s^{-1}\,rec^{-1}$. The unincremented mean intensity is estimated as $I_0 = 7 \times 10^5\,ph\,s^{-1}\,rec^{-1}$. **Right**, contrast kernels, in units $mV/(C\,ms)$. **Upper**, from an *Eristalis* receptor (rqba). **Lower**, from an *Eristalis* LMC (lkma).

degree kernels on H_1, but these will be of higher degree in ΔI_0, and thus less significant for small ΔI_0.

The contrast kernels, h_n, used throughout this thesis are related to intensity kernels as derived in section 2.1.4:

$$h_n = I_0^n H_n$$

The linear contrast kernel at the new mean intensity, h_1', is thus:

$$h_1'(t) = \frac{I_0'}{I_0} h_1(t) + 2\frac{\Delta I_0 I_0'}{I_0^2} \int_0^m h_2(t_1, t)\, dt_1$$

Figure 68 shows the linear kernels predicted in this way for increment and decrement of I_0 by 20%, for a receptor and an LMC. For the receptor intensity kernel, the quadratic effect reduces the amplitude when I_0 is incremented, and increases the amplitude when I_0 is decremented. When the contrast kernel is predicted however, the changes are reversed, with an increment in I_0 leading to greater contrast gain. The peak-time of

the kernel is also reduced and the kernel becomes more biphasic, as expected.

The predicted LMC intensity kernel shows a slight increase in amplitude when I_0 is incremented, which becomes a large increase when the contrast kernel is predicted. This reflects the negative primary part of the LMC quadratic kernel, which reinforces the leading edge of the kernel in particular. The changes predicted are probably too large for a 20% change in I_0, indicating that other significant influences have been omitted, such as points of the quadratic kernel beyond the $50\,ms$ memory length considered, or fourth degree nonlinearity.

The relationship with light adaptation gives a functional interpretation of quadratic nonlinearities in early visual processing in the insect visual system, and will be further discussed in the conclusion.

Chapter 5

Conclusion

The conclusions of this study will now be discussed, covering the empirical results obtained, and their interpretation in terms of underlying mechanisms and in terms of the function of the system. Lastly, some comments will be made on the technical methods used in the study.

5.1 Empirical results

The receptors and LMCs of insect visual systems have received considerable attention in the past. By generating more general forms of description of system behaviour, this study has extended the empirical knowledge of this system in a number of new directions, besides supplementing existing results.

Studies of the visual system can be characterised by the aspects of system behaviour which are described. Among the aspects of response behaviour of neurons involved in early visual processing are: temporal dynamics, spatial properties, nonlinearities, and light adaptation.

The linear spatiotemporal model represents temporal and spatial aspects together. We have seen that the LMC kernels are not space-time separable, hence this is a valuable representation, and temporal filtering and lateral antagonism cannot accurately be treated as separate processes. The distribution of antagonism on the spatiotemporal domain is variable, particularly in the presence and amplitude of the laterally extended antagonistic flanks. Where these flanks are present they occur not at the same latency as the primary response, nor at the same latency as the antagonistic phase on-axis, but at an intermediate latency.

The distribution of antagonism on two-dimensional space, as seen in simulated step-responses, is concentrated in two lobes, placed horizontally or diagonally relative to the receptive field centre.

The study of nonlinearity in the receptor-LMC system has in the past been mainly restricted to static models. The sigmoidal dependence of response amplitude on the size of a step stimulus has been measured at different mean intensities (*eg* Laughlin and Hardie 1978, Laughlin *et al* 1987). Kernels from the spot-annulus experiments in this study represent the temporal dynamics of nonlinear components of response. These are estimated to second degree for stimulation in centre and surround, and to third degree in the centre.

The kernels display a number of characteristic parts which are repeated across experiments, although parts have variable amplitudes and are sometimes absent. Quadratic and cubic kernels seem to have both tensor product structure, with regions oriented parallel to the axes, and structure oriented diagonally on their domains. In the quadratic LMC kernels the two components have considerable variation in relative amplitude. The time courses of the linear and cubic kernels is comparable, while the quadratic kernels have different timing.

Light adaptation was not extensively studied, with only two levels of illumination used. The changes in properties between the two levels were significant, and generally as expected. Briefly, at the lower level, latencies were longer and kernels were less biphasic. Contrast gain was reduced, and responses had smaller percentages nonlinear contribution. Spatial properties did not change markedly. Properties at the two levels were examined separately, hence the dynamics of adaptation was not studied, apart from the role of the quadratic kernel discussed in section 4.8.

Although the study of noise properties was not a principal goal of the project, examination of the deviation in response between stimulus repeats produced interesting evidence counter to the almost universal assumption of independent additive noise, in the case of LMC cells. The distribution of LMC response amplitudes is seen to be skewed towards positive values, particularly in the case of the spot-annulus experiments.

5.2 Models derived from the kernels

The kernels derived from recorded responses produce an empirical model of system behaviour. A number of models have been developed at a second level, in which Parametric curves and structural models have been fitted to the observed kernels.

The temporal linear kernels are fitted well by the double log-normal family of curves, providing a convenient parametric form for simulation of system behaviour. Simulation of model electrical networks suggests that the flow of currents across passive electrical elements in the lamina array may account not only for lateral antagonism, as suggested by Shaw (1975), but also for the temporal high-pass filtering occurring in retina-LMC transmission, as suggested by Laughlin (1974). The production of both phenomena by the same mechanism is made possible by assuming the presence of significant capacitance and resistance of the glial cell membranes separating lamina cartridges.

Concerning the nonlinear kernels, great effort was made not merely to present them, but to use them to make inferences about the organisation of the system by fitting structural models. Linear and parts of the cubic kernels are fitted well by assuming a presynaptic high-pass filtering operation and a sigmoidal characteristic curve for the receptor-LMC synaptic transmission.

The quadratic kernels produce difficulties for structural modelling, and the puzzle is not yet entirely solved. The quadratic kernels introduce polarity asymmetry into the model system, and may reflect light adaptation processes, as described in section 4.8. Light adaptation is a regulatory process operating over many log-units of intensity range. We can state with confidence that feedback will play a central role in such a process. Structural modelling of feedback networks is a much less developed theoretical field than the modelling of feedforward-only networks. Furthermore, the work which has been done perhaps uses a formalism which is not appropriate in the present context, as it generally considers systems in which a nonlinear operator produces a feedback signal which is added linearly at an earlier point in the network. The formalisation appropriate for treating adaptation processes, I would suggest, is where a feedback signal causes modification of the *operators* in earlier parts of the network.

The simplest example is a system with *gain control*, such as the phototransduction process, whereby large values of output lead to a reduction in transduction gain, hence

in the amplitude of the transduction intensity kernels. In the case of phototransduction, the time-course of kernels is also altered. This approach may hold the key to the interpretation of quadratic nonlinearities in this system.

5.3 Function of the retina-LMC transformation

The interpretation of the processing in the early stages of the insect visual system in terms of function has been most developed in the work of Laughlin and collaborators (review, Laughlin 1989a). The retinal array of the insect forms a neural image of the visual scene, transducing light intensity into intracellular voltages. The mechanisms of transduction, however, may impose constraints on the form of the receptor response. Thus the transmission from the receptors to the LMCs of the lamina can be seen as a dynamic image processing operation which recodes the neural image in a form more suitable for subsequent levels of visual processing.

Following the conceptual path of Barlow (1961), the recoding is examined in terms of the concepts of the information theory of Shannon (Shannon and Weaver 1949). The limitations on information capacity of the channels in this system are of three kinds: the noise introduced at each stage of the system, the limitation of dynamic range of the cells set by the reversal potentials of the ions involved, and the restricted frequency bandwidth of the system.

The convergence of six receptors onto each LMC reduces the effect of receptor noise power by a factor of six. Amplification during the receptor-LMC transmission produces a stronger signal, lessening the effect of noise added at later stages. The large number of receptor-LMC synapses, 200 per receptor, ensures that the high gain of transmission does not introduce excessive synaptic noise (Laughlin 1973).

To avoid saturation of the LMC response, this amplification is complemented by filtering, to reduce the low frequency components in space and time. The form of this filtering has been compared with the optimum given by the predictive coding formalisation (Srinivasan *et al* 1982), which leads to broad, weak antagonistic fields when the signal to noise ratio is low, at low levels of illumination, and narrow, strong antagonistic fields at high light levels. The temporal results in this thesis are compatible with these predictions, although the weakness of the lateral antagonism found suggests that spatial effects are of less importance than the theory predicts. The nonseparability

of the kernels on the space-time domain further complicates the issue. I have applied the predictive coding formalisation in the spatiotemporal case, however the results lacked stability, and were at variance with the observed LMC kernels.

The limitation in dynamic range of neural signals distinguishes these systems from many engineering applications. The limitation to signal strength in electrical and radio communication systems is generally the mean power passing through the channel. The distribution of signal amplitudes having the maximum entropy for a given mean power is the Gaussian distribution, which also leads to the simplest mathematical treatment.

Laughlin (1981b, 1982) suggested that the sigmoidal characteristic curve of the receptor-LMC synapse optimised the coding of visual signals by transforming the Gaussian distribution of contrasts seen in the environment to a uniform distribution of response amplitude in the LMC. This would be the optimum distribution given additive noise present in the LMC. As noted in this thesis, LMC noise appears to be non-additive, although the results are still qualitatively consistent with the optimisation, since the amplitude distributions indicate that positive amplitudes occur more frequently, for which the noise power is less. The difficulty in pursuing this question quantitatively is in estimating the statistical properties of the signals occurring during the normal physiological functioning of the fly.

We thus conclude that the results obtained in this study are generally compatible with information theoretic interpretations, although they in some cases suggest complexities not yet taken into account which would require further study.

Concerning the nonlinear components of response, the percentages of power present suggest that the receptor-LMC system is *primarily* linear, but with significant nonlinearity present. The nonlinearities can be interpreted as providing secondary functions, complementing the primary linear processes. The cubic component appeared largely to reflect the sigmoidal shape of the synaptic characteristic curve, and is thus involved in the transformation of amplitude distribution described above. Quadratic nonlinearities may reflect light adaptation of the system, and thus have an important functional role in that respect.

Considering the overall visual system of the fly, the processing taking place can be viewed as a data reduction, from the ten thousand signals in the ommatidia of the retina, to the small number of actions of which the fly is capable. Another approach to early visual processing is to assume that data reduction is already occurring in the

receptor-LMC transformation. The two approaches are largely consistent, in that many of the concepts of information theory are applicable to a data reduction process: the goal of producing output data with the minimum possible noise contamination, and the coding of the output data in a form suitable for transmission through the subsequent channel.

Classical information theory, developed in the context of communications engineering, is concerned with the preservation and transmission of information. It produces definitions for measuring information production rates and channel capacities, in bits per second, and produces coding algorithms for effectively using channel capacities. What is required is a more general theory of *information processing*. Classical information theory would then be a special case, in which the aim is to maximise the total mutual information between a systems input and output. In an information processing system in general, some aspects of information might be deliberately discarded, while some derived quantities are calculated from the inputs in a many-to-one fashion.

5.4 Technical conclusion

Some comments are due concerning the techniques used in this study. The essence of the system identification methodology used is, in my opinion, the form of representation of system behaviour which is produced.

The kernel-operator model of the mapping from input to output gives a quantitative description of the behaviour of the system in response to a large class of stimuli. The models are readily generalised to account for multiple input channels or a general spatiotemporal input, and to account for nonlinear components of response, at least of low degree.

The kernels produced provide empirical results of general interest, as well as giving a description of system behaviour suitable for interpretation in terms of function.

The kernel-operator description is also readily suited to the construction of structural models consisting of networks of operators, as pursued in chapter 4. The notation devised was found to be of great use in the treatment of such networks. By removing the extraneous parts of the usual model representation, in particular the time variables and variables of integration, a notation is produced which allows more fluent algebraic expression of models, as well as allowing high-level translation into machine-usable

form for numerical calculation.

The kernel description allows some inferences to be made about the mechanisms underlying a system's behaviour, although in this respect it is probably best regarded as complementary to techniques which probe mechanisms more directly, such as voltage and current clamp and pharmacological techniques. Similarly, although the stimulus used is natural, in the sense of involving low contrast modulation which keeps the system in its physiological range, the more traditional stimuli such as high contrast flashes may be more revealing in terms of mechanism precisely because they drive the system beyond its normal operating range.

The use of a stochastic stimulus is a less essential aspect of the method. Wiener suggested the use of a white-noise test input envisaging that the signal would be produced by a truly random process, shot-noise, and that the data analysis would be done using analog computation.

At present most system identification is done using digital computer equipment, allowing complete control over the stimulus presented. This control, when available, allows the use of deterministic test inputs producing precisely orthogonal designs, as described in section 2.4.5. The theoretical development of the white-noise technique has come mainly from an electrical engineering or signal processing perspective. When viewed from the perspective of mathematical statistics, the use of orthogonal design in experimentation is quite traditional. In fact, in statistics, orthogonal design is of less importance now than previously, since many statistical calculations have computational requirements easily met by modern computers. In the identification of dynamical systems, however, the size of designs is so large that orthogonal design is an important concept. Thus, in active system identification, methods such as the m-sequence technique developed by Sutter may be of increasing value.

The methods of obtaining least-squares kernel estimates for large designs developed in this thesis may have their greatest applicability in the area of *passive system identification*, where system inputs are sampled by the experimenter but cannot be controlled, thus greatly extending the range of applications for nonlinear system identification.

Concerning the spatial design of stimuli, in the introduction it was noted that previous reports of implementations of spatiotemporal white-noise analysis have stressed the technical viability of the technique, rather than presenting new scientific results.

This study has developed another implementation and used it to produce results, by addressing an issue for which the analysis could give useful answers, that is, the precise form of antagonism of the LMC response on the spatiotemporal domain. We note that the spatiotemporal representation was only fitted to first degree, with the nonlinear analysis being performed for a stimulus with reduced dimensionality. A conclusion of this study is that the spatiotemporal stimulus cannot be viewed as a universal stimulus rendering all other stimuli obsolete, due to the combinatorial explosion in the number of kernel points involved, a limitation which will hold irrespective of the data analysis techniques used. Rather, the design of the stimuli must be developed interactively according to the system under examination, with a variety of designs addressing different aspects of system behaviour.

Bibliography

Abramowitz M, Stegun IA (1984) *Pocketbook of mathematical functions*. Verlag Harri Deutsch, Thun Frankfurt/Main

Arnett DW (1971) Receptive field organisation in the first ganglion of Diptera. *Science* 173:929–931

Arnett DW (1972) Spatial and temporal integration properties of units in first optic ganglion of dipterans. *J Neurophysiol* 35:429–444

Barlow HB (1961) The coding of sensory messages. In: Thorpe WH, Zangwill OL (eds) *Current problems in animal behaviour*. University Press, Cambridge

Bell RA (1970) Principles of cathode-ray tubes, phosphors, and high-speed oscillography. Application note 115. Hewlett Packard, Colorado.

Billings SA, Fakhouri SY (1978) Identification of a class of nonlinear systems using correlation analysis. *Proc IEE* 7:691–697

Boschek CB (1971) On the fine structure of the peripheral retina and lamina ganglionaris of the fly, *Musca domestica. Z Zellforsch* 118:369–409

Braitenberg V (1967) Patterns of projection in the visual system of the fly. I. Retina-lamina projections. *Exp Brain Res* 16:184–209

Bullock TH, Horridge GA (1965) *Structure and function in the nervous systems of invertebrates*. W H Freeman, San Francisco and London

Cajal SR, Sánchez D (1915) Contribución al conocimiento de los céntros nerviosos de los inséctos. *Trab Lab Invest Biol Univ Madrid* 13:1–164

Chen HW, Ishii N, Suzumura N (1986) Structural classification of non-linear systems by input and output measurements. *Int J Systems Sci* 17:741–774

Citron MC, Emerson RC, Levick WR (1988) Nonlinear measurement and classification of receptive fields in cat retinal ganglion cells. *Ann Biomed Eng* 16:65–77

Dongarra JJ, Moler CB, Bunch JR, Stewart GW (1979) *LINPACK user's guide*. SIAM, Philadelphia

Dubs A (1982) The spatial integration of signals in the retina and lamina of the fly compound eye under different conditions of luminance. *J Comp Physiol A* 146:321–343

Dubs A, Laughlin SB, Srinivasan MV (1981) Single photon signals in fly photoreceptors and first order interneurons at behavioural threshold. *J Physiol* 317:317–334

Emerson RC, Citron MC, Vaughn WJ, Klein SA (1987) Nonlinear directionally selective subunits in complex cells of cat striate cortex. *J Neurophysiol* 58:33–65

Enroth-Cugell C, Robson JG, Schweitzer-Tong DE, Watson AB (1983) Spatio-temporal interactions in cat retinal ganglion cells showing linear spatial summation. *J Physiol* 341:279–307

Falk G, Fatt P (1972) Physical changes induced by light in the rod outer segments of vertebrates. In: Dartnell HJA (ed) *Handbook of sensory physiology, Vol 7/1*. Springer-Verlag, Berlin

Fein P, Payne R (1989) Phototransduction in *Limulus* ventral photoreceptors: roles of calcium and inositol trisphosphate. In: Stavenga DG, Hardie RC (eds) *Facets of vision*. Springer-Verlag, Berlin Heidelberg

Frechet M (1910) Sur les fonctionnels continues. *Ann Ec Norm Sup* 27:193–219

French AS (1979) The effect of light adaptation on the dynamic properties of phototransduction in the fly *Phormia regina*. *Biol Cybern* 32:115–123

French AS (1980) The linear dynamic properties of phototransduction in the fly compound eye. *J Physiol* 308:385–401

French AS, Järvilehto M (1978) The transmission of information by first and second order neurons in the fly visual system. *J Comp Physiol* 126:87–96

Fuortes MGF, Hodgkin AL (1964) Changes in the time scale and sensitivity in the ommatidia of *Limulus*. *J Physiol* 172:239–263

Hardie RC (1985) Functional organisation of the fly retina. In: Autrum H, Ottoson D (eds) *Progress in sensory physiology 5*. Springer-Verlag, Berlin Heidelberg New York Toronto

Hardie RC (1987) Is histamine a neurotransmitter in insect photoreceptors? *J Comp Physiol* 161:201–213

Hardie RC (1989) A histamine-activated chloride channel involved in neurotransmission at a photoreceptor synapse. *Nature* 339:704–706

Hateren JH van (1986b) An efficient algorithm for cable theory, applied to blowfly photoreceptor cells and LMCs. *Biol Cybern* 54:301–311

Hida E, Naka K-I (1982) Spatio-temporal receptive field as revealed by spatio-temporal random noise. *Z Naturforsch* 37c:1048–1049

Horridge GA, Mimura K, Tsukahara Y (1975) Fly photoreceptors. II. Spectral and polarized light sensitivity in the drone fly *Eristalis*. *Proc R Soc B* 190:225–237

Howard J, Dubs A, Payne R (1984) The dynamics of phototransduction in insects: a comparative study. *J Comp Physiol A* 154:707–718

Howard J, Blakeslee B, Laughlin SB (1987) The intracellular pupil mechanism and photoreceptor signal:noise ratios in the fly *Lucilia cuprina*. *Proc R Soc Lond B* 231:415–435

Jack JJB, Noble D, Tsien RW (1975) *Electric current flow in excitable cells*. Clarendon Press, Oxford

Järvilehto M, Weckström M, Kouvalainen E (1989) Signal coding and sensory processing in the peripheral retina of the compound eye. In: Naresh Singh R, Strausfeld NJ (eds) *Neurobiology of sensory systems*. Plenum Publishing Corporation, New York

Kirschfeld K (1967) Die projektion der optischen Umwelt auf das Raster der Rhabdomere im Komplexauge von *Musca*. *Exp Brain Res* 3:248–270

Korenberg MJ (1973) Identification of biological cascades of linear and static nonlinear systems. *Proceedings of the 16th Midwest symposium circuit theory* 18-2:1–9

Korenberg MJ (1988) Identifying nonlinear difference equation and functional expansion representations: the fast orthogonal algorithm. *Ann Biomed Eng* 16:123–142

Korenberg MJ, Hunter IW (1986) The identification of nonlinear biological systems: LNL cascade models. *Biol Cybern* 55:125–134

Korenberg MJ, Bruder SB, McIlroy PJ (1988a) Exact orthogonal kernel estimation from finite data records: extending Wiener's identification of nonlinear systems. *Ann Biomed Eng* 16:201–214

Korenberg MJ, French AS, Voo SKL (1988b) White-noise analysis of nonlinear behavior in an insect sensory neuron: kernel and cascade approaches. *Biol Cybern* 58:313–320

Kuster JE, French AS (1985) Changes in the dynamic properties of locust photoreceptors at three levels of light adaptation. *Biol Cybern* 52:333–337

Laughlin SB (1973) Neural integration in the first optic neuropile of dragonflies. I. Signal amplification in dark-adapted second order neurons. *J Comp Physiol* 84:335–355

Laughlin SB (1974) Neural integration in the first optic neuropile of dragonflies. III. The transfer of angular information. *J Comp Physiol* 92:377–396

Laughlin SB (1981a) Neural principles in the peripheral visual system of invertebrates. In: Autrum H (ed) *Handbook of sensory physiology, Vol VII/6B*. Springer-Verlag, Berlin Heidelberg New York

Laughlin SB (1981b) A simple coding procedure enhances a neurons information coding capacity. *Z Naturforsch* 36c:910–912

Laughlin SB (1982) Matching coding to scenes to enhance efficiency. In: Braddick OJ, Sleigh AC (eds) *The physical and biological processing of images*. Springer, Berlin-Heidelberg-New York

Laughlin SB (1984) The roles of parallel channels in early visual processing by the arthropod compound eye. In: Ali MA (ed) *Photoreception and vision in invertebrates*. Plenum Press, New York London

Laughlin SB (1989a) Coding efficiency and design in visual processing. In: Stavenga DG, Hardie RC (eds) *Facets of vision*. Springer-Verlag, Berlin

Heidelberg

Laughlin SB (1989b) The role of sensory adaptation in the retina. *J Exp Biol* 146:39–62

Laughlin SB, Hardie RC (1978) Common strategies for light adaptation in the peripheral visual systems of fly and dragonfly. *J Comp Physiol A* 128:319–340

Laughlin SB, Osorio D (1989) Mechanisms for neural signal enhancement in the blowfly compound eye. *J Exp Biol* 144:113–146

Laughlin SB, Howard J, Blakeslee B (1987) Synaptic limitations to contrast coding in the retina of the blowfly *Calliphora*. *Proc R Soc Lond B* 231:437–467

Lee YW, Schetzen M (1965) Measurement of the Wiener kernels of a non-linear system by cross-correlation. *Int J Control* 2:237–254

Lillywhite PG (1977) Single photon signals and transduction in an insect eye. *J Comp Physiol* 122:189–200

Little J, Shure L (1988) *Signal processing toolbox for use with Matlab*. Mathworks, MA

McCann G (1974) Nonlinear identification theory models for successive stages of visual nervous systems of flies. *J Neurophysiol* 37:869–895

McCann GD, Fargason RD, Shantz VT (1977) The response properties of retinula cells in the fly *Calliphora erythrocephala* as a function of the wavelength and polarization properties of visible and ultraviolet light. *Biol Cybern* 26:93–107

Marmarelis PZ, McCann GD (1973) Development and application of white-noise modeling techniques for studies of insect visual nervous system. *Kybernetik* 12:74–89

Marmarelis PZ, Marmarelis VZ (1978) *Analysis of physiological systems. The white noise approach*. Plenum Press, New York

Marmarelis PZ, Naka K-I (1972) White-noise analysis of a neuron chain: an application of the Wiener theory. *Science* 175:1276–1278

Marmarelis PZ, Naka K-I (1973a) Nonlinear analysis and synthesis of receptive-field responses in the catfish retina, Part I: Horizontal cell → ganglion cell chain. *J Neurophysiol* 36:605–618

Marmarelis PZ, Naka K-I (1973b) Nonlinear analysis and synthesis of receptive-field responses in the catfish retina, Part II: One-input white-noise analysis. *J Neurophysiol* 36:619–633

Marmarelis PZ, Naka K-I (1973c) Nonlinear analysis and synthesis of receptive-field responses in the catfish retina, Part III: Two-input white-noise analysis. *J Neurophysiol* 36:634–648

Marmarelis VZ, McCann GD (1977) A family of quasi-white random signals and its optimal use in biological system identification. Part II: Application to the photoreceptors of *Calliphora erythrocephala*. *Biol Cybern* 27:57–62

Mizuno M, Imai S, Tsukada M, Hida E, Naka K-I (1985) A micro-computer system for spatio-temporal visual receptive field analysis. *IEEE Trans Biomed Eng* BME–32:56–59

Muijser H (1979) The receptor potential of retinular cells of the blowfly *Calliphora*:The role of sodium, potassium and calcium ions. *J Comp Physiol* 132:87–95

Nässel DR (1988) Serotonin and serotonin-immunoreactive neurons in the nervous system of insects. *Progress Neurobiol* 30:1–86

Nässel DR, Hagberg M, Seyan HS (1983) A new, possibly serotonergic neuron in the lamina of the blowfly optic lobe: an immunocytochemical and Golgi-EM study. *Brain Res* 280:361–367

Payne R, Howard J (1981) Response of an insect photoreceptor: a simple log-normal model. *Nature* 290:415–416

Powers RL, Arnett DW (1981) Spatio-temporal cross-correlation analysis of catfish retinal neurons. *Biol Cybern* 42:179–196

Press WH, Flannery BP, Teukolsky SA, Vettering WT (1988) Numerical Recipes in C. Cambridge University Press

Rugh WJ (1981) *Nonlinear system theory. The Volterra/Wiener approach.* Johns Hopkins University Press, Baltimore and London

Sakai HM, Naka K-I, Korenberg MJ (1988) White-noise analysis in visual neuroscience *Vis Neurosci* 1:287–296

Sakuranaga M, Sato S, Hida E, Naka K-I (1986) Nonlinear analysis: mathematical theory and biological applications. *CRC Critical Reviews in Biomedical Engineering* 14:127–184

Schetzen M (1980) *The Volterra and Wiener theory of nonlinear systems*. John Wiley, New York

Scholes JH (1964) Discrete subthreshold potentials from the dimly lit insect eye. *Nature* 202:572–573

Shannon CE, Weaver W (1949) *The mathamatical theory of communication*. University of Illinois Press, Urbana.

Shaw SR (1975) Retinal resistance barriers and electrical lateral inhibition. *Nature* 255:480–483

Shaw SR (1981) Anatomy and physiology of identified non-spiking cells in the photoreceptor-lamina complex of the compound eye of insects, especially Diptera. In: Roberts A, Bush BMH (eds) *Neurons without impulses*. Cambridge University Press

Shaw SR (1984) Early visual processing in insects. *J Exp Biol* 112:225–251

Shaw SR (1989) The retina-lamina pathway in insects, particularly Diptera, viewed from an evolutionary perspective. In: Stavenga DG, Hardie RC (eds) *Facets of vision*. Springer-Verlag, Berlin Heidelberg

Srinivasan MV, Laughlin SB, Dubs A (1982) Predictive coding: a fresh look at inhibition in the retina. *Proc R Soc Lond B* 216:427–459

Stark L (1969) The pupillary control system: its nonlinear adaptive and stochastic engineering design characteristics. *Automatica* 5:655–676

Strausfeld NJ (1971) The organization of the insect visual system (Light microscopy). I. Projections and arrangements of neurons in the lamina ganglionaris of Diptera. *Z Zellforsch* 121:377–441

Strausfeld NJ, Nässel DR (1981) Neuroarchitecture of brain regions that subserve the compound eyes of crustacea and insects. In: Autrum H (ed) *Handbook of sensory physiology, Vol VII/6B*. Springer-Verlag, Berlin Heidelberg New York

Sutter EE (1975) A revised conception of visual receptive fields based on pseudorandom spatio-temporal pattern stimuli. In: McCann GD, Marmarelis PZ (eds) *Proceedings of the first symposium on testing and identification of nonlinear systems*. California Institute of Technology, Pasadena

Sutter EE (1987) A practical nonstochastic approach to nonlinear time-domain anaysis. In: Marmarelis VZ (ed) *Advanced methods of physiological system modelling, Vol I*. Biomedical Simulations Resource, USC, Los Angeles

Victor JD, Knight BW (1979) Nonlinear analysis with an arbitrary stimulus ensemble. *Q Appl Math* 37:113–136

Victor JD, Shapley RM (1980) A method of nonlinear analysis in the frequency domain. *Biophys J* 29:459–484

Victor JD, Shapley RM, Knight BW (1977) Nonlinear analysis of cat retinal ganglion cells in the frequency domain. *Proc Natl Acad Sci* 74:3068–3072

Volterra V (1958) *Theory of functionals and of integro-differential equations*. Dover Publications, New York

Weckström M, Kouvalainen E, Järvilehto M (1988) Non-linearities in response properties of insect visual cells: An analysis in time and frequency domain. *Acta Physiol Scand* 132:103–113

Weckström M, Kouvalainen E, Djupsund K, Järvilehto M (1989) More than one type of conductance is activated during responses of blowfly monopolar neurones. *J Exp Biol* 144:147–154

Weckström M, Hardie RC, Laughlin SB (in press) The role of voltage activated potassium channels in blowfly photoreceptors.

Wiener N (1958) *Nonlinear problems in random theory*. Wiley, New York

Yasui S, Davis W, Naka K-I (1979) Spatio-temporal receptive field measurement of retinal neurons by random pattern stimulation and cross-correlation. *IEEE Trans Biomed Eng* BME–26:263–272

Zettler F, Järvilehto M (1971) Decrement-free conduction of graded potentials along the axon of a monopolar neuron. *Z Vergl Physiol* 68:202–210

Zettler F, Järvilehto M (1972) Lateral inhibition in an insect eye. *Z Vergl Physiol* 76:233–244

Zettler F, Straka H (1987) Synaptic chloride channels generating hyperpolarising responses in monopolar neurones of the blowfly visual system. *J Exp Biol* 131:435–438